



저작자표시-비영리-변경금지 2.0 대한민국

이용자는 아래의 조건을 따르는 경우에 한하여 자유롭게

- 이 저작물을 복제, 배포, 전송, 전시, 공연 및 방송할 수 있습니다.

다음과 같은 조건을 따라야 합니다:



저작자표시. 귀하는 원저작자를 표시하여야 합니다.



비영리. 귀하는 이 저작물을 영리 목적으로 이용할 수 없습니다.



변경금지. 귀하는 이 저작물을 개작, 변형 또는 가공할 수 없습니다.

- 귀하는, 이 저작물의 재이용이나 배포의 경우, 이 저작물에 적용된 이용허락조건을 명확하게 나타내어야 합니다.
- 저작권자로부터 별도의 허가를 받으면 이러한 조건들은 적용되지 않습니다.

저작권법에 따른 이용자의 권리는 위의 내용에 의하여 영향을 받지 않습니다.

이것은 [이용허락규약\(Legal Code\)](#)을 이해하기 쉽게 요약한 것입니다.

[Disclaimer](#)

공학박사 학위논문

산화 환원 매개체를 활용한 고용량
고효율 리튬-공기 전지 개발에 관한
연구

**Exploitation of redox mediators for the development
of lithium-oxygen batteries with high energy density
and high efficiency**

2021 년 2 월

서울대학교 대학원

재료공학부

고영민

산화 환원 매개체를 활용한 고용량 고효율
리튬-공기 전지 개발에 관한 연구

**Exploitation of redox mediators for the development
of lithium-oxygen batteries with high energy density
and high efficiency**

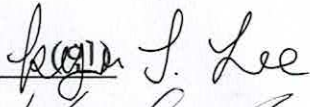
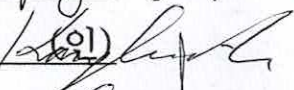
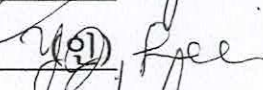
지도교수 강 기 석

이 논문을 공학박사 학위논문으로 제출함
2021 년 2 월

서울대학교 대학원
재료공학부

고 영 민

고영민의 박사 학위논문을 인준함
2021년 1월

위원장	이규태	
부위원장	강기석	(인) 
위원	최장욱	(인) 
위원	이윤정	(인) 
위원	류원희	(인) 

Abstract

Exploitation of redox mediators for the development of lithium-oxygen batteries with high energy density and high efficiency

Ko, Youngmin

Department of Materials Science and Engineering

College of Engineering

The Graduate School

Seoul National University

Encounter with energy and environment issue is inevitable for human being to construct a clean and sustainable future. In this regard, the development of energy storage system to facilitate the exploitation of renewable energy resources is essential mission. After continued research during last decades, Li-ion battery is widely employed as the state-of-the-art battery system. However, exploiting heavy transition metal as core component, Li-ion battery possesses clear limitation in terms of energy density enhancement. Scientists have explored various battery chemistry to replace current Li-ion battery such as metal-air, metal-sulfur and organic battery. Especially, Li-O₂ battery has received enormous research interest owing to its extremely high theoretical energy density of 3500 Wh kg⁻¹. Despite of its potential, however, limitations stemmed from intrinsic nature of the system still prevents the practical use of Li-O₂ battery.

In this dissertation, I developed and designed high-performance Li-O₂ battery by introducing redox-mediating catalyst, redox mediator to regulate reaction chemistry of Li-O₂ battery. With a virtue of redox mediator capable of controlling reaction path, disadvantageous conventional discharge/charge path could be circumvented. Under redirected redox-mediated reaction path, problems originated from conventional path could be successfully released. For the design of better redox mediators, multidisciplinary study from the exploration of a new materials to the understanding on fundamental aspects was conducted. Furthermore, practical issues in cell environment such as shuttle phenomena was also addressed to optimize the use of redox mediators.

Charter 2 introduces the procedure of exploration of a novel redox mediator from biological system. Inspired by the similarity between cell respiration process in biology and redox-mediated oxygen reduction reaction process in Li-O₂ battery, the biological catalyst, vitamin K2 was introduced into Li-O₂ battery as redox mediator to facilitate oxygen reduction reaction, and it was demonstrated that it successfully works as catalyst and boosts the performance of the cell. This chapter will provide guideline on how similarity can motivate new findings.

Chapter 3 describes research approach to understand fundamental aspects of redox mediator from reaction kinetics to reaction mechanism. With comparative study employing various redox mediators, I revealed the factors affecting catalytic kinetics and its significant on cell performance. On oxygen reduction reaction, (*i.e.* discharge) kinetics of redox mediators is governed by steric hindrance around redox center, which reveals that the nature of electron transfer during redox-mediated reaction is inner-sphere electron transfer where intermediate state presents. Further

study on its implication on cell performance demonstrated the presence of volcano behavior between kinetics and cell performance. Similarly, kinetics of redox mediator during oxygen evolution reaction (*i.e.* charge) was also investigated and it was shown that its kinetic is primarily determined by redox potential of mediator following Marcus theory. Followed study showed that higher kinetics results in better rate capability of Li-O₂ cell. This chapter demonstrates the importance of understanding intrinsic properties of redox mediator to design highly performing catalyst.

Lastly, chapter 4 demonstrates strategies to address practical shuttle phenomena of redox mediators. Owing to freely diffusible nature, redox mediator easily diffuses to unwanted reactive anode side causing severe side reactions such as anode degradation and mediator decomposition. By anchoring redox mediator in polymer chain, shuttle phenomenon was suppressed while still maintaining charge-carrying property by polymer in-chain hole diffusion mechanism. As the second approach, a novel Janus liquid electrolyte was employed to fully maintain diffusion behavior and at the same time prevent shuttle phenomena. With the simultaneous use of two liquid electrolytes with distinct solvation capability at two electrodes, the diffusion of redox mediator from cathode to anode side was blocked and thus, shuttle effect was prevented. This chapter demonstrates appropriate treatment on cell system can suppress shuttle phenomena and enables sustainable use of redox mediators.

I believe the multifaceted study in this dissertation on redox mediator with three major approaches, i) exploration of a new catalyst, ii) investigation on fundamentals, and iii) dealing with practical issues will serve as the solid foundation in developing high-performance redox mediator for Li-O₂ battery. In addition, it will

provide research motivation and insight to design optimized catalyst for metal-air battery and furthermore, next-generation energy storage system.

Keywords: Electrochemistry, Secondary batteries, Lithium-oxygen batteries, Redox mediators, Reaction kinetics, Shuttle phenomena

Student Number: 2016-20847

Contents

List of Tables	x
----------------------	---

List of Figures	xi
-----------------------	----

Chapter 1. Introduction	1
--------------------------------------	----------

1.1. Research objectives	1
--------------------------------	---

1.2. Introduction to lithium-oxygen batteries.....	2
--	---

1.3. Principle of redox mediators	5
---	---

1.4. References	10
-----------------------	----

Chapter 2. Exploring a novel redox mediator inspired by biological system	14
--	-----------

2.1 Research background.....	14
------------------------------	----

2.2 Experimental method.....	17
------------------------------	----

2.2.1 Preparation of cells and conditions for electrochemical tests	17
---	----

2.2.2 Characterization	18
------------------------------	----

2.2.3 Quantitative analysis of discharge product	19
--	----

2.3 Result and discussion	20
---------------------------------	----

2.3.1 Similarity between redox mediation in biological system and lithium-oxygen cell	20
---	----

2.3.2 Vitamin K2 as a stable mediator for lithium–oxygen batteries.....	23
2.3.3 Mechanism of vitamin K2-mediated discharge	39
2.3.4 Charging the cell discharged with vitamin K2.....	43
2.4 Concluding remarks.....	52
2.5 References	53

Chapter 3. Investigation on the fundamentals of redox

mediators	61
3.1 Understanding fundamental aspects of redox mediator for oxygen reduction reaction	61
3.1.1 Research background.....	61
3.1.2 Experimental method.....	64
3.1.2.1 Material preparation.....	64
3.1.2.2 Lithium-oxygen cell assembly.....	65
3.1.2.3 Electrochemical analysis and characterization.....	65
3.1.2.4 Calculation detail.....	66
3.1.3 Results and discussions.....	67
3.1.3.1 The principles of redox mediator for the oxygen reduction reaction.....	67
3.1.3.2 The catalytic activity of quinones and its kinetics	73
3.1.3.3 The dependence of kinetic parameters on the kinetics of redox mediators.....	82
3.1.3.4 Marcus theory: steric effect and inner-sphere electron transfer.....	92

3.1.3.5 Reaction mechanism: a significance of inner-sphere electron transfer	97
3.1.3.6 The implication of kinetics in the performance of lithium-oxygen cell	101
3.1.4. Supplement note.....	113
3.1.5. Concluding remarks	114
3.1.6. References.....	116
3.2 Kinetics of redox mediator for oxygen evolution reaction.....	124
3.2.1 Research background.....	124
3.2.2 Experimental method.....	127
3.2.2.1 Preparation of lithium–oxygen cells	127
3.2.2.2 Conditions for electrochemical tests	128
3.2.3 Results and discussions.....	129
3.2.4. Concluding remarks	156
3.2.5. References.....	157

Chapter 4. Addressing practical issue of redox mediators

: shuttle phenomena	162
4.1 Anchorage of redox mediator for sustainable redox mediation in lithium-oxygen batteries	162
4.1.1 Research background.....	162
4.1.2 Experimental method.....	165
4.1.2.1 Synthesis of PTMA.....	165
4.1.2.2 Fabrication of cell components	167

4.1.2.3 Assembly of lithium–oxygen cell.....	168
4.1.2.4 Conditions for electrochemical tests and characterization	168
4.1.3 Results and discussions.....	170
4.1.4. Supplement note.....	198
4.1.4.1 Calculations of Nitroxyl Radical Concentration.....	198
4.1.4.2 Electron diffusion phenomenon in PTMA.....	199
4.1.4.3 PTMA as catalysts for lithium–oxygen batteries.....	199
4.1.4.4 Degradation mechanism of the lithium–oxygen cell containing PTMA.....	201
4.1.4.5 Abnormal initial discharge plateau.....	202
4.1.5. Concluding remarks.....	205
4.1.6. References.....	206
4.2 Janus liquid electrolyte for shuttle-free redox mediation in lithium- oxygen batteries.....	214
4.2.1 Research background.....	214
4.2.2 Experimental method.....	217
4.2.2.1 Materials preparation.....	217
4.2.2.2 Cell assembly and conditions for electrochemical test.....	218
4.2.2.3 Characterization.....	219
4.2.3 Results and discussions.....	220
4.2.3.1 Design and preparation of Janus liquid electrolyte.....	220
4.2.3.2 Electrochemical properties of lithium–oxygen cell employing Janus liquid electrolyte.....	228
4.2.4. Concluding remarks.....	244
4.2.5. References.....	245

Chapter 5. Conclusion 253

Chapter 6. Abstract in Korean 256

Curriculum Vitae..... 259

List of Tables

Table 3.1. The redox potential of quinones obtained from cyclic voltammetry.	72
Table 3.2. Kinetic collection efficiency of quinones obtained by the ratio of ring current to disk current in the RRDE experiment.....	80
Table 3.3. Diffusivity of quinones. It was calculated by the RDE experiment with various rotating speeds.....	86
Table 3.4. Heterogeneous electron transfer rate constant for quinones. It was calculated by the RDE experiment.....	89
Table 3.5. Discharge capacity with average and standard deviation. The galvanostatic discharge experiment was conducted three time	106

List of Figures

Figure 1.1. Basic reaction mechanism of Li-O ₂ battery on discharge and charge process.	7
Figure 1.2. Schematics showing the formation and decomposition of discharge product, Li ₂ O ₂ , with the mediation of redox mediator	8
Figure 1.3. The properties of the RM-employing Li-O ₂ battery critically influenced by the intrinsic characteristics of RM	9

Figure 2.1. (a) Simplified biological system in <i>E. coli</i> . The electron transfer with proton shuttling between NADH dehydrogenases and the cytochrome b-c ₁ complex is mediated by vitamin K ₂ . (b) Comparison of relative redox potentials among vitamin K ₂ and other species in the redox mediating processes in <i>E. coli</i> and lithium-oxygen batteries. (c) Lithium-oxygen battery system with vitamin K ₂ as potential ORR RM. The electron transfer with lithium ion shuttling between the electrode and Li ₂ O ₂ is mediated by the ORR RM, vitamin K ₂	22
---	----

Figure 2.2. (a) Cyclic voltammogram of vitamin K ₂ in 1 M LiTFSI DME showing consistent profile up to 200 cycles, confirming the stability of vitamin K ₂ and reduced vitamin K ₂ under the electrolyte. (b) Cyclic voltammogram of coenzyme Q in 1 M LiTFSI DME showing irreversible redox reaction	29
--	----

Figure 2.3. (a) Cyclic voltammograms of vitamin K ₂ showing stable redox reaction of vitamin K ₂ in 1 M LiTFSI DME under various scan rates. (b) Cyclic voltammograms of vitamin K ₂ showing the catalytic effect of vitamin K ₂ under an O ₂ atmosphere with the presence of Li ⁺ ions under a scan rate of 50 mV s ⁻¹ ..	30
--	----

Figure 2.4. (a) Discharge profile of the lithium-oxygen cell with and without	
--	--

vitamin K2 at various current rates. The discharge capacity is enhanced by 30 times with the use of vitamin K2. (b) Enlarged view of (a) showing the discharge capacity in the absence of vitamin K2..... 31

Figure 2.5. The amount of oxygen consumption during discharge measured by tracking change of oxygen pressure 32

Figure 2.6. Optical images and SEM images of pristine electrode and electrodes discharged without vitamin K2 and with vitamin K2 33

Figure 2.7. SEM images of (a), (d) pristine electrode, (b), (e) fully discharged electrode of the cell not containing vitamin K2, and (c), (f) fully discharged electrode of the cell containing vitamin K2. With the use of vitamin K2, the morphology of the discharge product transformed into toroidal-like particles..... 34

Figure 2.8. X-ray diffraction pattern of discharge electrode 35

Figure 2.9. Raman and IR spectra of electrode discharged with vitamin K2. 36

Figure 2.10. (a) Ultraviolet–visible (UV–vis) spectra for various amounts of Li_2O_2 powder (purity of 92.8%). (b) Fitted graph showing proportionality between peak intensity at 407 nm and amount of Li_2O_2 powder (black dots) and the same data for an electrode discharged with and without vitamin K2 (orange dots) showing yields of 86% and 78%, respectively. The capacities for the electrode samples were converted based on the dilution ratio difference between the powder and electrode samples. For the electrode without vitamin K2, commercial carbon paper was used. All the titration solutions containing Li_2O_2 powder or discharged electrode were produced as described in the experimental section. 37

Figure 2.11. (a) Galvanostatic discharge profile under current rate of 0.18 mA cm^{-2} and (b) bar graph, comparing the catalytic activity of vitamin K2 with that of DBBQ, coenzyme Q and other quinone derivatives. All experiments were done with 0.01 M of each molecule in 1 M LiTFSI in DME. Vitamin K2 and DBBQ show exceptionally

better catalytic activity (i.e. discharge capacity) than coenzyme Q and other quinone derivatives. (Notations for each species are as follows; BBQ(2-tert-Butyl-1,4-benzoquinone), MBQ(Methyl-p-benzoquinone), MD(Menadion), CoQ(Coenzyme Q)) 38

Figure 2.12. Schematic illustrations comparing the mechanism of Li_2O_2 formation with and without vitamin K2. Without the presence of vitamin K2, Li_2O_2 is formed through a surface-absorbed intermediate, LiO_2 , because of its low stability in a low-DN solvent. However, with the presence of vitamin K2, Li_2O_2 is formed in the electrolyte solution through disproportionation by generating a new intermediate, which is stable even in low-DN solvent..... 41

Figure 2.13. Electron energy (redox potential) diagram related to the working mechanism of vitamin K2. Because vitamin K2 has a higher redox potential than O_2 in the presence of both Li^+ and O_2 , it is reduced by an electron from the electrode before O_2 . Then, because of the difference in electron energy in LiVKO_2 and Li_2O_2 , the electron flow is thermodynamically driven from LiVKO_2 to Li_2O_2 while forming Li_2O_2 in the solution..... 42

Figure 2.14. Inability to charge the cell containing only vitamin K2. Because of the poor contact of the discharge product with the electrode, it was rarely possible to decompose (charge) via direct electron conduction through the electrode surface 46

Figure 2.15. Cyclic voltammograms under scan rate of 50 mV s^{-1} showing that vitamin K2 and TEMPO can undergo redox reactions independently in the presence of each other 47

Figure 2.16. Galvanostatic profile of $\text{Li}-\text{O}_2$ cell with current density of 0.18 mA cm^{-2} containing vitamin K2 (0.01 M) and TEMPO (0.1 M). 48

Figure 2.17. Analysis of gas evolved during the charge process showing the

evolution of oxygen due to decomposition of Li_2O_2 with TEMPO 49

Figure 2.18. SEM image of the electrode from the cell containing vitamin K2 and TEMPO after (a) discharge to 0.7 mAh cm^{-2} and (b) charge to the same capacity 50

Figure 2.19. (a) Digital photo of the solutions for UV-vis titration prepared by discharged and charged cells. The solutions were prepared using air electrode and separator together with H_2O and TiOSO_4 solution as explained in experimental section. Considering the yellow color of the solution is indication of Li_2O_2 , it is shown that Li_2O_2 was clearly decomposed during charge. (b) UV-vis absorption spectrum of the solutions. Peak intensity at 407 nm is assigned to the yellow color from $[\text{Ti}(\text{O}_2)]^{2+}$ complex in the solutions 51

Figure 3.1. Energy relationship during oxygen reduction reaction with a redox mediator. Electrochemical reduction of quinone occurs, followed by chemical electron transfer to oxygen to form lithium peroxide..... 69

Figure 3.2. Benzoquinone candidates with various functional groups. 12 different colors were assigned to each quinone. Each abbreviation denotes following quinones: MBQ (Methyl-p-benzoquinone), DMBQ (2,5-Dimethyl-1,4-benzoquinone), TMBQ (2,3,5-Trimethyl-1,4-benzoquinone), DQ (Duroquinone), TQ (Thymoquinone), BBQ (2-tert-Butyl-1,4-benzoquinone), 25DBBQ (2,5-Di-tert-butyl-1,4-benzoquinone), 26DBBQ (2,6-Di-tert-butyl-1,4-benzoquinone), DOBQ (2,5-Di-tert-octyl-1,4-benzoquinone), PBQ (2-Phenyl-1,4-benzoquinone), DPBQ (2,5-Di-phenyl-1,4-benzoquinone), and DCBQ (2,5-Dichloro-1,4-benzoquinone)..... 70

Figure 3.3. Cyclic voltammetry profile of quinones at the scan rate of 50 mV s^{-1} . 1 M LiTFSI TEGDME electrolyte containing 10 mM of quinone was used as an

electrolyte	71
Figure 3.4. Cyclic voltammetry profiles quinones in Ar and O ₂ atmosphere. 1M LiTFSI TEGDME with 10 mM of each quinone and the scan rate of 50 mV s ⁻¹ were used. A distinct amount of current increase in O ₂ atmosphere which is related to the catalytic activity was observed.....	76
Figure 3.5. Schematics showing the reactions occurring at rotating ring disk electrode. At disk electrode quinone is reduced and drifts out to ring electrode where reduced quinone is oxidized.....	77
Figure 3.6. Linear sweep voltammetry profile with rotating ring disk electrode. 1M LiTFSI TEGDME containing 1 mM of quinone and the scan rate of 10 mV s ⁻¹ were used. Ring current, disk current, and kinetic collection efficiency (ratio of two current) were shown.....	78
Figure 3.7. Kinetic collection efficiency of all quinones showing a wide range of distribution	79
Figure 3.8. Linear sweep voltammetry profile with RRDE of PBQ under Ar atmosphere. Theoretical maximum collection efficiency was obtained.....	81
Figure 3.9. LSV profile with RRDE at various rotating speeds. 1M LiTFSI TEGDME with 1 mM of quinone and the scan rate of 10 mV s ⁻¹ were used..	84
Figure 3.10. The plot of (rotating speed) ^{1/2} vs. limiting current and linear fitting line. Diffusivity can be calculated by the slope of the fitting line.....	85
Figure 3.11. The plot of (rotating speed) ^{-1/2} vs. current ⁻¹ profile of quinones at various overpotential and linear fitting lines whose y-intercept indicates i _k ⁻¹	87
Figure 3.12. The plot of overpotential vs. log(i _k) and linear fitting line whose y-intercept indicates log(i ₀)	88
Figure 3.13. The dependence of diffusivity on catalytic kinetics.....	90
Figure 3.14. The dependence of heterogeneous electron transfer rate on catalytic	

kinetics	91
Figure 3.15. The dependence of catalytic kinetics on driving force, which is explained by Marcus theory and steric effect. The shaded area denotes inverted region	95
Figure 3.16. (a) several functional groups' A-value that quantifies the magnitude of steric hindrance.54 (b) the order of steric hindrance of DMBQ, TQ, 25DBBQ, and DOBQ	96
Figure 3.17. DFT calculation result showing the stable formation of LiQO ₂ species. Reduced state of several representative quinones (a) DMBQ, (b) 25DBBQ, and (c) 26DBBQ form stable complex with Li ⁺ to form LiQ. Then it is followed by the formation of LiQO ₂ complex. d) two LiQ complexes do not form stable complex between two	99
Figure 3.18. Schematics showing the reaction mechanism of redox-mediated discharge in lithium-oxygen batteries	100
Figure 3.19. Galvanostatic discharge experiment profiles under the current density of 0.2 mA cm ⁻² . 1M LiTFSI TEGDME containing 10 mM of quinone was used as an electrolyte.....	104
Figure 3.20. The relationship between discharge capacity and catalytic kinetics showing volcano behavior. Quinones are grouped into three depending on their discharge capacity	105
Figure 3.21. Scanning electron microscopy images of a representative quinone from each group; MBQ from group 1,(left) 25DBBQ from group 2,(mid) and TMBQ from group 3.(right)	107
Figure 3.22. SEM images of the electrode before discharge and discharged without quinone. The surface of the electrode discharged without quinone is passivated by a film-like discharge product	108

Figure 3.23. X-ray diffraction pattern of discharged electrode in quinone-containing cells confirmed that the toroidal discharge product is lithium peroxide 109

Figure 3.24. (a) SEM images of quinone included in group 1. In all three quinones, BBQ, PBQ, DPBQ, low magnification SEM images show not much difference from the quinone-free case. A higher magnification image shows that the formation of toroidal discharge products is limited so that electrode is passivated without achieving high discharge capacity. (b) SEM images of DOBQ (group 2). Low magnification SEM images show consistent result with 25DBBQ case, the formation of discharge product filling void space between fibers 110

Figure 3.25. SEM images of quinone belonging to group 3. In all cases, the formation of the discharge product was observed. However, the discharge product covers the electrode surface, leading to the passivation and low discharge capacity 111

Figure 3.26. Schematic illustration showing the influence of kinetics on the passivation behavior in three different cases, limited kinetics, moderate kinetics, and excessive kinetics 112

Figure 3.27. Schematic illustrations showing detailed mechanism of RM-assisted charge with the effect of each step on the RM concentration at the electrode surface and galvanostatic charge profiles under various kinetic conditions. Detailed mechanism of RM-assisted charge consisting of 1) electrochemical oxidation of the RM, 2) diffusion of RM^+ and RM, and 3) chemical decomposition of lithium peroxide by RM^+ . Step 1 causes an increase of $\frac{C_{RM^+}}{C_{RM}}$ at the electrode surface and step 2 and step 3 result in a decrease of $\frac{C_{RM^+}}{C_{RM}}$ 139

Figure 3.28. Schematic illustrations of galvanostatic charge profile in (a) ideal case and (b) actual case. With an infinite rate of diffusion and decomposition of lithium

peroxide (ideal case), the RM concentration remains constant, and therefore, the voltage also remains constant. In the real case, however, because the rates of diffusion and lithium peroxide decomposition are finite, and the RM concentration decreases and the charge voltage increases as charge proceeds. The increase in charge voltage is accelerated by increasing current, thereby shortening the stable voltage plateau. 140

Figure 3.29. RDE experiment to analyze the rate of lithium peroxide decomposition by RM^+ . Schematic illustrations displaying the oxidative current increase by the EC mechanism 141

Figure 3.30. LSV profiles with RDE of (a) TEMPO, (b) MPT, (c) DMPZ, and (d) TTF. All the voltage scans were conducted at a scan rate of 1 mV s^{-1} using 1 M LiTFSI in DME containing 1 mM of the RM and 30 mM of dispersed Li_2O_2 powder. 142

Figure 3.31. LSV profile with RDE using redox reaction that is unreactive toward Li_2O_2 powder. The reduction of butyl-benzoquinone, where the reduced species is inert to Li_2O_2 powder, was utilized to investigate the limiting current decrease from the decreased diffusivity with dispersed Li_2O_2 powder. The reduction in $i_{l,a}$ was observed to be reduced by approximately 28.6% because of the decreased diffusivity in the Li_2O_2 -dispersed solution. This result implies that a decrease of $i_{l,a}$ of less than 28.6% indicates the regeneration of RM because of reaction with lithium peroxide. 143

Figure 3.32. (a) Corrected increase in $i_{l,a}$ of selected redox couple; the corrected current increases from each redox couple are as follows: TEMPO/TEMPO⁺, 50.05%; MPT/MPT⁺, 31.91%; DMPZ/DMPZ⁺, 23.14%; DMPZ⁺/DMPZ²⁺, 59.51%; TTF/TTF⁺, 27.92%; and TTF⁺/TTF²⁺, 25.43%. (b) Plot of increase in $i_{l,a}$ vs. redox

potential 144

Figure 3.33. Cyclic voltammogram using 1 M LiTFSI in DME containing 50 mM of (a) TEMPO, (b) MPT, (c) DMPZ, and (d) TTF. The scan rate was 100 mV s^{-1} . All the redox reactions were measured to be reversible with the following calculated equilibrium redox potentials: TEMPO/TEMPO⁺, 3.73 V; MPT/MPT⁺, 3.82 V; DMPZ/DMPZ⁺, 3.26 V; DMPZ⁺/DMPZ²⁺, 3.94 V; TTF/TTF⁺, 3.42 V; and TTF⁺/TTF²⁺, 3.76 V (all the values are expressed vs. Li/Li⁺ potential) 145

Figure 3.34. Cyclic voltammograms of (a) TEMPO, (b) MPT, (c) DMPZ, and (d) TTF for scan rates ranging from 100 to 500 mV s^{-1} . The experiment was conducted using 1 M LiTFSI in DME containing 50 mM of the RM 146

Figure 3.35. The plot of (scan rate)^{1/2} vs. peak current of cyclic voltammogram using 1 M LiTFSI in DME containing 50 mM of (a) TEMPO, (b) MPT, (c) DMPZ, and (d) TTF for various scan rates ranging from 100 to 500 mV^{-1} . The diffusivity of each RM was calculated from the linear relationship between (scan rate)^{1/2} and the peak current using the Randles–Sevcik equation..... 147

figure 3.36. (a) Calculated diffusivities of RMs determined using Randles–Sevcik equation. (b) Plot of diffusivity vs. increase in $i_{l,a}$ showing overall kinetic properties RM 148

Figure 3.37. Galvanostatic cycling and corresponding dQ/dV profiles of lithium–oxygen cells containing RMs. Galvanostatic cycling profiles under various current rate from 0.2 to 5.0 mA cm^{-2} of the cell containing (a) TEMPO, (b) MPT, (c) DMPZ, and (d) TTF. Corresponding dQ/dV profiles for the cell containing (e) TEMPO, (f) MPT, g) DMPZ, and h) TTF 149

Figure 3.38. DEMS gas analysis while charging a lithium–oxygen battery under a current rate of 1.0 mA cm^{-2} using (a) TEMPO, (b) MPT, (c) DMPZ, and (d) TTF.

The grey and black lines indicate the O₂ and CO₂ emission, respectively 151

Figure 3.39. Cyclic voltammograms and corresponding plots of peak current vs. (scan rate)^{1/2}. Cyclic voltammograms of 1 M LiTFSI in (a) DEGDME and in (c) TEGDME with 50 mM TEMPO for scan rates ranging from 100 to 500 mV s⁻¹. Plots showing a linear relationship between peak current and (scan rate)^{1/2} for 1 M LiTFSI in (b) DEGDME and (d) TEGDME 152

Figure 3.40. Viscosity of DME, DEGDME, and TEGDME and diffusivity of TEMPO in these ether-based electrolytes 153

Figure 3.41. Ionic conductivity and viscosity of various ether-based electrolyte. The measured ionic conductivity is 13.39, 7.62, and 2.62 mS cm⁻¹ at 300 K for 1M LiTFSI DME, 1M LiTFSI DEGDME, and 1M LiTFSI TEGDME, respectively. The electrolytes with higher viscosity have a tendency to show lower ionic conductivity 154

Figure 3.42. Galvanostatic cycling profiles and dQ/dV profiles of TEMPO-containing lithium–oxygen cell with 50 mM TEMPO in 1 M LiTFSI in DEGDME (a and b) and 50 mM TEMPO in 1 M LiTFSI in TEGDME (c and d)..... 155

Figure 4.1. Galvanostatic charge profile using 2 M LiTFSI TEGDME with 10 mM of TEMPO, showing the capacity from TEMPO far exceeding the theoretical value 177

Figure 4.2. (a) Images of lithium metal before cycling (top) and after 5 cycles without TEMPO (left) and with TEMPO (right). (b) SEM images of lithium metal surface of cell cycled without TEMPO (left) and with TEMPO. (right)..... 178

Figure 4.3. UV–vis absorption spectra of TEMPO-containing electrolyte before cycling and after cycling 179

Figure 4.4. (a) Profiles of lithium–oxygen cell without any RMs, showing significant charge overpotential. (b) Profiles of cell containing 10 mM TEMPO, showing that the effect of TEMPO in reducing the charge overpotential weakens with repeated cycling

..... 180

Figure 4.5. Cycling performance of lithium–oxygen cells without and with TEMPO. The cells were cycled with a current density of 300 mA g⁻¹..... 181

Figure 4.6. Schematic illustrations of the working processes of TEMPO and PTMA. For typical RMs such as TEMPO, oxidation of the RM occurs in the electrolyte. Then, RM⁺ diffuses to Li₂O₂ and chemically decomposes it. In addition, the diffusible nature of RMs leads to the movement of RM⁺ toward the reactive lithium metal anode side, which is referred to as the shuttle phenomenon. The shuttle phenomenon reduces the efficiency of Li₂O₂ decomposition by RM⁺. Furthermore, when RM⁺ makes contact with the lithium metal anode, it promotes side reactions such as lithium metal oxidation and RM decomposition. However, as a polymer-based RM, PTMA is not accompanied by the shuttle phenomenon because it is fixed at the air electrode in the solid state. The electron transfer between polymer chains replaces the diffusion of RM molecules of typical RMs..... 182

Figure 4.7. Reaction scheme of PTMA synthesis by GTP and RP methods. (a) Reaction scheme of GTP-PTMA synthesized by group transfer polymerization (GTP) after the nitroxyl radical formation. (b) Reaction scheme of RP-PTMA synthesized by radical polymerization (RP) before the nitroxyl radical formation..... 183

Figure 4.8. SQUID profiles and EPR spectra of the two PTMA polymers. Plots of $\chi_{paramagnetic}^{-1}$ vs. temperature and Curie–Weiss fittings of (a) GTP-PTMA and (b) RP-PTMA. EPR spectra of 10⁻³ M chloroform solution containing (c) GTP-PTMA and d) RP-PTMA 184

Figure 4.9. Galvanostatic charge profile of PTMA synthesized by GTP method. PTMA synthesized by the GTP method had a clear charge voltage plateau at ~3.6 V (vs. Li/Li⁺) and delivered almost the theoretical specific capacity 185

Figure 4.10. Images of PTMA dissolved in electrolyte. The PTMA did not dissolve in 2 M LiTFSI TEGDME until 1 month. The ratio between PTMA and the electrolyte was the same as that in assembled PTMA-loaded lithium–oxygen cells 186

Figure 4.11. Linear sweep voltammetry profiles of electrodes showing that PTMA-mediated Li₂O₂ decomposition occurs 187

Figure 4.12. SEM images of (a) pristine carbon electrode and (b) electrode after PTMA coating. TEM images of each sample are presented in the insets 188

Figure 4.13. X-ray diffraction patterns of pristine, discharged, and charged electrodes using PTMA 189

Figure 4.14. SEM images of (a) pristine Ketjen black air electrode and electrode (b) after discharge and (c) after charge 190

Figure 4.15. Profile of first galvanostatic cycle of PTMA-containing lithium–oxygen cell compared with those without PTMA or TEMPO. The cell was cycled using 2 M LiTFSI TEGDME at a current density of 300 mA g_{carbon}⁻¹ 191

Figure 4.16. Gas evolution profile during the first charging 192

Figure 4.17. UV–vis absorption spectra of electrolyte of PTMA-containing lithium–oxygen cell before and after 5 cycles 193

Figure 4.18. Images of (a) pristine lithium metal anode and anode after 5 cycles (b) without and (c) with PTMA 194

Figure 4.19. Titration result for Li₂O₂ pre-loaded electrode after charging with TEMPO and PTMA. The standard deviation is also displayed 195

Figure 4.20. Cyclability of RM-free and TEMPO-/PTMA-containing lithium–oxygen cells. All the cells were cycled at a current density of 300 mA g_{carbon}⁻¹

.....	196
Figure 4.21. Profile of PTMA-containing lithium–oxygen cell showing the sustainable charge voltage plateau from PTMA for more than 50 cycles, which is attributed to the prevention of shuttling	197
Figure 4.22. (a) Galvanostatic full discharge and charge profile of PTMA-loaded lithium-oxygen cells with voltage cut-off of 2.2 V (orange line) and 2.6 V (red line). (b) Galvanostatic cycling profile with the capacity cut-off of 500 mAh g ⁻¹ after experiencing a full cycling with the voltage cut-off of 2.2 V (orange line). For comparisons, the profile of the PTMA-free cell following the same experimental sequence with 2.2 V cut-off is displayed together. (black line)	204
Figure 4.23. Photographs showing the immiscibility behavior of the control electrolyte (1 M LiTFSI DMSO/1 M LiTFSI TEGDMEL) (left) and Janus liquid electrolyte (1 M LiTFSI DMSO/2.3 M TEGDME) (right)	224
Figure 4.24. (a) NMR and (b) Raman spectra of the top and bottom phases of the Janus liquid electrolyte (shown in figure 4.23, left).....	225
Figure 4.25. Photographs showing the dissolution of 16.7 mM I ₃ ⁻ (oxidized RM) in the control electrolyte (left) and Janus liquid electrolyte (right)	226
Figure 4.26. <i>In-situ</i> observation of I ₃ ⁻ diffusion behavior using transparent beaker cell. (a) The beaker-cell construction with the single-phase electrolyte (left) and Janus liquid electrolyte (right). Gold and nickel foam were used as the working and counter electrode, respectively. A Ag/Ag ⁺ electrode was used as the reference electrode. (b) Time-dependent I ₃ ⁻ diffusion behavior in single-phase and Janus liquid electrolyte. In the single-phase electrolyte, the yellow I ₃ ⁻ diffused to all areas of the electrolyte after 120 min of oxidation. In contrast, for the Janus liquid electrolyte, I ₃ ⁻ did not diffuse to the anode side and instead remained at the cathode side ..	227
Figure 4.27. Schematic illustration of the fabrication of the gel-state electrolyte	

using UV-curing-assisted printing process. Details of the procedure are elaborated in the experimental section.....	233
Figure 4.28. Photographs of lithium metal anode: (a) pristine, (b) cycled with single-phase electrolyte, and (c) cycled with Janus liquid electrolyte	234
Figure 4.29. Photographs of lithium metal after cycling 20 times in a lithium/1 M LiTFSI DMSO/lithium symmetric cell under oxygen atmosphere	235
Figure 4.30. SEM images of lithium metal surface: (a) pristine, (b) cycled 20 times with single-phase electrolyte, and (c) cycled 20 times with Janus liquid electrolyte	236
Figure 4.31. Galvanostatic profiles showing remaining active lithium metal after cycling with single-phase and Janus liquid electrolyte. Thin lithium metal foil with a thickness of 20 μm was used	237
Figure 4.32. Structure of lithium–oxygen cell with single-phase bi-layer electrolyte. For the bottom layer, DMSO-EL was fabricated as a gel-state electrolyte. For the upper layer, a glass fiber separator was soaked in the same DMSO-EL as that used in the bottom layer	238
Figure 4.33. (a) Digital and (b) SEM images of lithium metal cycled 20 times in the cell with single-phase bi-layer electrolyte, showing that the presence of the gel-state electrolyte does not improve the stability of lithium metal.....	239
Figure 4.34. Quantitative analysis of the remaining Li_2O_2 in the air electrode after cycling with the single-phase and Janus liquid electrolytes.....	240
Figure 4.35. Galvanostatic cycling profile of cell with (a) single-phase electrolyte and (b) Janus liquid electrolyte under current rate of 1000 mA g^{-1}	241
Figure 4.36. Cycling performance of cells under current rate of (c) 1000 mA g^{-1} and (d) 200 mA g^{-1}	242
Figure 4.37. Schematic illustrations of RM diffusion behavior in cell with (left)	

single-phase and (right) Janus liquid electrolyte. (left) The oxidized RM freely diffuses toward the reactive lithium-metal anode, which causes lithium-metal degradation and the consumption of oxidized RM. (right) The oxidized RM does not diffuse through the phase interface and thus remains at the cathode side without the shuttle effect 243

Chapter 1. Introduction

1.1 Research objectives

With the prosperity of human technology, society not only take fruits of it, but also faces accompanied problems such as energy and environmental issues. Among them, the heavy use of fossil fuel is considered the major issue causing severe pollution problem. To this end, the development of sustainable energy resources such as solar and wind energy is the urgent mission for human being, and therefore, energy storage system to store electricity is a key technology to realize renewable future energy society. After continued development during last decades, Li ion battery is currently widely used as most promising storage system.¹⁻⁴ However, further enhancement of its energy density is limited because heavy transition metal such as manganese, cobalt, iron, and nickel sets upper boundary for gravimetric energy density.

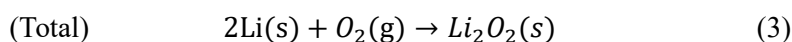
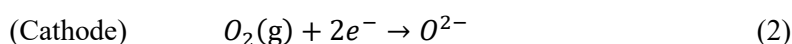
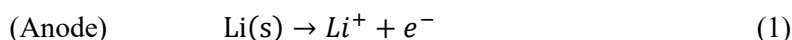
To develop a new system whose energy density surpasses that of current Li-ion battery, researchers have explored various chemistry such as metal-air⁵⁻⁹, metal-sulfur^{7, 10-12}, and organic battery.¹³ Among them, metal-air battery has received intensive attention due to its potentially high energy density attributed to the use of light gas species as redox active materials. Especially, Li-O₂ battery exhibits highest theoretical energy density among metal-air chemistry, and has been developed since its first advent in 1996.¹⁴ Although its great potentiality for extremely high energy density, however, Li-O₂ battery have numerous problems. Most severely, the insulating nature of discharge product, Li₂O₂, causes integrated problems during both discharge and charge process.^{5, 6, 8} For example, electrode passivation by Li₂O₂

during discharge leads to practically low energy density,¹⁵ and low conductivity causes high IR drop during charge leading to low coulombic efficiency.¹⁶

The aim of this research is to develop high-performance Li-O₂ battery by addressing limitations induced by intrinsic nature of discharge product. Main approach is to drive a new discharge/charge path bypassing conventional reaction path by introducing redox-mediating catalyst.

1.2 Introduction to lithium-oxygen battery

Li-O₂ battery exhibits highest theoretical energy density among various metal-air chemistry because it exploits lightest metal, lithium as anode, and light oxygen gas as redox active species at cathode side. The electrochemical reactions occurring in Li-O₂ battery are as follows.



On discharge (*i.e.* oxygen reduction reaction (ORR)), the oxidation of lithium metal to Li⁺ occurs at anode side (reaction 1). At the same time, the reduction of oxygen gas occurs at cathode side (reaction 2) where Li⁺ and reduced oxygen forms Li₂O₂ as a final discharge product. (reaction 3) On charge (*i.e.* oxygen evolution reaction (OER)), the reverse reactions (*i.e.* reduction of Li⁺ to lithium metal at anode, and decomposition of Li₂O₂ to Li⁺ and O₂ at cathode) happens. Considering solid discharge product forms from gas phase, the cathode consists of conductive and porous matrix such as carbon to store discharge product. Since the operation of Li-O₂ battery is entirely controlled by the formation and decomposition of discharge product of Li₂O₂, its native property plays a critical role in determining the chemistry of Li-O₂ battery.⁸ The basic reaction process is illustrated in figure 1.1.

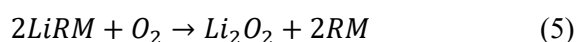
Based on the weight of Li₂O₂ (MW=46) and its theoretical formation potential (2.96 V vs. Li/Li⁺), Li-O₂ battery is calculated to have high theoretical energy density of 3500 Wh kg⁻¹, which much exceeds that of conventional Li-ion battery.⁵ However,

the fact that Li_2O_2 has extremely poor electrical conductivity prevent the realization of high energy density, and also causes further problems regarding system stability, and round-trip efficiency. For example, the formation of insulating Li_2O_2 on electrode surface during discharge triggers electrode passivation.¹⁵ It leads to premature termination of discharge process and limited discharge capacity. Accordingly, the practical energy density of Li-O₂ battery is not as high as 3500 Wh kg⁻¹, and rather strongly dependent on microstructure of cathode (*e.g.* surface area, and porosity) The insulating nature of Li_2O_2 is also problematic on charge process during which electrochemical decomposition of Li_2O_2 occurs. Owing to low electrical conductivity, the amount of IR drop and increased overpotential cannot be ignored. It results in low round-trip efficiency.¹⁷ Moreover, increased charge potential creates oxidative environment promoting decomposition of cell components such as electrolyte and carbon electrode.¹⁸⁻²⁰ Consequently, to develop Li-O₂ battery with practically high energy density and high round-trip efficiency, limitation stemmed from insulating nature of Li_2O_2 must be overcome.

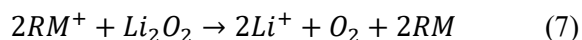
1.3 Principle of redox mediator

Redox mediator (RM) is the type of catalyst that mediates redox reaction by reduced or oxidized itself.²¹⁻²⁵ How RM can mediate discharge and charge process of Li-O₂ battery is expressed as follows.

(On discharge, ORR)



(On charge, OER)



On discharge (*i.e.* ORR), RM is reduced instead of O₂ to form LiRM, (reaction 4) followed by transfer of electron from LiRM to O₂ to form Li₂O₂. (reaction 5) Here, RM mediates reduction of O₂ by itself undergoing redox reaction.^{22, 24} Similarly, on charge, RM is first oxidized to RM⁺. (reaction 6) Then, it reacts with Li₂O₂ to decompose into Li⁺ and O₂.^{21, 23, 25} (reaction 7) Although the consequence of discharge and charge process (*i.e.* formation and decomposition of Li₂O₂) is identical regardless of the presence of RM, the reaction path is entirely shifted with the introduction of RM. Accordingly, limitations originated from conventional discharge/charge path, such as electrode passivation and high charge overpotential might be circumvented. The RM-mediated discharge/charge process is schematically shown in figure 1.2.

It is obvious that intrinsic property of RM critically affects the performance of itself

and RM-employing Li-O₂ battery. Firstly, in RM-mediated discharge/charge, the cell potential is directly reflected by redox potential of RM, implying the importance of selecting RM with high/low redox potential for discharge/charge to achieve lower overpotential.^{23,24} Secondly, the kinetics of RM-mediated process determines the rate of Li₂O₂ formation and decomposition, thereby governing the rate capability of Li-O₂ battery.^{26, 27} Furthermore, the selectivity of RM toward O₂/Li₂O₂ on discharge/charge also plays an important role affecting coulombic efficiency.²⁵ Accordingly, understanding the properties of RM is essential to design high-performance RM and it is a key step to develop RM-employing Li-O₂ battery with high energy density and high efficiency. The characteristics of RM that influence its performance is schematically illustrated in figure 1.3.

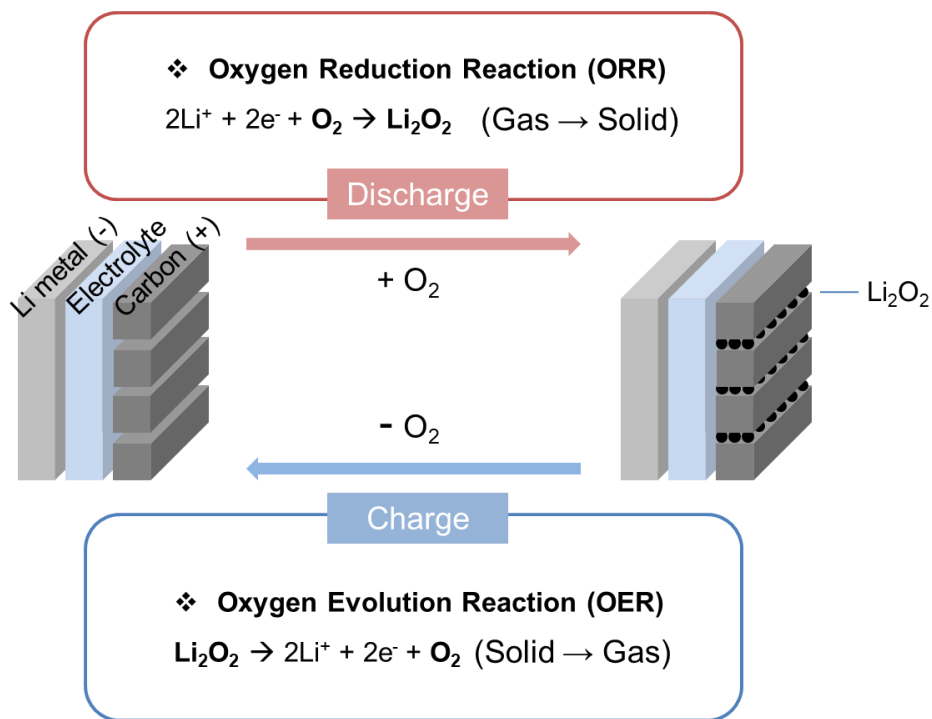


Figure 1.1. Basic reaction mechanism of Li-O₂ battery on discharge and charge process.

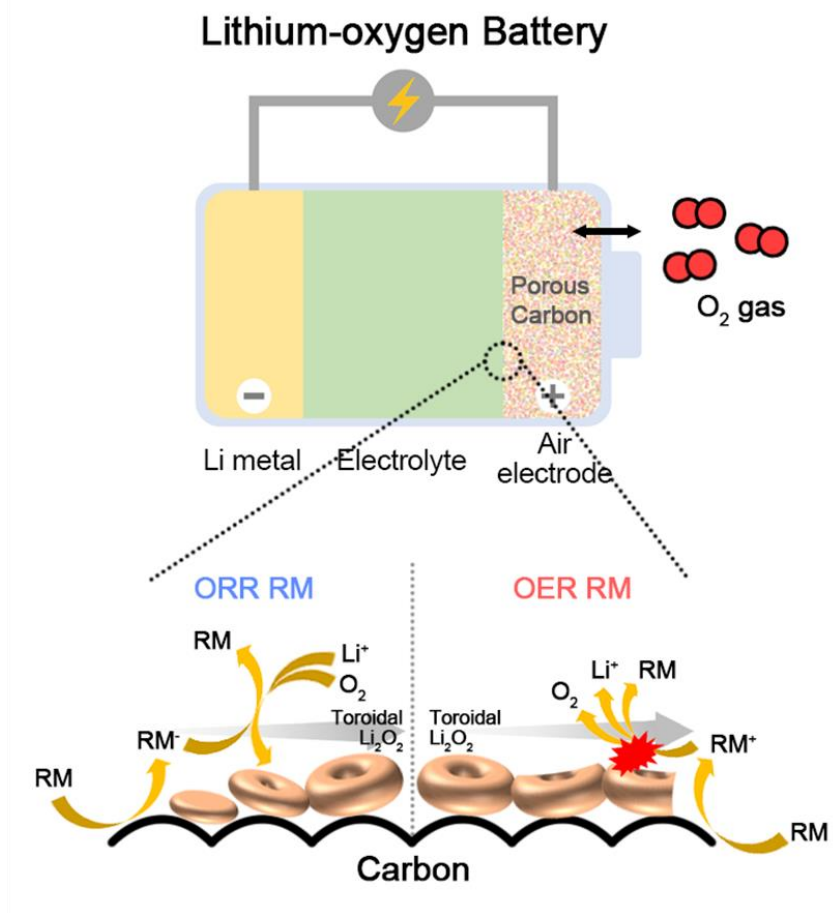


Figure 1.2. Schematics showing the formation and decomposition of discharge product, Li_2O_2 , with the mediation of redox mediator.

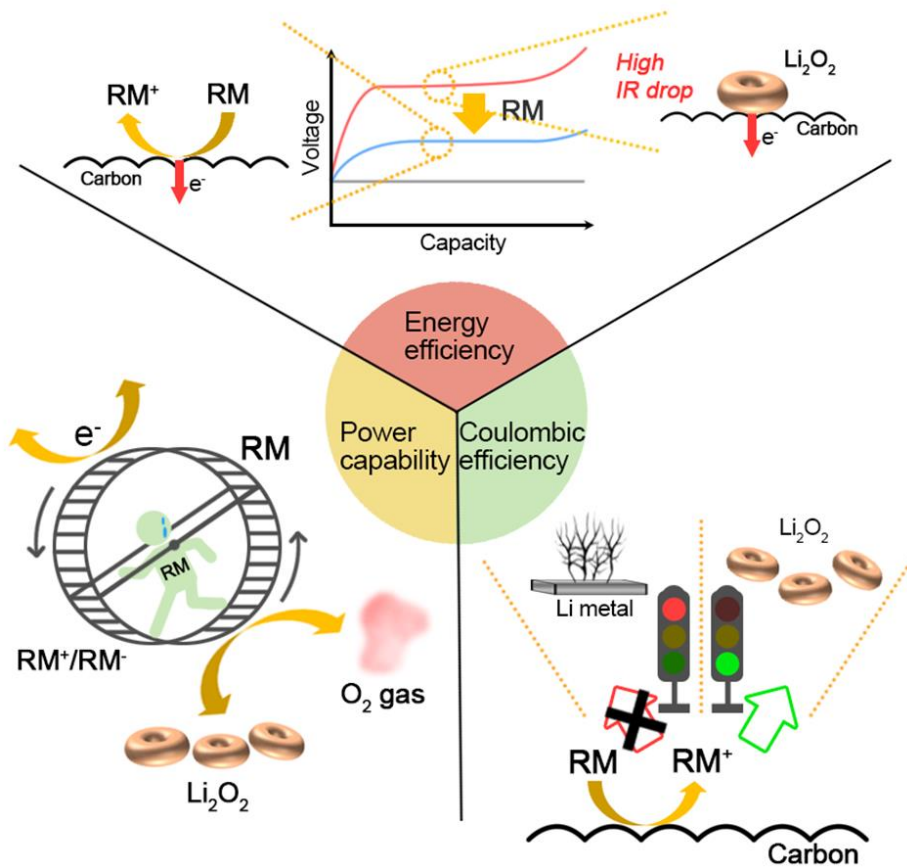


Figure 1.3. The properties of the RM-employing Li-O₂ battery critically influenced by the intrinsic characteristics of RM.

1.4 References

1. Kang K, Meng YS, Bréger J, Grey CP, Ceder G. Electrodes with High Power and High Capacity for Rechargeable Lithium Batteries. *Science* 2006, **311**(5763): 977-980.
2. Armand M, Tarascon J-M. Building better batteries. *Nature* 2008, **451**(7179): 652-657.
3. Tarascon J-M, Armand M. Issues and challenges facing rechargeable lithium batteries. *Materials for sustainable energy: a collection of peer-reviewed research and review articles from Nature Publishing Group*. World Scientific, 2011, pp 171-179.
4. Choi JW, Aurbach D. Promise and reality of post-lithium-ion batteries with high energy densities. *Nat. Rev. Mater.* 2016, **1**(4): 1-16.
5. Girishkumar G, McCloskey B, Luntz AC, Swanson S, Wilcke W. Lithium– air battery: promise and challenges. *J. Phys. Chem. Lett.* 2010, **1**(14): 2193-2203.
6. Christensen J, Albertus P, Sanchez-Carrera RS, Lohmann T, Kozinsky B, Liedtke R, *et al.* A critical review of Li/air batteries. *J. Electrochem. Soc.* 2011, **159**(2): R1.
7. Bruce PG, Freunberger SA, Hardwick LJ, Tarascon J-M. Li–O₂ and Li–S batteries with high energy storage. *Nat. Mater.* 2012, **11**(1): 19.
8. Lim H-D, Lee B, Bae Y, Park H, Ko Y, Kim H, *et al.* Reaction chemistry in rechargeable Li–O₂ batteries. *Chem. Soc. Rev.* 2017, **46**(10): 2873-

2888.

9. Song K, Agyeman DA, Park M, Yang J, Kang YM. High-Energy-Density Metal–Oxygen Batteries: Lithium–Oxygen Batteries vs Sodium–Oxygen Batteries. *Adv. Mater.* 2017, **29**(48): 1606572.
10. Zhao X, Cheruvally G, Kim C, Cho K-K, Ahn H-J, Kim K-W, *et al.* Lithium/sulfur secondary batteries: a review. *J. Electrochem. Sci. Technol.* 2016, **7**(2): 97-114.
11. Kumar D, Rajouria SK, Kuhar SB, Kanchan D. Progress and prospects of sodium-sulfur batteries: a review. *Solid State Ionics* 2017, **312**: 8-16.
12. Fang R, Zhao S, Sun Z, Wang DW, Cheng HM, Li F. More reliable lithium-sulfur batteries: status, solutions and prospects. *Adv. Mater.* 2017, **29**(48): 1606823.
13. Lee S, Kwon G, Ku K, Yoon K, Jung SK, Lim HD, *et al.* Recent progress in organic electrodes for Li and Na rechargeable batteries. *Adv. Mater.* 2018, **30**(42): 1704682.
14. Abraham K, Jiang Z. A polymer electrolyte-based rechargeable lithium/oxygen battery. *J. Electrochem. Soc.* 1996, **143**(1): 1.
15. Johnson L, Li C, Liu Z, Chen Y, Freunberger SA, Ashok PC, *et al.* The role of LiO₂ solubility in O₂ reduction in aprotic solvents and its consequences for Li–O₂ batteries. *Nat. Chem.* 2014, **6**(12): 1091.
16. Luntz AC, Viswanathan V, Voss J, Varley JB, Nørskov JK, Scheffler R, *et al.* Tunneling and Polaron Charge Transport through Li₂O₂ in Li–O₂

- Batteries. *J. Phys. Chem. Lett.* 2013, **4**(20): 3494-3499.
17. Ganapathy S, Adams BD, Stenou G, Anastasaki MS, Goubitz K, Miao X-F, *et al.* Nature of Li₂O₂ oxidation in a Li–O₂ battery revealed by operando X-ray diffraction. *J. Am. Chem. Soc.* 2014, **136**(46): 16335-16344.
 18. Ottakam Thotiyil MM, Freunberger SA, Peng Z, Bruce PG. The carbon electrode in nonaqueous Li–O₂ cells. *J. Am. Chem. Soc.* 2013, **135**(1): 494-500.
 19. Itkis DM, Semenenko DA, Kataev EY, Belova AI, Neudachina VS, Sirotnina AP, *et al.* Reactivity of carbon in lithium–oxygen battery positive electrodes. *Nano Lett.* 2013, **13**(10): 4697-4701.
 20. Freunberger SA, Chen Y, Drewett NE, Hardwick LJ, Bardé F, Bruce PG. The lithium–oxygen battery with ether-based electrolytes. *Angew. Chem., Int. Ed.* 2011, **50**(37): 8609-8613.
 21. Chen Y, Freunberger SA, Peng Z, Fontaine O, Bruce PG. Charging a Li–O₂ battery using a redox mediator. *Nat. Chem.* 2013, **5**(6): 489.
 22. Gao X, Chen Y, Johnson L, Bruce PG. Promoting solution phase discharge in Li–O₂ batteries containing weakly solvating electrolyte solutions. *Nat. Mater.* 2016, **15**(8): 882-888.
 23. Lim H-D, Lee B, Zheng Y, Hong J, Kim J, Gwon H, *et al.* Rational design of redox mediators for advanced Li–O₂ batteries. *Nat. Energy* 2016, **1**(6): 1-9.

24. Ko Y, Park H, Kim J, Lim HD, Lee B, Kwon G, *et al.* Biological redox mediation in electron transport chain of bacteria for oxygen reduction reaction catalysts in lithium–oxygen batteries. *Adv. Funct. Mater.* 2019, **29**(5): 1805623.
25. Ko Y, Park H, Kim B, Kim JS, Kang K. Redox Mediators: A Solution for Advanced Lithium–Oxygen Batteries. *Trends Chem.* 2019, **1**(3): 349-360.
26. Chen Y, Gao X, Johnson LR, Bruce PG. Kinetics of lithium peroxide oxidation by redox mediators and consequences for the lithium–oxygen cell. *Nat. Commun.* 2018, **9**(1): 1-6.
27. Ko Y, Park H, Lee B, Bae Y, Park SK, Kang K. A comparative kinetic study of redox mediators for high-power lithium–oxygen batteries. *J. Mater. Chem. A* 2019, **7**(11): 6491-6498.

Chapter 2. Exploring a new redox mediator inspired by biological system

2.1 Research background

(The essence of this chapter has been published in *Advanced Functional Materials*. Reproduced with permission from [Ko, Y. *et al.*, *Adv. Funct. Mater.* **2019**, 29, 1805623] Copyright (2019) WILEY-VCH)

Lithium–oxygen batteries have been considered promising next-generation energy storage systems because of their high theoretical specific capacity, which far exceeds that of conventional Li-ion batteries.¹⁻⁷ The high specific capacity of lithium–oxygen batteries is attributed to the exploitation of oxygen as a redox-active material to store Li without the need to use transition metals in the electrochemical reaction. Recent studies have revealed, however, that the utilization of high discharge capacity is sensitively affected by the mechanism under which Li_2O_2 , the main final discharge product, is formed in the electrochemical cell.⁸⁻¹¹ The generation of the intermediate species and its solubility (*i.e.*, stability of solvated LiO_2) in the electrolyte have been observed to be critical in determining the discharge routes and capacity. The use of an electrolyte that exhibits strong solvating ability and can stabilize the intermediate LiO_2 leads to the growth of large toroidal Li_2O_2 particles from the solution (‘solution route’), resulting in a high discharge capacity. However, in an electrolyte with weak solvating ability, the intermediate LiO_2 is prone to be absorbed/decomposed on the electrode surface and form a film-like discharge product on the electrode (‘surface

route'), which often causes premature passivation of the electrode (*i.e.*, cell death). Thus, it is believed that discharge through the solution route is essential to achieve a high discharge capacity and should thus be induced.^{8,9,11-14}

One of the major factors that govern the stability of solvated LiO_2 is the nature of the electrolyte.⁸⁻¹⁰ An electrolyte with higher donor number can stabilize LiO_2 in an electrolyte because of its stronger solvating ability and, therefore, tends to induce the solution-route discharge. However, such an electrolyte is also known to be more vulnerable to side reactions because reactive radicals such as LiO_2 and O_2^- can be simultaneously enriched by the increased solubility degrading the electrolyte.¹⁵⁻¹⁷ Although this 'trade-off' issue is a major challenge for the development of lithium–oxygen batteries, redox mediators (RMs) for the oxygen reduction reaction (ORR) have been suggested as a promising solution. With the introduction of an appropriate ORR RM in lithium–oxygen cells, the RMs are reduced prior to O_2 . The reduced RMs deliver electrons to O_2 in the electrolyte, which, in principle, triggers the solution-route discharge of Li_2O_2 regardless of the electrolyte species with a reduced risk of reactive radicals. Several additives such as quinones¹⁸ and viologens^{19,20} have been reported as ORR RMs. Notably, Gao *et al.* recently demonstrated that 2,5-di-tert-butyl-1,4-benzoquinone (DBBQ) can promote solution-route discharge even in low-donor-number electrolytes (*e.g.* ethers) by generating soluble $\text{RM-O}_2\text{-Li}$ intermediates, which disproportionate into large-particle Li_2O_2 and neutral RM.²¹ The activity of the ORR RM in the lithium–oxygen cell was attributed to its redox potential, which lies between that of O_2 and the theoretical potential of Li_2O_2 (2.96

V vs. Li/Li⁺), thereby enabling sequential electron transport among them in the solution phase. The discovery of an ORR RM that triggers the solution route implies that decoupling of the high energy density and stability is feasible, which is pivotal to the development of high-performance lithium–oxygen batteries.

Here, we demonstrated that vitamin K2, well-known biological RM functioning in the electron transport chain (ETC) in *Escherichia coli*, also can work as a ORR RM in lithium oxygen batteries. The new ORR RM was explored under the consideration of appropriate redox potential and reversibility of its redox reaction. The lithium oxygen cell with vitamin K2 exhibited enormously increased discharge capacity forming lithium peroxide compared to the reference cell due to the transformation of discharge pathway from surface-driven to solution-driven discharge.

2.2 Experimental method

2.2.1 Preparation of cells and conditions for electrochemical tests

The electrolyte was prepared by adding 1 M lithium bis(trifluoromethane)sulfonamide (99.95% trace metals basis, Sigma–Aldrich) in dimethoxyethane (anhydrous, 99.5%, Sigma–Aldrich). Lithium bis(trifluoromethane)sulfonamide was stored at 180 °C under vacuum for more than a week before use. Dimethoxyethane was dried using a freshly washed molecular sieve (type 3Å, Sigma Aldrich) for more than several days. Menatetrenone (vitamin K2), ubiquinone-10 (coenzyme Q), 2,2,6,6-tetramethyl-1-piperidinyloxy (TEMPO), 2-tert-Butyl-1,4-benzoquinone (BBQ), Methyl-p-benzoquinone (MBQ), and Menadion (MD) were purchased from Sigma–Aldrich and used as received. To prepare the RM-containing electrolyte, 0.01 M of vitamin K2 and 0.1 M of TEMPO were added to 1 M LiTFSI DME. The final water content of the electrolyte was under 50 ppm (as determined by Karl Fischer titration). A sheet of a gas diffusion layer (H2315, Quintech) was used as an air electrode after heat treatment at 900 °C for 3 h under an Ar:H₂ (95:5 volume ratio) atmosphere. Lithium iron phosphate (LFP), which has a fixed two-phase region potential of 3.45 V (vs. Li/Li⁺), was used at the counter electrode. The LFP electrode was prepared with a mixture of LFP powder, super P carbon, and polyvinylidene fluoride binder in a weight ratio of 90:1.5:8.5. The LFP electrode was designed to have at least twice as much capacity as that of the air electrode. Two sheets of glass fiber (GF/F, Whatman) were used as a separator.

Anode and separator had diameters of 1/2 inch and air electrode had diameters of 3/8 inch. The cells were assembled as a Swagelok-type cell with the diameters of 1/2 inch. The amount of electrolyte used in the cell was 300 μl . Assembly of the cell was performed in an Ar-filled glove box (O_2 level < 0.5 ppm and H_2O level < 0.5 ppm). After assembly, the cell was saturated with O_2 (> 99.999%) and operated as closed. All the electrochemical tests for the lithium–oxygen batteries were conducted with a potentiogalvanostat (WonA Tech, WBCS 3000, Korea). For galvanostatic discharge experiments, all the cells were relaxed for 30 min before the tests. For the cyclic voltammetry tests, 1 M LiTFSI DME containing 0.01 M of each RM (vitamin K2 and TEMPO) was used. The three-electrode cell was composed of an Au working electrode, Pt counter electrode, and 0.01 M Ag/Ag^+ in acetonitrile as a reference solution.

2.2.2 Characterization

For characterization of the discharged electrodes, the cells were disassembled in an Ar-filled glove box. The electrode and separator were rinsed with a small amount of anhydrous DME and dried under Ar. Raman spectra of the electrode and reference powder were obtained using a Horiba Jobin Yvon LabRam Aramis with a He–Ne laser beam using <2 mW of 632.8-nm light from a He–Ne laser in a confocal geometry with the $\times 50$ microscope objective lens. Fourier-transform infrared spectroscopy (FTIR; FT-IR-4200, JASCO, Japan) and X-ray diffraction (D8 Advance, Bruker, Germany) were also used for identification of the discharge product. To examine the morphology of the discharge product on the electrode, field-

emission scanning electron microscopy (FE-SEM; SUPRA 55VP, Carl Zeiss, Germany) was used. For *in situ* DEMS analysis, a mass spectrometer (MS; HPR-20, Hiden Analytical) connected with a potentio-galvanostat was used. A detailed description of DEMS is provided elsewhere.^{22, 23}

2.2.3 Quantitative analysis of discharge product

To quantitatively analyze the amount of Li_2O_2 in the discharge product, UV-vis titration using UV-vis spectroscopy (Cary 5000, Agilent, United States) was conducted, as previously reported.^{21, 24, 25} For the powder reference, lithium peroxide powder (technical grade, >90%, Sigma-Aldrich), which was known to have an actual purity of 92.8% based on thermogravimetric analysis was used.²⁶ A known amount of Li_2O_2 powder was added to a certain amount of deionized water to produce LiOH via the reaction between Li_2O_2 and H_2O . This solution was mixed with TiOSO_4 solution (2 wt% in H_2SO_4) to generate a yellow $[\text{Ti}(\text{O}_2)]^{2+}$ complex that was diluted with deionized water. The intensity of the UV-vis absorption spectrum at 407 nm of this solution was observed to be proportional to the amount of $[\text{Ti}(\text{O}_2)]^{2+}$ complex in the solution. The reference calibration curve (amount of Li_2O_2 powder vs. intensity of absorption peak at 407 nm) was obtained based on the results. To analyze the discharge product, an unwashed electrode and separator were used instead of Li_2O_2 powder following the same process explained above. The obtained intensity of the absorption peak was compared with the calibration curve to quantify the amount of Li_2O_2 in the discharge product considering the different dilution ratios of the solution between the powder and electrode samples.

2.3 Result and discussion

2.3.1 Similarity between redox mediation in biological system and lithium-oxygen cell

As a first step of discovering new ORR RM for lithium-oxygen batteries, we noted that similar redox-mediated electron transport in solution phase is commonly observed in biological systems among biomolecules, which may inspire the discovery of novel effective ORR RMs for lithium-oxygen batteries. In a cell respiratory system, electrons can be transferred from one catalyst complex to another by biomolecules in a cell membrane through the ETC.²⁷⁻³¹ In an animal cell, bio-RMs such as vitamin K2 and coenzyme Q are known to be capable of transferring electrons between two remote catalyst complexes in ETC.²⁹⁻³¹ For example, in common bacteria such as *E. coli*, vitamin K2 functions as a RM between nicotinamide adenine dinucleotide hydrogen (NADH) dehydrogenases and the cytochrome b-c₁ complex, where proton shuttling by vitamin K2 occurs, enabling the oxidation of flavin mononucleotide (FMN) and the reduction of cytochrome b, as illustrated in figure 2.1.a. Similarly, in the mitochondria of an animal cell, coenzyme Q (0.045 V vs. SHE) plays the role of a RM between the two catalyst complexes. These biological processes of electron transport via bio-RMs bear significant resemblance to the processes required in the electrochemical reaction in lithium-oxygen batteries. In figure 2.1, the sequential electron transport is schematically illustrated for a simplified biological system and the lithium-oxygen

battery system. In the cell respiration process in *E. coli* (figure 2.1.a), the electron transfer with proton shuttling should occur from NADH dehydrogenases to the cytochrome b-c₁ complex through the cell membrane, which is energetically permitted by the difference in their relative redox potential. Although the redox-active parts in NADH dehydrogenases and the cytochrome b-c₁ complex are stationary species and remote from each other, the electron transfer between them is enabled because of the mobile vitamin K₂, whose redox potential (-0.08 V vs. SHE) lies between those of FMN/FMNH₂ (-0.30 V vs. SHE) in NADH dehydrogenases and cytochrome b(oxi)/cytochrome b(red) (0.08 V vs. SHE) in the cytochrome b-c₁ complex, not disturbing the downhill electron transport (figure 2.1.b).^{27, 30} The discharge of the lithium-oxygen battery aided by the ORR RM is based on the same mechanism as that illustrated in figure 2.1.c, where the electrons are mediated from the electrode to the oxygen with lithium ion shuttling. If these bio-RMs can exhibit appropriate redox potentials in an aprotic environment and temporarily capture Li ions, as demonstrated for the proton capture in the *E. coli*, they may function as RMs for lithium-oxygen batteries.

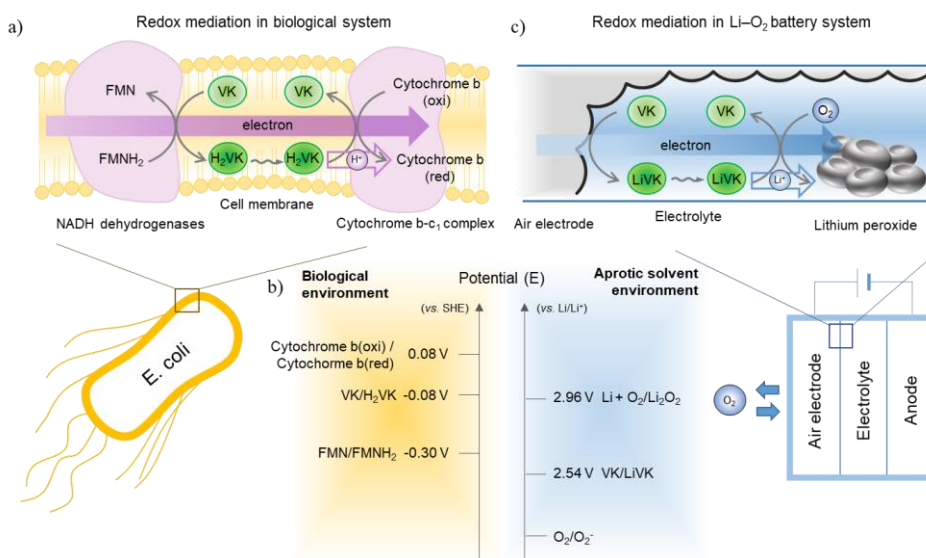


Figure 2.1. (a) Simplified biological system in *E. coli*. The electron transfer with proton shuttling between NADH dehydrogenases and the cytochrome b–c₁ complex is mediated by vitamin K2. (b) Comparison of relative redox potentials among vitamin K2 and other species in the redox mediating processes in *E. coli* and lithium–oxygen batteries. (c) Lithium–oxygen battery system with vitamin K2 as potential ORR RM. The electron transfer with lithium ion shuttling between the electrode and Li₂O₂ is mediated by the ORR RM, vitamin K2.

2.3.2 Vitamin K2 as a stable mediator for lithium–oxygen batteries

Inspired by this similarity, we selected two representative bio-RMs, *i.e.*, vitamin K2 and coenzyme Q, as candidates for ORR RMs for lithium–oxygen batteries, as they are known to be capable of mediating redox reactions in solution phase and, more importantly, their redox potentials are close to the Li_2O_2 formation potential (0.08 and 0.045 V vs. SHE, respectively).²⁷ As shown in figure 2.2, we first examined the redox potentials of vitamin K2 and coenzyme Q in an aprotic environment, dimethoxyethane (DME) with 1 M LiTFSI, under an Ar atmosphere using cyclic voltammetry. The redox activities were observed at ~ 2.54 and ~ 2.71 V (vs. Li/Li^+) for vitamin K2 and coenzyme Q, respectively, which were slightly lower than the values in an aqueous medium. Nevertheless, the redox potentials of vitamin K2 and coenzyme Q were located between that of O_2 and the theoretical formation potential of Li_2O_2 (2.96 V vs. Li/Li^+), indicating their viability for ORR mediation in lithium–oxygen batteries. As demonstrated by the relative potential energy plot of figure 2.1.c, the bio-RMs are expected to be capable of transporting the electrons from the electrode instead of oxygen and triggering the formation of Li_2O_2 . However, the stabilities of these bio-RMs differed distinctively in the aprotic electrolyte, as demonstrated in figure 2.2. Although the cyclic voltammogram of vitamin K2 indicates a reversible redox reaction over 200 cycles, the redox activity of coenzyme Q gradually degraded with increasing cycles, which is attributable to its chemical instability in the aprotic environment.

Given the adequate redox potential and stability of vitamin K2, the following

investigation was focused on its use as an ORR RM in lithium–oxygen batteries. To investigate the activity of vitamin K2 as an ORR RM in greater detail, electrochemical experiments were conducted under various conditions using 1 M LiTFSI in DME containing 0.01 M of vitamin K2, and the results are presented in figure 2.3. Figure 2.3.a presents the cyclic voltammetry measurements of vitamin K2 at different scan rates, which confirms the reversible redox activity at 2.54 V. Notably, negligible polarization was observed upon increasing the scan rate by ten times, indicating the fast redox activity of vitamin K2 in the aprotic environment. The catalytic activity of vitamin K2 in an O₂ environment was also examined, and the results are presented in figure 2.3.b. Vitamin K2 exhibits a higher intrinsic redox potential than O₂, which ensures the earlier reduction of vitamin K2 than O₂ during the discharge. Comparison of the redox activities of vitamin K2 with and without O₂ clearly demonstrates that the reduction peak of vitamin K2 significantly increases in the presence of O₂. This behavior is attributed to a catalyzed reduction process (EC mechanism)³², where the ORR RM after reduction successively participates in a chemical reaction in the O₂ environment, recovering its initial state, and undergoes the reduction process again, which is consistent with previous observations for DBBQ mediators.²¹ The enhanced reduction peak in the cathodic scan provides clear evidence that the electrochemically reduced vitamin K2 is capable of reverting to its initial neutral state via the sequential chemical reaction in the lithium–oxygen cell, thereby functioning as a mediator. Figure 2.4.a presents galvanostatic discharge profiles of the lithium–oxygen cell with and without vitamin K2 under an O₂

atmosphere. Lithium–oxygen cells were constructed using a single sheet of gas diffusion layer (GDL) (H2315, Quintech) as an air electrode and LiFePO_4 as a counter electrode in 1 M LiTFSI DME.³³ In the absence of vitamin K2, the cell delivered a negligibly small discharge capacity of $\sim 0.15 \text{ mAh cm}^{-2}$ (normalized with geometric area) even at a low current rate of 0.09 mA cm^{-2} (figure 2.4.b), which is attributed to the low surface area of the GDL air-electrode (Brunauer–Emmett–Teller (BET) surface area of $\sim 1 \text{ m}^2 \text{ g}^{-1}$) and the surface-route formation of Li_2O_2 in the DME electrolyte system. Note that surface-route discharge is more driven by using the electrode with low surface area which increases local current density.¹¹ The surface-route discharge in DME with low DN^{8, 10} and the formation of a thin Li_2O_2 film on such a small-surface air-electrode is expected to result in a limited discharge capacity.²¹ In the presence of vitamin K2, however, the cell exhibits remarkably higher discharge capacity (30 times higher than that of the cell without vitamin K2 at all the current rates tested). The significant increase in the discharge capacity explicitly demonstrates the catalytic activity of vitamin K2 as an ORR RM. Furthermore, figure 2.5 clearly demonstrated that the elongation of discharge process was accompanied with the consumption of oxygen close to theoretical amount yielding oxygen efficiency of 99.85 %.

The morphological change of the discharge product supports the shift of the discharge mechanism from a surface route to a solution route with the presence of vitamin K2. Figure 2.6 compare optical and low-magnification SEM images, respectively, of a pristine electrode (up) and electrodes discharged without (left) and

with vitamin K2 (right). The carbon fibers in the pristine GDL electrode and the one without vitamin K2 are barely covered by discharge products in both the optical and SEM images in accordance with the negligibly small discharge capacity for the cell without vitamin K2. However, white-colored dots are apparent on the surface of the electrode discharged with vitamin K2 in the optical image. The accumulation of small particles is also observed on the electrode in the low-magnification SEM image. Accordingly, more detailed investigations were conducted on the morphologies of the discharge products in the electrodes, and the results are presented in figure 2.7. Compared with the pristine images in figure 2.7.a and d, the surface of the GDL electrode only roughened after discharge of the cell without vitamin K2, as shown in figure 2.7.b and e, suggesting a thin Li_2O_2 discharge product deposited on the carbon fiber without a particular morphology. However, as shown in figure 2.7.c and f many micron-size Li_2O_2 discharge products were clearly observed on the electrode with the addition of vitamin K2, showing the typical toroidal morphology commonly observed for solution-route discharge mechanisms. This finding provides clear evidence that the solution-route discharge was successfully derived with the use of vitamin K2 as an ORR RM. Note that discharge through the solution route is also possible with the addition of H_2O as an additive in an electrolyte.^{9, 25} However, the H_2O contents in both electrolytes, with and without vitamin K2, were confirmed to be less than 50 ppm, which is far less than the content necessary to promote the solution-phase discharge (200–500 ppm).^{9, 25} Hence, it is believed that the promotion of the solution-phase discharge is solely due to the activity of vitamin K2 as an ORR

RM.

To verify that the increased capacity of the cell containing vitamin K2 is due to the formation of Li_2O_2 and not from any side reactions, the discharge products were further investigated using several qualitative analysis methods.³⁴⁻³⁷ The X-ray diffraction patterns in figure 2.8 confirm that the only detectable discharge product was Li_2O_2 without any trace of crystalline byproducts such as Li_2CO_3 or LiOH . The Raman spectroscopy results in figure 2.9.a and infrared (IR) spectroscopy results in figure 2.9.b also unequivocally support the conclusion that the main discharge product was Li_2O_2 and not LiOH , Li_2CO_3 , or lithium acetate which are commonly detected byproducts in lithium–oxygen batteries.^{34, 38} For more precise quantification of the discharge product, the amount of Li_2O_2 in the discharged electrode was determined by titration using TiOSO_4 solution^{24, 39}. Details on the titration methodology are presented in the experimental section. The titration in figure 2.10 revealed that approximately 86% of the total discharge product was Li_2O_2 , which is higher than the yield of Li_2O_2 in typical lithium–oxygen cells without using an ORR RM (~78%). The higher Li_2O_2 yield of the lithium–oxygen cell containing vitamin K2 is attributed to that the generation of reactive LiO_2 species being significantly suppressed with the introduction of vitamin K2 as an ORR RM. It is worth noting that the yield of Li_2O_2 with vitamin K2 is still less than 100 % although oxygen consumption efficiency of 99.85 % was measured with gas analysis. It is because the surface of small Li_2O_2 particles is all covered by Li_2CO_3 due to chemical reactions with the electrolyte.⁴⁰

In order to evaluate the use of vitamin K2 as ORR RM, it is required to compare the catalytic activity of vitamin K2 with other previously reported RMs.^{21, 41} For fair comparison, galvanostatic discharge experiment were conducted using the same type of air-electrode with identical dimension (*i.e.* the number of stacked GDL sheet and electrode area). The discharge profile result with vitamin K2, coenzyme Q, DBBQ and several quinone derivatives is shown in figure 2.11. Noticeable is that vitamin K2 and DBBQ exhibit remarkable catalytic activity (*i.e.* increase of discharge capacity). Although the performance of vitamin K2 does not reach that of DBBQ, vitamin K2 shows outstanding catalytic activity compared to other molecules including coenzyme Q which has recently been reported.⁴¹ The catalytic activity of vitamin K2 superior to that of coenzyme Q is attributed to highly reversible redox reaction of vitamin K2 compared to coenzyme Q as demonstrated in figure 2.2, which indicates the importance of reversible redox reaction when designing successfully working RM.

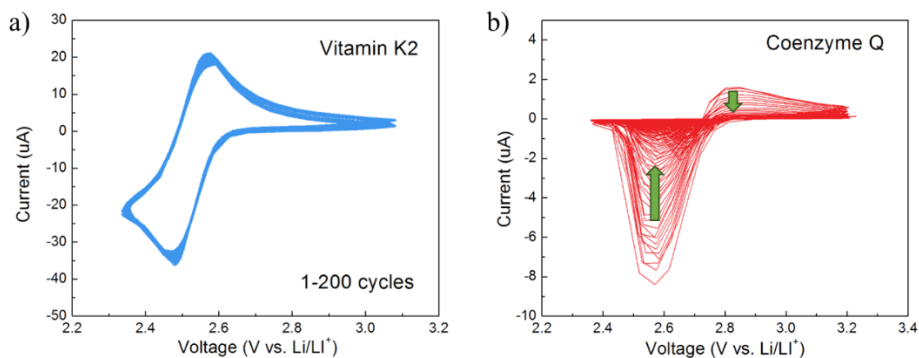


Figure 2.2. (a) Cyclic voltammogram of vitamin K2 in 1 M LiTFSI DME showing consistent profile up to 200 cycles, confirming the stability of vitamin K2 and reduced vitamin K2 under the electrolyte. (b) Cyclic voltammogram of coenzyme Q in 1 M LiTFSI DME showing irreversible redox reaction.

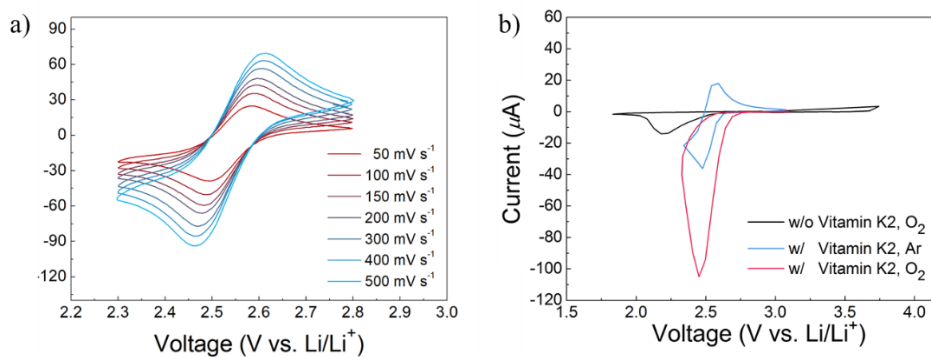


Figure 2.3. (a) Cyclic voltammograms of vitamin K2 showing stable redox reaction of vitamin K2 in 1 M LiTFSI DME under various scan rates. (b) Cyclic voltammograms of vitamin K2 showing the catalytic effect of vitamin K2 under an O₂ atmosphere with the presence of Li⁺ ions under a scan rate of 50 mV s⁻¹.

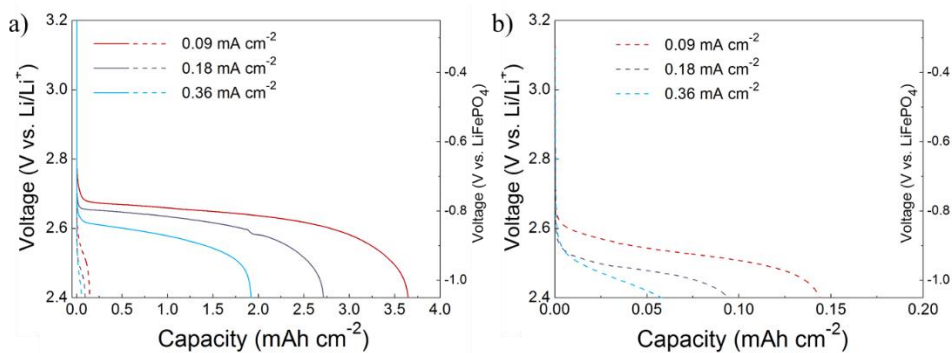


Figure 2.4. (a) Discharge profile of the lithium–oxygen cell with and without vitamin K2 at various current rates. The discharge capacity is enhanced by 30 times with the use of vitamin K2. (b) Enlarged view of (a) showing the discharge capacity in the absence of vitamin K2.

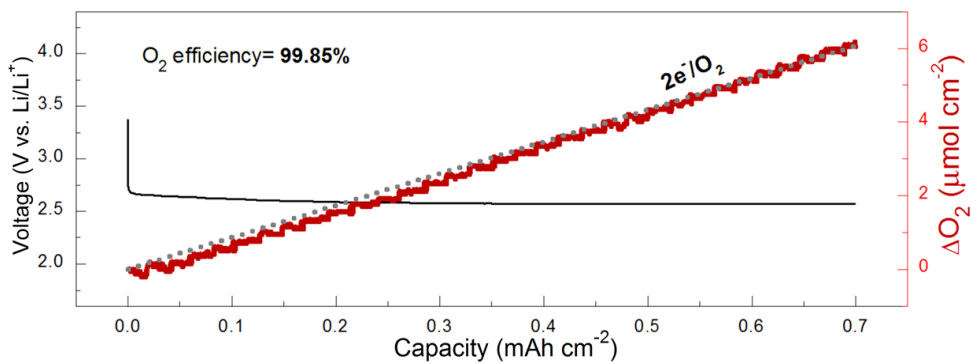


Figure 2.5. The amount of oxygen consumption during discharge measured by tracking change of oxygen pressure.

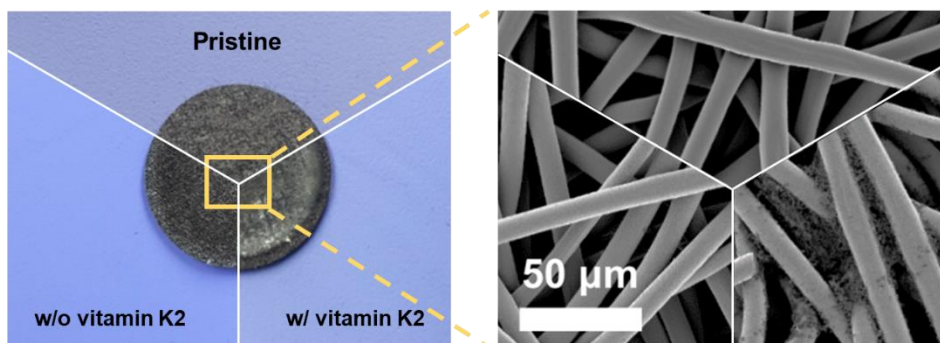


Figure 2.6. Optical images and SEM images of pristine electrode (top) and electrodes discharged without vitamin K2 (left) and with vitamin K2 (right).

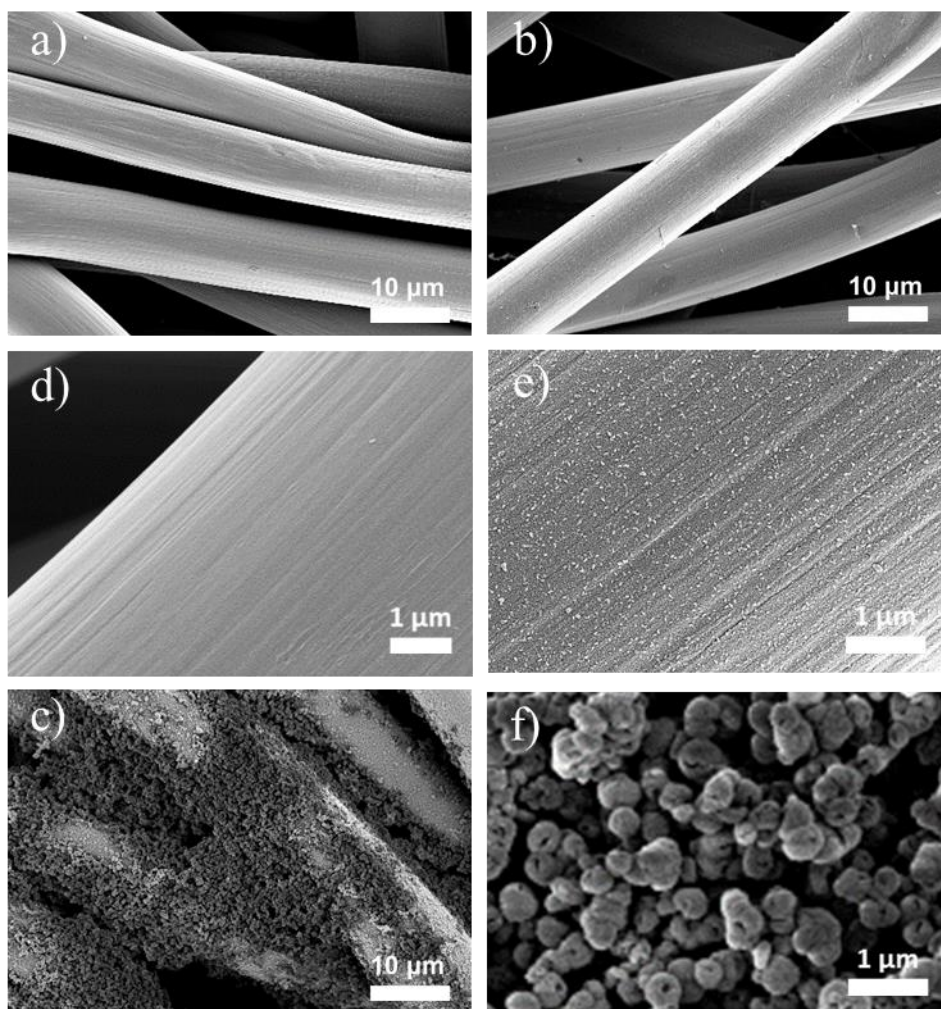


Figure 2.7. SEM images of (a), (d) pristine electrode, (b), (e) fully discharged electrode of the cell not containing vitamin K2, and (c), (f) fully discharged electrode of the cell containing vitamin K2. With the use of vitamin K2, the morphology of the discharge product transformed into toroidal-like particles.

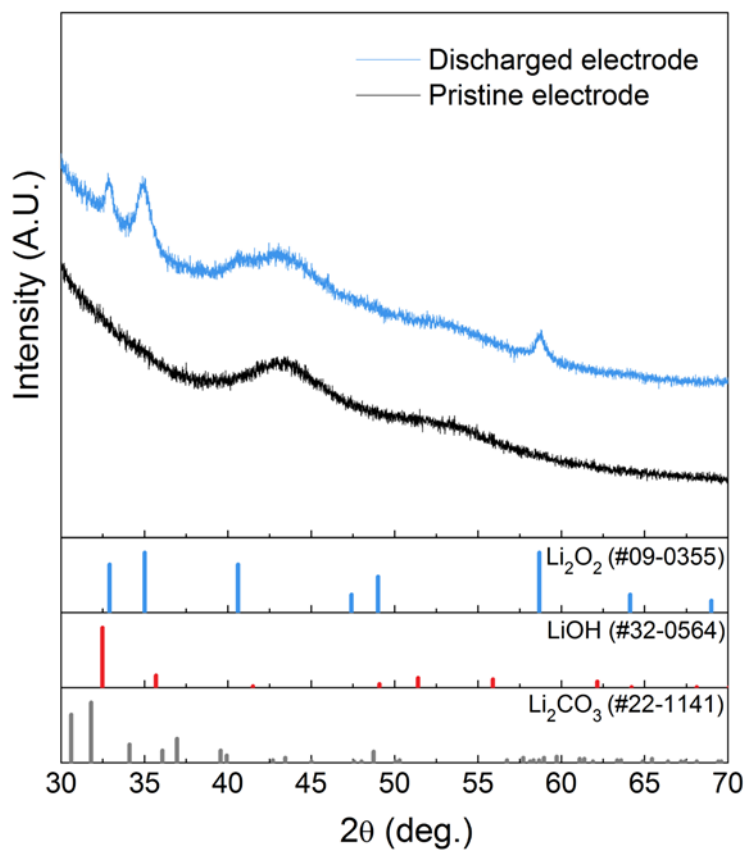


Figure 2.8. X-ray diffraction pattern of discharge electrode.

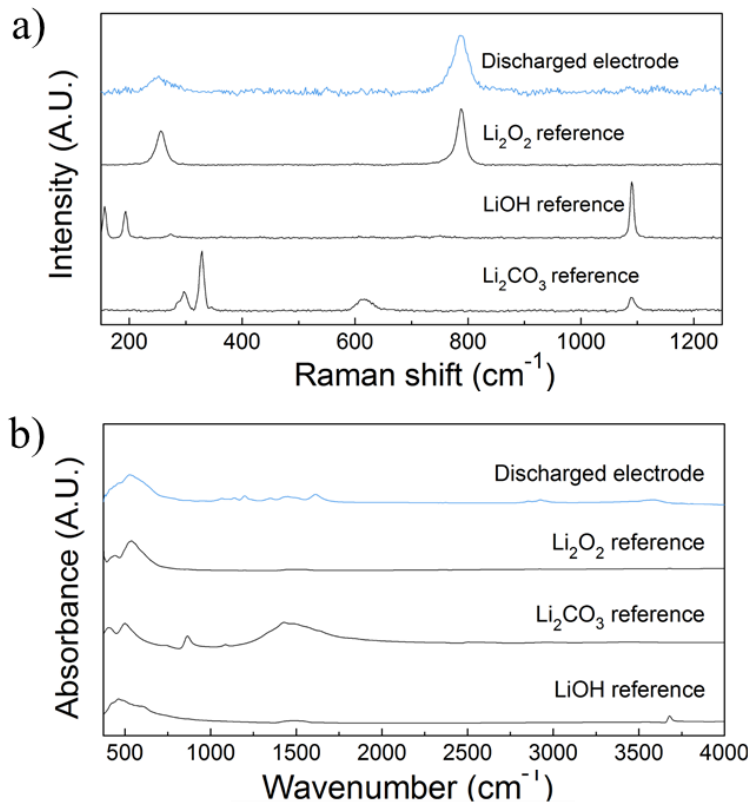


Figure 2.9. (a) Raman and (b) IR spectra of electrode discharged with vitamin K2.

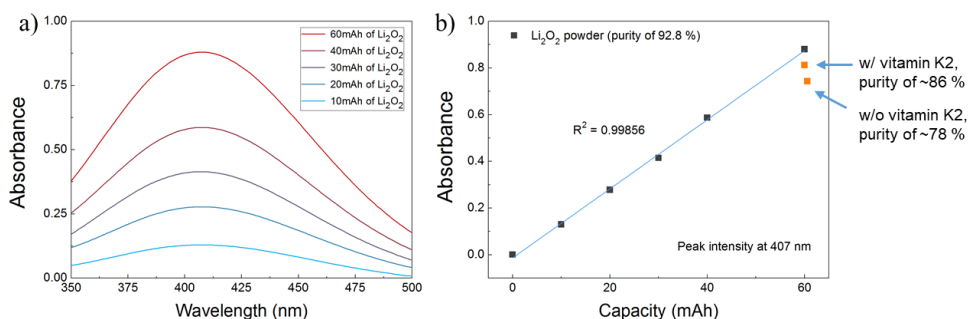


Figure 2.10. (a) Ultraviolet–visible (UV–vis) spectra for various amounts of Li_2O_2 powder (purity of 92.8%). (b) Fitted graph showing proportionality between peak intensity at 407 nm and amount of Li_2O_2 powder (black dots) and the same data for an electrode discharged with and without vitamin K2 (orange dots) showing yields of 86% and 78%, respectively. The capacities for the electrode samples were converted based on the dilution ratio difference between the powder and electrode samples. For the electrode without vitamin K2, commercial carbon paper (P50, Fuelcellerth) was used. All the titration solutions containing Li_2O_2 powder or discharged electrode were produced as described in the experimental section.

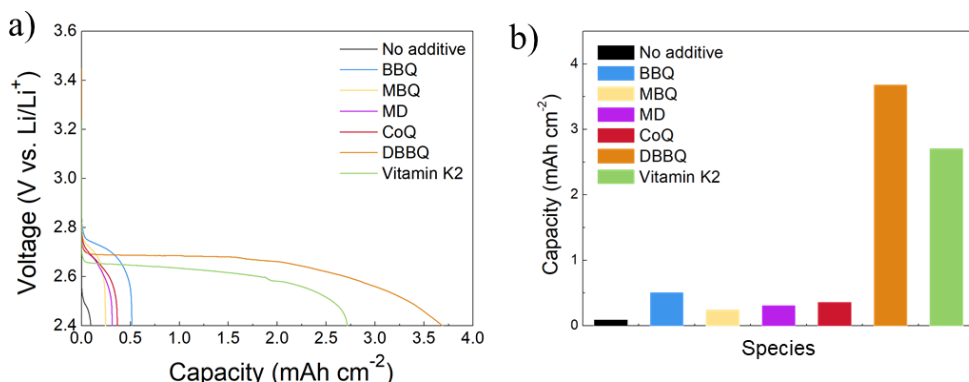
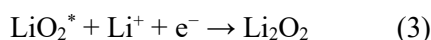
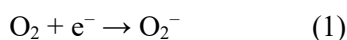


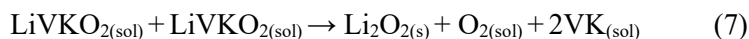
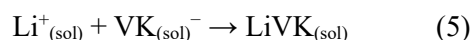
Figure 2.11. (a) Galvanostatic discharge profile under current rate of 0.18 mA cm^{-2} and (b) bar graph, comparing the catalytic activity of vitamin K2 with that of DBBQ, coenzyme Q and other quinone derivatives. All experiments were done with 0.01 M of each molecule in 1 M LiTFSI in DME. Vitamin K2 and DBBQ show exceptionally better catalytic activity (*i.e.* discharge capacity) than coenzyme Q and other quinone derivatives. (Notations for each species are as follows; BBQ(2-tert-Butyl-1,4-benzoquinone), MBQ(Methyl-p-benzoquinone), MD(Menadion), CoQ(Coenzyme Q))

2.3.3 Mechanism of vitamin K2-mediated discharge

The proposed mechanism by which the solution-phase discharge is promoted in the presence of vitamin K2 is schematically illustrated in figure 2.12. In an ether-based electrolyte (with low DN), the discharge is known to proceed as follows (Rxn. (1)–(3)).^{8, 10, 42}



First, O_2 is reduced to O_2^- , which subsequently forms LiO_2 as an intermediate in the presence of lithium ions. Because of the low solubility of LiO_2 in low-DN solvent (DME), the LiO_2 is mostly absorbed on the surface of the electrode as LiO_2^* (Rxn. (1–2)), followed by the formation of film-like Li_2O_2 via additional reduction (Rxn (3)). However, with the addition of vitamin K2, the vitamin K2 is reduced in the first stage of discharge because of its higher redox potential than that of O_2 (Rxn (4)). The reduced vitamin K2 in the solution phase is thought to immediately combine with lithium ions to form a new species, LiVK (Rxn (5)). Vitamin K2 is expressed as VK in Rxn. (4–7).



Subsequently, the LiVK species are expected to combine with O_2 (Rxn (6)) to form

a new intermediate, LiVKO_2 , two of which undergo disproportionation reactions generating Li_2O_2 , O_2 , and VK, which would trigger the growth of Li_2O_2 in a toroidal morphology in the electrolyte (Rxn (7)). Because the reduction potential of vitamin K2 in the presence of Li^+ and O_2 is lower than the formation potential of Li_2O_2 (2.96 V vs. Li/Li^+), there is a thermodynamic driving force for the reduced vitamin K2 species, *i.e.*, LiVKO_2 complex, to chemically transfer electrons to Li_2O_2 seeds whose electron energy levels are lower than that of LiVKO_2 . This process results in the formation of large toroidal Li_2O_2 in electrolyte solution ((2) in figure 2.13).

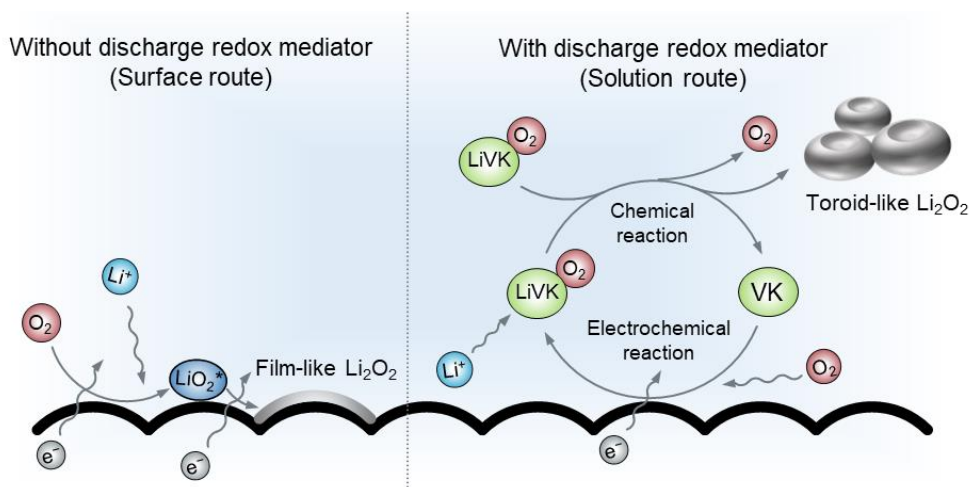


Figure 2.12. Schematic illustrations comparing the mechanism of Li_2O_2 formation with and without vitamin K2. Without the presence of vitamin K2, Li_2O_2 is formed through a surface-absorbed intermediate, LiO_2 , because of its low stability in a low-DN solvent. However, with the presence of vitamin K2, Li_2O_2 is formed in the electrolyte solution through disproportionation by generating a new intermediate, which is stable even in low-DN solvent.

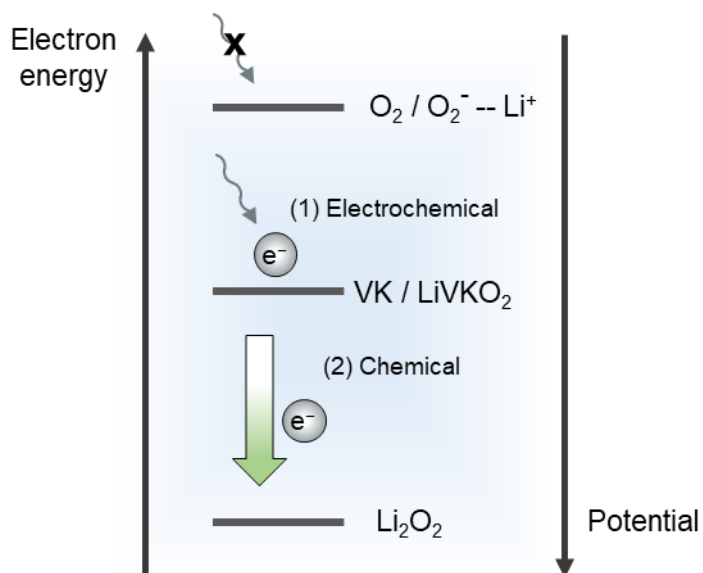


Figure 2.13. Electron energy (redox potential) diagram related to the working mechanism of vitamin K2. Because vitamin K2 has a higher redox potential than O_2 in the presence of both Li^+ and O_2 , it is reduced by an electron from the electrode before O_2 . Then, because of the difference in electron energy in $LiVKO_2$ and Li_2O_2 , the electron flow is thermodynamically driven from $LiVKO_2$ to Li_2O_2 while forming Li_2O_2 in the solution.

2.3.4 Charging the cell discharged with vitamin K2

To test the practical viability of employing the vitamin K2 ORR RM that yields a large toroidal Li_2O_2 discharge product, a dual RM-based lithium–oxygen cell was constructed.⁴³ Note that the use of an oxygen evolution reaction (OER) RM is indispensable in this case because the large toroidal Li_2O_2 particles are formed inside the pore of the electrode, which has a limited surface area and poor electrical contact. Indeed, in our own experiment in figure 2.14, the charge process without the OER RM was barely possible. TEMPO was introduced as the OER RM in our lithium–oxygen cell to examine the feasibility of decomposing the Li_2O_2 produced by the vitamin K2 mediator.⁴⁴ Before the cell test, the compatibility of the two RMs, vitamin K2 and TEMPO, was first tested as shown in figure 2.15. The redox reactions of both mediators were stable in the presence of each other, and no other side reactions were observed in the operating voltage range, implying that vitamin K2 and TEMPO can function independently in the same cell. Figure 2.16 presents the galvanostatic charge and discharge profiles of the dual RM cell with current density of 0.18 mA cm^{-2} . The cell could be charged and discharged without a noticeable change of the profile for multiple cycles. The charging of the cell by TEMPO mainly involved the evolution of O_2 as a gas product, as demonstrated with the differential electrochemical mass spectroscopy (DEMS) analysis in figure 2.17. The evolution of O_2 coincided with the time of cell charging but was also detected even after the end of charge because the unreacted oxidized TEMPO remained at the end of charge and required more time to diffuse to the residual Li_2O_2 to decompose.⁴⁵ Figure 2.18

present SEM images of the electrode discharged to $\sim 0.7 \text{ mAh cm}^{-2}$ and the charged electrode with the same amount of charge $\sim 0.7 \text{ mAh cm}^{-2}$, respectively. With the vitamin K2 and TEMPO, the discharge product formed was toroidal Li_2O_2 and was completely decomposed after the charge process. UV-vis titration method using TiOSO_4 solution also supports that the Li_2O_2 is completely decomposed by TEMPO during charge. White color of the sample solution prepared by charged electrode clearly shows the absence of Li_2O_2 after charge.(figure 2.19) These results support the viability of a lithium–oxygen battery system operated *via* the redox-mediated-solution-based formation and decomposition of Li_2O_2 , where the surface area of the air electrode is no longer an issue. Although carbon air electrodes with high surface area are vulnerable to side reactions with Li_2O_2 or carbon corrosion, which leads to the accumulation of an irreversible product such as Li_2CO_3 ,⁴⁶⁻⁴⁹ it is possible to use air electrodes with low surface area in all redox-mediated lithium–oxygen batteries because the main discharge/charge processes occur in the solution with little dependence on the air-electrode morphology. Accordingly, in such a system, the development of a carbon air electrode with high stability (low surface area) and a geometry that promotes facile diffusion of RMs should be the aim of the further research. Additionally, the introduction of an all redox-mediated lithium–oxygen battery system makes lithium–oxygen batteries more flexible in terms of the cell-configuration design. For instance, as recently proposed, the redox flow type of lithium–oxygen batteries can be more thoroughly considered, where the site for the electrochemical reaction (reduction or oxidation of the RM at the electrode) is

separated from the site for chemical reaction (generation or decomposition of Li_2O_2 by the RM).^{50, 51}

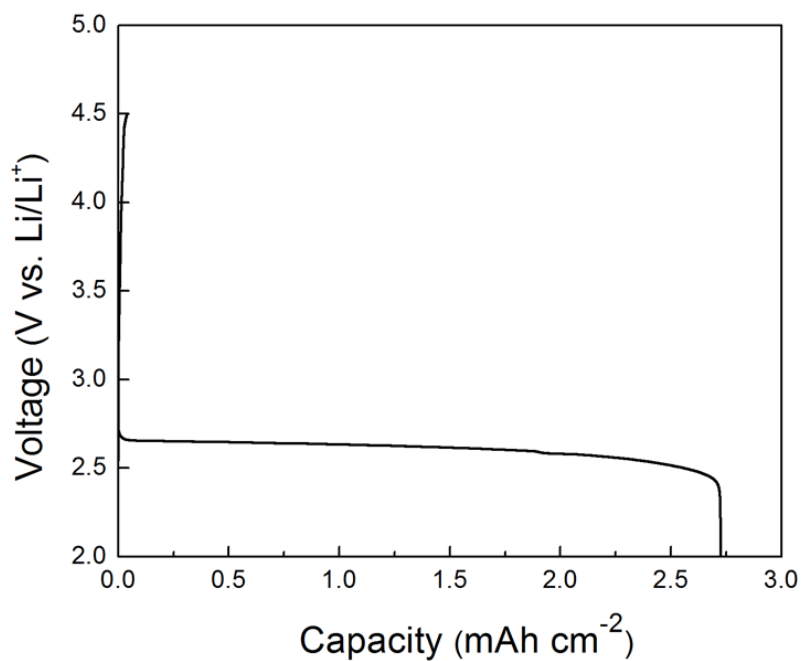


Figure 2.14. Inability to charge the cell containing only vitamin K2. Because of the poor contact of the discharge product with the electrode, it was rarely possible to decompose (charge) via direct electron conduction through the electrode surface.

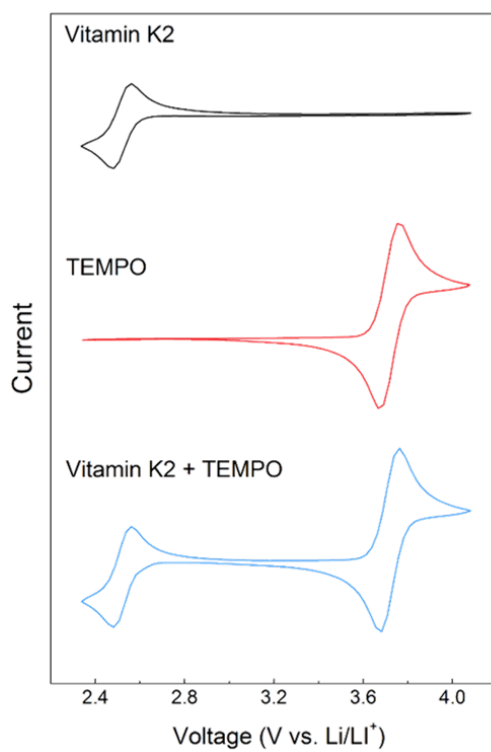


Figure 2.15. Cyclic voltammograms under scan rate of 50 mV s^{-1} showing that vitamin K2 and TEMPO can undergo redox reactions independently in the presence of each other.

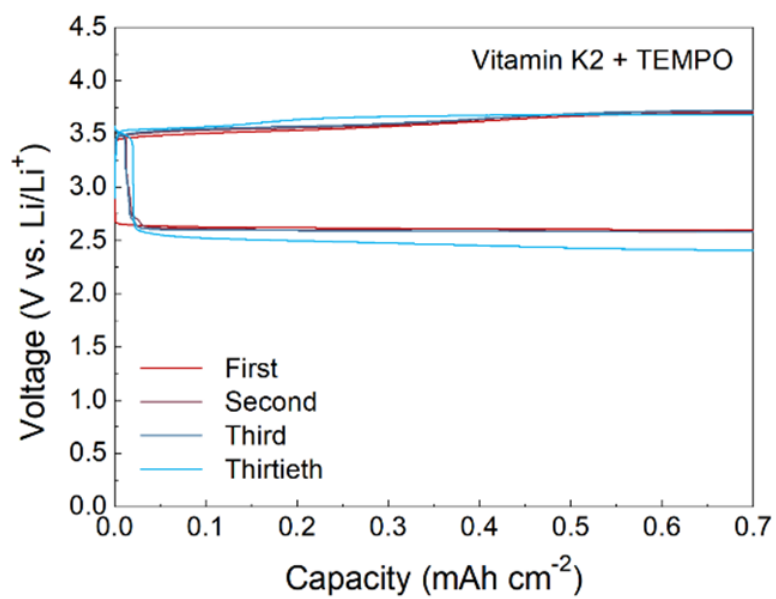


Figure 2.16. Galvanostatic profile of Li–O₂ cell with current density of 0.18 mA cm⁻² containing vitamin K2 (0.01 M) and TEMPO (0.1 M).

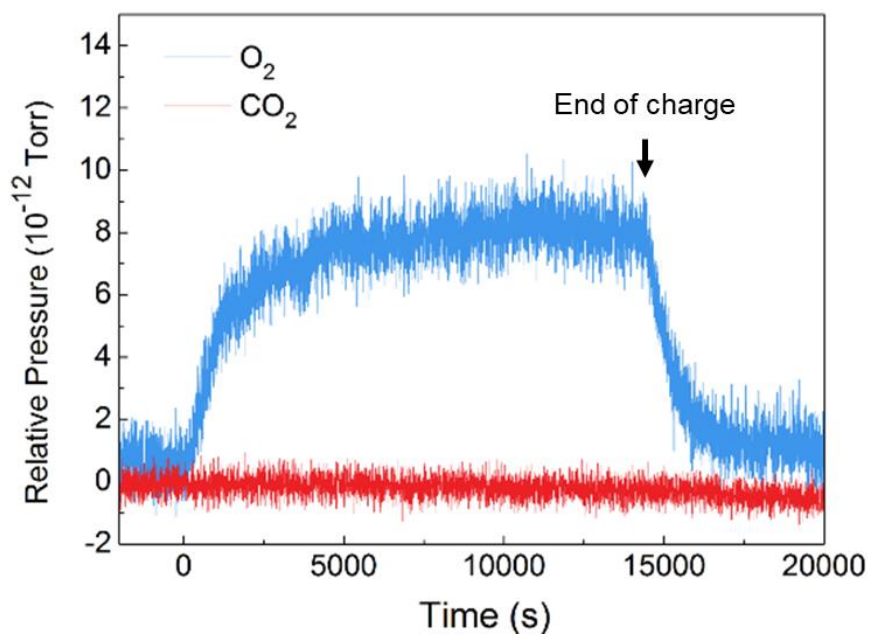


Figure 2.17. Analysis of gas evolved during the charge process showing the evolution of oxygen due to decomposition of Li₂O₂ with TEMPO

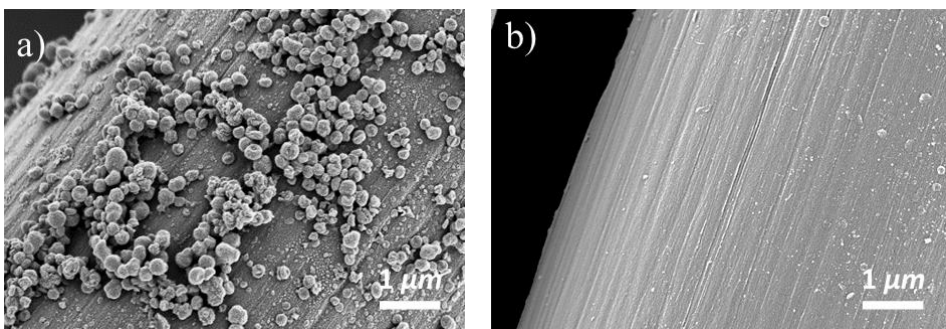


Figure 2.18. SEM image of the electrode from the cell containing vitamin K2 and TEMPO after (a) discharge to 0.7 mAh cm^{-2} and (b) charge to the same capacity.

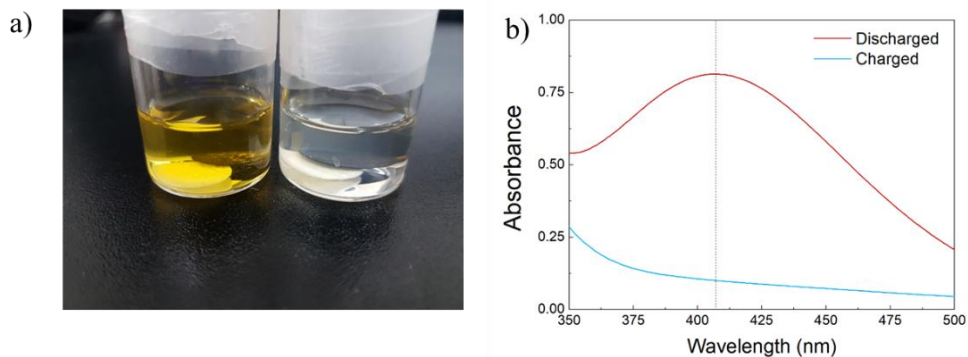


Figure 2.19. (a) Digital photo of the solutions for UV-vis titration prepared by discharged and charged cells. The solutions were prepared using air electrode and separator together with H_2O and TiO_5O_4 solution as explained in experimental section. Considering the yellow color of the solution is indication of Li_2O_2 , it is shown that Li_2O_2 was clearly decomposed during charge. (b) UV-vis absorption spectrum of the solutions. Peak intensity at 407 nm is assigned to the yellow color from $[\text{Ti}(\text{O}_2)]^{2+}$ complex in the solutions.

2.4 Concluding remarks

In summary, we successfully decoupled the charge-carrying redox property of RMs and the shuttling phenomenon by introducing a polymer-based RM, PTMA, where the typical charge carrying by mass diffusion in the electrolyte was replaced by charge carrying by electron transfer between polymer chains while retaining the redox-mediating capability. The suppression of shuttling was enabled by anchoring of TEMPO in the form of PTMA at an air electrode with reduced solubility. The stability of lithium metal and the efficiency of RM-assisted Li_2O_2 decomposition were substantially improved by inhibiting the migration of the RMs within the PTMA polymer. Consequently, the sustainable use of RMs was achieved, leading to significantly improved electrochemical performance of the RM-containing lithium-oxygen cell. This study suggests a new pathway for the more effective use of RMs in lithium-oxygen batteries, regulating the transport of the RMs without compensating for their redox-mediating capability.

2.5 References

1. Armand M, Tarascon J-M. Building better batteries. *Nature* 2008, **451**(7179): 652-657.
2. Bruce PG, Freunberger SA, Hardwick LJ, Tarascon J-M. Li–O₂ and Li–S batteries with high energy storage. *Nat. Mater.* 2012, **11**(1): 19.
3. Christensen J, Albertus P, Sanchez-Carrera RS, Lohmann T, Kozinsky B, Liedtke R, *et al.* A critical review of Li/air batteries. *J. Electrochem. Soc.* 2011, **159**(2): R1-R30.
4. Luntz AC, McCloskey BD. Nonaqueous Li–air batteries: a status report. *Chem. Rev.* 2014, **114**(23): 11721-11750.
5. Girishkumar G, McCloskey B, Luntz A, Swanson S, Wilcke W. Lithium–air battery: promise and challenges. *J. Phys. Chem. Lett.* 2010, **1**(14): 2193-2203.
6. Shao Y, Park S, Xiao J, Zhang J-G, Wang Y, Liu J. Electrocatalysts for nonaqueous lithium–air batteries: status, challenges, and perspective. *ACS Catal.* 2012, **2**(5): 844-857.
7. Black R, Adams B, Nazar L. Non-Aqueous and Hybrid Li–O₂ Batteries. *Adv. Energy Mater.* 2012, **2**(7): 801-815.
8. Johnson L, Li C, Liu Z, Chen Y, Freunberger SA, Ashok PC, *et al.* The role of LiO₂ solubility in O₂ reduction in aprotic solvents and its consequences for Li–O₂ batteries. *Nat. Chem.* 2014, **6**(12): 1091-1099.
9. Aetukuri NB, McCloskey BD, García JM, Krupp LE, Viswanathan V,

- Luntz AC. Solvating additives drive solution-mediated electrochemistry and enhance toroid growth in non-aqueous Li–O₂ batteries. *Nat. Chem.* 2015, **7**(1): 50-56.
10. Laoire CO, Mukerjee S, Abraham K, Plichta EJ, Hendrickson MA. Influence of nonaqueous solvents on the electrochemistry of oxygen in the rechargeable lithium– air battery. *J. Phys. Chem. C* 2010, **114**(19): 9178-9186.
 11. Adams BD, Radtke C, Black R, Trudeau ML, Zaghbi K, Nazar LF. Current density dependence of peroxide formation in the Li–O₂ battery and its effect on charge. *Energy Environ. Sci.* 2013, **6**(6): 1772-1778.
 12. Xia C, Black R, Fernandes R, Adams B, Nazar LF. The critical role of phase-transfer catalysis in aprotic sodium oxygen batteries. *Nat. Chem.* 2015, **7**(6): 496-501.
 13. Luntz A, Viswanathan V, Voss J, Varley J, Nørskov J, Scheffler R, *et al.* Tunneling and polaron charge transport through Li₂O₂ in Li–O₂ batteries. *J. Phys. Chem. Lett.* 2013, **4**(20): 3494-3499.
 14. Kim J, Park H, Lee B, Seong WM, Lim H-D, Bae Y, *et al.* Dissolution and ionization of sodium superoxide in sodium-oxygen batteries. *Nat. Commun.* 2016, **7**.
 15. Khetan A, Pitsch H, Viswanathan V. Solvent degradation in nonaqueous Li-O₂ batteries: oxidative stability versus H-abstraction. *J. Phys. Chem. Lett.* 2014, **5**(14): 2419-2424.

16. Khetan A, Pitsch H, Viswanathan V. Identifying descriptors for solvent stability in nonaqueous Li–O₂ batteries. *J. Phys. Chem. Lett.* 2014, **5**(8): 1318-1323.
17. Khetan A, Luntz A, Viswanathan V. Trade-offs in capacity and rechargeability in nonaqueous Li–O₂ batteries: solution-driven growth versus nucleophilic stability. *J. Phys. Chem. Lett.* 2015, **6**(7): 1254-1259.
18. Matsuda S, Hashimoto K, Nakanishi S. Efficient Li₂O₂ Formation via Aprotic Oxygen Reduction Reaction Mediated by Quinone Derivatives. *J. Phys. Chem. C* 2014, **118**(32): 18397-18400.
19. Lacey MJ, Frith JT, Owen JR. A redox shuttle to facilitate oxygen reduction in the lithium air battery. *Electrochem. Commun.* 2013, **26**: 74-76.
20. Yang L, Frith J, Garcia-Araez N, Owen JR. A new method to prevent degradation of lithium–oxygen batteries: reduction of superoxide by viologen. *Chem. Commun.* 2015, **51**(9): 1705-1708.
21. Gao X, Chen Y, Johnson L, Bruce PG. Promoting solution phase discharge in Li–O₂ batteries containing weakly solvating electrolyte solutions. *Nat. Mater.* 2016, **15**(8): 882-888.
22. Lim H-D, Gwon H, Kim H, Kim S-W, Yoon T, Choi JW, *et al.* Mechanism of Co₃O₄/graphene catalytic activity in Li–O₂ batteries using carbonate based electrolytes. *Electrochim. Acta* 2013, **90**: 63-70.
23. Adams BD, Black R, Radtke C, Williams Z, Mehdi BL, Browning ND, *et*

- al.* The Importance of nanometric passivating films on cathodes for Li–air batteries. *ACS nano* 2014, **8**(12): 12483-12493.
24. McCloskey BD, Valery A, Luntz AC, Gowda SR, Wallraff GM, Garcia JM, *et al.* Combining accurate O₂ and Li₂O₂ assays to separate discharge and charge stability limitations in nonaqueous Li–O₂ batteries. *J. Phys. Chem. Lett.* 2013, **4**(17): 2989-2993.
25. Schwenke KU, Metzger M, Restle T, Piana M, Gasteiger HA. The influence of water and protons on Li₂O₂ crystal growth in aprotic Li–O₂ cells. *J. Electrochem. Soc.* 2015, **162**(4): A573-A584.
26. Beyer H, Meini S, Tsiouvaras N, Piana M, Gasteiger H. Thermal and electrochemical decomposition of lithium peroxide in non-catalyzed carbon cathodes for Li–air batteries. *Phys. Chem. Chem. Phys.* 2013, **15**(26): 11025-11037.
27. Kracke F, Vassilev I, Krömer JO. Microbial electron transport and energy conservation—the foundation for optimizing bioelectrochemical systems. *Front. Microbiol.* 2015, **6**: 575.
28. Green DE, Tzagoloff A. The mitochondrial electron transfer chain. *Arch. Biochem. Biophys.* 1966, **116**: 293-304.
29. Pandya K, King H. Ubiquinone and menaquinone in bacteria: a comparative study of some bacterial respiratory systems. *Arch. Biochem. Biophys.* 1966, **114**(1): 154-157.
30. Prince RC, Dutton PL, Bruce JM. Electrochemistry of ubiquinones:

- menaquinones and plastoquinones in aprotic solvents. *FEBS Lett.* 1983, **160**(1-2): 273-276.
31. Lemma E, Uden G, Kröger A. Menaquinone is an obligatory component of the chain catalyzing succinate respiration in *Bacillus subtilis*. *Arch. Microbiol.* 1990, **155**(1): 62-67.
 32. Savéant J-M. *Elements of molecular and biomolecular electrochemistry: an electrochemical approach to electron transfer chemistry*, vol. 13. John Wiley & Sons, 2006.
 33. Hartmann P, Bender CL, Vračar M, Dürr AK, Garsuch A, Janek J, *et al.* A rechargeable room-temperature sodium superoxide (NaO₂) battery. *Nat. Mater.* 2013, **12**(3): 228-232.
 34. Freunberger SA, Chen Y, Peng Z, Griffin JM, Hardwick LJ, Bardé F, *et al.* Reactions in the rechargeable lithium–O₂ battery with alkyl carbonate electrolytes. *J. Am. Chem. Soc.* 2011, **133**(20): 8040-8047.
 35. Freunberger SA, Chen Y, Drewett NE, Hardwick LJ, Bardé F, Bruce PG. The Lithium–Oxygen Battery with Ether-Based Electrolytes. *Angew. Chem., Int. Ed.* 2011, **50**(37): 8609-8613.
 36. Chen Y, Freunberger SA, Peng Z, Bardé F, Bruce PG. Li–O₂ battery with a dimethylformamide electrolyte. *J. Am. Chem. Soc.* 2012, **134**(18): 7952-7957.
 37. McCloskey B, Bethune D, Shelby R, Girishkumar G, Luntz A. Solvents' critical role in nonaqueous lithium–oxygen battery electrochemistry. *J.*

- Phys. Chem. Lett.* 2011, **2**(10): 1161-1166.
38. Burke CM, Black R, Kochetkov IR, Giordani V, Addison D, Nazar LF, *et al.* Implications of 4 e⁻ Oxygen Reduction via Iodide Redox Mediation in Li–O₂ Batteries. *ACS Energy Lett.* 2016, **1**(4): 747-756.
 39. McCloskey BD, Addison D. A viewpoint on heterogeneous electrocatalysis and redox mediation in nonaqueous Li–O₂ batteries. *ACS Catal.* 2016.
 40. Olivares-Marín M, Sorrentino A, Lee R-C, Pereiro E, Wu N-L, Tonti D. Spatial distributions of discharged products of lithium–oxygen batteries revealed by synchrotron X-ray transmission microscopy. *Nano Lett.* 2015, **15**(10): 6932-6938.
 41. Zhang Y, Wang L, Zhang X, Guo L, Wang Y, Peng Z. High-Capacity and High-Rate Discharging of a Coenzyme Q10-Catalyzed Li–O₂ Battery. *Adv. Mater.* 2018, **30**(5): 1705571.
 42. McCloskey BD, Scheffler R, Speidel A, Girishkumar G, Luntz AC. On the mechanism of nonaqueous Li–O₂ electrochemistry on C and its kinetic overpotentials: some implications for Li–air batteries. *J. Phys. Chem. C* 2012, **116**(45): 23897-23905.
 43. Gao X, Chen Y, Johnson LR, Jovanov ZP, Bruce PG. A rechargeable lithium–oxygen battery with dual mediators stabilizing the carbon cathode. *Nat. Energy* 2017, **2**(9): 17118.
 44. Bergner BJ, Schürmann A, Peppeler K, Garsuch A, Janek Jr. TEMPO: a

- mobile catalyst for rechargeable Li-O₂ batteries. *J. Am. Chem. Soc.* 2014, **136**(42): 15054-15064.
45. Lim HD, Song H, Kim J, Gwon H, Bae Y, Park KY, *et al.* Superior rechargeability and efficiency of lithium–oxygen batteries: hierarchical air electrode architecture combined with a soluble catalyst. *Angew. Chem., Int. Ed.* 2014, **53**(15): 3926-3931.
46. McCloskey B, Speidel A, Scheffler R, Miller D, Viswanathan V, Hummelshøj J, *et al.* Twin problems of interfacial carbonate formation in nonaqueous Li–O₂ batteries. *J. Phys. Chem. Lett.* 2012, **3**(8): 997-1001.
47. Itkis DM, Semenenko DA, Kataev EY, Belova AI, Neudachina VS, Sirotnina AP, *et al.* Reactivity of carbon in lithium–oxygen battery positive electrodes. *Nano Lett.* 2013, **13**(10): 4697-4701.
48. Ottakam Thotiyl MM, Freunberger SA, Peng Z, Bruce PG. The carbon electrode in nonaqueous Li–O₂ cells. *J. Am. Chem. Soc.* 2012, **135**(1): 494-500.
49. Bae Y, Yun YS, Lim H-D, Lee H, Kim Y-J, Kim J, *et al.* Tuning the Carbon Crystallinity for Highly Stable Li–O₂ Batteries. *Chem. Mater.* 2016, **28**(22): 8160-8169.
50. Zhu YG, Wang X, Jia C, Yang J, Wang Q. Redox-Mediated ORR and OER Reactions: Redox Flow Lithium Oxygen Batteries Enabled with a Pair of Soluble Redox Catalysts. *ACS Catal.* 2016, **6**(9): 6191-6197
51. Zhu YG, Jia C, Yang J, Pan F, Huang Q, Wang Q. Dual redox catalysts for

oxygen reduction and evolution reactions: towards a redox flow Li–O₂
battery. *Chem. Commun.* 2015, **51**(46): 9451-9454.

Chapter 3. Investigation on the fundamentals of redox mediators

3.1 Understanding fundamental aspects of redox mediator for oxygen reduction reaction

3.1.1 Research Background

With a widespread employment of energy storage system and increasing market size, world demands higher performance standard and requires the development of next-generation energy storage systems, especially whose energy density surpasses that of a conventional lithium-ion battery.^{1,2} Triggered by such demand, a worldwide effort has been continued to develop post battery systems with high energy density such as metal-air batteries,³⁻⁷ metal-sulfur batteries,^{3, 8-10} and organic batteries.^{11, 12} Among them, lithium-oxygen batteries have received much attention owing to their extremely high theoretical energy density of 3500 Wh kg⁻¹ attributed to the use of light oxygen molecules as redox-active materials.^{4, 13, 14} The reaction chemistry of the lithium-oxygen battery is based on the formation of insulating solid discharge product (*i.e.* lithium peroxide, Li₂O₂) initiated by an electrochemical oxygen reduction reaction (ORR).⁶ The electrochemical formation of lithium peroxide leads to the coverage of an electrode surface by a solid product and its insulating nature consequently causes electrode passivation and premature cell death (*i.e.* end of

discharge).^{15, 16} Such inevitable electrode passivation prevents lithium-oxygen battery from achieving a truly high energy density.

To circumvent problematic electrode passivation during ORR, redox-mediating catalysts, so-called redox mediators (RMs) have been recently introduced.¹⁷⁻²⁰ On RM-mediated ORR, RMs are reduced instead of oxygen molecules due to their higher redox potential (electrochemical electron transfer (ET) step). Then, they chemically transfer an electron to oxygen with reducing oxygen to the final discharge product of lithium peroxide (chemical ET step), while reduced RMs returning back to their neutral form. Because the chemical ET between reduced RMs and oxygen chemically occurs away from the electrode surface, RM-mediated ORR could suppress the electrode passivation leading to much-prolonged discharge time and thereby, enhanced discharge capacity.¹⁹⁻²¹ Although several classes of materials such as quinones¹⁹⁻²³ and viologens^{24, 25} have been reported to show catalytic activity as RMs for ORR, the researches mostly focused on the demonstration of catalytic performance of individual RMs. However, a fundamental study such as kinetic and mechanistic investigation in catalytic reaction has not been paid attention to. When it comes to the performance of catalysts, fundamental aspects are known to play a critical role. For example, catalytic kinetics and catalyst-driven reaction path governs the efficiency of water-splitting catalysts.²⁶⁻²⁸ Likewise, kinetics of oxygen evolution reaction catalyst for lithium-oxygen batteries is closely related to the power capability of the system.^{17, 29-31} Accordingly, the investigation on fundamental feature would be essential step to develop highly efficient RMs and further, lithium-oxygen

batteries with truly high energy density.

Here, we conducted a comparative study employing various derivatives of benzoquinone family taking advantage of its chemical diversity. By measuring the kinetics of the catalytic reaction, we found that the distinct kinetics of quinones is fully interpretable by the Marcus theory coupled with consideration on steric hindrance. Based on the observed steric effect in kinetics, we concluded that the RM-mediated ORR occurs via inner-sphere ET with confirming the presence of the intermediate state. To investigate how kinetics determine the catalytic performance (*i.e.* increase in discharge capacity), we conducted a galvanostatic discharge experiment. Volcano behavior was clearly observed in the relationship between kinetics *vs.* performance, which indicates the intermediate kinetics region achieves most enhanced discharge capacity by effectively forming a discharge product and preventing surface passivation simultaneously. This study provides fundamental understanding in terms of kinetics and mechanism and also reveals the correlation between an intrinsic property (*i.e.* kinetics) and extrinsic property (*i.e.* catalytic performance). The findings in this study will suggest a guideline for the design of highly efficient RMs which is a key to realize lithium-oxygen batteries with truly high energy density.

3.1.2 Experimental Method

3.1.2.1 Material preparation

Tetraethylene glycol dimethyl ether (TEGDME, $\geq 99\%$, Sigma-Aldrich) used as organic solvent for the electrolyte was dried for more than 2 days with a molecular sieve (type 3Å, Sigma-Aldrich). The bis(trifluoromethane)sulfonimide lithium salt (LiTFSI, $> 99.95\%$) was purchased from Sigma-Aldrich. It was dried for more than 2 days at $180\text{ }^{\circ}\text{C}$ under vacuum. Benzoquinone derivatives, Methyl-p-benzoquinone, 2,5-Dimethyl-1,4-benzoquinone, Duroquinone, Thymoquinone, 2-tert-Butyl-1,4-benzoquinone, 2,5-Di-tert-butyl-1,4-benzoquinone, 2,6-Di-tert-butyl-1,4-benzoquinone, 2,5-Di-tert-octyl-1,4-benzoquinone, and 2,5-Dichloro-1,4-benzoquinone were purchased from Sigma-Aldrich and used as received. 2-Phenyl-1,4-benzoquinone, 2,3,5-Trimethyl-1,4-benzoquinone were purchased from Tokyo chemical industry and 2,5-Di-phenyl-1,4-benzoquinone was purchased from Santa Cruz biotechnology. Quinones were used as received. 1 M of LiTFSI was dissolved in TEGDME solvent to produce quinone-free electrolyte. Quinone-containing electrolyte was made by additionally dissolving 1 or 10 mM of each quinone. The final water content of all electrolyte was confirmed to be less than 50 ppm by Karl Fischer titration). Before used as air electrode, gas diffusion layer (H23, Freudenberg) was heat-treated at $900\text{ }^{\circ}\text{C}$ for 3 hours with Ar:H₂ (95:5 volume ratio) atmosphere. Lithium iron phosphate (LFP) electrode was fabricated by coating slurry on Al foil. The slurry was prepared by mixing LFP powder, polyvinylidene fluoride, and super P with the weight ratio of 90:7:3 into 1-methyl-2-pyrrolidinone. Before used as

separator, glass fiber (GF/D, Whatman) was washed with acetone and dried at 70 °C under vacuum for more than a day.

3.1.2.2 Lithium-oxygen cell assembly

To construct lithium-oxygen cell, swagelok-type cell was used. A sheet of gas diffusion layer was used as air electrode. A sheet of glass fiber and LFP electrode was used as separator and counter electrode, respectively. Air electrode, separator, and counter electrode was prepared to have a diameter of 1/2 inch. The amount of electrolyte used in assembling the cells was 200 μ l. After cell assembly in Ar-filled glove box (O_2 level < 0.1 ppm and H_2O level < 0.1 ppm), the atmosphere of empty space above air electrode was changed to O_2 (> 99.999%) and the cells were operated as closed.

3.1.2.3 Electrochemical analysis and characterization

For cyclic voltammetry three-electrode beaker cell was used. Gold electrode and platinum wire was used as working and counter electrode, respectively. For reference electrode, 0.01 M Ag/Ag⁺ in acetonitrile was used. For linear sweep voltammetry, glassy carbon rotating disk electrode, and rotating ring disk electrode with glassy carbon disk and Pt ring (PINE research) were used as working electrodes, and the same counter and reference electrode as cycling voltammetry experiment was used. To rotate electrodes, the rotator (PINE research, AFMSRCE) was employed. For cyclic voltammetry and galvanostatic discharge experiment, a potentiostat (WonA Tech, WBCS 3000) was employed. For linear sweep voltammetry with RDE and RRDE, bi-potentiostat (Biologics, VSP-300) was employed. To calculate diffusivity

and heterogeneous electron transfer rate from RDE profile, kinematic viscosity was measured by viscometer (Cannon-Fenske Routine Viscometer, Cannon Instrument Company) For the observation on the electrode surface, field-emission scanning electron microscopy (SUPRA 55VP, Carl Zeiss) was used. The characterization on discharged electrode was conducted by X-ray diffractometer. (D2 phaser, Bruker)

3.1.2.4 Calculation detail

Density functional theory (DFT) based quantum mechanics calculation was conducted for geometry optimization, and energy evaluation, which was carried out by Gaussian 09 software package.³² All of calculations was spin-unrestricted calculation at the Becke-Lee-Yang-Parr (B3LYP) level of theory³³⁻³⁵ with basis set 6-311G.^{36, 37} All of structures was confirmed by absence of imaginary frequencies. A polarizable continuum model (PCM)^{38, 39} was used to describe solvation effect of TEGDME solvent.

3.1.3 Results and Discussions

3.1.3.1 The principles of redox mediator for the oxygen reduction reaction

Figure 3.1 shows the energy levels relating to the working mechanism of RMs. As a first step of RM-mediated ORR, RMs are electrochemically reduced earlier than oxygen molecule due to their higher potential than that of O_2/O_2^- , which is followed by an instant formation of LiRM complex. (reaction 1, electrochemical ET) Then, reduced RMs chemically transfer an electron to oxygen with reducing it to lithium peroxide whose redox potential is 2.96 V vs. Li/Li⁺ (reaction 2, chemical ET). Giving electron to oxygen, reduced RMs are oxidized back to neutral form and it participates in the following catalytic cycle. The deviation of the redox potential of RMs from 2.96 V is the driving force for chemical ET.



Considering the basic energy relationship between RMs, oxygen, and lithium peroxide, the redox potential of RMs should be located between that of O_2/O_2^- and lithium peroxide. To investigate fundamentals on RMs, a comparative study is to be conducted employing benzoquinone family selected due to its versatility in chemical structure. A molecular structure of 12 benzoquinone derivatives is shown in figure 3.2 with 12 distinct colors assigned to each quinone. Figure 3.3 shows the overlay of cyclic voltammetry (CV) profiles of quinones with the CV profile of oxygen reduction (black line) and the potential of lithium peroxide (dotted line) plotted

together. The experiment was conducted with 1 M LiTFSI tetraethylene glycol dimethyl ether (TEGDME) containing 10 mM of each quinone under the Ar atmosphere with the scan rate of 50 mV s⁻¹. All quinones exhibit reversible redox reaction ensuring the basic requirement for RMs. In terms of redox potential, all candidates except DCBQ have redox potential located within the boundary, (Table 3.1) which suggests all quinones but DCBQ satisfy the redox potential requirement.

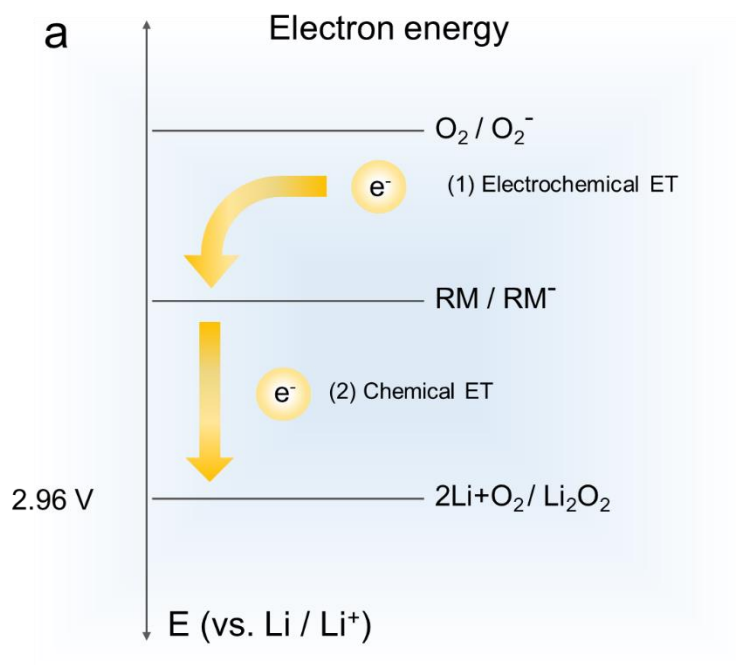


Figure 3.1. Energy relationship during oxygen reduction reaction with a redox mediator. Electrochemical reduction of quinone occurs, followed by chemical electron transfer to oxygen to form lithium peroxide.

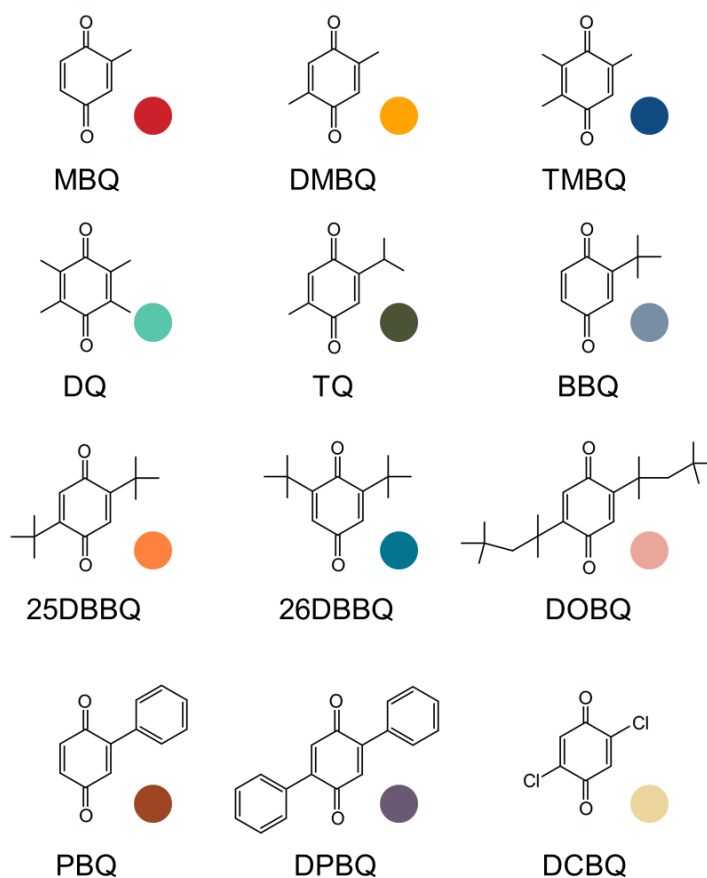


Figure 3.2. Benzoquinone candidates with various functional groups. 12 different colors were assigned to each quinone. Each abbreviation denotes following quinones: MBQ (Methyl-p-benzoquinone), DMBQ (2,5-Dimethyl-1,4-benzoquinone), TMBQ (2,3,5-Trimethyl-1,4-benzoquinone), DQ (Duroquinone), TQ (Thymoquinone), BBQ (2-tert-Butyl-1,4-benzoquinone), 25DBBQ (2,5-Di-tert-butyl-1,4-benzoquinone), 26DBBQ (2,6-Di-tert-butyl-1,4-benzoquinone), DOBQ (2,5-Di-tert-octyl-1,4-benzoquinone), PBQ (2-Phenyl-1,4-benzoquinone), DPBQ (2,5-Di-phenyl-1,4-benzoquinone), and DCBQ (2,5-Dichloro-1,4-benzoquinone).

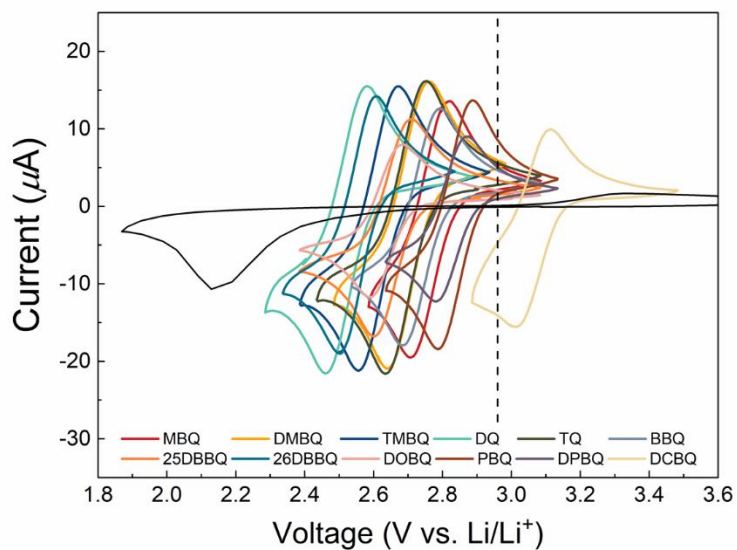


Figure 3.3. Cyclic voltammetry profile of quinones at the scan rate of 50 mV s^{-1} . 1 M LiTFSI TEGDME electrolyte containing 10 mM of quinone was used as an electrolyte.

Species	E^0 (V vs. Li/Li ⁺)	Species	E^0 (V vs. Li/Li ⁺)
MBQ	2.765	25DBBQ	2.658
DMBQ	2.698	26DBBQ	2.565
TMBQ	2.610	DOBQ	2.639
DQ	2.513	PBQ	2.832
TQ	2.696	DPBQ	2.830
BBQ	2.748	DCBQ	3.065

Table 3.1. The redox potential of quinones obtained from cyclic voltammetry.

3.1.3.2 The catalytic activity of quinones and its kinetics

To confirm catalytic activity, the redox behavior in an oxygen atmosphere was observed and compared with that in Ar atmosphere. Figure 3.4 are CV profiles of quinones under the same experimental condition as used in figure 3.3. Grey and black line is the CV profiles of blank electrolyte under Ar and O₂ atmosphere, respectively, and darker and lighter line of each characteristic color is the CV profile of Q-containing electrolyte under Ar and O₂ atmosphere, respectively. In all cases except DCBQ, the cathodic current from quinone reduction in the O₂ atmosphere increased compared to that in the Ar atmosphere. It is because that quinone undergoes the series of electrochemical, chemical, and electrochemical reaction (ECE mechanism)⁴⁰; quinone undergoes electrochemical reduction followed by chemical oxidation with catalytic reaction and electrochemically reduced again at an electrode. Accordingly, the current increase indicates the presence of catalytic activity and it suggests that all quinones with appropriate redox potential shows the activity.^{19, 20} It is noticeable that the amount of current increase depends on the type of quinone species. For example, MBQ and TQ show ~2 and ~3 times of current increase, respectively. On the other hand, PBQ exhibits only a slight amount of increase. We suppose the amount of current increase is intimately linked with the kinetics of the catalytic reaction. To investigate the catalytic reaction in more detail, especially in terms of the kinetics, we performed linear sweep voltammetry (LSV) coupled with a rotating ring disk electrode (RRDE).⁴¹⁻⁴³ The experiment was performed with 1 M LiTFSI TEGDME electrolyte containing 1 mM of quinone

under the O₂ atmosphere. The disk potential was scanned with the rate of 10 mV s⁻¹ and the ring potential was fixed at 3.5 V (vs. Li/Li⁺) to ensure the overpotential high enough to generate mass transport-limited anodic current.⁴⁰ Figure 3.5 is the schematics showing the reactions occurring at the surface of RRDE. With sweeping disk potential, quinone starts to be reduced at disk electrode generating disk current (I_d). Reduced quinone drifts out toward ring disk owing to electrolyte flux made by electrode rotation and it is oxidized at ring electrode generating ring current. (I_r) While reduced quinone drifted from disk to ring electrode, it instantly undergoes a chemical reaction with surrounding oxygen molecules, which ends up a decrease in the amount of reduced quinone reaching to ring electrode and thus, a decrease in I_r. Accordingly, the ratio of I_r to I_d (I_r/I_d), also referred to as kinetic collection efficiency (N_k) is directly influenced by the rate of a chemical reaction.^{41, 43, 44} Consequently, the measurement of N_k enables measurement and comparison on the rate of chemical ET step. (reaction 2) The obtained I_r, I_d, and N_k profiles for quinones are shown in figure 3.6. The deviation of disk potential from theoretical redox potential of each quinone (Table 3.1) was used for comparison. It is observed that the magnitude of N_k is largely dependent on the types of quinone species as expected from the current increase behavior in CV profiles. Note that N_k was averaged in the potential range low enough (E_{disk}-E₀ < -0.1 V) for N_k to be stabilized and however, not too low (-0.15 V < E_{disk}-E₀) so that the second reduction of quinone to Q²⁻ does not occur. The obtained N_k for all quinones are listed in figure 3.7 and the exact value is shown in Table 3.2. The dotted line denotes the N_{theoretical} value of 0.144 measured under the

environment where reduced species does not chemically react during the flight from disk to ring electrode. (Figure 3.8) Slower kinetics yields N_k value closer to $N_{\text{theoretical}}$ and faster kinetics yields N_k value closer to zero.^{41, 44} As can be seen in figure 3.7, the kinetics of chemical ET of quinones is widely distributed depending on the type of quinone.

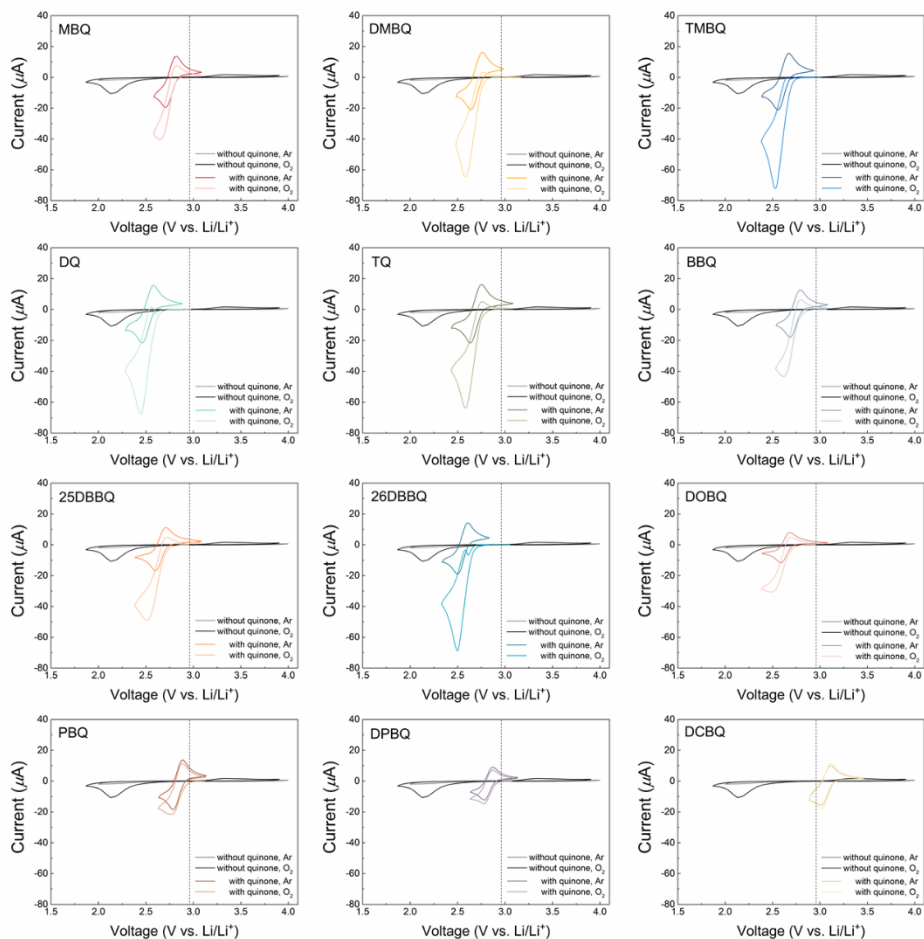


Figure 3.4. Cyclic voltammety profiles quinones in Ar and O₂ atmosphere. 1M LiTFSI TEGDME with 10 mM of each quinone and the scan rate of 50 mV s⁻¹ were used. A distinct amount of current increase in O₂ atmosphere which is related to the catalytic activity was observed.

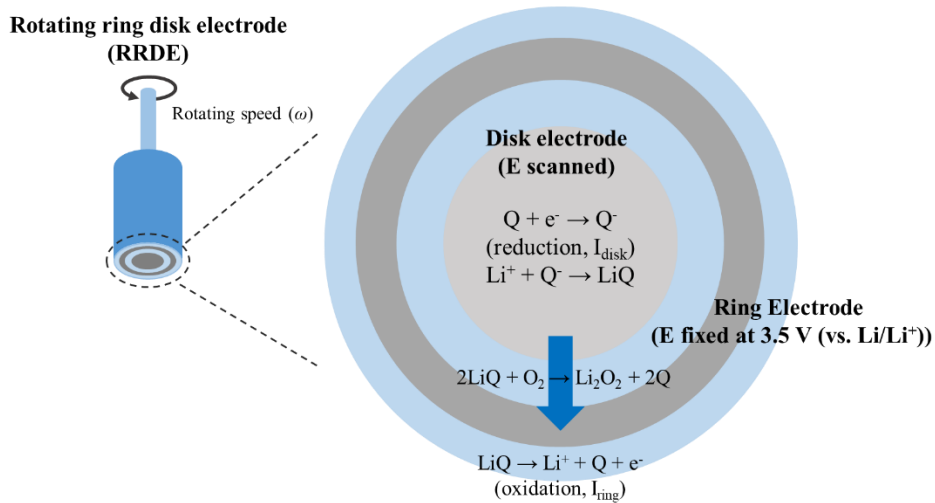


Figure 3.5. Schematics showing the reactions occurring at rotating ring disk electrode. At disk electrode quinone is reduced and drifts out to ring electrode where reduced quinone is oxidized.

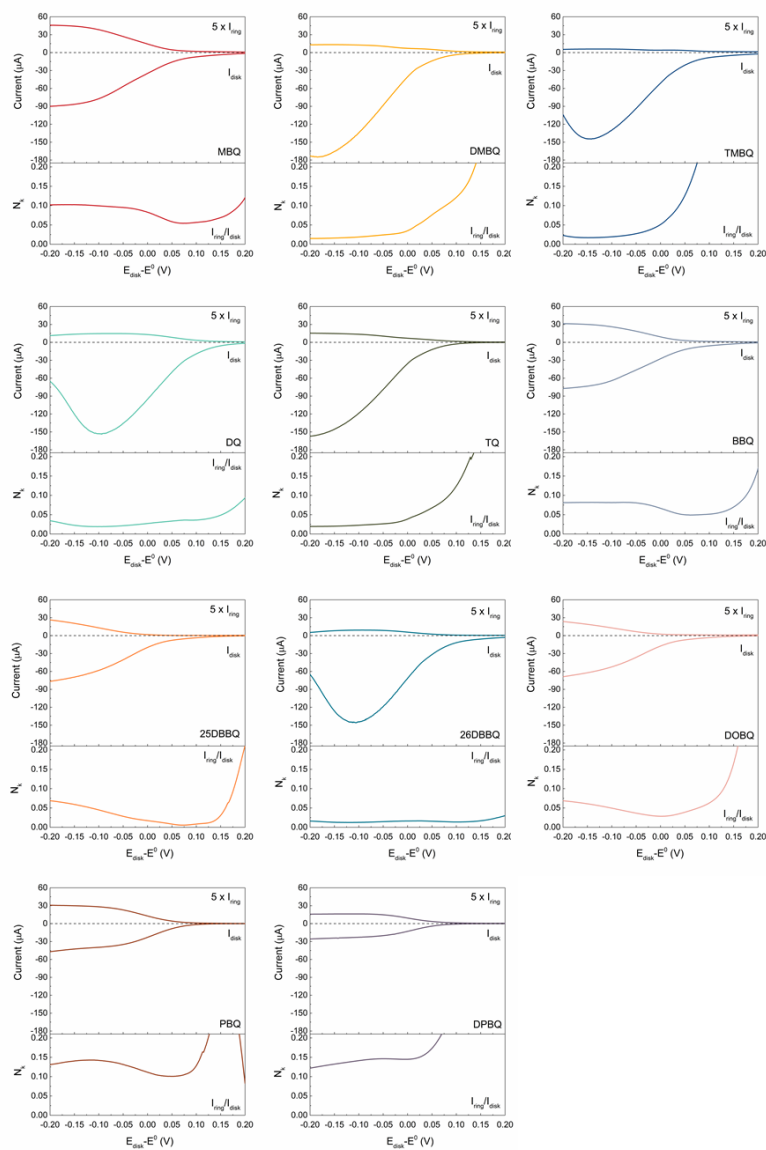


Figure 3.6. Linear sweep voltammetry profile with rotating ring disk electrode. 1M LiTFSI TEGDME containing 1 mM of quinone and the scan rate of 10 mV s^{-1} were used. Ring current, disk current, and kinetic collection efficiency (ratio of two current) were shown.

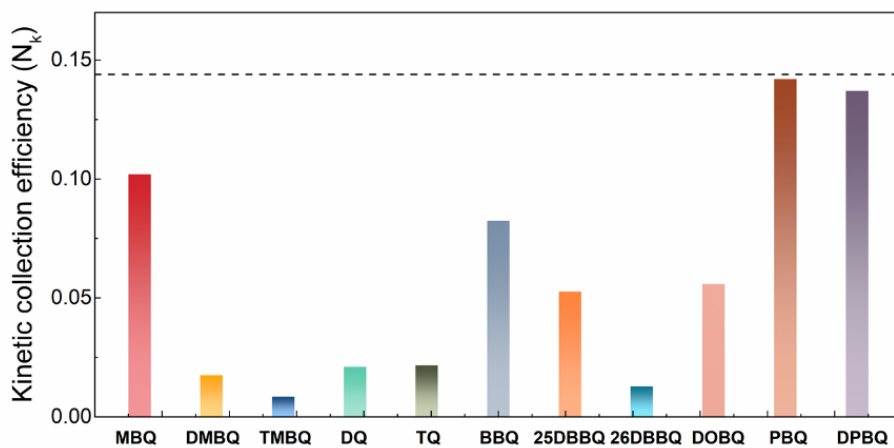


Figure 3.7. Kinetic collection efficiency of all quinones showing a wide range of distribution.

Species	Kinetic collection efficiency, N_k	Species	Kinetic collection efficiency, N_k
MBQ	0.1020	25DBBQ	0.0526
DMBQ	0.0175	26DBBQ	0.0128
TMBQ	0.0085	DOBQ	0.0558
DQ	0.0210	PBQ	0.1420
TQ	0.0216	DPBQ	0.1370
BBQ	0.0824	PBQ, Ar	0.1440

Table 3.2. Kinetic collection efficiency of quinones obtained by the ratio of ring current to disk current in the RRDE experiment.

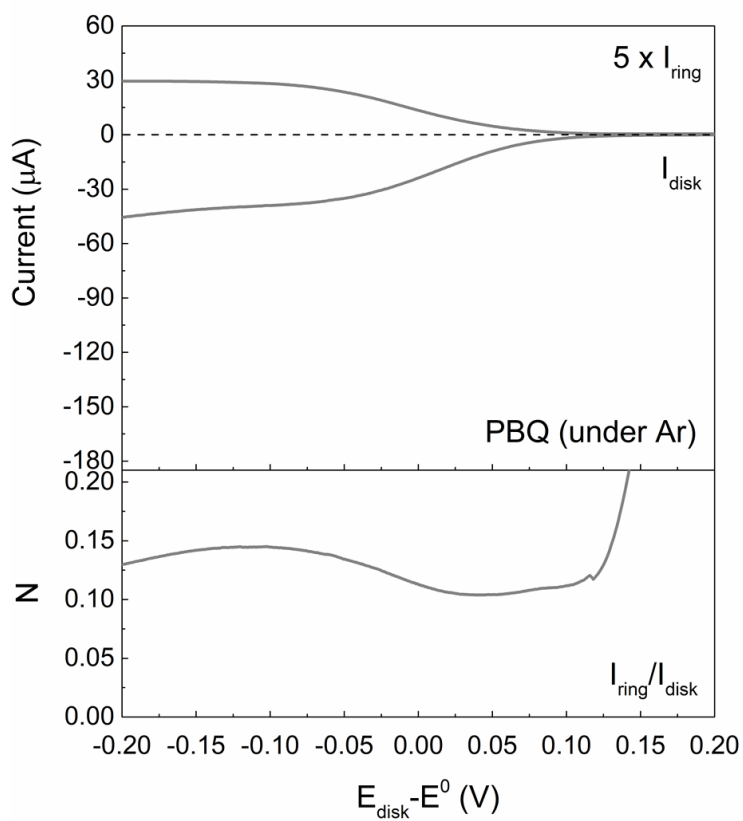


Figure 3.8. Linear sweep voltammetry profile with RRDE of PBQ under Ar atmosphere. Theoretical maximum collection efficiency was obtained.

3.1.3.3 The dependence of kinetic parameters on the kinetics of redox mediators

To study the factors governing the kinetics of chemical ET, a possible dependence between various kinetic parameters and N_k was investigated. Ring disk electrode (RDE) with LSV experiment was employed to measure a diffusivity (D) and heterogeneous electron transfer rate (k_0).^{40, 45, 46} RDE experiment was conducted with the same electrolyte and scan rate as the RRDE experiment. Figure 3.9 is LSV profiles of quinones with various rotating speeds. According to the Levich equation, the plot of (rotating speed, ω)^{1/2} vs. (limiting current, i_L) shows a linear relationship whose slope enables diffusivity calculation.⁴⁰ Figure 3.10 shows the plot of ω ^{1/2} vs. i_L and its linear fitting line for all quinones. Diffusivity was calculated based on the slope of the fitting line and listed in Table 3.3. The other kinetic parameter, k_0 was also measured using the Koutecky-Levich equation. According to the equation, the y-intercept of a linear fitting line from the plot of ω ^{-1/2} vs. i^{-1} indicates kinetic current (i_k).⁴⁰ Figure 3.11 is the plot of ω ^{-1/2} vs. i^{-1} at various overpotential (η). Then, we calculated k_0 as y-intercept of the linear fitting in the Tafel plot as shown in figure 3.12.⁴⁰ The calculated k_0 values are shown in Table 3.4. (See supplement note for more detailed explanation on the relating equations and calculation of diffusivity and heterogeneous electron transfer rate using RDE) As shown in figure 3.13 and 3.14, neither D nor k_0 show a clear dependence on N_k . It implies that D and k_0 are not the factors governing the kinetics of chemical ET. Rather, the other factor, such as

driving force (*i.e.* energy difference between reactants and product) would govern the kinetics of chemical ET.

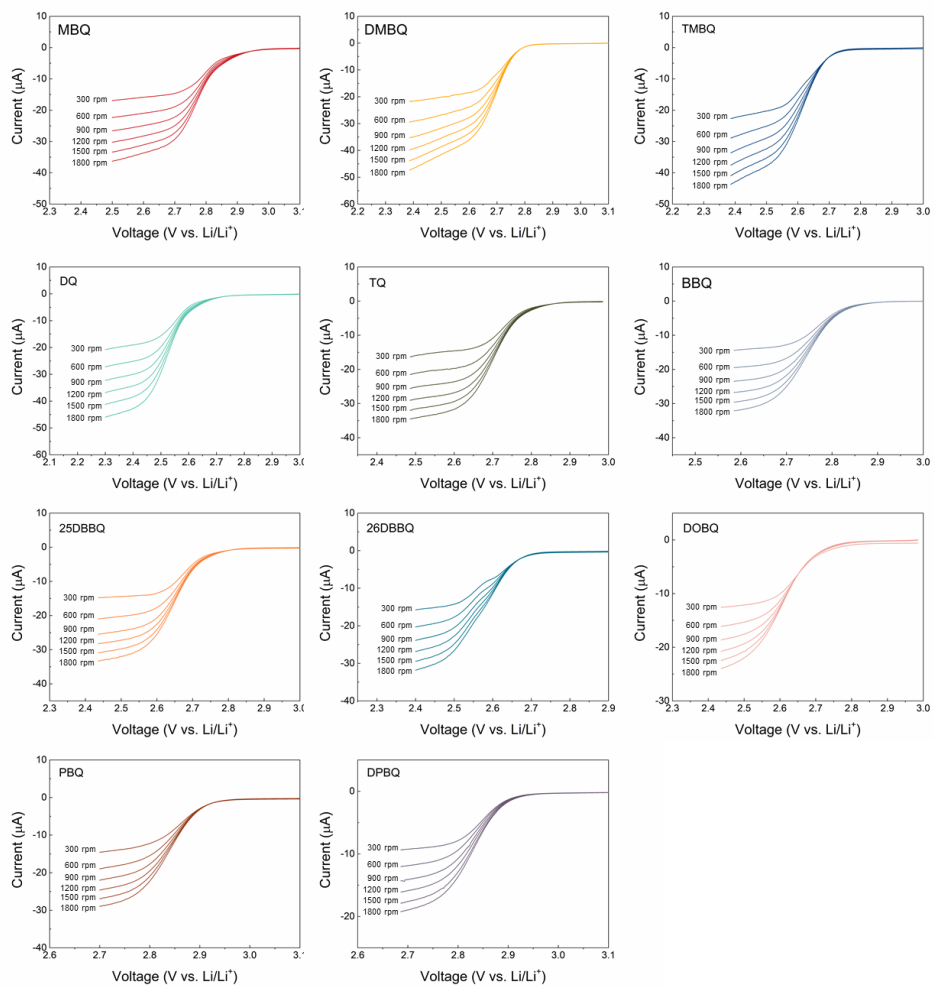


Figure 3.9. LSV profile with RRDE at various rotating speeds. 1M LiTFSI TEGDME with 1 mM of quinone and the scan rate of 10 mV s⁻¹ were used.

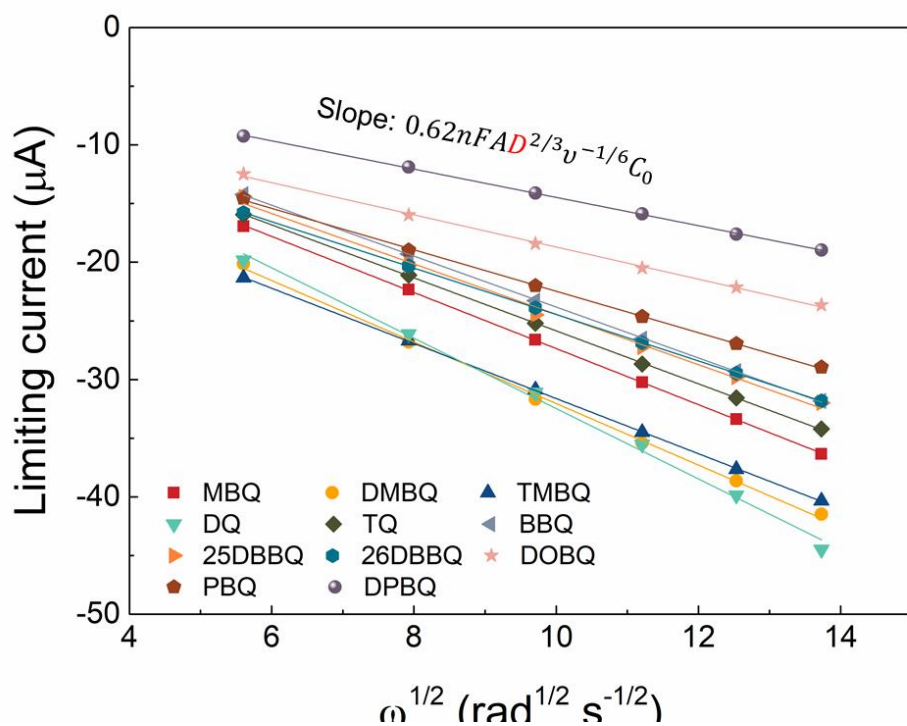


Figure 3.10. The plot of (rotating speed)^{1/2} vs. limiting current and linear fitting line.

Diffusivity can be calculated by the slope of the fitting line.

Species	Diffusivity, D (cm ² s ⁻¹)	Species	Diffusivity, D (cm ² s ⁻¹)
MBQ	1.632E-06	25DBBQ	1.390E-06
DMBQ	1.876E-06	26DBBQ	1.229E-06
TMBQ	1.592E-06	DOBQ	7.091E-07
DQ	2.295E-06	PBQ	1.037E-06
TQ	1.499E-06	DPBQ	5.848E-07
BBQ	1.413E-06		

Table 3.3. Diffusivity of quinones. It was calculated by the RDE experiment with various rotating speeds.

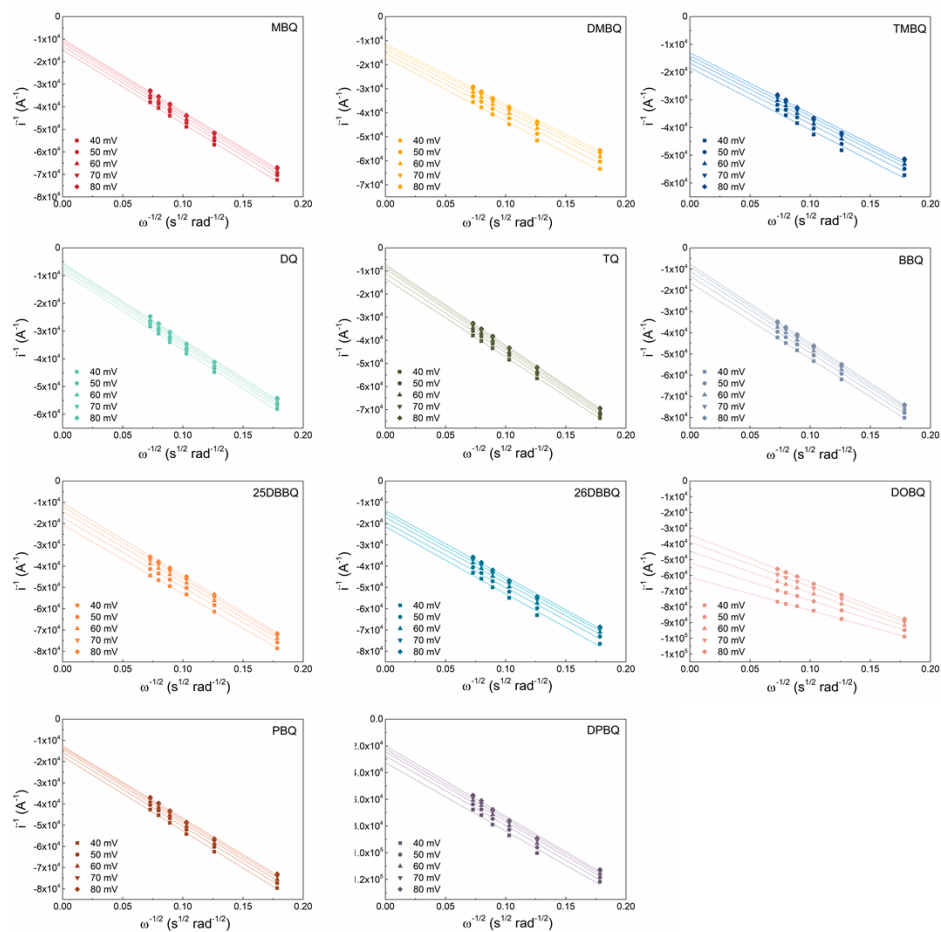


Figure 3.11. The plot of (rotating speed)^{-1/2} vs. current⁻¹ profile of quinones at various overpotential and linear fitting lines whose y-intercept indicates i_k^{-1} .

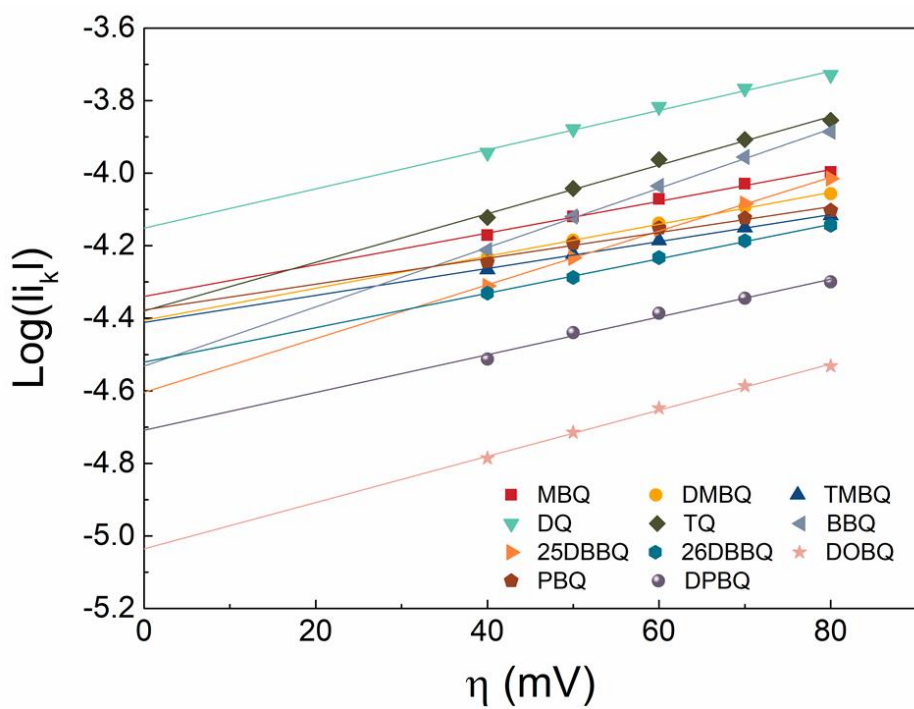


Figure 3.12. The plot of overpotential vs. $\log(i_k)$ and linear fitting line whose y-intercept indicates $\log(i_0)$.

Species	Heterogeneous electron transfer rate constant, k_0 (cm s ⁻¹)	Species	Heterogeneous electron transfer rate constant, k_0 (cm s ⁻¹)
MBQ	2.41E-03	25DBBQ	1.31E-03
DMBQ	2.08E-03	26DBBQ	1.59E-03
TMBQ	2.05E-03	DOBQ	4.87E-04
DQ	3.72E-03	PBQ	2.22E-03
TQ	2.20E-03	DPBQ	1.03E-03
BBQ	1.55E-03		

Table 3.4. Heterogeneous electron transfer rate constant for quinones. It was calculated by the RDE experiment.

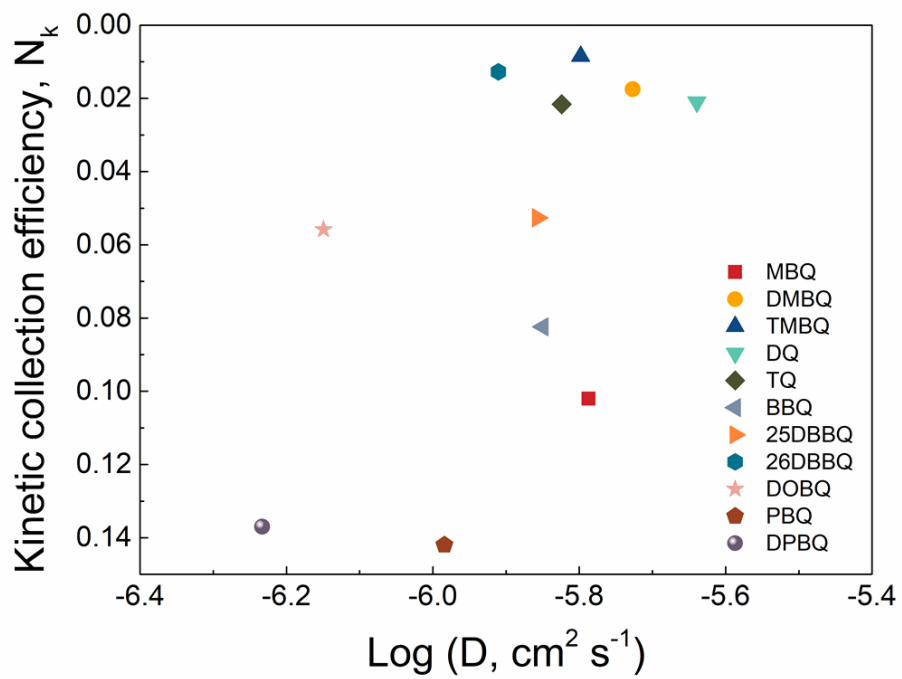


Figure 3.13. The dependence of diffusivity on catalytic kinetics.

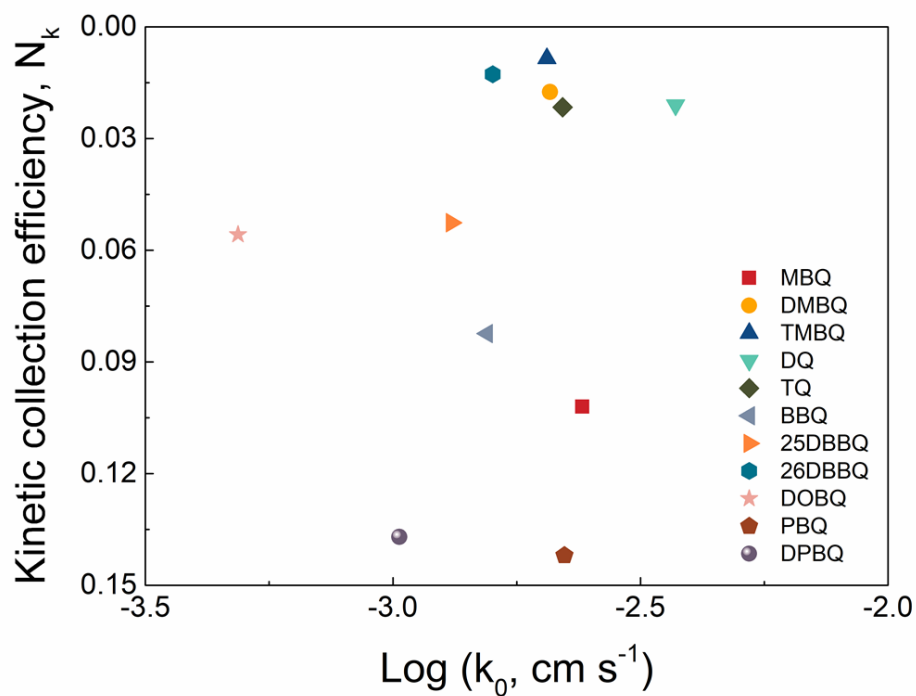


Figure 3.14. The dependence of heterogeneous electron transfer rate on catalytic kinetics.

3.1.3.4 Marcus theory: steric effect and inner-sphere electron transfer

The dependence of N_k on the driving force is shown in figure 3.15. Driving force is expressed as the deviation of quinone redox potential from the formation potential of lithium peroxide. (figure 3.1) Interestingly, the relationship between kinetics (N_k) and driving force is shown to generally follow the Marcus theory. In the classical Marcus theory, the correlation between the kinetics of outer-sphere ET and driving force is simply expressed according to

$$k_{et} = A e^{\frac{-\Delta G^\ddagger}{k_B T}} \quad \text{Equation 1}$$

$$\Delta G^\ddagger = \frac{\lambda}{4} \left(1 - \frac{-\Delta G^0}{\lambda}\right)^2 \quad \text{Equation 2}$$

where k_{et} is the rate constant of chemical ET, A is collision factor, ΔG^\ddagger is the activation free energy (\ddagger denotes transition state), k_B is Boltzmann constant, T is the absolute temperature, ΔG^0 is the energy difference between reactants and product, and λ is the summation of solvational and vibrational reorganization energy.⁴⁷ Note that the magnitude of ΔG^0 , (i.e. $-\Delta G^0$) is the driving force. According to equation 1 and 2, two key messages of Marcus theory on the kinetics of outer-sphere ET are as follows; 1) the rate of outer-sphere ET enhances with increasing $-\Delta G^0$ until $-\Delta G^0$ reaches to λ , and 2) once $-\Delta G^0$ exceeds λ , the rate of outer-sphere ET decreases with increasing $-\Delta G^0$. Here, the region corresponding to the situation of 2) is termed ‘Marcus inverted region’.^{47,48} In figure 3.15, when $0 \text{ eV} < -\Delta G^0 < 0.35 \text{ eV}$, the kinetics of ET generally enhances with increasing $-\Delta G^0$. On the other hand, when $0.35 \text{ eV} < -\Delta G^0$, the kinetics

decreases with increasing driving force. We suppose the region of $0.35 \text{ eV} < -\Delta G^0$ is 'Marcus inverted region'. Notable is that there are several points not explainable by the classical Marcus theory assuming outer-sphere ET. Despite their higher driving force, 25DBBQ and DOBQ exhibit slower kinetics than DMBQ and TQ and even slower than those in the inverted region. It implies the kinetics of chemical ET between LiQ and O₂ (reaction 2) cannot be fully understood based on the assumption that it is outer-sphere ET. Accordingly, we assume here that reaction 2 is not a simple outer-sphere ET, and rather inner-sphere ET. Inner-sphere ET refers to the reaction in which the electron transfer from one to the other occurs via the formation of tightly bound intermediate species.^{49, 50} In this case, not only the driving force but also the redox center and a molecular structure of reactants concurrently affect the rate of ET.^{30, 51} Considering that all materials here have the same redox center as quinone, it is expected that a molecular structure would influence the kinetics and thereby, enabling the interpretation on the kinetics of 25DBBQ and DOBQ. The effect of a molecular structure is generally handled as steric hindrance, the magnitude of which can be quantified as A-value.⁵² Figure 3.16.a shows the A-value of several functional groups contained in DMBQ, TQ, 25DBBQ, and DOBQ.⁵³ Note that the A-value of octyl- is estimated to be larger than that of butyl-. Figure 3.16.b shows the magnitude of the steric hindrance of quinone molecules estimated based on A-value, which increases in the order of DMBQ, TQ, 25DBBQ, and DOBQ. Interestingly, the order of steric hindrance well matches with the order of kinetics. In other words, the molecule with a more sterically hindered functional group shows more sluggish ET

kinetics. Such phenomena is referred to as ‘steric effect’.^{54, 55} It is because the steric hindrance of the reactant interrupts the formation of an intermediate state during inner-sphere ET.⁵⁵ For this reason, the presence of a steric effect has been considered a probe for inner-sphere ET.⁵¹ Therefore, we concluded that the nature of chemical ET (reaction 2) is inner-sphere ET rather than a simple outer-sphere ET. Furthermore, we suggest that three reactants, LiQ and O₂ form tightly bound intermediate species during inner-sphere ET.

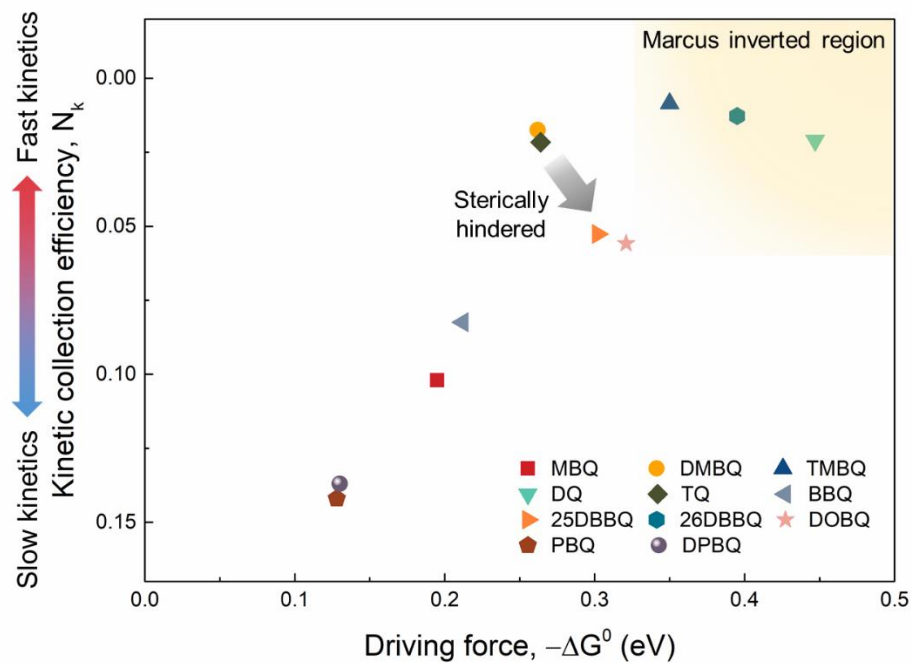


Figure 3.15. The dependence of catalytic kinetics on driving force, which is explained by Marcus theory and steric effect. The shaded area denotes inverted region.

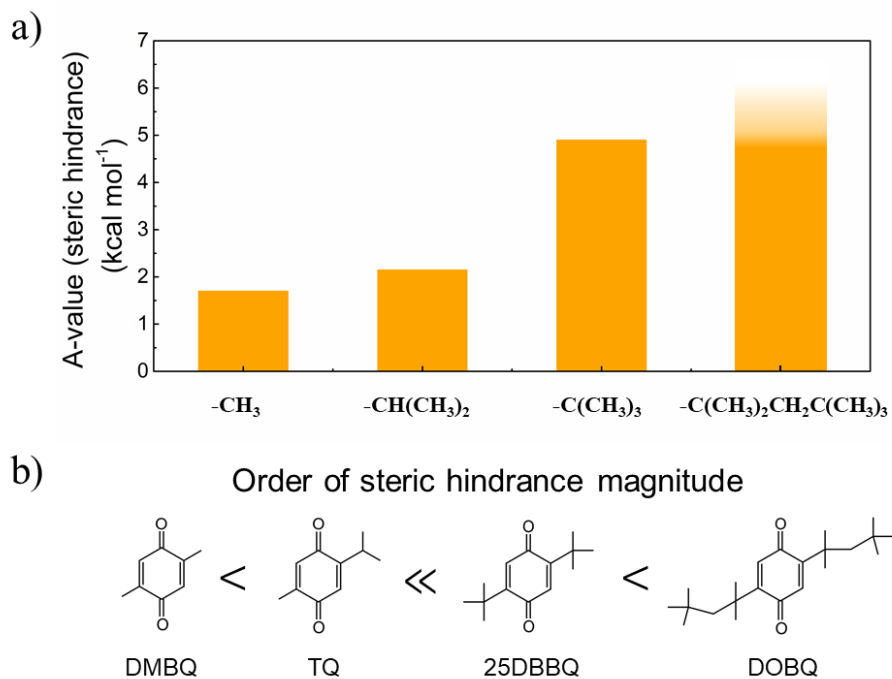


Figure 3.16. (a) several functional groups' A-value that quantifies the magnitude of steric hindrance.⁵³ (b) the order of steric hindrance of DMBQ, TQ, 25DBBQ, and DOBQ.

3.1.3.5 Reaction mechanism: a significance of inner-sphere electron transfer

To elucidate the significance of inner-sphere ET and the presence of an intermediate state, reaction chemistry needs to be considered in detail. The chemical ET step (reaction 2) includes three reactants, two LiQs, and O₂. From the perspective of collision probability, it is rational to suppose that three reactants react by two-step two-body reactions, rather than one-step three-body reaction. Given that serial two-body reaction occurs, the first two-body reaction is either reaction 3 or reaction 4. Note that ET does not occur either in reaction 3 or reaction 4.



DFT calculation confirmed reaction 3 is more feasible among two possible paths and defined the stable configuration of LiQO₂. (Figure 3.17) Following the formation of LiQO₂, the second two-body reaction is expected to occur as reaction 5.



Considering the chemical ET occurs during the second two-body step (reaction 5), we suppose that reaction 5 corresponds to an inner-sphere ET reaction, and two reactants, LiQO₂ and LiQ form a tightly bound intermediate species of LiQO₂LiQ. Consequently, we found that the lithium peroxide formation by two LiQs and O₂ proceeds by serial two-body reactions initiated by LiQO₂ generation, and we, for the first time, demonstrated the presence of intermediate species in RM-based catalytic

reaction. The schematics in figure 3.18 summarizes reaction mechanism during RM-mediated ORR.

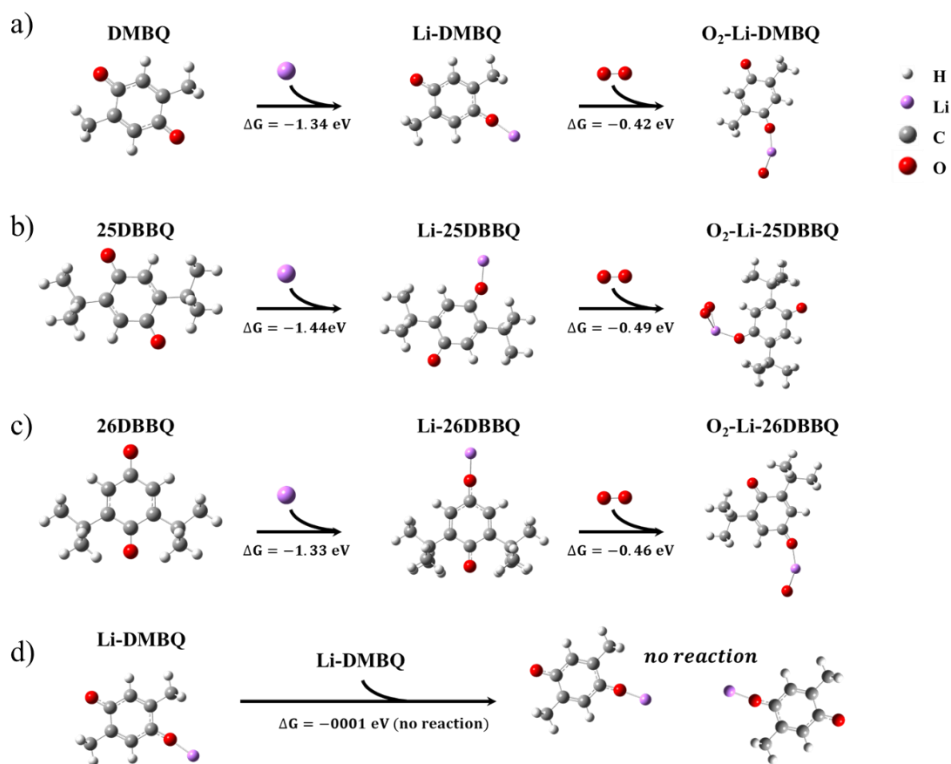


Figure 3.17. DFT calculation result showing the stable formation of LiQO₂ species. Reduced state of several representative quinones (a) DMBQ, (b) 25DBBQ, and (c) 26DBBQ form stable complex with Li⁺ to form LiQ. Then it is followed by the formation of LiQO₂ complex. (d) two LiQ complexes do not form stable complex between two.

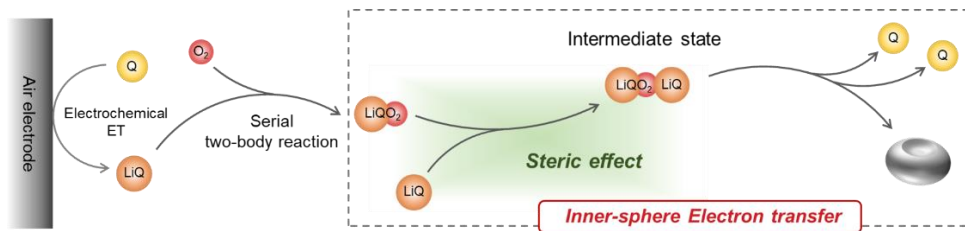


Figure 3.18. Schematics showing the reaction mechanism of redox-mediated discharge in lithium-oxygen batteries.

3.1.3.6 The implication of kinetics in the performance of lithium-oxygen cell

As shown in figure 3.7, the kinetics exhibits quite a wide variation depending on the type of quinone. To investigate the impact of kinetics in the performance of catalysts (*i.e.* delaying electrode passivation and enhancing discharge capacity), a galvanostatic discharge experiment was conducted. 1M LiTFSI TEGDME containing 10 mM of each quinone was used as an electrolyte. For the air electrode and anode, H23 carbon paper and lithium iron phosphate were used, respectively. Figure 3.19 is galvanostatic profiles obtained with the current density of 0.2 mA cm^{-2} . The profiles of quinone-containing cells are plotted as solid lines with characteristic color assigned to each quinone. A dotted line is the profile of the quinone-free cell. The distinct voltage plateau for each quinone is observed due to characteristic redox potential. Not only the voltage, however, but also the discharge capacity is shown to largely depend on the type of quinone. To study a influence of kinetics on discharge capacity, discharge capacity and N_k were displayed together in figure 3.20. Note that average discharge capacity and standard deviation was obtained by 3 times of discharge experiment. (Table 3.5) Surprisingly, volcano behavior is found in the relationship between kinetics and performance, which means not low or high kinetics, but intermediate kinetics results in the best catalytic performance. It is a similar phenomenon observed in the field of heterogeneous catalysts where binding energy of catalysts toward reactants and performance shows a similar trend.^{28, 56, 57} We categorized quinones into three groups to elucidate how

kinetics and performance create volcano behavior. Group 1 includes MBQ, BBQ, PBQ, DPBQ, all of which show slow kinetics and limited capacity. 25DBBQ and DOBQ with intermediate kinetics and high capacity belong to group 2. Lastly, group 3 includes the rest, DMBQ, TMBQ, DQ, TQ, 26DBBQ, all of which have fast kinetics and relatively lower capacity than group 2. Because the discharge capacity is strongly related to surface passivation, scanning electron microscopy (SEM) was used to observe electrode surface. Figure 3.21 are SEM images of fully discharged electrodes with representative quinones from each group. For the quinone in slow kinetic region, (MBQ, group 1) SEM image at low magnification does not show much difference from the images of pristine electrode and the electrode discharged without quinone as shown in figure 3.22. High magnification image reveals that the electrode surface is passivated by film-like discharge products the same as a quinone-free case. It implies that quinones in group 1 have limited capability to form discharge products owing to their sluggish catalytic kinetics, and thus not preventing electrode passivation and leading to low capacity. For the quinone in intermediate kinetic region, (25DBBQ, group 2) totally different images of the electrode were obtained. In low magnification SEM image, it is clearly shown that the discharge product fills void space between fibers, which is indicative of much-boosted discharge capacity. SEM image with higher magnification confirms the morphology of discharge product as toroid-shaped, which was analyzed as lithium peroxide by X-ray diffraction as shown in figure 3.23. It is worth noting that the electrode surface not passivated is observed in a high magnification image even after the end of

discharge. We suppose that quinones in group 2 have kinetics fast enough to form toroidal discharge products so that they suppress electrode passivation and enable prolonged discharge. Lastly, for the quinone in fast kinetic region, (TMBQ, group 3) electrode image with low magnification shows that unlike group 2, no discharge product presents in void space in spite of fast kinetics. Higher magnification SEM images reveal that the electrode surface is all covered by the toroidal discharge products. It implies that quinones in group 3 have enough kinetics to form toroidal discharge products. However, kinetics is too fast compared with group 2 so that it triggers the rapid formation of discharge products in the vicinity of electrode surface, which causes surface passivation. SEM images of other quinones in group 1, group 2, and group 3 are shown in figure 3.24 and 2.25. How intrinsic kinetics determines extrinsic catalytic performance (*i.e.* enhancement of discharge capacity) is schematically illustrated in figure 3.26 and can be summarized as follows. 1) Quinones with limited kinetics fail to suppress electrode passivation and leads to low capacity, 2) Quinones with moderate kinetics efficiently form discharge product while preventing electrode passivation, and thereby continuing discharge, and 3) Quinone with excessive kinetics form discharge product too rapidly and rather passivates electrode surface resulting in limited capacity.

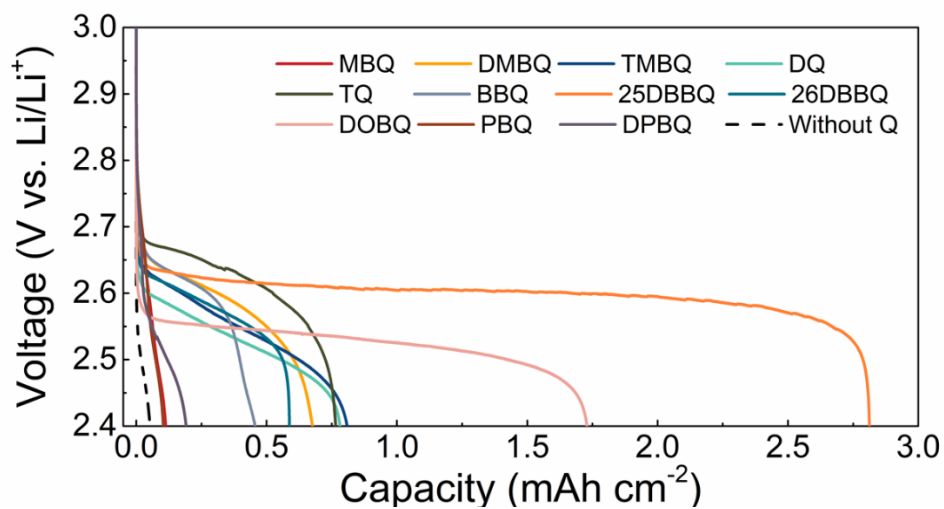


Figure 3.19. Galvanostatic discharge experiment profiles under the current density of 0.2 mA cm^{-2} . $1 \text{ M LiTFSI TEGDME}$ containing 10 mM of quinone was used as an electrolyte.

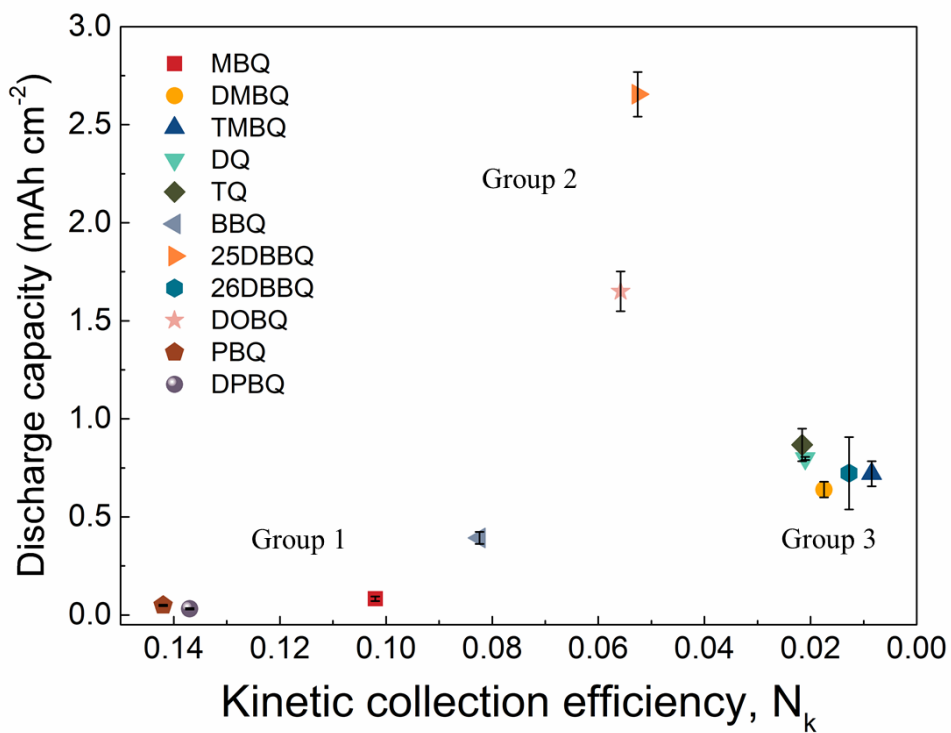


Figure 3.20. The relationship between discharge capacity and catalytic kinetics showing volcano behavior. Quinones are grouped into three depending on their discharge capacity.

Species	Discharge capacity (mAh cm ⁻²)			Average capacity (mAh cm ⁻²)	Standard deviation
	1st	2nd	3rd		
MBQ	0.098	0.0786	0.0702	0.0823	0.01173
DMBQ	0.599	0.625	0.693	0.639	0.03972
TMBQ	0.688	0.809	0.664	0.720	0.06367
DQ	0.793	0.809	0.793	0.798	0.00764
TQ	0.776	0.849	0.977	0.867	0.08308
BBQ	0.421	0.407	0.351	0.393	0.03034
25DBBQ	2.565	2.585	2.815	2.655	0.11343
26DBBQ	0.984	0.595	0.589	0.723	0.18481
DOBQ	1.507	1.729	1.715	1.651	0.10142
PBQ	0.0484	0.0449	0.0533	0.0489	0.00345
DPBQ	0.0291	0.0362	0.0281	0.0312	0.00359

Table 3.5. Discharge capacity with average and standard deviation. The galvanostatic discharge experiment was conducted three times.

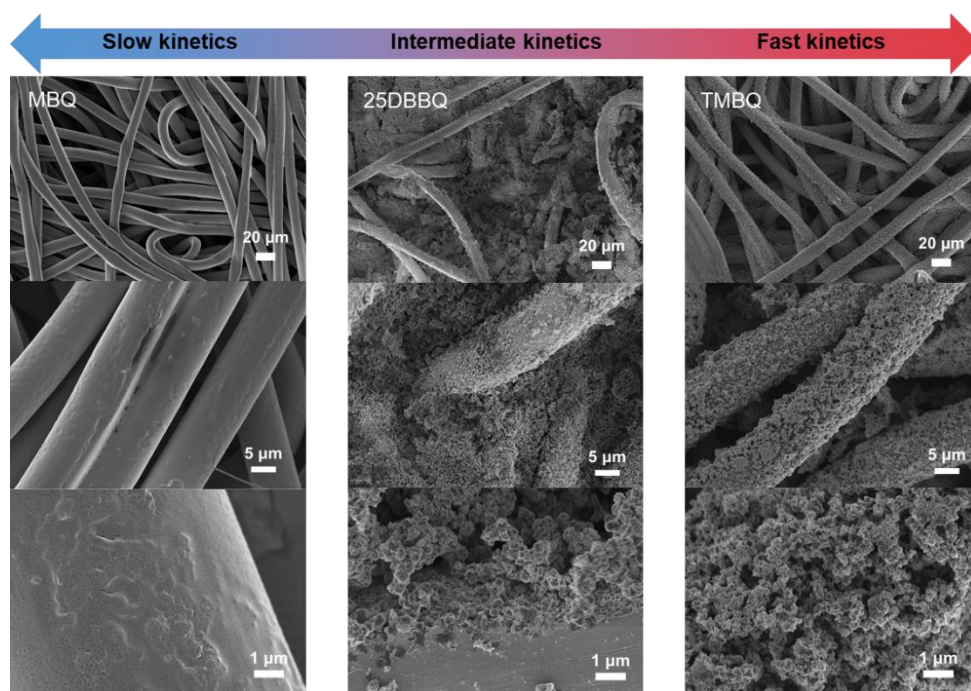


Figure 3.21. Scanning electron microscopy images of a representative quinone from each group; MBQ from group 1,(left) 25DBBQ from group 2,(mid) and TMBQ from group 3.(right)

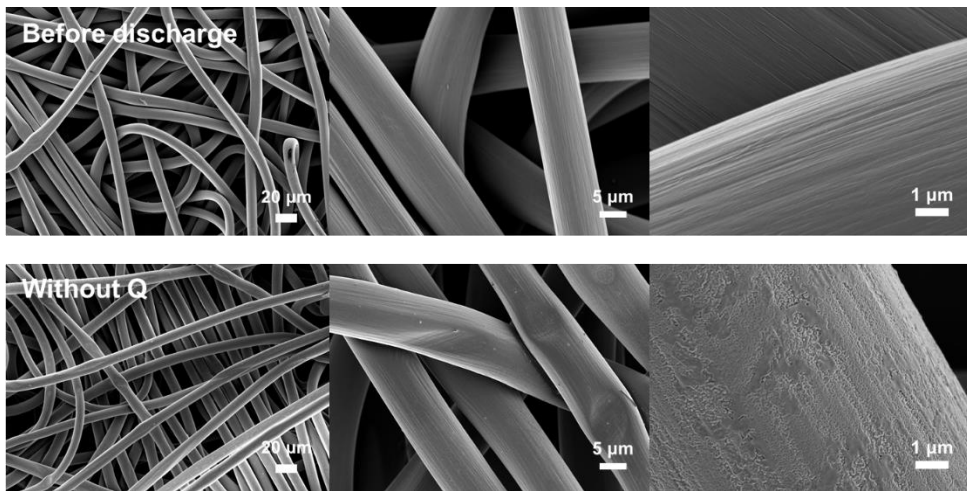


Figure 3.22. SEM images of the electrode before discharge and discharged without quinone. The surface of the electrode discharged without quinone is passivated by a film-like discharge product.

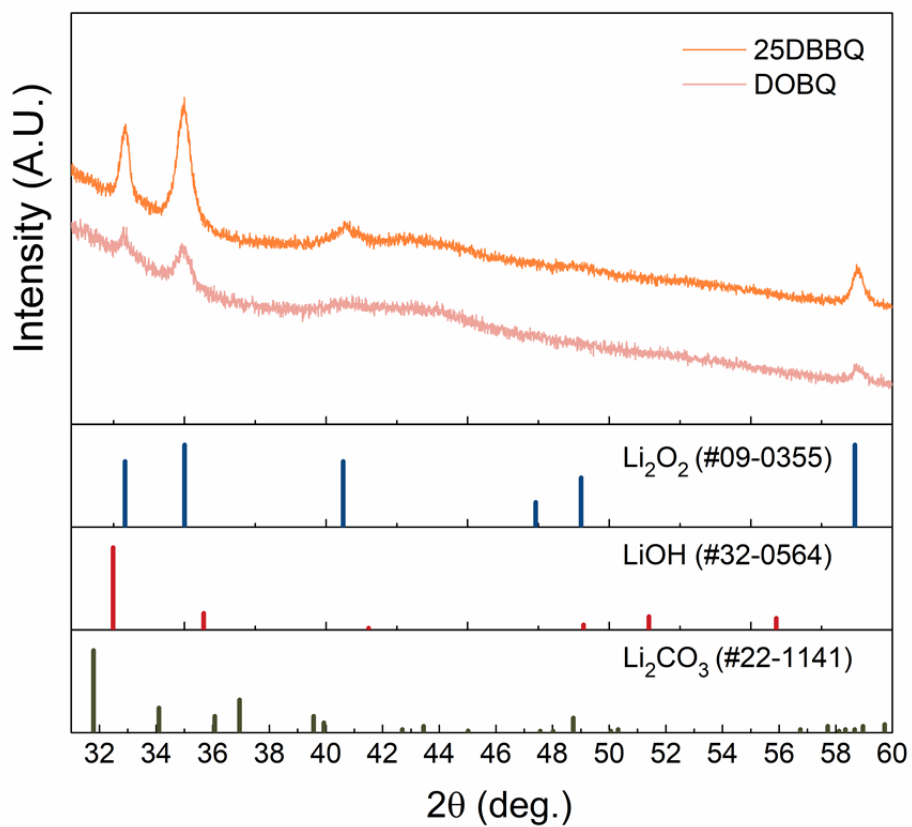


Figure 3.23. X-ray diffraction pattern of discharged electrode in quinone-containing cells confirmed that the toroidal discharge product is lithium peroxide.

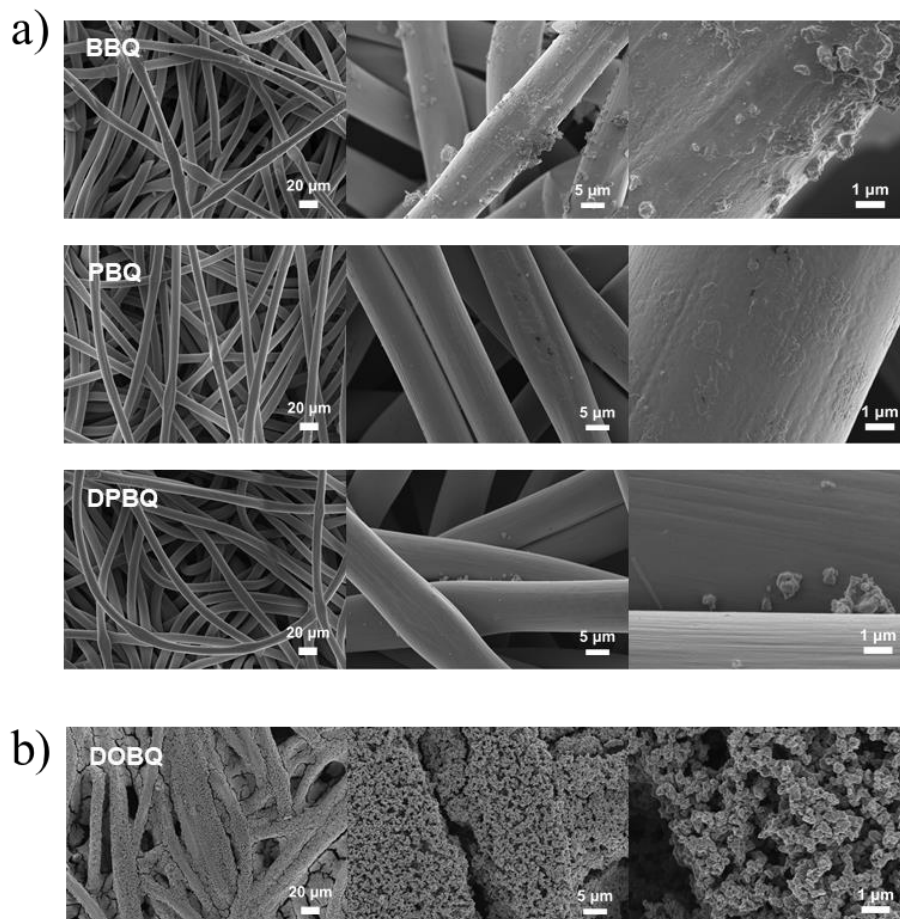


Figure 3.24. (a) SEM images of quinone included in group 1. In all three quinones, BBQ, PBQ, DPBQ, low magnification SEM images show not much difference from the quinone-free case. A higher magnification image shows that the formation of toroidal discharge products is limited so that electrode is passivated without achieving high discharge capacity. (b) SEM images of DOBQ (group 2). Low magnification SEM images show consistent result with 25DBBQ case, the formation of discharge product filling void space between fibers.

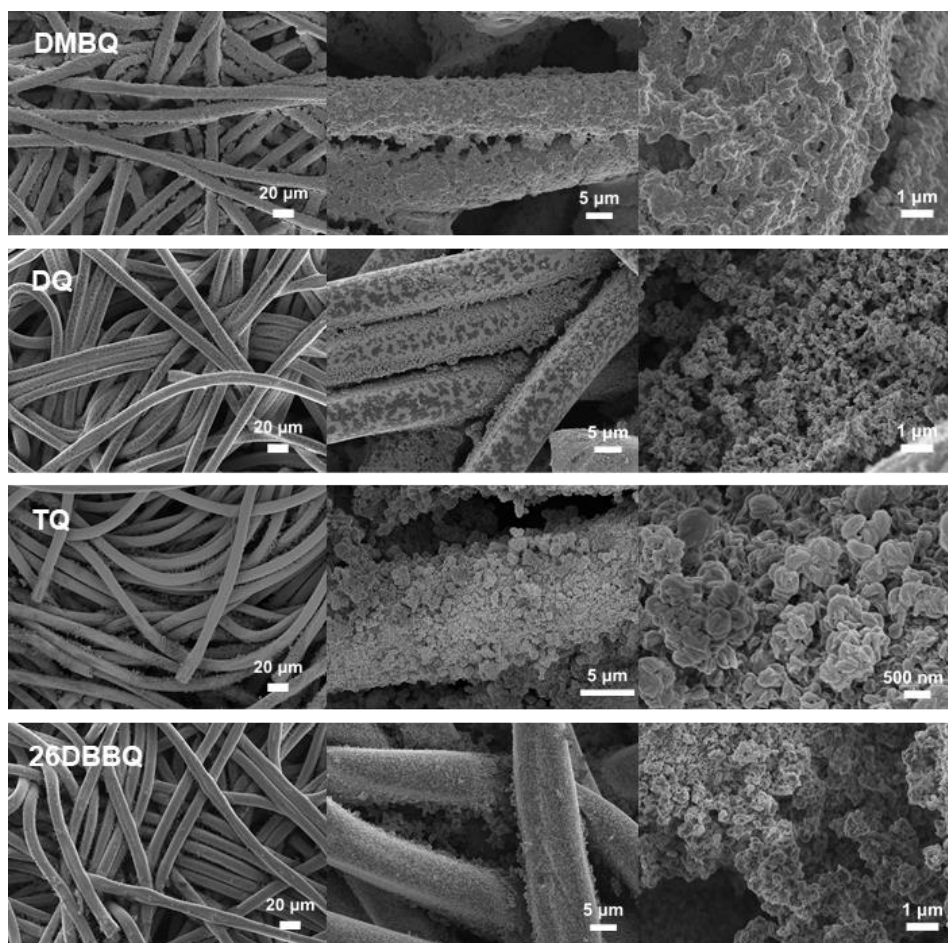


Figure 3.25. SEM images of quinone belonging to group 3. In all cases, the formation of the discharge product was observed. However, the discharge product covers the electrode surface, leading to the passivation and low discharge capacity.



Figure 3.26. Schematic illustration showing the influence of kinetics on the passivation behavior in three different cases, limited kinetics, moderate kinetics, and excessive kinetics.

3.1.4 Supplement note

Measurement of diffusivity and heterogeneous electron transfer rate constant using rotating disk electrode

Current from LSV experiment with RDE is expressed as follows according to Koutecky-Levich equation,

$$\frac{1}{i} = \frac{1}{i_k} + \frac{1}{i_L} \quad \text{Equation 1 (Koutecky-Levich equation)}$$

where i is total current, i_k is kinetic current, and i_L is limiting current. According to the equation, when overpotential is large enough to induce sufficiently high i_k to make $\frac{1}{i_k}$ term almost zero, i remains unchanged and equals to i_L . Therefore, we could obtain i_L from LSV profile at high overpotential region. Meanwhile, i_L is expressed by Levich equation as follows,

$$i_L = 0.62nFAD^{2/3}\omega^{1/2}\nu^{-1/6}C_0 \quad \text{Equation 2 (Levich equation)}$$

where n is the number of electron during redox reaction, F is Faraday constant, A is the area of electrode, D is diffusivity, ω is rotating speed, ν is kinematic viscosity, and C_0 is the concentration of redox active species. Here, the plot of $\omega^{1/2}$ vs. i_L with various rotating speeds shows linear relationship with the slope of $0.62nFAD^{2/3}\nu^{-1/6}C_0$ which enables diffusivity (D) calculation.

Combining equation 1 and 2 yield the equation 3 as follows,

$$\frac{1}{i} = \frac{1}{i_k} + \frac{1}{0.62nFAD^{2/3}\omega^{1/2}\nu^{-1/6}C_0} \quad \text{Equation 3}$$

According to the equation, the plot of $\frac{1}{i}$ vs. $\omega^{-1/2}$ follows linear relationship yielding fitting line with y-intercept of $\frac{1}{i_k}$. Once we calculate i_k at various overpotential, we could calculate i_0 , exchange current by drawing well-known Tafel plot. Finally, i_0 can be converted to heterogeneous electron transfer rate constant (k_0) by a simple equation as follows.

$$i_0 = nFAk_0C_0 \quad \text{Equation 4}$$

3.1.5 Concluding remarks

We suppose that fundamental understanding in this study will spur the development of high-performance RMs and finally, high energy and highly efficient lithium-oxygen batteries. For example, fine chemical tuning on steric hindrance of the RM molecule would enable the development of new RMs exhibiting better performance than the state-of-the-art RM. On the other hand, optimizing the cell system to fully exploit kinetics of RMs can be another approach. The RMs with fast kinetics (*i.e.* quinones in group 3) would display remarkable performance in redox flow lithium-oxygen batteries⁵⁸ where the place for electrochemical and chemical reaction is physically separated so that electrode passivation issue is addressed.

In conclusion, we have elucidated the nature of ET during the RM-mediated ORR in lithium-oxygen batteries, and how the intrinsic kinetics affects extrinsic catalytic performance in the cell environment. By comparatively analyzing the kinetic with various quinone species, we demonstrated that the kinetics can be entirely explained by Marcus theory coupled with steric effect. It leads us to the conclusion that the chemical ET step of RM-mediated ORR is inner-sphere ET and accompanies the formation of the intermediate state. Following consideration on reaction mechanism revealed that LiQO_2LiQ presents as an intermediate state. Moreover, the implication of understood intrinsic kinetics on catalytic performance was examined by conducting a galvanostatic discharge experiment. Volcano behavior in which not too slow or too fast, but intermediate kinetics results in the best catalytic performance was clearly observed. We suppose the current study on the fundamental on RM-

based ORR would promote the rational design and development of highly efficient RMs, which further accelerates the development of lithium-oxygen batteries with truly high energy density. In addition, it would also motivate researchers in the field of catalyst to design high-performance catalysts by concurrently considering the intrinsic property and its significance on the resulting performance.

3.1.6 References

1. Armand M, Tarascon J-M. Building better batteries. *Nature* 2008, **451**(7179): 652.
2. Kang K, Meng YS, Bréger J, Grey CP, Ceder G. Electrodes with High Power and High Capacity for Rechargeable Lithium Batteries. *Science* 2006, **311**(5763): 977-980.
3. Bruce PG, Freunberger SA, Hardwick LJ, Tarascon J-M. Li–O₂ and Li–S batteries with high energy storage. *Nat. Mater.* 2012, **11**(1): 19.
4. Christensen J, Albertus P, Sanchez-Carrera RS, Lohmann T, Kozinsky B, Liedtke R, *et al.* A critical review of Li/air batteries. *J. Electrochem. Soc.* 2011, **159**(2): R1.
5. Song K, Agyeman DA, Park M, Yang J, Kang YM. High-Energy-Density Metal–Oxygen Batteries: Lithium–Oxygen Batteries vs Sodium–Oxygen Batteries. *Adv. Mater.* 2017, **29**(48): 1606572.
6. Lim H-D, Lee B, Bae Y, Park H, Ko Y, Kim H, *et al.* Reaction chemistry in rechargeable Li–O₂ batteries. *Chem. Soc. Rev.* 2017, **46**(10): 2873-2888.
7. Jeong J, Shin H-C. In-Depth Analysis of Coulombic Efficiency of Zinc-Air Secondary Batteries. *J. Electrochem. Sci. Technol.* 2020, **11**(1): 26-32.
8. Kumar D, Rajouria SK, Kuhar SB, Kanchan D. Progress and prospects of sodium-sulfur batteries: a review. *Solid State Ionics* 2017, **312**: 8-16.
9. Fang R, Zhao S, Sun Z, Wang DW, Cheng HM, Li F. More reliable

- lithium-sulfur batteries: status, solutions and prospects. *Adv. Mater.* 2017, **29**(48): 1606823.
10. Jeon J, Jeong JW, Jung YS. Titanium (III) Sulfide Nanoparticles Coated with Multicomponent Oxide (Ti–S–O) as a Conductive Polysulfide Scavenger for Lithium–Sulfur Batteries. *Electron. Mater. Lett.* 2019, **15**(5): 613-622.
 11. Liang Y, Tao Z, Chen J. Organic electrode materials for rechargeable lithium batteries. *Adv. Energy Mater.* 2012, **2**(7): 742-769.
 12. Lee S, Kwon G, Ku K, Yoon K, Jung SK, Lim HD, *et al.* Recent progress in organic electrodes for Li and Na rechargeable batteries. *Adv. Mater.* 2018, **30**(42): 1704682.
 13. Girishkumar G, McCloskey B, Luntz AC, Swanson S, Wilcke W. Lithium– air battery: promise and challenges. *J. Phys. Chem. Lett.* 2010, **1**(14): 2193-2203.
 14. Kwak W-J, Rosy, Sharon D, Xia C, Kim H, Johnson LR, *et al.* Lithium–Oxygen Batteries and Related Systems: Potential, Status, and Future. *Chem. Rev.* 2020, **120**(14): 6626-6683.
 15. Johnson L, Li C, Liu Z, Chen Y, Freunberger SA, Ashok PC, *et al.* The role of LiO₂ solubility in O₂ reduction in aprotic solvents and its consequences for Li–O₂ batteries. *Nat. Chem.* 2014, **6**(12): 1091.
 16. Luntz AC, Viswanathan V, Voss J, Varley JB, Nørskov JK, Scheffler R, *et al.* Tunneling and Polaron Charge Transport through Li₂O₂ in Li–O₂

- Batteries. *J. Phys. Chem. Lett.* 2013, **4**(20): 3494-3499.
17. Bae Y, Park H, Ko Y, Kim H, Park SK, Kang K. Bifunctional Oxygen Electrocatalysts for Lithium–Oxygen Batteries. *Batteries & Supercaps* 2019, **2**(4): 311-325.
 18. Bae Y, Park H, Ko Y, Kim H, Park SK, Kang K. Bifunctional Oxygen Electrocatalysts for Lithium–Oxygen Batteries. *Batteries Supercaps* 2019, **2**(4): 311-325.
 19. Gao X, Chen Y, Johnson L, Bruce PG. Promoting solution phase discharge in Li–O₂ batteries containing weakly solvating electrolyte solutions. *Nat. Mater.* 2016, **15**(8): 882-888.
 20. Ko Y, Park H, Kim J, Lim HD, Lee B, Kwon G, *et al.* Biological redox mediation in electron transport chain of bacteria for oxygen reduction reaction catalysts in lithium–oxygen batteries. *Adv. Funct. Mater.* 2019, **29**(5): 1805623.
 21. Zhang Y, Wang L, Zhang X, Guo L, Wang Y, Peng Z. High-Capacity and High-Rate Discharging of a Coenzyme Q10-Catalyzed Li–O₂ Battery. *Adv. Mater.* 2018, **30**(5): 1705571.
 22. Matsuda S, Hashimoto K, Nakanishi S. Efficient Li₂O₂ formation via aprotic oxygen reduction reaction mediated by quinone derivatives. *J. Phys. Chem. C* 2014, **118**(32): 18397-18400.
 23. Liu T, Frith JT, Kim G, Kerber RN, Dubouis N, Shao Y, *et al.* The effect of water on quinone redox mediators in nonaqueous Li–O₂ batteries. *J. Am.*

- Chem. Soc.* 2018, **140**(4): 1428-1437.
24. Lacey MJ, Frith JT, Owen JR. A redox shuttle to facilitate oxygen reduction in the lithium air battery. *Electrochem. Commun.* 2013, **26**: 74-76.
 25. Yang L, Frith JT, Garcia-Araez N, Owen JR. A new method to prevent degradation of lithium–oxygen batteries: reduction of superoxide by viologen. *Chem. Commun.* 2015, **51**(9): 1705-1708.
 26. Grimaud A, Demortière A, Saubanère M, Dachraoui W, Duchamp M, Doublet M-L, *et al.* Activation of surface oxygen sites on an iridium-based model catalyst for the oxygen evolution reaction. *Nat. Energy* 2016, **2**(1): 16189.
 27. Grimaud A, Diaz-Morales O, Han B, Hong WT, Lee Y-L, Giordano L, *et al.* Activating lattice oxygen redox reactions in metal oxides to catalyse oxygen evolution. *Nat. Chem.* 2017, **9**(5): 457-465.
 28. Kim JS, Kim B, Kim H, Kang K. Recent Progress on Multimetal Oxide Catalysts for the Oxygen Evolution Reaction. *Adv. Energy Mater.* 2018, **8**(11): 1702774.
 29. Ko Y, Park H, Lee B, Bae Y, Park SK, Kang K. A comparative kinetic study of redox mediators for high-power lithium–oxygen batteries. *J. Mater. Chem. A* 2019, **7**(11): 6491-6498.
 30. Chen Y, Gao X, Johnson LR, Bruce PG. Kinetics of lithium peroxide oxidation by redox mediators and consequences for the lithium–oxygen

- cell. *Nat. Commun.* 2018, **9**(1): 1-6.
31. Zhang W, Shen Y, Sun D, Huang Z, Zhou J, Yan H, *et al.* Promoting Li₂O₂ oxidation via solvent-assisted redox shuttle process for low overpotential Li-O₂ battery. *Nano Energy* 2016, **30**: 43-51.
 32. Frisch M, Trucks G, Schlegel H, Scuseria G, Robb M, Cheeseman J, *et al.* Gaussian, Inc., Wallingford CT. *Gaussian 09* 2009.
 33. Lee C, Yang W, Parr RG. Development of the Colle-Salvetti correlation-energy formula into a functional of the electron density. *Phys. Rev. B* 1988, **37**(2): 785.
 34. Becke AD. Density-functional thermochemistry. I. The effect of the exchange-only gradient correction. *J. Chem. Phys.* 1992, **96**(3): 2155-2160.
 35. Stephens PJ, Devlin FJ, Chabalowski CF, Frisch MJ. Ab initio calculation of vibrational absorption and circular dichroism spectra using density functional force fields. *J. Phys. Chem.* 1994, **98**(45): 11623-11627.
 36. McLean A, Chandler G. Contracted Gaussian basis sets for molecular calculations. I. Second row atoms, Z= 11–18. *J. Chem. Phys.* 1980, **72**(10): 5639-5648.
 37. Krishnan R, Binkley JS, Seeger R, Pople JA. Self-consistent molecular orbital methods. XX. A basis set for correlated wave functions. *J. Chem. Phys.* 1980, **72**(1): 650-654.
 38. Miertuš S, Scrocco E, Tomasi J. Electrostatic interaction of a solute with a

- continuum. A direct utilization of AB initial molecular potentials for the prediction of solvent effects. *Chem. Phys.* 1981, **55**(1): 117-129.
39. Scalmani G, Frisch MJ. Continuous surface charge polarizable continuum models of solvation. I. General formalism. *J. Chem. Phys.* 2010, **132**(11): 114110.
40. Bard AJ, Faulkner LR. Fundamentals and applications. *Electrochem. Methods* 2001, **2**(482): 580-632.
41. Albery W, Bruckenstein S. Ring disc electrodes. Part 6.—Second-order reactions. *Trans. Faraday Soc.* 1966, **62**: 2584-2595.
42. Albery W. Ring-disc electrodes. Part 8.—Transient currents and first-order kinetics. *Trans. Faraday Soc.* 1967, **63**: 1771-1781.
43. Herranz J, Garsuch A, Gasteiger HA. Using rotating ring disc electrode voltammetry to quantify the superoxide radical stability of aprotic Li-air battery electrolytes. *J. Phys. Chem. C* 2012, **116**(36): 19084-19094.
44. Albery W, Hitchman M, Ulstrup J. Ring-disc electrodes. Part 10.—Application to second-order kinetics. *Trans. Faraday Soc.* 1969, **65**: 1101-1112.
45. Nakanishi A, Thomas ML, Kwon H-M, Kobayashi Y, Tatara R, Ueno K, *et al.* Electrolyte Composition in Li/O₂ Batteries with LiI Redox Mediators: Solvation Effects on Redox Potentials and Implications for Redox Shuttling. *J. Phys. Chem. C* 2018, **122**(3): 1522-1534.

46. Wang H, Sayed SY, Luber EJ, Olsen BC, Shirurkar SM, Venkatakrishnan S, *et al.* Redox Flow Batteries: How to Determine Electrochemical Kinetic Parameters. *ACS nano* 2020, **14**(3): 2575-2584.
47. Marcus RA. Electron transfer reactions in chemistry. Theory and experiment. *Rev. Mod. Phys.* 1993, **65**(3): 599.
48. Miller JR, Calcaterra L, Closs G. Intramolecular long-distance electron transfer in radical anions. The effects of free energy and solvent on the reaction rates. *J. Am. Chem. Soc.* 1984, **106**(10): 3047-3049.
49. Taube H, Myers H, Rich RL. OBSERVATIONS ON THE MECHANISM OF ELECTRON TRANSFER IN SOLUTION1. *J. Am. Chem. Soc.* 1953, **75**(16): 4118-4119.
50. Hush NS. Adiabatic theory of outer sphere electron-transfer reactions in solution. *Trans. Faraday Soc.* 1961, **57**(0): 557-580.
51. Wong C, Kochi J. Electron transfer with organometals. Steric effects as probes for outer-sphere and inner-sphere oxidations of homoleptic alkylmetals with iron (III) and iridate (IV) complexes. *J. Am. Chem. Soc.* 1979, **101**(19): 5593-5603.
52. Muller P. Glossary of terms used in physical organic chemistry (IUPAC Recommendations 1994). *Pure Appl. Chem.* 1994, **66**(5): 1077-1184.
53. Eliel EL, Wilen SH. *Stereochemistry of organic compounds*. John Wiley & Sons, 2008.
54. Rosokha SV, Kochi JK. Continuum of outer-and inner-sphere mechanisms

- for organic electron transfer. Steric modulation of the precursor complex in paramagnetic (ion-radical) self-exchanges. *J. Am. Chem. Soc.* 2007, **129**(12): 3683-3697.
55. Hubig SM, Rathore R, Kochi JK. Steric control of electron transfer. Changeover from outer-sphere to inner-sphere mechanisms in arene/quinone redox pairs. *J. Am. Chem. Soc.* 1999, **121**(4): 617-626.
56. Nørskov JK, Bligaard T, Hvolbæk B, Abild-Pedersen F, Chorkendorff I, Christensen CH. The nature of the active site in heterogeneous metal catalysis. *Chem. Soc. Rev.* 2008, **37**(10): 2163-2171.
57. Logadottir A, Rod TH, Nørskov JK, Hammer B, Dahl S, Jacobsen C. The Brønsted–Evans–Polanyi relation and the volcano plot for ammonia synthesis over transition metal catalysts. *J. Catal.* 2001, **197**(2): 229-231.
58. Zhu YG, Wang X, Jia C, Yang J, Wang Q. Redox-mediated ORR and OER reactions: redox flow lithium oxygen batteries enabled with a pair of soluble redox catalysts. *ACS Catal.* 2016, **6**(9): 6191-6197.

3.2 Kinetics of redox mediator for oxygen evolution reaction

(The essence of this chapter has been published in *Journal of Materials Chemistry A*. Reproduced with permission from [Ko, Y. *et al.*, *J. Mater. Chem. A*, **2019**, 7, 6491–6498] Copyright (2019) Royal Society of Chemistry)

3.2.1 Research Background

During the last decade, the development of lithium–oxygen batteries has been extensively sought after owing to the quest for the high-energy-density rechargeable batteries that can overcome the limitations of current lithium ion batteries.^{1–18} It is because lithium-oxygen batteries can potentially offer the highest energy density among reported battery chemistries. However, the realization of a practical lithium–oxygen battery has been retarded by limitations in achieving a reversible electrochemical reaction, exploring appropriate cell components that are stable during the electrochemical reaction, and overcoming high polarization/low energy efficiency.^{15, 19} A recent development of redox mediators (RMs), sometimes called soluble catalysts, have played a key role in addressing some of these issues by converting the electrochemical decomposition of lithium peroxide to a chemical pathway during charge.^{9, 15, 20–23} With the aid of the RM, the charging process becomes simply dependent on the intrinsic redox activity of the RM, thus the polarization can be significantly reduced despite the insulating nature of the discharge product, leading to the enhancement of the energy efficiency. For example, in the RM-assisted charging process, RMs are electrochemically oxidized first,

followed by a chemical reaction between the oxidized RMs and discharge product, which results in the oxidation of discharge product. In this series of reactions, the low electrical conductivity of the discharge product is no longer problematic because it is chemically decomposed by the freely mobile RMs. In a number of studies, the use of RMs has been demonstrated to effectively decrease charge polarization and therefore increase the round-trip efficiency.^{9, 20, 21, 23} Nevertheless, the intrinsic power capability of lithium-oxygen batteries adopting the RMs in the system still remains elusive. It is also uncertain how the activity of RMs would be altered at practically high current density. Considering the lithium-oxygen reaction is mediated by RMs, these aspects should be investigated with regards to the correlation between the intrinsic kinetics of RMs and the power capability of the system. However, to date, only a few studies have addressed the kinetic features of RM-assisted charge.^{24, 25} Moreover, the correlation among intrinsic charge transfer kinetics, the mobility of RM and the electrolyte species has not been comprehensively elucidated. Here, we conducted a comparative study to understand the kinetics of RM-assisted charge in lithium–oxygen batteries using several previously reported RMs: 2,2,6,6-tetramethyl-1-piperidinyloxy (TEMPO),²¹ methyl-phenothiazine (MPT),²² tetrathiafulvalene (TTF),^{20, 26} and 5,10-dihydro-5,10-dimethylphenazine (DMPZ).²³ Two critical kinetic parameters of RMs were comparatively measured; the reaction rate of lithium peroxide oxidation by RM^+ and the diffusivity of the RM. By measuring the reaction rate, we were able to find a ‘trade-off’ between the theoretical potential of the redox couple and the reaction rate. This trade-off suggested that not

only thermodynamic aspects (*i.e.*, the theoretical voltage) but also kinetic aspects (*i.e.*, the reaction rate of the chemical oxidation of lithium peroxide) must be considered when designing high-performance RMs. Considering both the reaction rate and diffusivity, it is revealed that TEMPO, which has fast kinetics in terms of both kinetic parameters, would exhibit the best rate performance among the investigated RMs. The better performance than others was confirmed by galvanostatic cycling tests, where TEMPO-assisted charge showed a stable voltage plateau of ~ 3.65 V (vs. Li/Li⁺) extended to a state of charge (SoC) of 80% at a high current density of 5.0 mA cm⁻². This finding implies that the kinetic aspects of RMs should be carefully considered in the selection of RMs for the realization of high-power lithium–oxygen batteries.

3.2.2 Experimental Method

3.2.2.1 Preparation of lithium–oxygen cells

For the preparation of the electrolytes, LiTFSI (99.95% trace metals basis, Sigma–Aldrich) was dried at 180 °C under vacuum for at least 1 week before use. The organic solvents DME (anhydrous, 99.5%, Sigma-Aldrich), DEGDME (anhydrous, 99.5%, Sigma-Aldrich), and TEGDME ($\geq 99\%$, Sigma-Aldrich) were dried for more than 3 days using a molecular sieve (type 3Å, Sigma-Aldrich), which was freshly washed and dried at 180 °C under vacuum for at least 1 week. TEMPO, MPT and TTF were purchased from Sigma-Aldrich and used as received. DMPZ was purchased from Tokyo Chemical Industry and used as received as well. Each of the electrolytes was prepared by adding 1 M LiTFSI and 50 mM of the RM in an organic solvent. The final water contents of all the electrolytes were under 50 ppm, as determined by Karl Fischer titration. An air electrode was prepared by casting Ketjen black on carbon paper (TGPH030, Toray). Ketjen black and polytetrafluoroethylene binder with a weight ratio of 8:2 were mixed with 1-methyl-2-pyrrolidinone and isopropanol to make an electrode slurry. The slurry was cast on carbon paper with a thickness of 150 μm and dried at 70 °C under vacuum for more than 3 h. The average loading amount of carbon was $\sim 0.4 \text{ mg cm}^{-2}$. The lithium–oxygen cells were assembled using the carbon electrode as the air electrode, two sheets of glass fiber (GF/F, Whatman) as a separator, and lithium metal as an anode with 200 μl of the electrolyte. Assembly of the cells was performed in an Ar-filled glove box (H_2O level $< 0.5 \text{ ppm}$ and O_2 level $< 0.5 \text{ ppm}$). After cell assembly, the air chamber of the

assembled cell was changed from Ar to O₂ (> 99.999%) and operated as closed.

3.2.2.2 Conditions for electrochemical tests

To construct lithium-oxygen cell, swagelok-type cell was used. A sheet of gas diffusion layer was used as air electrode. A sheet of glass fiber and LFP electrode was used as separator and counter electrode, respectively. Air electrode, separator, and counter electrode was prepared to have a diameter of 1/2 inch. The amount of electrolyte used in assembling the cells was 200 μ l. After cell assembly in Ar-filled glove box (O₂ level < 0.1 ppm and H₂O level < 0.1 ppm), the atmosphere of empty space above air electrode was changed to O₂ (> 99.999%) and the cells were operated as closed.

3.2.3 Results and Discussions

The charging voltage of lithium-oxygen cell with the active RM is determined by the electrochemical oxidation potential of the RM. The oxidation of the RM occurs at the equilibrium potential governed by the Nernst equation (equation 1), where the RM and RM^+ concentrations are variables. Accordingly, the concentration ratio of RM^+ to RM at the electrode surface can affect the charge voltage of the cells.

$$E_{eq} = E^{o'} + \frac{RT}{F} \ln \frac{C_{RM^+}}{C_{RM}} \quad \text{Equation 1}$$

where E_{eq} and $E^{o'}$ are the equilibrium potential and formal potential of the half-cell, respectively; R is the universal gas constant; T is the temperature, F is the Faraday constant; and C_{RM^+} and C_{RM} are the concentrations of the oxidized RM and neutral RM, respectively.²⁷ Figure 3.27 presents a schematic illustration of the reaction mechanism of the RM-assisted charge, which consists of 1) electrochemical oxidation of the RM, 2) diffusion, and 3) chemical decomposition of lithium peroxide by RM^+ . In the process, the RM is electrochemically oxidized to RM^+ at the electrode surface, whose potential reflects the output charge voltage. The oxidized RM^+ diffuses to the vicinity of lithium peroxide followed by a chemical reaction for decomposition into a lithium ion and oxygen gas while RM^+ returning into a neutral RM. The RM is oxidized again at the electrode surface and the charge process continues. All three steps are believed to critically govern the value of $\frac{C_{RM^+}}{C_{RM}}$ at the electrode surface. Electrochemical oxidation causes a decrease in the RM concentration and an increase in the RM^+ concentration at the electrode surface, thus

effectively increasing the local value of $\frac{C_{RM^+}}{C_{RM}}$. In contrast, the conversion of RM^+ into RM with the chemical decomposition of lithium peroxide leads to a decrease of $\frac{C_{RM^+}}{C_{RM}}$ at the electrode surface. Spontaneous diffusion of RM^+ away from the electrode surface and diffusion back of RM toward the electrode surface result in a decrease of $\frac{C_{RM^+}}{C_{RM}}$ at the electrode surface. The combination of these would regulate the overall change in $\frac{C_{RM^+}}{C_{RM}}$ and thus the practical charging voltage of the cell.

A noticeable feature of the change in $\frac{C_{RM^+}}{C_{RM}}$ is that the increasing rate of $\frac{C_{RM^+}}{C_{RM}}$ by electrochemical oxidation relies on the applied current density (*i.e.*, the rate of RM oxidation); however, the decreasing rate of $\frac{C_{RM^+}}{C_{RM}}$ by diffusion and chemical decomposition is roughly independent of the current. Accordingly, under galvanostatic charge, where the RM is oxidized at a constant rate, a higher current induces a relatively faster increase of $\frac{C_{RM^+}}{C_{RM}}$ locally at the electrode surface, thus increasing the charge voltage. Figure 3.28 schematically illustrates the charge voltage during galvanostatic charge. In the ideal case, where the diffusion and chemical reaction are sufficiently fast, an increase in $\frac{C_{RM^+}}{C_{RM}}$ would be immediately compensated regardless of the current density by a fast decrease in $\frac{C_{RM^+}}{C_{RM}}$, resulting in a constant voltage during the overall charge (figure 3.28.a). However, in the practical cell environment, the finite rates of diffusion and chemical reaction will cause the increase in the relative concentration of C_{RM^+} , and thus the charge voltage

will continuously increase. It would be more dramatic at the latter part of the charge process when the decomposition rate gets affected by less amount of discharge product left (figure 3.28.b). Moreover, a higher current would induce a faster increase in $\frac{C_{RM^+}}{C_{RM}}$ at the electrode surface, which would result in an accelerated increase of the charge voltage. Consequently, the length of the stable voltage plateau from RM/RM⁺ would appear to be shortened with increasing current, as indicated with the arrow in figure 3.28.b. It is noteworthy that the diffusivity and the rate of chemical lithium peroxide oxidation would not be identical for every type of redox couple. A redox couple with high diffusivity and a high rate of chemical reaction would maintain a low increasing rate of $\frac{C_{RM^+}}{C_{RM}}$ even at relatively high current, leading to a slow increase of the charge voltage with higher currents. Thus, it is indispensable to elucidate the intrinsic kinetic nature of RMs with respect to the diffusivity in the working electrolyte and their reactivity with lithium peroxide to understand the power capability of RM-mediated lithium-oxygen cells.

We selected several previously reported organic RMs, *e.g.* TEMPO, MPT, TTF, and DMPZ, in studying the kinetics of RM-assisted charge process, focusing on the two intrinsic kinetic parameters; the diffusivity and the reaction rate of chemical decomposition. The reaction rate of RM in the chemical decomposition of lithium peroxide was approximated by probing linear sweep voltammetry (LSV) using a rotating disk electrode (RDE), where the limiting anodic current ($i_{l,a}$) is given for a specific RM. It was assumed that $i_{l,a}$ would be dependent on the effective concentration of RM and the reaction kinetics of RM⁺ with lithium peroxide. For

example, when an excess amount of lithium peroxide powder is dispersed in solution with the RM, the amount of oxidizable RM increases because of the regeneration of the RM, as depicted in figure 3.29. The successive reaction between RM^+ and lithium peroxide following the oxidation of RM is referred to as the EC (electrochemical-chemical) mechanism in which a product of electrochemical reaction successively participates in the following chemical reaction as a reactant.²⁷ In this case, the regeneration of the RM in the vicinity of electrode surface results in an increase of $i_{l,a}$ in the LSV profile. The higher increase of limiting current represents a faster reaction rate between RM^+ and lithium peroxide. Even though an increase of $i_{l,a}$ does not provide a precise value of the reaction rate constant k of chemical lithium peroxide oxidation, it is a meaningful value when comparing a relative difference. The resulting LSV profiles of selected RMs with the RDE are presented in figure 3.30. Note that a general decrease in $i_{l,a}$ was expected because of the increase in the viscosity in the lithium peroxide powder-dispersed solution, and thus it was corrected for the compensation. (See figure 3.31 for detail) Figure 3.32.a presents a bar graph with the corrected increase in $i_{l,a}$ for all the redox couples. The results for the multi redox capable RMs (DMPZ and TTF) are presented separately for each oxidation states. Figure 3.32.b shows the relationship between the increase in $i_{l,a}$ and the theoretical redox potential for each redox couple, which was calculated using cyclic voltammetry (CV) in figure 3.33. The redox potential and the increase in $i_{l,a}$ exhibited a roughly linear relationship as indicated with blue colored area. The linear relationship can be explained by classical electron transfer theory relating

thermodynamics (*i.e.*, driving force) to kinetics (*i.e.*, reaction rate) in that an increased driving force induces a lower activation energy, thereby leading to an enhanced reaction rate.²⁸ As the redox potentials of the RMs are located further from the equilibrium potential of lithium peroxide (~ 2.96 V vs. Li/Li⁺), the driving force for the charge transfer gets greater. This result suggests that the conventional design strategy for RMs, which has been focused on achieving a high round-trip efficiency by adjusting RM's redox potential close to ~ 2.96 V (*i.e.*, equilibrium potential of lithium peroxide formation), should be revised to also consider the kinetics of the chemical decomposition. The RM with a low redox potential close to ~ 2.96 V (vs. Li/Li⁺) is likely to exhibit slow kinetics toward the oxidation of lithium peroxide because of the trade-off between these two factors.

The diffusivity of each RM was also comparatively examined through CV experiments at various conditions. Figure 3.34 present CV profiles of TEMPO, MPT, DMPZ, and TTF in 1 M LiTFSI in DME at scan rates ranging from 100 to 500 mV s⁻¹. Reversible redox reaction of the RM was observed for all the cases. The diffusivity of each RM was determined from each CV profiles using the Randles–Sevcik equation (equation 2) from the relation between the scan rate and peak current defined by

$$i_p = 0.4463nFAC\left(\frac{nFvD}{RT}\right)^{\frac{1}{2}} \quad \text{Equation 2}$$

where i_p is the peak current, n is the number of electrons, F is the Faraday constant, A is the area of the electrode, C is the concentration of reduced/oxidized species, v is the scan rate, D is the diffusion coefficient of reduced/oxidized

species, R is the universal gas constant, and T is the temperature. In figure 3.35, the linear relationship was confirmed in the plot of $v^{\frac{1}{2}}$ vs. i_p . From the linear correlations, the diffusivities were calculated for TEMPO, MPT, DMPZ and TTF, which are 3.32, 2.60, 2.16, and $2.21 \times 10^{-6} \text{ m}^2 \text{ s}^{-1}$, respectively, as shown in figure 3.36.a. The RMs show similar orders of magnitudes of diffusivity, while smaller molecules present slightly higher diffusivities in general. The two independent kinetic parameters, the increase in $i_{l,a}$ in figure 3.32.a and the diffusivity in figure 3.36.a, are displayed together in figure 3.36.b to graphically represent the overall kinetic performances of the RMs. Considering both the reaction rates and the diffusivity, TEMPO-assisted charge was expected to result in better rate capability than the charge process assisted by the other RMs. In contrast, TTF-assisted charge was predicted to result in comparatively low rate capability because of the low diffusivity and the small increase of $i_{l,a}$. For DMPZ, which undergoes two redox reactions, the second redox reaction was expected to present the fastest kinetics among RMs, so that it may aid in achieving a high power capability despite the relatively slow kinetics of the first redox.

To investigate how these kinetic parameters practically affect the rate capability of RM-assisted charge in a lithium–oxygen cell environment, we carried out galvanostatic cycling tests under various charge current densities. Figure 3.37 presents the galvanostatic cycling profiles (figure 3.37.a, b, c, and d) and the corresponding dQ/dV profiles (figure 3.37.e, f, g, and h) using cells containing 50 mM of the respective RM dissolved in 1 M LiTFSI in DME. All the cells were

discharged with an identical current density of 0.2 mA cm^{-2} before charging to exclude the factor of morphological change of the discharge product, which is affected by the current density,²⁹ and charged with varying current densities ranging from 0.2 to 5.0 mA cm^{-2} . Figures show that all the RMs efficiently reduce the charge polarization compared with the cells without any RM (light-grey dotted line for 0.2 mA cm^{-2} and dark-grey dotted line for 1.0 mA cm^{-2}). However, the responses of each RM for the higher current rates were markedly dissimilar, which is attributable to the different kinetic properties of RMs as presented above. The voltage increase owing to the insufficient kinetics of RMs can be seen in the dQ/dV profile, along with the broader nature of the peak shape at higher current density. In the comparison between TEMPO and MPT, which undergo a single redox reaction, it was observed that TEMPO exhibited better rate capability than MPT. For TEMPO-assisted charge, a stable voltage plateau from TEMPO/TEMPO⁺ redox was observed during the entire range of charge up to a current density of 1.0 mA cm^{-2} and a voltage plateau was maintained until a SoC of 80% at a high current density of 5.0 mA cm^{-2} (figure 3.37.a and e). In contrast, MPT-assisted charge showed a stable voltage plateau until the end of charge only at a low current density of 0.2 mA cm^{-2} . At a current density of 5.0 mA cm^{-2} , the charge voltage started to sharply increase even at a SoC of 60% (figure 3.37.b and f). Note that the additional voltage plateau of MPT of approximately 4.3 V is from MPT⁺/MPT²⁺. For DMPZ and TTF, both of which undergo two-step redox reactions, the rate capability from the first/second redox was examined separately, as indicated by small arrows in the dQ/dV profile. For the first

redox, both DMPZ and TTF exhibited relatively poor rate capability, as observed in the galvanostatic profiles (figure 3.37.c and d) and dQ/dV profiles (figure 3.37.g and h), which can be explained by the low values of the kinetic parameters in figure 3.36.b. However, DMPZ and TTF exhibited different behaviors in the second redox reactions. The second redox peak of DMPZ in the dQ/dV profile remains sharp up to a current density of 5.0 mA cm^{-2} , while that of TTF significantly broadens even at a low current density of 0.2 mA cm^{-2} . Note that the additional dQ/dV peak of TTF at approximately 4.5 V originates from the electrolyte decomposition. This noticeable difference in the rate capability of the second redox is attributed to the distinct kinetic parameters, particularly the reactivity with lithium peroxide, as displayed in figure 3.36.b. The comparison between DMPZ and TTF also suggests that even though the first redox of the RM is relatively sluggish in kinetics, an overall high rate capability can be achieved if the kinetics of the second redox is remarkably fast. The rate capability observed in the galvanostatic charge experiment is well explicated by the two measured kinetic parameters, which implies the validity of estimating the kinetics of RM-assisted charge by simple analysis of individual parameters.

The resulting increased cell voltage at high current density due to the slow kinetics of RM-assisted charge is predicted to cause side reactions, since the high charge voltage is closely related to side reactions such as carbon degradation³⁰ and singlet oxygen generation^{31, 32}, both of which cause evolution of CO_2 via degradation of carbon and the electrolyte. To verify the extent of the side reactions, the gas evolution

during RM-assisted charge at 1.0 mA cm^{-2} was monitored using differential electrochemical mass spectroscopy (DEMS), and the results are presented in figure 3.38. No evolution of CO_2 was observed for the TEMPO-assisted charge because the cell voltage remained stable owing to the fast kinetics of TEMPO. However, the RM-assisted charge using the other RMs (MPT, DMPZ, TTF) resulted in the emission of CO_2 because of the increased cell voltage at the end of charge.³⁰⁻³² Specifically, TTF-assisted charge, which has the lowest rate capability, showed the highest amount of CO_2 evolution. The gas analysis results indicate that the use of RMs is beneficial not only for enhancing the round-trip efficiency and rate capability but also for improving the stability/reversibility of the system by avoiding possible side reactions caused by the high-voltage charge.

Another variable that should be considered for RM-assisted charge is the selection of the electrolyte, as it can potentially affect the diffusivity of the dissolved RM. To investigate the effect of the electrolyte in RM-assisted charge, the same set of experiments were performed using various ether-based electrolytes as a model system (*e.g.*, 1 M LiTFSI in DME, diethylene glycol dimethyl ether (DEGDME), and tetraethylene glycol dimethyl ether (TEGDME)) while fixing the RM as TEMPO. From CV experiments in figure 3.39, the diffusivities of TEMPO in the three electrolytes could be obtained, as presented in figure 3.40. It reveals that the diffusivity of TEMPO was largely governed by the viscosity of the organic solvent³³,³⁴ and decreased in the order of DME, DEGDME, and TEGDME. Note that the ionic conductivity was also measured to be related with the viscosity of electrolytes.

(figure 3.41) figure 3.42 illustrates the results of galvanostatic cycling and dQ/dV profiles comparatively obtained in the DEGDME- and TEGDME-based electrolytes. The light-grey dotted lines are the charge profiles in the absence of the RM at 0.2 mA cm^{-2} . It is evident that the variation in diffusivity due to the selection of the electrolyte noticeably affects the rate capability of TEMPO-assisted charge. Whereas a stable voltage plateau from TEMPO/TEMPO⁺ was maintained until a SoC of 80% at 5.0 mA cm^{-2} with the DME-based electrolyte as presented in figure 3.37.a, the voltage plateau was only observed until a SoC of 70% and 40% for the DEGDME- and TEGDME-based electrolytes, respectively, at the same current density in figure 3.42.a and c. Moreover, it was observed that, when higher current rates are applied to the cells, the broadenings of the redox peak in dQ/dV curves are notably faster in DEGDME- and TEGDME-based electrolytes (figure 3.42.b and d), indicating the sluggish kinetics of RM-assisted charging process. This finding suggests that not only the type of RM but also the choice of electrolyte should be considered to achieve the RM-assisted charge with high rate capability.

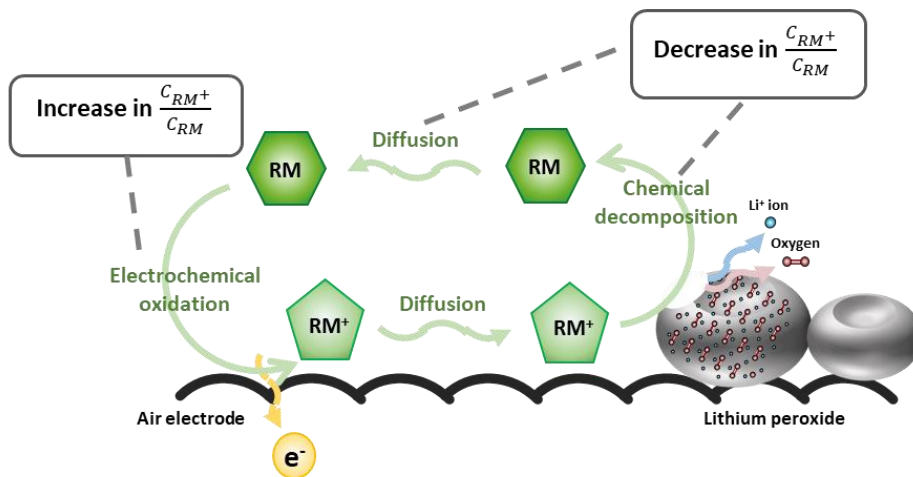


Figure 3.27. Schematic illustrations showing detailed mechanism of RM-assisted charge with the effect of each step on the RM concentration at the electrode surface and galvanostatic charge profiles under various kinetic conditions. Detailed mechanism of RM-assisted charge consisting of 1) electrochemical oxidation of the RM, 2) diffusion of RM^+ and RM, and 3) chemical decomposition of lithium peroxide by RM^+ . Step 1 causes an increase of $\frac{C_{RM^+}}{C_{RM}}$ at the electrode surface and step 2 and step 3 result in a decrease of $\frac{C_{RM^+}}{C_{RM}}$.

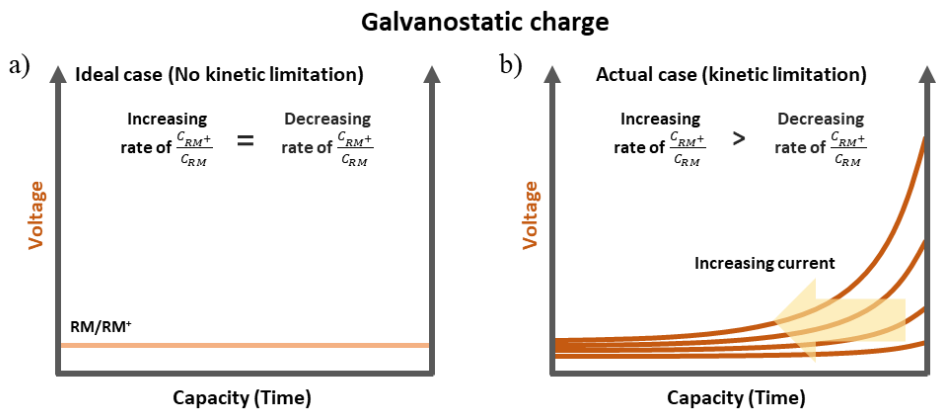


Figure 3.28. Schematic illustrations of galvanostatic charge profile in (a) ideal case and (b) actual case. With an infinite rate of diffusion and decomposition of lithium peroxide (ideal case), the RM concentration remains constant, and therefore, the voltage also remains constant. In the real case, however, because the rates of diffusion and lithium peroxide decomposition are finite, and the RM concentration decreases and the charge voltage increases as charge proceeds. The increase in charge voltage is accelerated by increasing current, thereby shortening the stable voltage plateau.

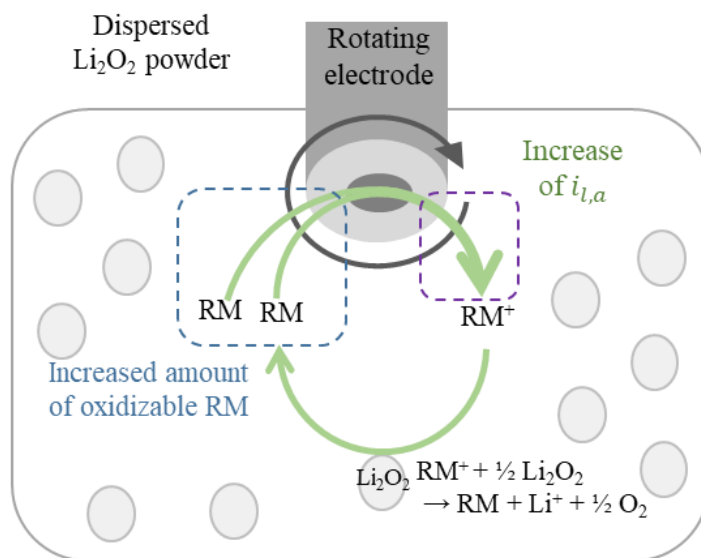


Figure 3.29. RDE experiment to analyze the rate of lithium peroxide decomposition by RM^+ . Schematic illustrations displaying the oxidative current increase by the EC mechanism.

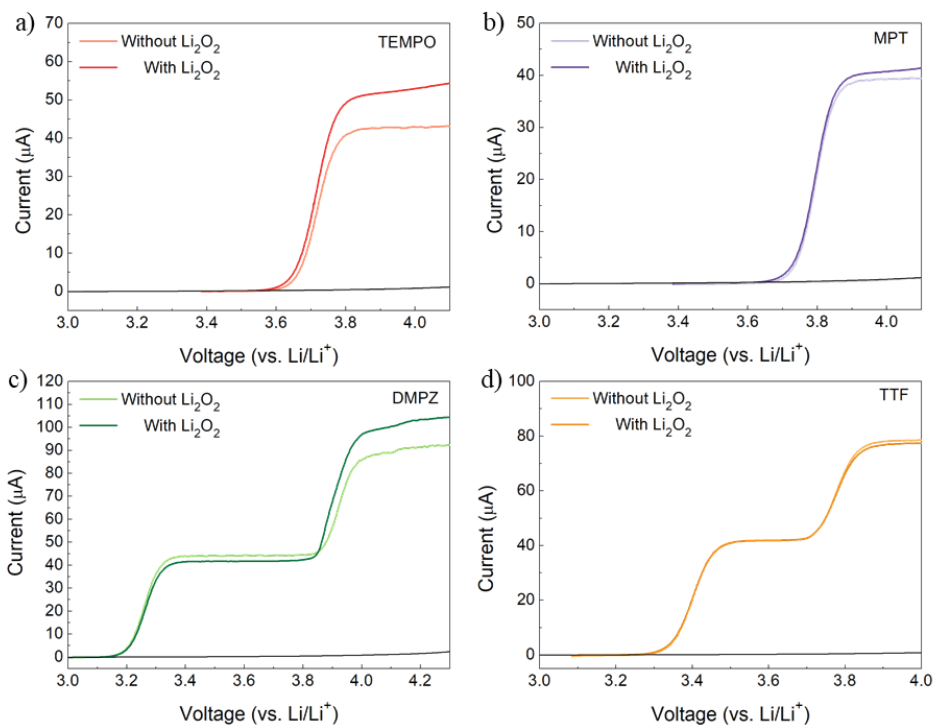


Figure 3.30. LSV profiles with RDE of (a) TEMPO, (b) MPT , (c) DMPZ, and (d) TTF. All the voltage scans were conducted at a scan rate of 1 mV s^{-1} using 1 M LiTFSI in DME containing 1 mM of the RM and 30 mM of dispersed Li_2O_2 powder.

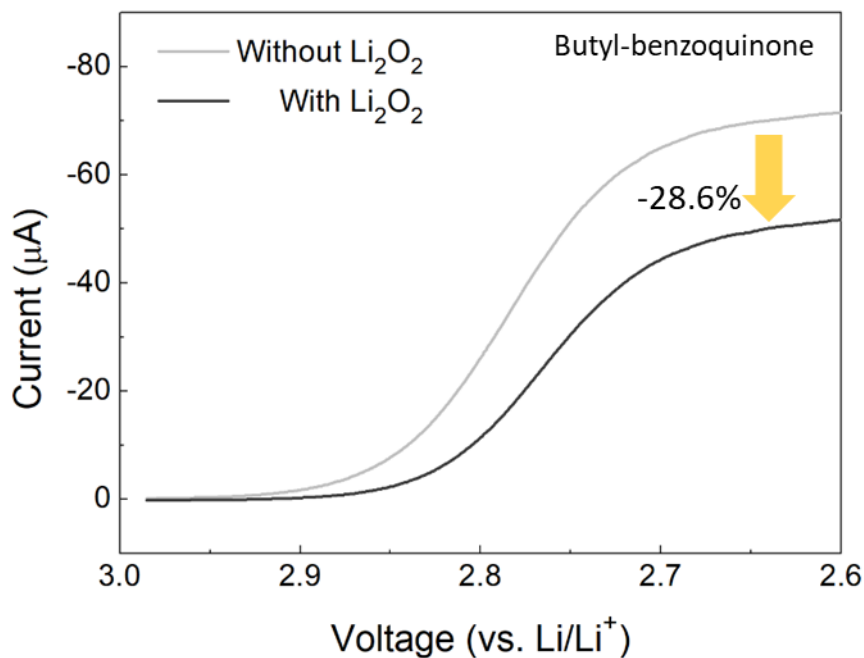


Figure 3.31. LSV profile with RDE using redox reaction that is unreactive toward Li₂O₂ powder. The reduction of butyl-benzoquinone, where the reduced species is inert to Li₂O₂ powder, was utilized to investigate the limiting current decrease from the decreased diffusivity with dispersed Li₂O₂ powder. The reduction in $i_{l,a}$ was observed to be reduced by approximately 28.6% because of the decreased diffusivity in the Li₂O₂-dispersed solution. This result implies that a decrease of $i_{l,a}$ of less than 28.6% indicates the regeneration of RM because of reaction with lithium peroxide.

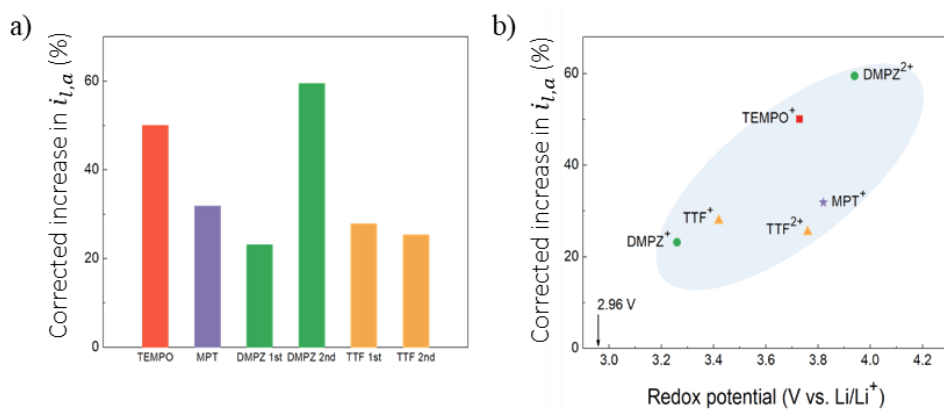


Figure 3.32. (a) Corrected increase in $i_{l,a}$ of selected redox couple; the corrected current increases from each redox couple are as follows: TEMPO/TEMPO⁺, 50.05%; MPT/MPT⁺, 31.91%; DMPZ/DMPZ⁺, 23.14%; DMPZ⁺/DMPZ²⁺, 59.51%; TTF/TTF⁺, 27.92%; and TTF⁺/TTF²⁺, 25.43%. (b) Plot of increase in $i_{l,a}$ vs. redox potential.

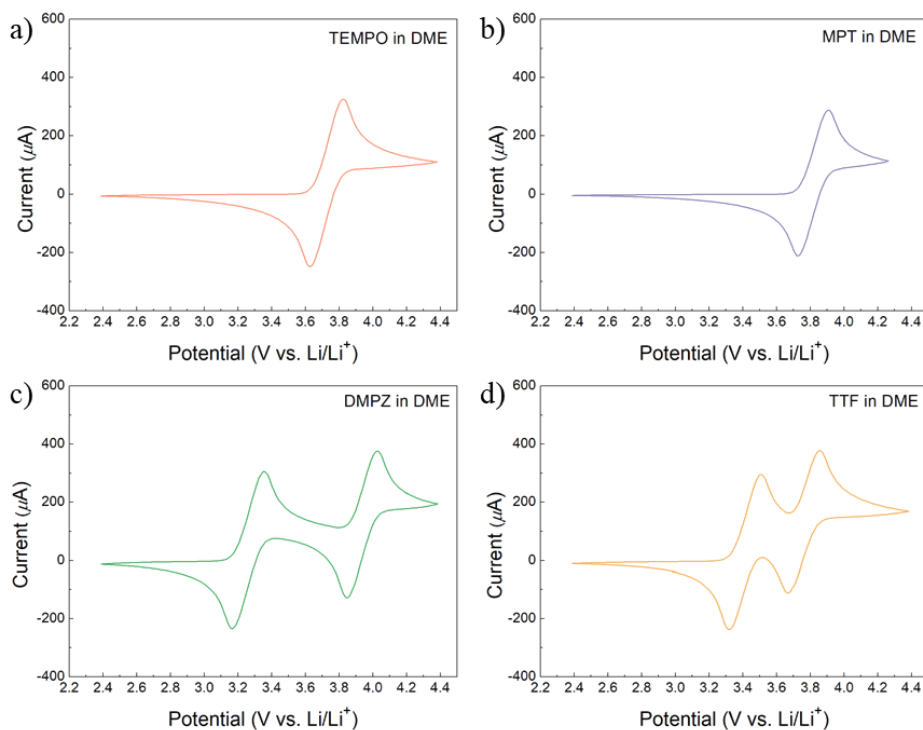


Figure 3.33. Cyclic voltammogram using 1 M LiTFSI in DME containing 50 mM of (a) TEMPO, (b) MPT, (c) DMPZ, and (d) TTF. The scan rate was 100 mV s^{-1} . All the redox reactions were measured to be reversible with the following calculated equilibrium redox potentials: TEMPO/TEMPO⁺, 3.73 V; MPT/MPT⁺, 3.82 V; DMPZ/DMPZ⁺, 3.26 V; DMPZ⁺/DMPZ²⁺, 3.94 V; TTF/TTF⁺, 3.42 V; and TTF⁺/TTF²⁺, 3.76 V (all the values are expressed vs. Li/Li⁺ potential).

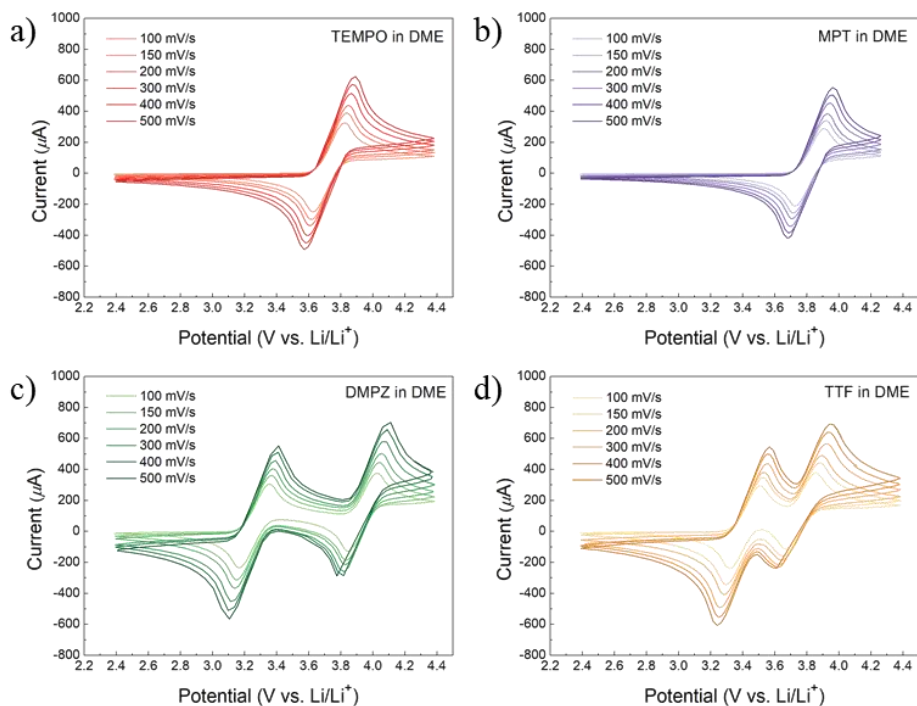


Figure 3.34. Cyclic voltammograms of (a) TEMPO, (b) MPT, (c) DMPZ, and (d) TTF for scan rates ranging from 100 to 500 mV s^{-1} . The experiment was conducted using 1 M LiTFSI in DME containing 50 mM of the RM.

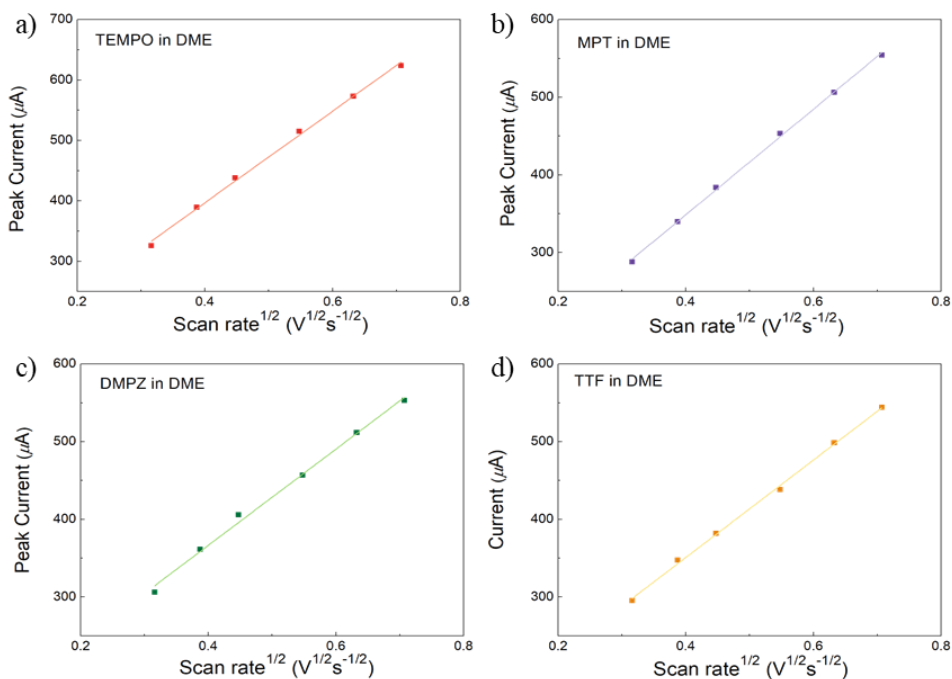


Figure 3.35. The plot of $(\text{scan rate})^{1/2}$ vs. peak current of cyclic voltammogram using 1 M LiTFSI in DME containing 50 mM of (a) TEMPO, (b) MPT, (c) DMPZ, and (d) TTF for various scan rates ranging from 100 to 500 mV^{-1} . The diffusivity of each RM was calculated from the linear relationship between $(\text{scan rate})^{1/2}$ and the peak current using the Randles–Sevcik equation.

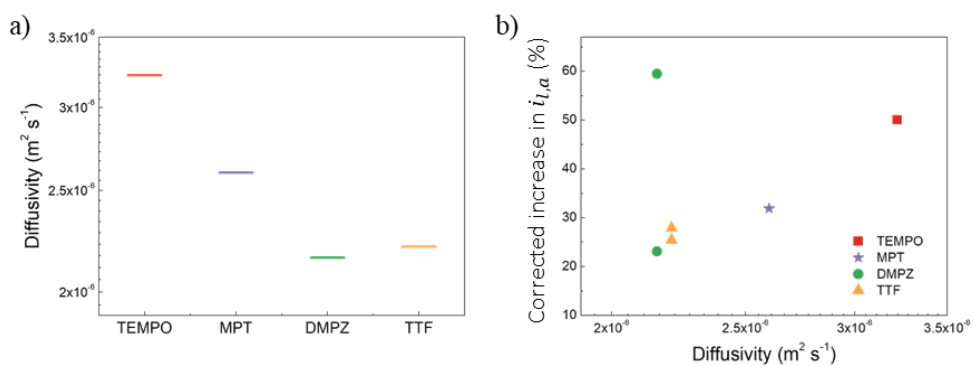


Figure 3.36. (a) Calculated diffusivities of RMs determined using Randles–Sevcik equation. (b) Plot of diffusivity vs. increase in $i_{l,a}$ showing overall kinetic properties.

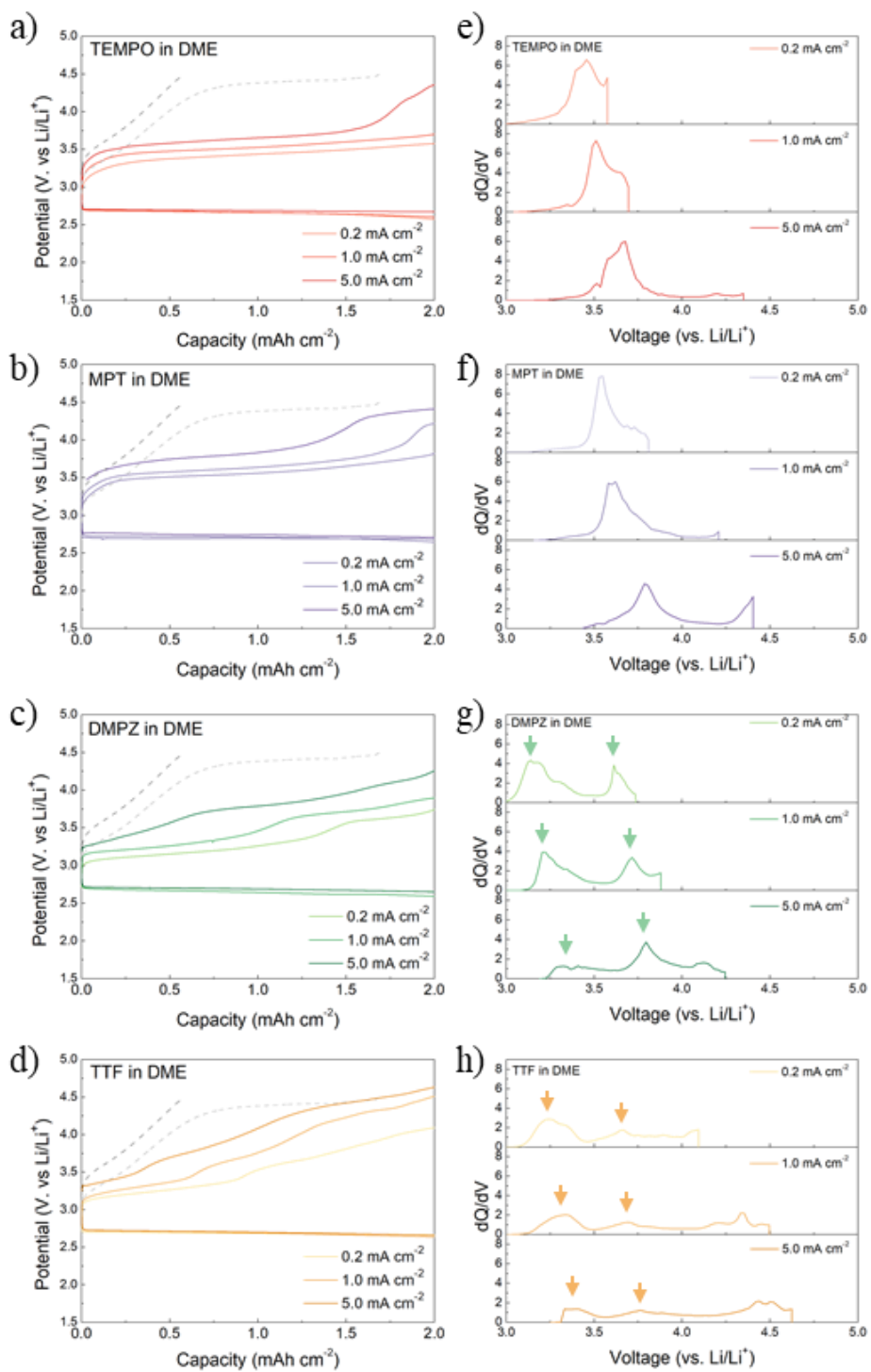


Figure 3.37. Galvanostatic cycling and corresponding dQ/dV profiles of lithium–oxygen cells containing RMs. Galvanostatic cycling profiles under various current rate from 0.2 to 5.0 mA cm⁻² of the cell containing (a) TEMPO, (b) MPT, (c) DMPZ, and (d) TTF. Corresponding dQ/dV profiles for the cell containing (e) TEMPO, (f) MPT, g) DMPZ, and h) TTF.

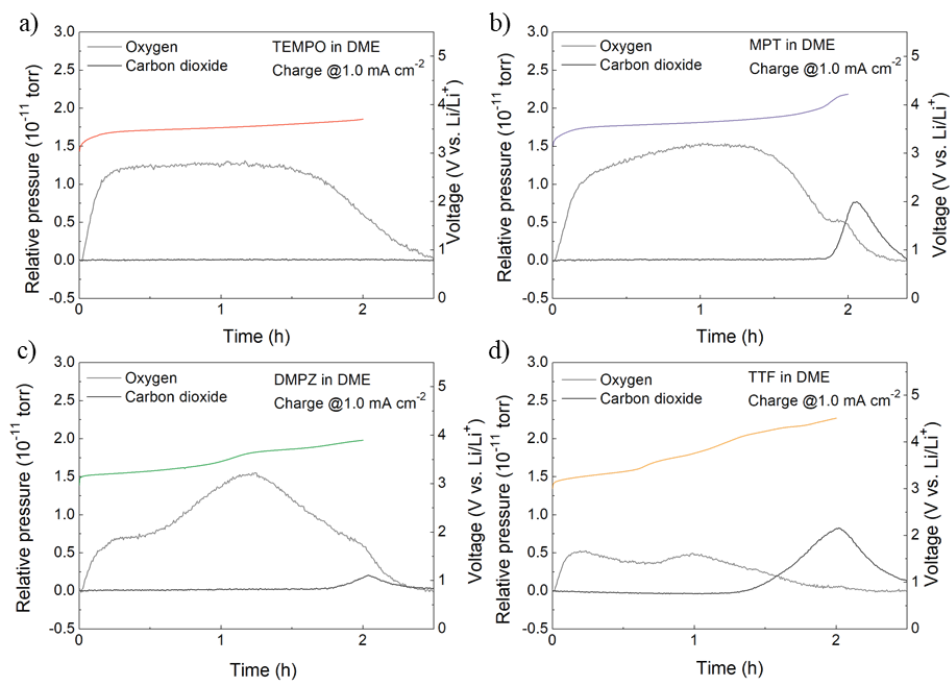


Figure 3.38. DEMS gas analysis while charging a lithium–oxygen battery under a current rate of 1.0 mA cm^{-2} using (a) TEMPO, (b) MPT, (c) DMPZ, and (d) TTF. The grey and black lines indicate the O_2 and CO_2 emission, respectively.

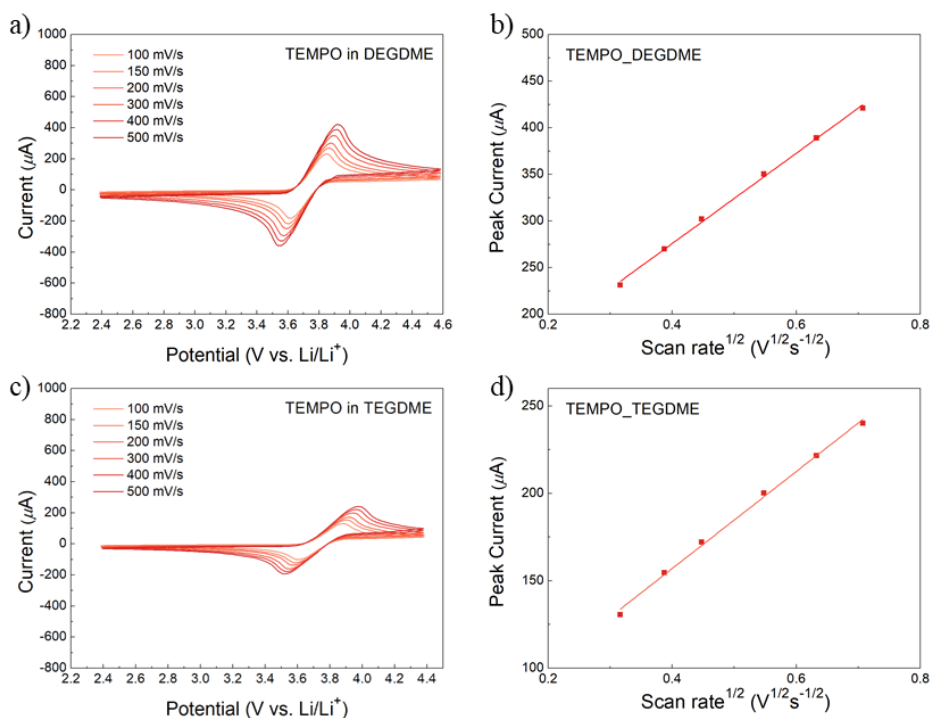


Figure 3.39. Cyclic voltammograms and corresponding plots of peak current vs. $(\text{scan rate})^{1/2}$. Cyclic voltammograms of 1 M LiTFSI in (a) DEGDM and in (c) TEGDM with 50 mM TEMPO for scan rates ranging from 100 to 500 mV s^{-1} . Plots showing a linear relationship between peak current and $(\text{scan rate})^{1/2}$ for 1 M LiTFSI in (b) DEGDM and (d) TEGDM.

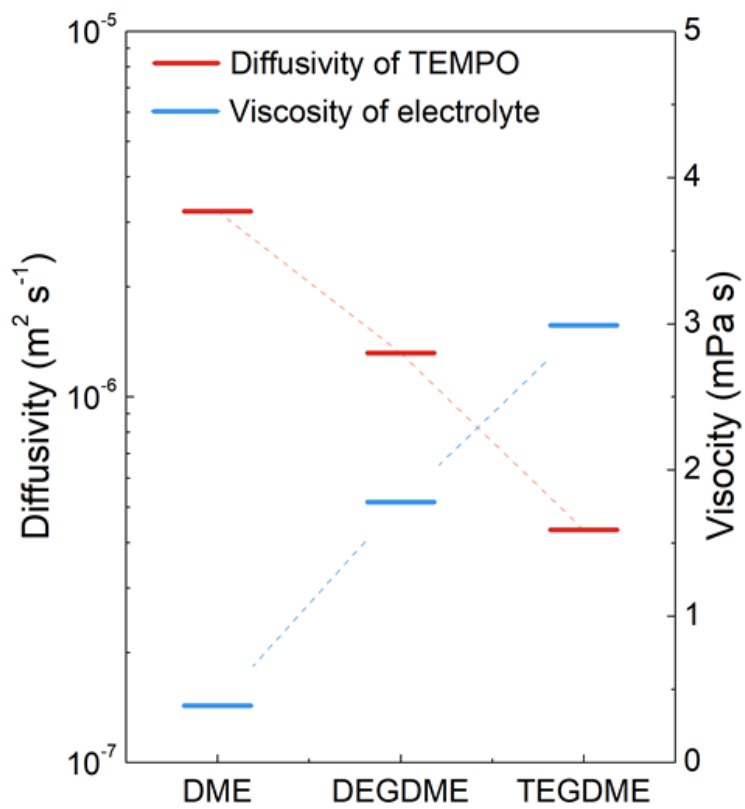


Figure 3.40. Viscosity of DME (ref³³), DEGDME (ref³⁴), and TEGDME (ref³⁴) and diffusivity of TEMPO in these ether-based electrolytes.

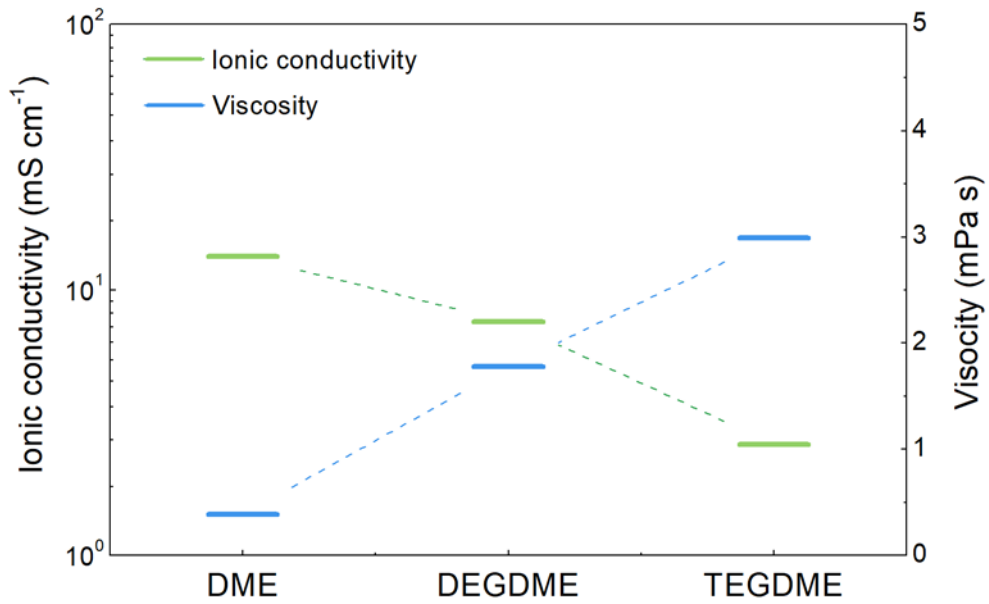


Figure 3.41. Ionic conductivity and viscosity of various ether-based electrolyte.^{33, 34}

The measured ionic conductivity is 13.39, 7.62, and 2.62 mS cm⁻¹ at 300 K for 1M LiTFSI DME, 1M LiTFSI DEGDME, and 1M LiTFSI TEGDME, respectively. The electrolytes with higher viscosity have a tendency to show lower ionic conductivity.

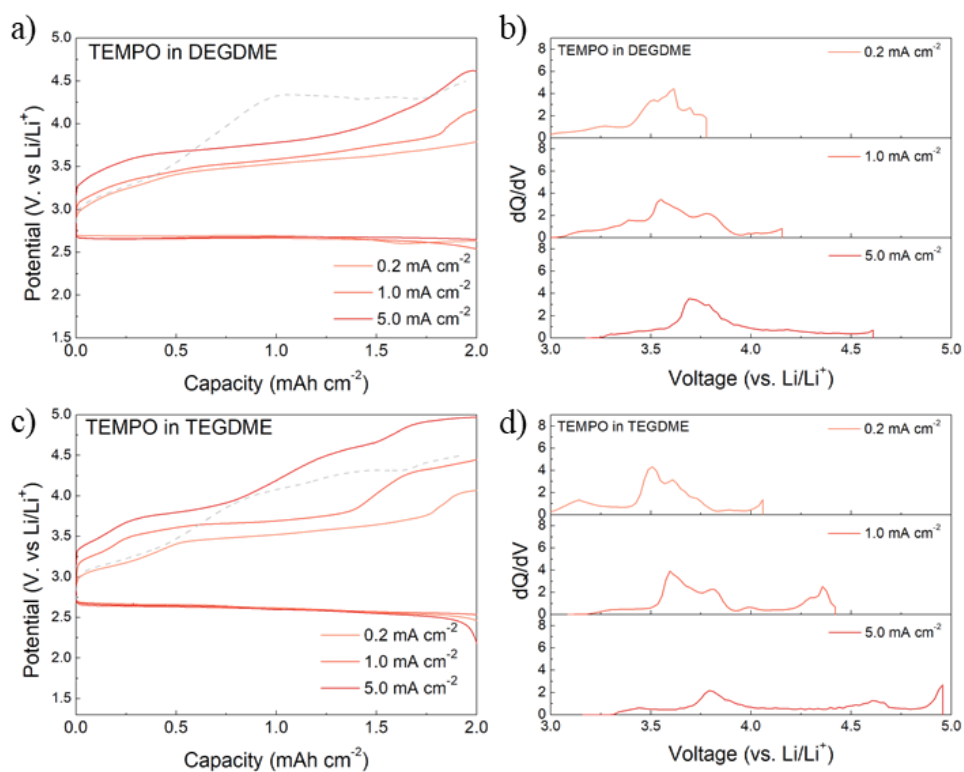


Figure 3.42. Galvanostatic cycling profiles and dQ/dV profiles of TEMPO-containing lithium–oxygen cell with 50 mM TEMPO in 1 M LiTFSI in DEGDM (a and b) and 50 mM TEMPO in 1 M LiTFSI in TEGDME (c and d).

3.2.4 Concluding remarks

We investigated the intrinsic kinetic properties of RMs and RM-assisted charge process in a lithium–oxygen battery using several important RMs that have been previously reported. They were analyzed considering the inherent reactivity/kinetics of RM and the diffusivity in a given condition. It was found that the overall kinetics of RMs have a positive correlation with the redox potential of RMs, and multi-redox RMs can display distinct properties depending on its oxidation states. Among RMs investigated, DMPZ^{2+} exhibited the highest reaction rate of lithium peroxide decomposition, while the mass diffusion rate was the highest for TEMPO^+ . Based on the scrutiny of these two independent kinetic parameters, we observed that TEMPO-assisted charge would result in the highest rate capability among investigated RMs, which could be verified in the various rate experiments in a practical cell environment. Additional *in situ* gas analysis revealed that the role of RMs is not only to reduce the apparent charge voltage but also to suppress side reactions caused by a high charge voltage. Moreover, experiments using various electrolytes demonstrated that the type of RM and the selection of electrolyte concurrently determine the rate capability of RM-assisted charge. This study suggests that selecting an appropriate RM/electrolyte combination based on understanding the kinetics is important for the realization of high-power and highly reversible lithium–oxygen batteries.

3.2.5 References

1. Bruce PG, Freunberger SA, Hardwick LJ, Tarascon J-M. Li-O₂ and Li-S batteries with high energy storage. *Nat. Mater.* 2012, **11**(1): 19.
2. Christensen J, Albertus P, Sanchez-Carrera RS, Lohmann T, Kozinsky B, Liedtke R, *et al.* A critical review of Li/air batteries. *J. Electrochem. Soc.* 2011, **159**(2): 1-30.
3. Girishkumar G, McCloskey B, Luntz A, Swanson S, Wilcke W. Lithium-air battery: promise and challenges. *J. Phys. Chem. Lett.* 2010, **1**(14): 2193-2203.
4. Li F, Chen J. Mechanistic Evolution of Aprotic Lithium-Oxygen Batteries. *Adv. Energy Mater.* 2017, **7**(24): 1602934.
5. Sun B, Wang B, Su D, Xiao L, Ahn H, Wang G. Graphene nanosheets as cathode catalysts for lithium-air batteries with an enhanced electrochemical performance. *Carbon* 2012, **50**(2): 727-733.
6. Lim H-D, Song H, Gwon H, Park K-Y, Kim J, Bae Y, *et al.* A new catalyst-embedded hierarchical air electrode for high-performance Li-O₂ batteries. *Energy Environ. Sci.* 2013, **6**(12): 3570-3575.
7. Lim HD, Park KY, Song H, Jang EY, Gwon H, Kim J, *et al.* Enhanced Power and Rechargeability of a Li-O₂ Battery Based on a Hierarchical-Fibril CNT Electrode. *Adv. Mater.* 2013, **25**(9): 1348-1352.
8. Bae Y, Lim H-D, Yun YS, Kang K. Catalytic Effects of Heteroatom-doped Graphene Nanosheets on the Performance of Li-O₂ Batteries. *J.*

Electrochem. Sci. Technol. 2014, **5**(2): 49-52.

9. Lim HD, Song H, Kim J, Gwon H, Bae Y, Park KY, *et al.* Superior rechargeability and efficiency of lithium–oxygen batteries: hierarchical air electrode architecture combined with a soluble catalyst. *Angew. Chem., Int. Ed.* 2014, **126**(15): 4007-4012
10. Sun B, Huang X, Chen S, Munroe P, Wang G. Porous graphene nanoarchitectures: an efficient catalyst for low charge-overpotential, long life, and high capacity lithium–oxygen batteries. *Nano Lett.* 2014, **14**(6): 3145-3152.
11. Bae Y, Yun YS, Lim H-D, Lee H, Kim Y-J, Kim J, *et al.* Tuning the Carbon Crystallinity for Highly Stable Li–O₂ Batteries. *Chem. Mater.* 2016, **28**(22): 8160-8169.
12. Lim H-D, Lee B, Zheng Y, Hong J, Kim J, Gwon H, *et al.* Rational design of redox mediators for advanced Li–O₂ batteries. *Nat. Energy* 2016, **1**(6): 16066.
13. Han X, Cheng F, Chen C, Li F, Chen J. A Co₃O₄@ MnO₂/Ni nanocomposite as a carbon-and binder-free cathode for rechargeable Li–O₂ batteries. *Inorg. Chem. Front.* 2016, **3**(6): 866-871.
14. Sun B, Guo L, Ju Y, Munroe P, Wang E, Peng Z, *et al.* Unraveling the catalytic activities of ruthenium nanocrystals in high performance aprotic Li–O₂ batteries. *Nano Energy* 2016, **28**: 486-494.
15. Lim H-D, Lee B, Bae Y, Park H, Ko Y, Kim H, *et al.* Reaction chemistry

- in rechargeable Li–O₂ batteries. *Chem. Soc. Rev.* 2017, **46**(10): 2873-2888.
16. Lim H-D, Yun YS, Cho SY, Park K-Y, Song MY, Jin H-J, *et al.* All-carbon-based cathode for a true high-energy-density Li-O₂ battery. *Carbon* 2017, **114**: 311-316.
 17. Bae Y, Park H, Ko Y, Kim H, Park SK, Kang K. Bifunctional Oxygen Electrocatalysts for Lithium–Oxygen Batteries. *Batteries & Supercaps* 2019, **2**(4): 311-325.
 18. Ko Y, Park H, Kim J, Lim HD, Lee B, Kwon G, *et al.* Biological Redox Mediation in Electron Transport Chain of Bacteria for Oxygen Reduction Reaction Catalysts in Lithium–Oxygen Batteries. *Adv. Funct. Mater.* 2019, **29**: 1805623.
 19. Aurbach D, McCloskey BD, Nazar LF, Bruce PG. Advances in understanding mechanisms underpinning lithium–air batteries. *Nat. Energy* 2016, **1**(9): 16128.
 20. Chen Y, Freunberger SA, Peng Z, Fontaine O, Bruce PG. Charging a Li–O₂ battery using a redox mediator. *Nat. Chem.* 2013, **5**(6): 489-494.
 21. Bergner BJ, Schürmann A, Pepler K, Garsuch A, Janek Jr. TEMPO: a mobile catalyst for rechargeable Li-O₂ batteries. *J. Am. Chem. Soc.* 2014, **136**(42): 15054-15064.
 22. Feng N, He P, Zhou H. Enabling Catalytic Oxidation of Li₂O₂ at the Liquid–Solid Interface: The Evolution of an Aprotic Li–O₂ Battery.

- ChemSusChem* 2015, **8**(4): 600-602.
23. Lim H-D, Lee B, Zheng Y, Hong J, Kim J, Gwon H, *et al.* Rational design of redox mediators for advanced Li–O₂ batteries. *Nat. Energy* 2016, **1**: 16066.
 24. Chen Y, Gao X, Johnson LR, Bruce PG. Kinetics of lithium peroxide oxidation by redox mediators and consequences for the lithium–oxygen cell. *Nat. Commun.* 2018, **9**(1): 767.
 25. Zhang W, Shen Y, Sun D, Huang Z, Zhou J, Yan H, *et al.* Promoting Li₂O₂ oxidation via solvent-assisted redox shuttle process for low overpotential Li-O₂ battery. *Nano Energy* 2016, **30**: 43-51.
 26. Zhang J, Sun B, Zhao Y, Kretschmer K, Wang G. Modified Tetrathiafulvalene as an Organic Conductor for Improving Performances of Li– O₂ Batteries. *Angew. Chem., Int. Ed.* 2017, **56**(29): 8505-8509.
 27. Bard AJ, Faulkner LR, Leddy J, Zoski CG. *Electrochemical methods: fundamentals and applications*, vol. 2. Wiley New York, 1980.
 28. Marcus RA, Sutin N. Electron transfers in chemistry and biology. *Biochim. Biophys. Acta, Rev. Bioenerg.* 1985, **811**(3): 265-322.
 29. Adams BD, Radtke C, Black R, Trudeau ML, Zaghbi K, Nazar LF. Current density dependence of peroxide formation in the Li–O₂ battery and its effect on charge. *Energy Environ. Sci.* 2013, **6**(6): 1772-1778.
 30. Ottakam Thotiyl MM, Freunberger SA, Peng Z, Bruce PG. The carbon electrode in nonaqueous Li–O₂ cells. *J. Am. Chem. Soc.* 2012, **135**(1): 494-

500.

31. Wandt J, Jakes P, Granwehr J, Gasteiger HA, Eichel RA. Singlet oxygen formation during the charging process of an aprotic lithium–oxygen battery. *Angew. Chem.* 2016, **128**(24): 7006-7009.
32. Mahne N, Schafzahl B, Leypold C, Leypold M, Grumm S, Leitgeb A, *et al.* Singlet oxygen generation as a major cause for parasitic reactions during cycling of aprotic lithium–oxygen batteries. *Nat. Energy* 2017, **2**(5): 17036.
33. Zheng P, Meng X, Wu J, Liu Z. Density and viscosity measurements of dimethoxymethane and 1, 2-dimethoxyethane from 243 K to 373 K up to 20 MPa. *Int. J. Thermophys.* 2008, **29**(4): 1244-1256.
34. Kodama D, Kanakubo M, Kokubo M, Hashimoto S, Nanjo H, Kato M. Density, viscosity, and solubility of carbon dioxide in glymes. *Fluid Phase Equilib.* 2011, **302**(1): 103-108.

Chapter 4. Addressing practical issue of redox mediators: shuttle phenomena

4.1 Anchorage of redox mediator for sustainable redox mediation in lithium-oxygen battery

(The essence of this chapter has been published in *Angewandte Chemie*. Reproduced with permission from [Ko, Y. *et al.*, *Angew. Chem. Int. Ed.* **2020**, 59, 5376–5380]
Copyright (2020) WILEY-VCH)

4.1.1 Research Background

Lithium–oxygen batteries have attracted significant research attention for the last decade owing to their exceptionally high theoretical energy density.^{1–4} However, the practical realization of lithium–oxygen batteries has been hampered by the insufficient reversibility of the associated electrochemical reaction and their low energy efficiency. These issues can be partly attributed to the difficulty of electrochemical charging of the insulating discharge product (lithium peroxide, Li_2O_2).^{5, 6} To address this concern, efforts were made to identify suitable catalysts to promote the reversible decomposition of Li_2O_2 , mostly focusing on novel metals^{7–10} or metal oxides^{11, 12}, resulting in improved reversibility afforded by the catalytic activities. However, despite the relatively high catalytic activities, it was later revealed that the catalysts generally exhibited poor selectivity, leading to various side reactions involving serious electrolyte decomposition.^{9, 13} Recently, as an alternative

to conventional catalysts, redox mediators (RMs) have been shown to be much more effective in promoting the reversible decomposition of the discharge product by exhibiting a high selectivity toward Li_2O_2 .¹⁴⁻¹⁶ The redox mediation, simply driven by the difference in the intrinsic redox potential of the RM and the charging potential of Li_2O_2 , enables RMs to selectively decompose Li_2O_2 . RMs such as tetramethylpiperidinyloxy (TEMPO),^{17, 18} tetrathiafulvalene,¹⁴ dimethylphenazine,^{15, 19} and lithium halides (*e.g.* lithium iodide,²⁰ lithium bromide²¹) have been reported to be capable of successfully decomposing Li_2O_2 with significantly reduced charge polarization and enhanced energy efficiency.

RMs generally act as charge carriers dissolved in the electrolyte. Upon charging, the RMs are oxidized on the electrode, and the freely mobile oxidized RM species can chemically decompose Li_2O_2 . However, their mobility also leads to unwanted side reactions, as the RMs (and especially oxidized RMs) can diffuse to the counter electrode, *i.e.* the lithium metal anode, resulting in a spontaneous reaction between the two components. This so-called shuttle phenomenon is considered the main cause of the degradation of RM-containing lithium-oxygen cells, including lithium metal degeneration and RM decomposition.^{22, 23} This trade-off stemming from the mobile nature of RMs results in the need for additional treatments such as the insertion of lithium protection layers or modified separators to prevent the side reactions with lithium metal.²⁴⁻²⁶ However, these approaches possess limitations, as they contribute to undesired increase in the cell weight and resistance.^{25, 27}

Herein, we report on the use of a polymer-based RM, 2,2,6,6-tetramethyl-1-piperidinyloxy-4-yl methacrylate (PTMA) exploiting the well-known TEMPO redox chemistry to decouple the redox property and shuttle phenomenon. We were able to suppress the transport of RMs toward lithium metal by anchoring the RMs at the air electrode surface; in addition, the RMs maintained the charge-carrying redox property enabled by the intrinsic electron transfer between polymer chains.^{28, 29} By replacing TEMPO with PTMA, we successfully eliminated the degradation caused by the shuttle phenomenon and, thereby, notably enhanced the stability of redox mediation, and cell operation was achieved.

4.1.2 Experimental Method

4.1.2.1 Synthesis of PTMA

PTMA was synthesized using two different reaction pathways: i) GTP-PTMA was polymerized by the group transfer polymerization (GTP) method after nitroxyl radical formation of the MTMP monomer and ii) RP-PTMA was polymerized by the free radical polymerization (RP) method of the MTMP monomer followed by nitroxyl radical formation. Tetrahydrofuran (THF) was distilled using sodium/benzophenone before use. All the other reagents and solvents were obtained from commercial suppliers and used as received without further purification. All glassware, syringes, magnetic stirring bars, and needles were thoroughly dried in a convection oven before use. The number-average molecular weight (M_n) and polydispersity index (PDI) of the polymers were measured using gel permeation chromatography (GPC) with THF as the eluent and polystyrene as the standard using a Waters 515 HPLC pump, PLgel 5.0 μm guard, MIXED-C and MIXED-D columns (Polymer Laboratories), and Viscotek LR125 laser refractometer.

GTP-PTMA was prepared according to a reported method with modifications.^{30, 31} To a stirred solution of 2,2,6,6-tetramethylpiperidine methacrylate (MTMP) (40 g, 178 mmol) and MgCl_2 (0.013 g, 0.178 mmol) in 7 mL methanol, 34.5% H_2O_2 (56 mL) was added dropwise using a dropping funnel. The mixture was refluxed and stirred overnight under an Ar atmosphere. The crude product obtained by evaporation of the liquid was purified by flash column chromatography on silica gel with ethyl acetate/n-hexane (1:9 v/v) as an eluent. Recrystallization from n-hexane

afforded red crystals of 4-methacryloyloxy-2,2,6,6-tetramethylpiperidine-N-oxyl, MTMPO (6.07 g, yield = 14.2%). In a flame-dried two-necked 100-mL round-bottom flask, MTMPO (3 g, 12.5 mmol) was dissolved in 10 mL of freshly distilled THF under an Ar atmosphere. To the rapidly stirred solution, 1-methoxy-2-methyl-1-trimethylsilyloxypropene (0.045 mL, 0.2 mmol) was added, and then, 1 M tetrabutylammonium fluoride solution in THF (0.01 mL, 0.01 mmol) was added. The viscous mixture was stirred at 20 °C for 12 h, and then, methanol (1.25 mL) was added to quench the polymerization. The mixture was further stirred for 5 min and then slowly poured onto vigorously stirred hexanes (125 mL). The orange precipitate was obtained by filtration and washed with hexanes. This precipitate was dissolved in dichloromethane and then added dropwise to hexane for reprecipitation. Repeating reprecipitation twice afforded GTP-PTMA as an orange powder (2.23 g, yield = 74.3%). GPC: (M_n = 25 kDa, PDI = 2.14). Nitroxide concentration: [NO*] = 94%. RP-PTMA was prepared according to previously reported procedures with minor modifications.^{32, 33} In a Pyrex tube, MTMP (2 g, 8.9 mmol) and 12 wt% 2,2'-azobisisobutyronitrile (AIBN) solution in acetone (0.3 mL, 0.187 mmol) were mixed in 10 mL of freshly distilled THF. The mixture was degassed by three freeze-pump-thaw cycles using liquid nitrogen for freezing, and then the Pyrex tube was sealed under vacuum. The degassed mixture was stirred at 70 °C for 6 h. The reaction mixture was added to hexane, and the precipitated pale white polymer PMTMP (1.2 g, yield = 60%) was obtained after filtration. To a solution of PMTMP (0.5 g, 4.1 mmol) in 10 mL methanol, $\text{Na}_2\text{WO}_4 \cdot 2\text{H}_2\text{O}$ (0.15 g, 0.45 mmol),

ethylenediaminetetraacetic acid (EDTA) (0.1 g, 0.34 mmol), 34.5% H₂O₂ (1 mL), and H₂O (5 mL) were added and stirred at 60 °C for 44 h. The reaction mixture was filtrated and washed thoroughly with H₂O and ethyl ether to afford RP-PTMA as a pale red solid (0.5 g, yield = 95%). GPC: (M_n = 34 kDa, PDI = 1.92). Nitroxide concentration: [NO*] = 70.3%.

4.1.2.2 Fabrication of cell components

The organic solvent, tetraethylene glycol dimethyl ether (TEGDME, ≥ 99%, Sigma-Aldrich), was dried for more than 3 days using a molecular sieve (type 3Å, Sigma-Aldrich). TEMPO was purchased from Sigma-Aldrich and used as received. The bis(trifluoromethane)sulfonimide lithium salt (LiTFSI, > 98.0%) was purchased from Tokyo Chemical Industry and dried for more than 3 days under 150 °C vacuum condition before use. The electrolyte was prepared by dissolving 2 M LiTFSI in TEGDME. The TEMPO-containing electrolyte was prepared by additionally adding 10 mM of TEMPO to the 2 M LiTFSI TEGDME. The Ketjen black air electrode with PTMA was fabricated by casting a 1-methyl-2-pyrrolidinone- and isopropanol-based slurry mixed with Ketjen black powder, PTMA, and polytetrafluoroethylene (PTFE) binder with a weight ratio of 8:4:2. PTMA-coated electrode was fabricated to have the PTMA/carbon ratio of 1:2. The PTMA-free air electrode was prepared in the same manner except without the addition of PTMA. The both slurries for PTMA/carbon composite electrode and PTMA-free electrode were casted on carbon paper (TGPH030, Toray) with a thickness of 120 μm and dried at 70 °C under vacuum for more than 3 h. The average loading amount of PTMA/carbon composite

is 0.2 mg cm^{-2} . The average carbon loading amount of PTMA-free electrode is 0.13 mg cm^{-2} . The Li_2O_2 pre-loaded electrode was prepared by casting an isopropanol-based slurry on the same carbon paper. The slurry contained Ketjen black, PTMA, Li_2O_2 , and PTFE binder with a weight ratio of 4:2:1:1. The slurry was casted and dried in Ar-filled glove box and stored before use at the same place.

4.1.2.3 Assembly of lithium–oxygen cell

For the air electrodes, coated carbon paper was punched into discs with a diameter of 1/2 inch. A sheet of glass fiber (GF/F, Whatman) with a diameter of 16.5 mm was used as the separator. Lithium metal with a diameter of 9/16 inches and a thickness of $300 \mu\text{m}$ was used as the anode. All the cell components, the air electrode, separator, and lithium metal anode, were assembled to construct a lithium–oxygen cell using a 2032 coin cell with $85 \mu\text{L}$ of electrolyte. The coin cells were assembled in an Ar-filled glove box (H_2O level $< 0.5 \text{ ppm}$ and O_2 level $< 0.5 \text{ ppm}$). After cell assembly, each coin cell was stored in a coin-cell container in a gas chamber. The atmosphere in the chamber was changed from Ar to O_2 ($> 99.999\%$) with a pressure of 1.5 bar, and the chamber was operated as closed.

4.1.2.4 Conditions for electrochemical tests and materials characterization

The lithium–oxygen cells for galvanostatic cycling were operated at room temperature after resting for 30 min. The Li_2O_2 pre-loaded carbon electrode was used for the LSV experiment, which was conducted using the same two-electrode cell configuration as that used for the galvanostatic cycling with a scan rate of 1 mV s^{-1} .

All the electrochemical tests were conducted using a potentio-galvanostat (WonA Tech, WBCS 3000, Korea). For the characterization of the cell components after cycling, the cells were disassembled in an Ar-filled glove box. The electrode and separator were rinsed with a small amount of anhydrous DME and dried under Ar. An X-ray diffractometer (D2 PHASER, Bruker, Germany) was also used for identification of the discharge product. To observe the morphologies of the air electrode and lithium metal anode, field-emission scanning electron microscopy (FE-SEM; SUPRA 55VP, Carl Zeiss, Germany) was used. The coating layer on the carbon surface was examined using transmission electron microscopy (TEM; JEM-2100F, JEOL Ltd., Japan). For *in situ* gas analysis, mass spectrometry (MS) (HPR-20, Hiden Analytical) combined with a potentio-galvanostat (WonA Tech, WBCS 3000, Korea) was used. The amount of Li_2O_2 was quantitatively measured using the iodometry titration method. A detailed description of the titration method has been elaborated elsewhere.³⁴ The radical concentrations of the two PTMA polymers were analyzed using a superconducting quantum interference device (SQUID, MPMS3-Evercool, Quantum Design Inc., U.S.A.). The Landé g-factor for the radical species was measured using electron paramagnetic resonance spectroscopy (EPR; EMXmicro, Bruker, Germany).

4.1.3 Results and Discussions

Most RMs, such as TEMPO, are susceptible to the shuttle phenomenon because of their mobile nature in the cell. As depicted in figure 4.1, the galvanostatic charge of TEMPO dissolved in an electrolyte typically shows a charge capacity that far exceeds the theoretical capacity, which is the characteristic behavior of the shuttle phenomenon.³⁵ This ‘overcharge’ capacity implies that the oxidized TEMPO is reduced at the counter electrode, *i.e.*, the lithium metal anode, generating neutral TEMPO, which is re-oxidized at the cathode side. The shuttling of the oxidized TEMPO is also accompanied by severe side reactions at the lithium anode when lithium–oxygen cells are cycled. Figure 4.2.a presents photographs of the lithium metal before cycling (top) and after 5 cycles without (left) and with (right) TEMPO in a lithium–oxygen cell. Without TEMPO in the cell, the lithium metal after cycling retained a relatively clean pristine surface. In contrast, that with TEMPO in the cell was notably degraded, which is attributed to the side reactions between the oxidized TEMPO and lithium metal during cycling. The scanning electron microscopy (SEM) images in figure 4.2.b also display consistent results. The degradation of the lithium metal surface was more pronounced when cycling with TEMPO. It should also be noted that the reaction between TEMPO and lithium metal results in substantial consumption of TEMPO in the cell. Figure 4.3 UV–vis absorption spectra of the TEMPO–containing electrolyte before and after cycling. The intensity of the characteristic TEMPO peak at approximately 355 nm notably decreased after cycling, indicating the significant loss of TEMPO. The consumption of TEMPO results in a

change in the galvanostatic cycling profile: an increasing charging overpotential with shortening of the characteristic TEMPO redox voltage plateau after a few cycles, as observed in figure 4.4. These side reactions, consequently, lead to failure in achieving the sufficient enhancement of the cyclability compared with that of the reference cell despite the TEMPO–assisted effective decomposition of Li_2O_2 (figure 4.5).

The working mechanism of RMs and the deterioration process by the shuttle phenomenon are schematically illustrated in figure 4.6 (left). During charging, the RM is oxidized at the air electrode to RM^+ , which migrates and chemically decomposes Li_2O_2 in the cell. However, because RM^+ can freely diffuse within the cell, it also drifts away from the air electrode to the lithium metal. Successively, the drifted RMs react with lithium metal, which causes both the degeneration of the lithium metal/ solid electrolyte interphase (SEI) layer and the consumption of RMs. The mobile nature of the RMs that enables the facile decomposition of Li_2O_2 simultaneously triggers a destructive shuttle phenomenon. This trade–off can be addressed by introducing a polymer–based RM, for which shuttling is prevented while still maintaining the charge–carrying redox property, as depicted in figure 4.6 (right). With this aim, we synthesized a radical polymer, PTMA, which has a TEMPO unit at each polymer chain, using two distinct polymerization methods: group transfer polymerization³⁶ (GTP) and radical polymerization^{33, 37} (RP). The procedures for both methods are described in figure 4.7. As observed in figure 4.8, the nitroxyl radical fractions in the PTMA samples, indicative of TEMPO–unit

activity, were calculated to be far higher when using the GTP method (~94%; see supplement note 3.1.4.1 for the details of the radical concentration calculation); thus, the PTMA synthesized using the GTP method was used for the subsequent experiments (figure 4.9). Using this PTMA as a platform for RM activity, the crossover toward the lithium anode was expected to be suppressed by the limited solubility of PTMA in the electrolyte (figure 4.10). Moreover, it was supposed that the PTMA would retain its charge-carrying redox property, as it is well-known that electron diffusion between redox centers occurs by self-exchange in PTMA (See details in supplement note 3.1.4.2)^{28,29}. Because the electron transfer along the redox center of PTMA can partly reflect and replace the physical migrations of TEMPO in the redox mediation, the PTMA may function as a RM that is capable of decomposing remotely dispersed Li_2O_2 particles, as long as they have physical contact with any PTMA in the electrode.

The capability of PTMA as a RM was first examined through electrochemical analysis using linear sweep voltammetry (LSV), as shown in Figure 4.11. The grey and black lines are the LSV profiles of typical carbon air electrodes without and with Li_2O_2 , respectively. The increase in current density above 4.0 V (vs. Li/Li^+) indicates that substantial electrochemical decomposition of Li_2O_2 occurs at the corresponding voltage. When comparing the LSV profiles of the PTMA-containing electrode (orange line) and the electrode containing both PTMA and Li_2O_2 (red line), it is apparent that for both cases, the appreciable current begins at 3.55 V (vs. Li/Li^+), which corresponds to the oxidation potential of PTMA. More importantly, a notable

increase in the current is observed for the electrode containing both PTMA and Li_2O_2 (red line), which supports the PTMA-mediated Li_2O_2 decomposition. Inspired by this finding, the effect of PTMA was further investigated in lithium–oxygen cells by preparing a PTMA-coated air electrode (see experimental section). No significant morphological differences between the bare carbon electrode and PTMA-coated electrode were observed in the electron microscopy images in figure 4.12 except for the thin coating layer with the thickness of ~ 4 nm (insets), indicating that the PTMA was homogeneously coated on the surface of the carbon. The PTMA-incorporated air electrode was observed to be capable of promoting the reversible formation and decomposition of Li_2O_2 in a lithium–oxygen cell. The X-ray diffraction pattern in figure 4.13 and morphological analysis of the air electrode by SEM (figure 4.14) indicate that Li_2O_2 formed after the discharge can be clearly removed after the subsequent charging process. Moreover, the galvanostatic cycling profile in figure 4.15 confirms that the charging overpotential was markedly lowered for the PTMA-coated air electrode, strongly suggesting that the PTMA served as an active RM. (See supplement note 3.1.4.3 for more discussion on the activity of PTMA) Notably, the charging overpotential of the PTMA case is almost comparable to that of the TEMPO case, even though PTMA was anchored in the electrode. This finding indicates that TEMPO units in the polymer are still capable of performing the role of RMs, resembling the conventional TEMPO. Finally, gas analysis of the PTMA-assisted charging process was performed. (figure 4.16). It provides further evidence that PTMA can mediate the decomposition of Li_2O_2 at low voltage, evolving primarily

O₂ gas during the charging process. Notable is that the oxygen evolution rate suddenly falls with the CO₂ gas emission at the latter part of charging. It is attributed to the decomposition of by-product, which was previously reported elsewhere.³⁸⁻⁴⁰ Investigations of the PTMA-containing lithium-oxygen cell suggest that employing PTMA as a RM can effectively suppress the shuttling phenomenon and corresponding side reactions during the cycling. Figure 4.17 presents UV-vis absorption spectra of the electrolyte before and after cycling for the PTMA-containing lithium-oxygen cell. No distinct differences are observed in the spectra after (yellow line) and before (grey line) cycling, indicating that the PTMA remained stably anchored at the air electrode during cycling and was not dissolved in the electrolyte while undergoing repeated oxidation and reduction. The absence of shuttling during cycling substantially enhanced the stability of the lithium metal anode. Figure 4.18 presents images of the lithium metal before cycling (top), after 5 cycles without any RMs as a reference (mid), and after 5 cycles with PTMA (bottom). The lithium metal of the PTMA-containing cell retained a clean pristine surface after cycling, indicating the greatly improved stability of the lithium metal compared with that of the TEMPO cell in figure 4.2. Furthermore, elimination of the shuttle phenomenon was also observed to enhance the efficiency of RM-mediated Li₂O₂ decomposition, as oxidized RM species were not wasted at the lithium anode. Using Li₂O₂ pre-loaded carbon electrodes, we quantitatively measured the remaining Li₂O₂ after charging to a certain state of charge (SoC) with TEMPO and PTMA using the iodometry titration method.³⁴ Figure 4.19 shows that the undecomposed amount of

Li_2O_2 after charging with TEMPO (red dots) is greater than that after charging with PTMA (orange dots) and is also greater than the amount expected according to the SoC (dotted line). This finding suggests that less Li_2O_2 than intended was actually decomposed when charging with TEMPO, indicating the non-negligible shuttling of TEMPO in the cell. In contrast, nearly all the expected amount of Li_2O_2 was decomposed with PTMA, which precisely accounts for the amount of oxidized PTMA. Consequently, the cyclability of the PTMA-loaded lithium-oxygen cell was remarkably enhanced compared with that of the RM-free and TEMPO-containing cells, as illustrated in Figure 4.20.

Although the cycle life of the TEMPO-containing cell could not be sufficiently elongated despite the enhancement of the charging process, the anchoring of TEMPO units in the form of a polymer, *i.e.* PTMA, could successfully achieve the improvement of both the charging efficiency and cycle stability. This finding suggests that the prevention of the shuttle phenomenon and the resulting enhancement of the efficiency of RM-mediated Li_2O_2 decomposition enable sustainable redox mediation, which can lead to stable cycling of RM-containing lithium-oxygen cells. Nevertheless, the charge potential slightly increases with the repeated cycle (figure 4.21) despite the enhanced RM-mediated Li_2O_2 decomposition. It is due to the commonly attributed factors that have been found to deteriorate the cycle performance of conventional lithium-oxygen batteries.^{34, 41-43} (see supplement note 3.1.4.4 for the detailed discussion) Notable is that an abnormal initial discharge plateau is observed in the galvanostatic cycling profile of PTMA-

loaded cell (figure 4.22),⁴⁴ which is not the case for TEMPO-containing cell. We suppose that this observation is a further evidence on the absence of the shuttle effect in PTMA.⁴⁴ (see supplement note 3.1.4.5 for the detailed discussion.)

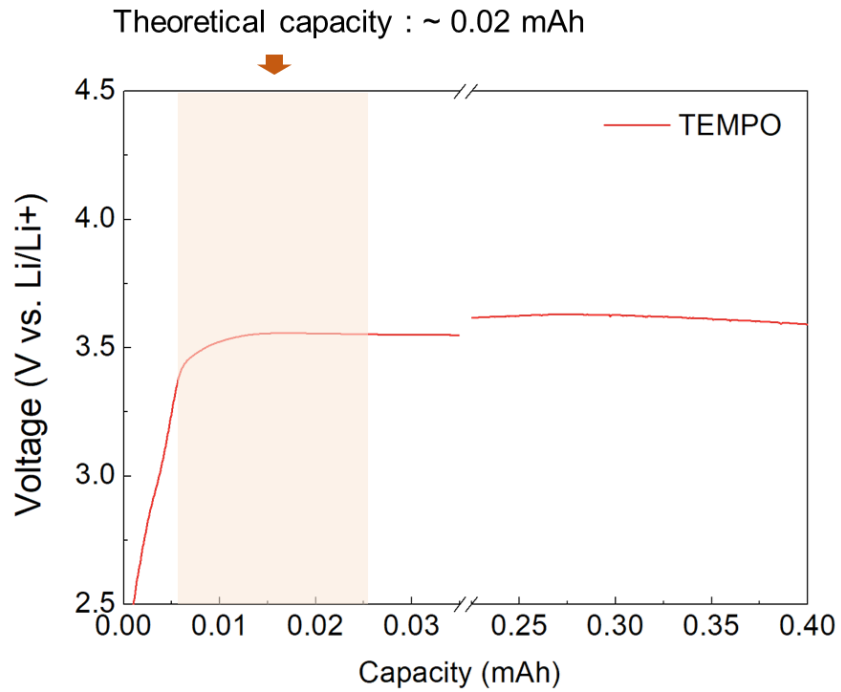


Figure 4.1. Galvanostatic charge profile using 2 M LiTFSI TEGDME with 10 mM of TEMPO, showing the capacity from TEMPO far exceeding the theoretical value.

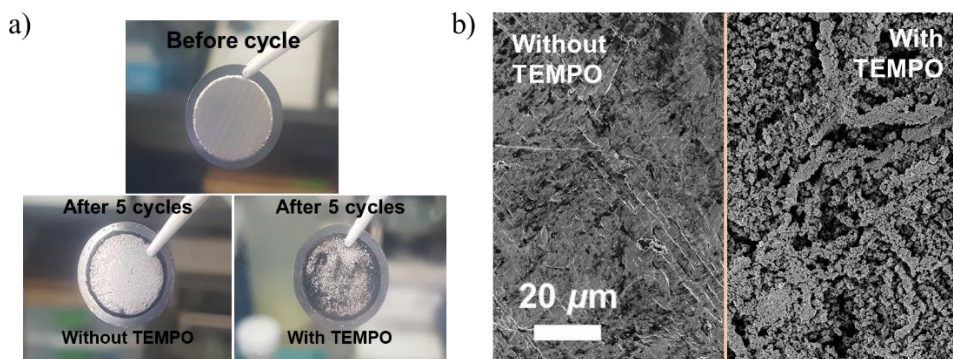


Figure 4.2. (a) Images of lithium metal before cycling (top) and after 5 cycles without TEMPO (left) and with TEMPO (right). (b) SEM images of lithium metal surface of cell cycled without TEMPO (left) and with TEMPO. (right)

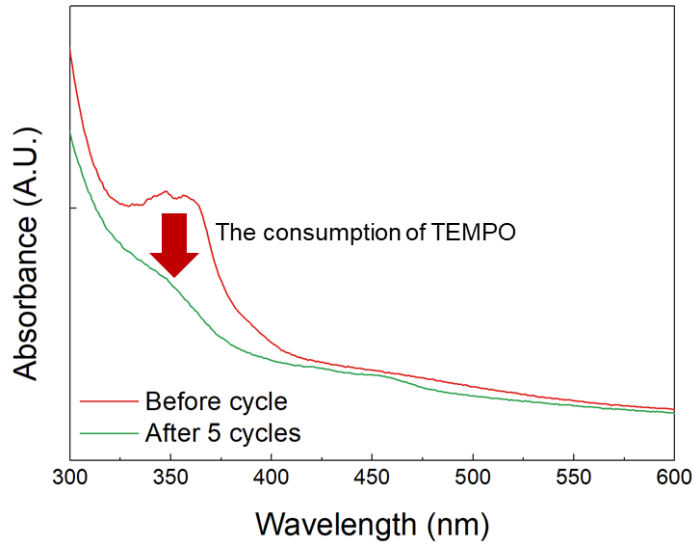


Figure 4.3. UV-vis absorption spectra of TEMPO-containing electrolyte before cycling and after cycling.

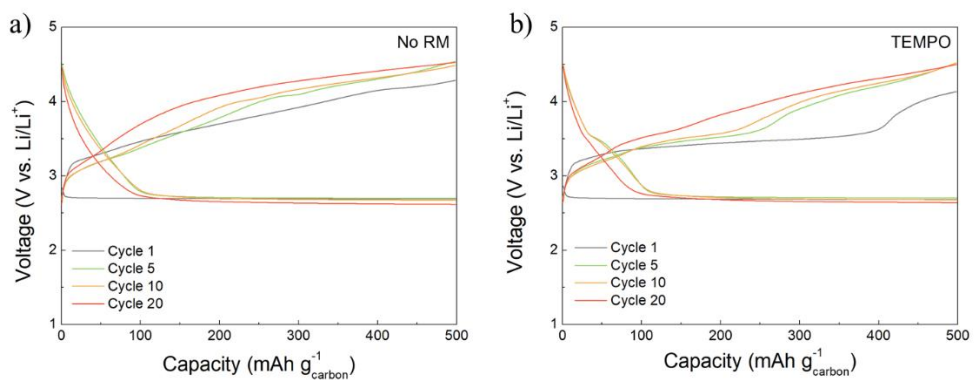


Figure 4.4. (a) Profiles of lithium–oxygen cell without any RMs, showing significant charge overpotential. (b) Profiles of cell containing 10 mM TEMPO, showing that the effect of TEMPO in reducing the charge overpotential weakens with repeated cycling.

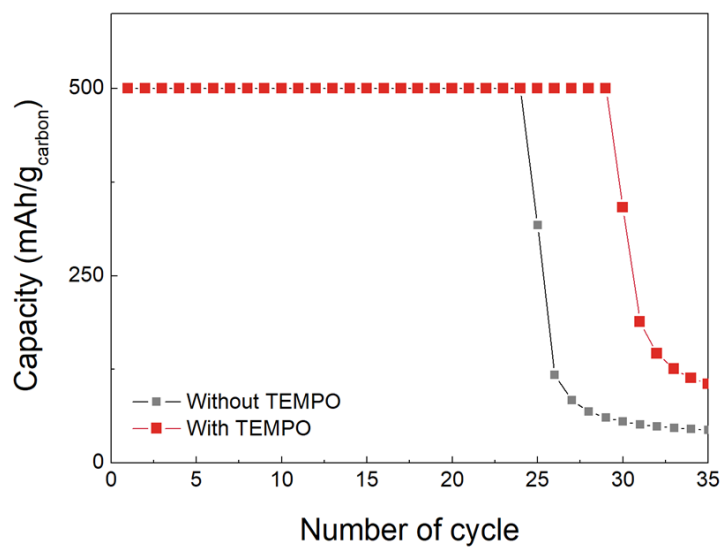


Figure 4.5. Cycling performance of lithium–oxygen cells without and with TEMPO.

The cells were cycled with a current density of 300 mA g^{-1} .

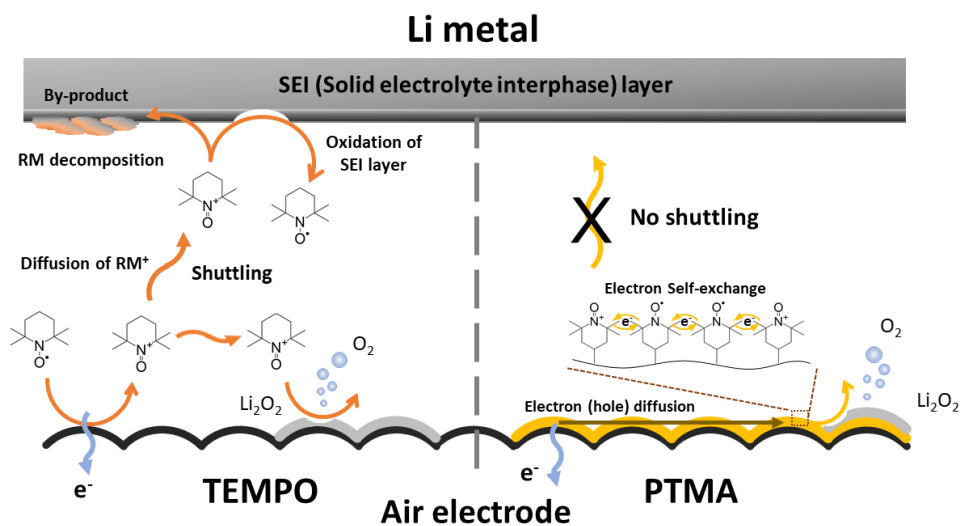


Figure 4.6. Schematic illustrations of the working processes of TEMPO and PTMA. For typical RMs such as TEMPO, oxidation of the RM occurs in the electrolyte. Then, RM^+ diffuses to Li_2O_2 and chemically decomposes it. In addition, the diffusible nature of RMs leads to the movement of RM^+ toward the reactive lithium metal anode side, which is referred to as the shuttle phenomenon. The shuttle phenomenon reduces the efficiency of Li_2O_2 decomposition by RM^+ . Furthermore, when RM^+ makes contact with the lithium metal anode, it promotes side reactions such as lithium metal oxidation and RM decomposition. However, as a polymer-based RM, PTMA is not accompanied by the shuttle phenomenon because it is fixed at the air electrode in the solid state. The electron transfer between polymer chains replaces the diffusion of RM molecules of typical RMs.

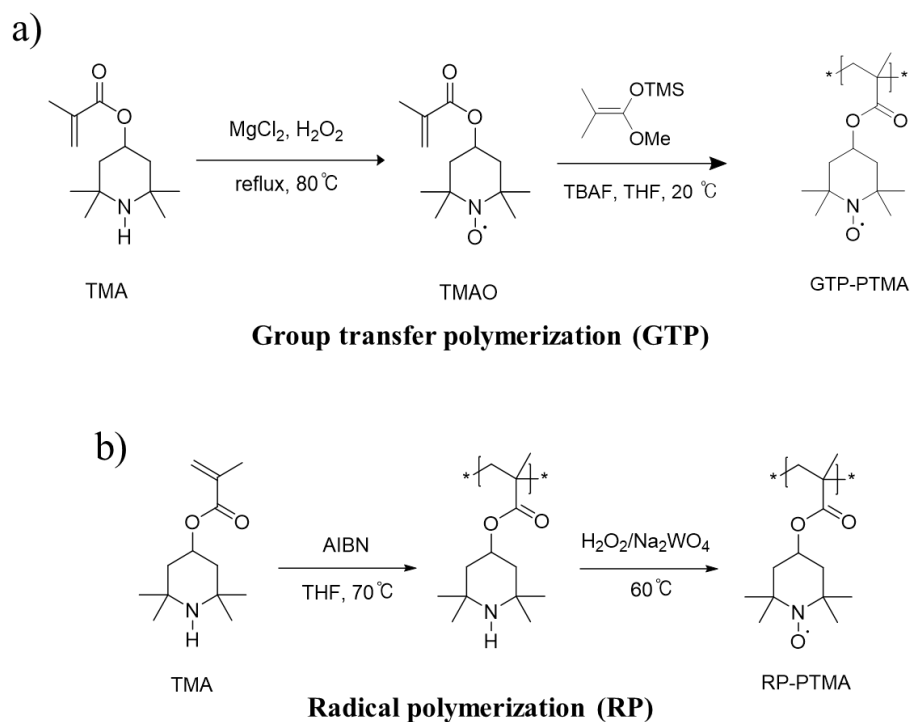


Figure 4.7. Reaction scheme of PTMA synthesis by GTP and RP methods. (a) Reaction scheme of GTP-PTMA synthesized by group transfer polymerization (GTP) after the nitroxyl radical formation. (b) Reaction scheme of RP-PTMA synthesized by radical polymerization (RP) before the nitroxyl radical formation.

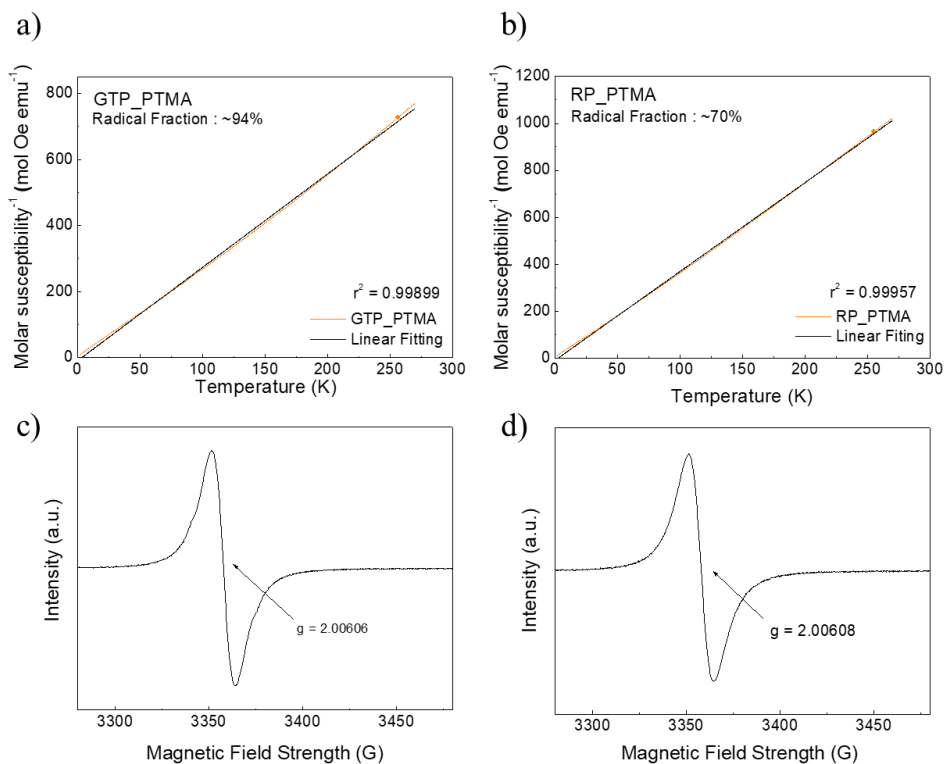


Figure 4.8. SQUID profiles and EPR spectra of the two PTMA polymers. Plots of $\chi_{paramagnetic}^{-1}$ vs. temperature and Curie–Weiss fittings of (a) GTP-PTMA and (b) RP-PTMA. EPR spectra of 10^{-3} M chloroform solution containing (c) GTP-PTMA and (d) RP-PTMA.

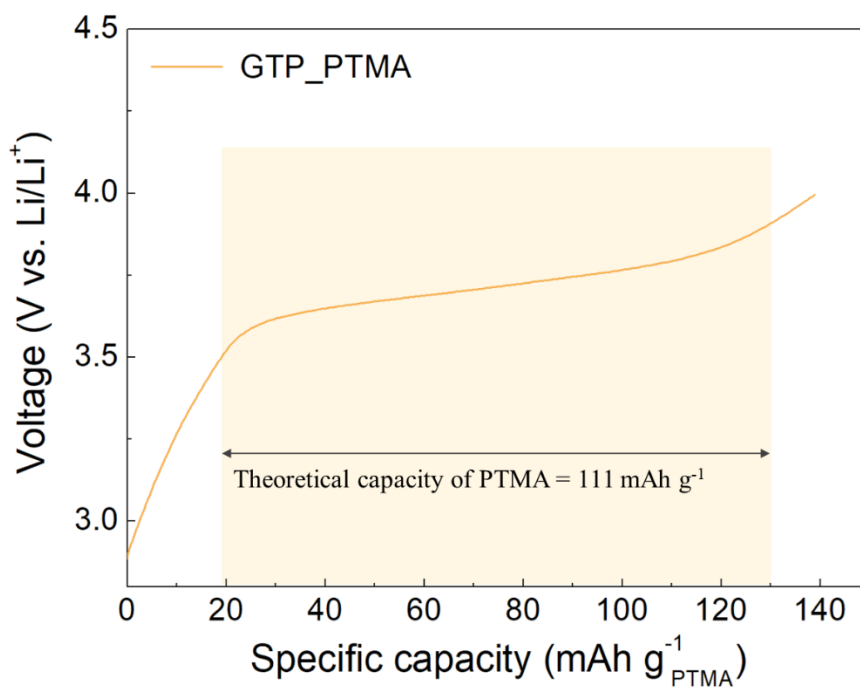


Figure 4.9. Galvanostatic charge profile of PTMA synthesized by GTP method. PTMA synthesized by the GTP method had a clear charge voltage plateau at ~3.6 V (vs. Li/Li⁺) and delivered almost the theoretical specific capacity.

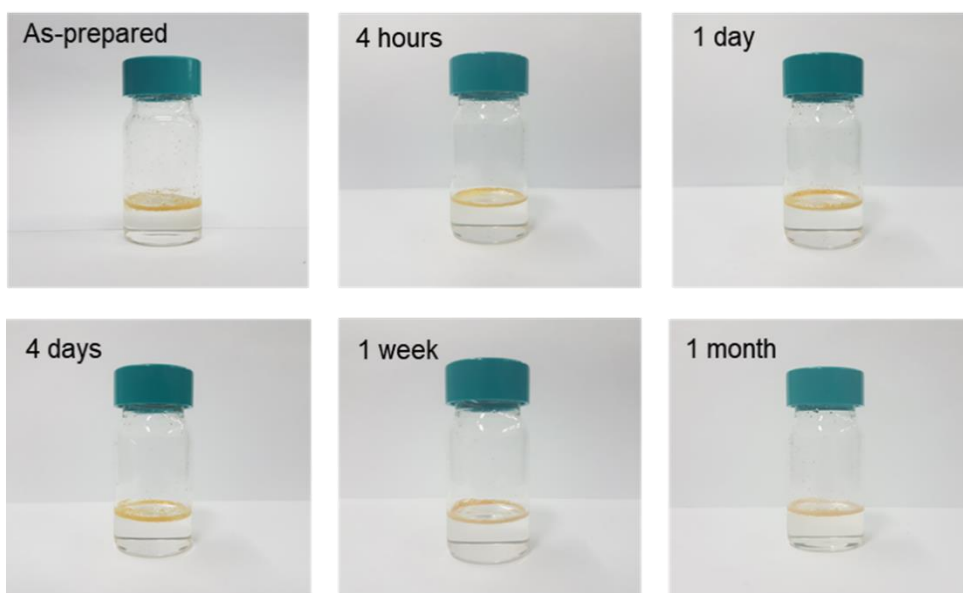


Figure 4.10. Images of PTMA dissolved in electrolyte. The PTMA did not dissolve in 2 M LiTFSI TEGDME until 1 month. The ratio between PTMA and the electrolyte was the same as that in assembled PTMA-loaded lithium–oxygen cells.

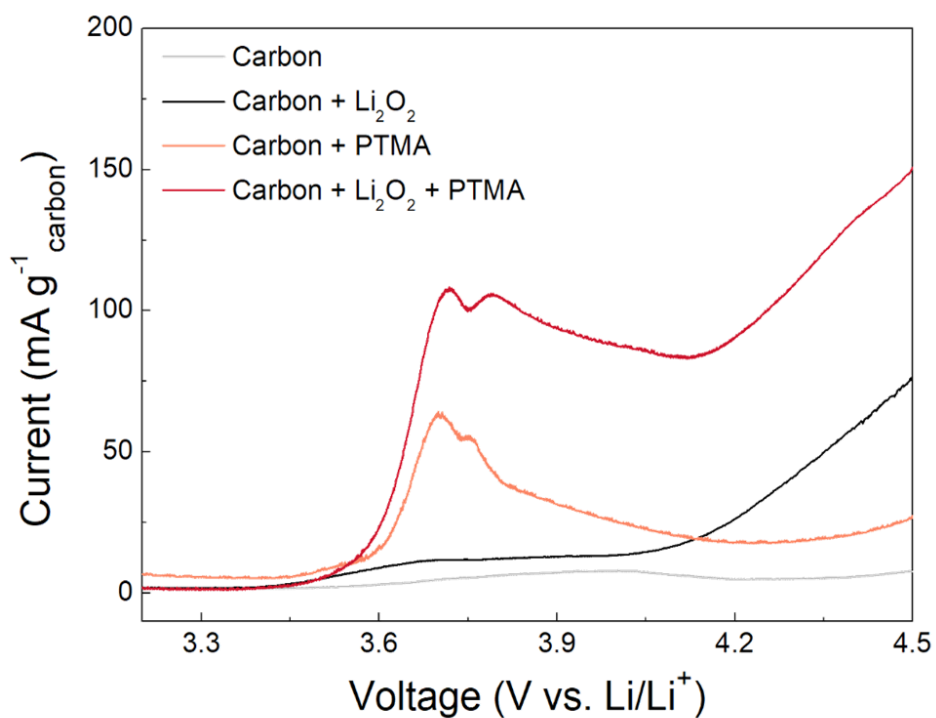


Figure 4.11. Linear sweep voltammetry profiles of electrodes showing that PTMA-mediated Li_2O_2 decomposition occurs.

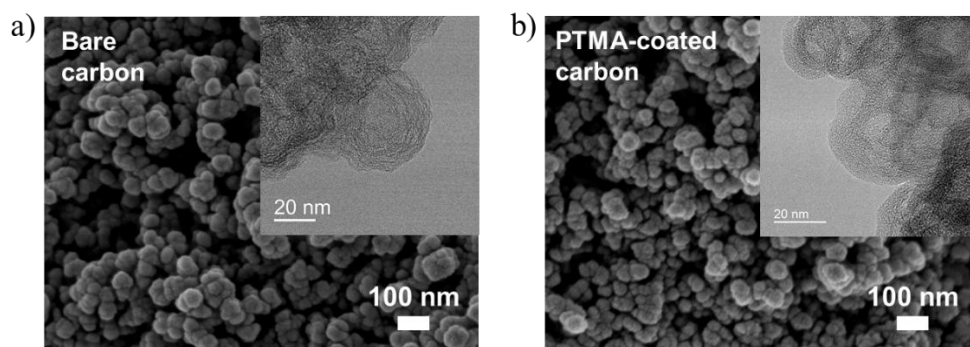


Figure 4.12. SEM images of (a) pristine carbon electrode and (b) electrode after PTMA coating. TEM images of each sample are presented in the insets.

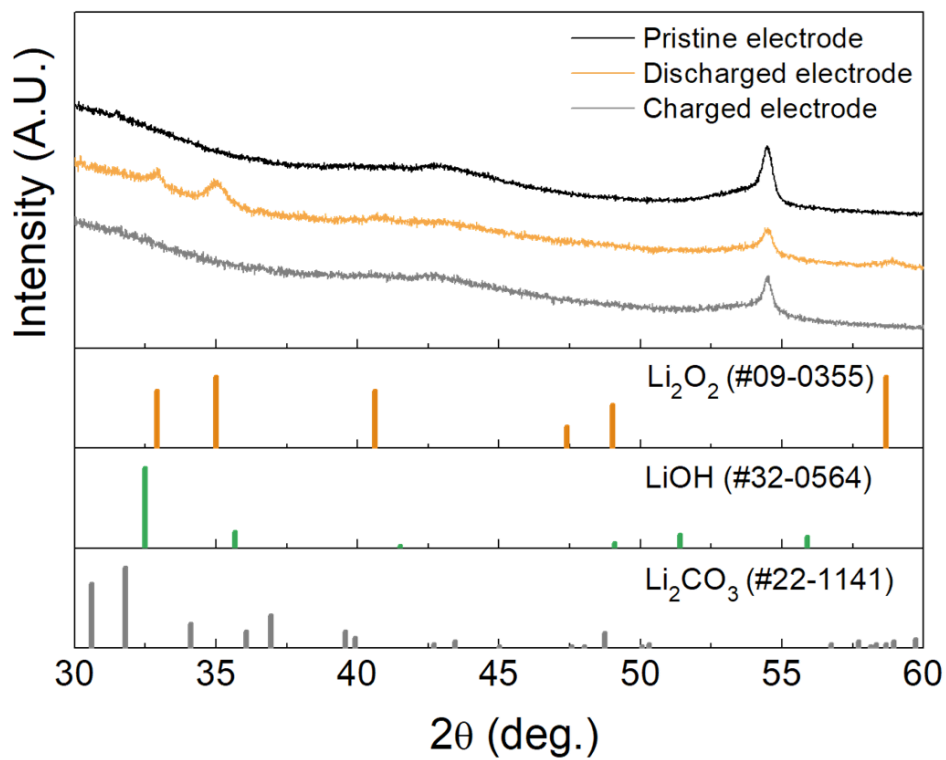


Figure 4.13. X-ray diffraction patterns of pristine, discharged, and charged electrodes using PTMA.

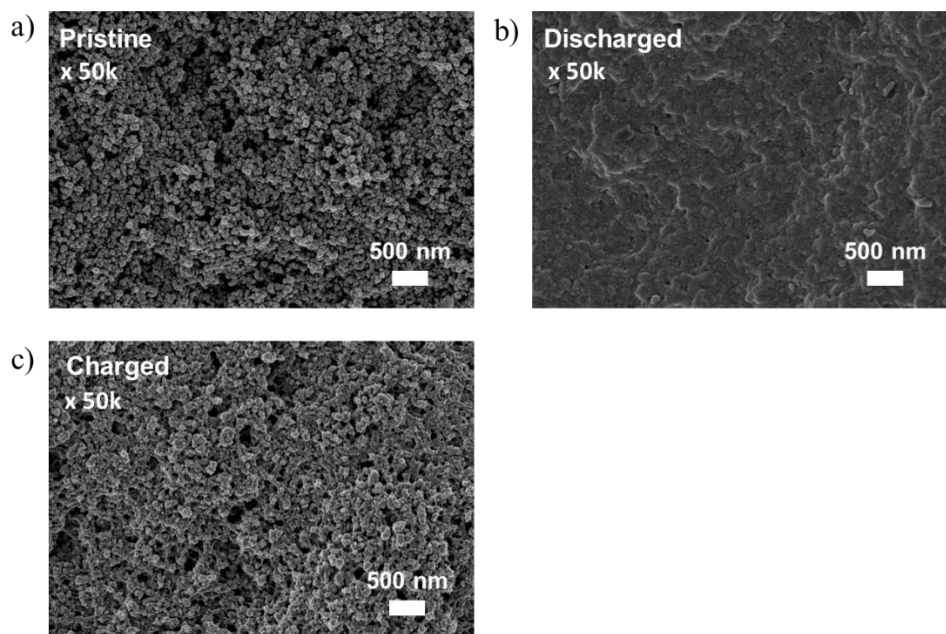


Figure 4.14. SEM images of (a) pristine Ketjen black air electrode and electrode (b) after discharge and (c) after charge.

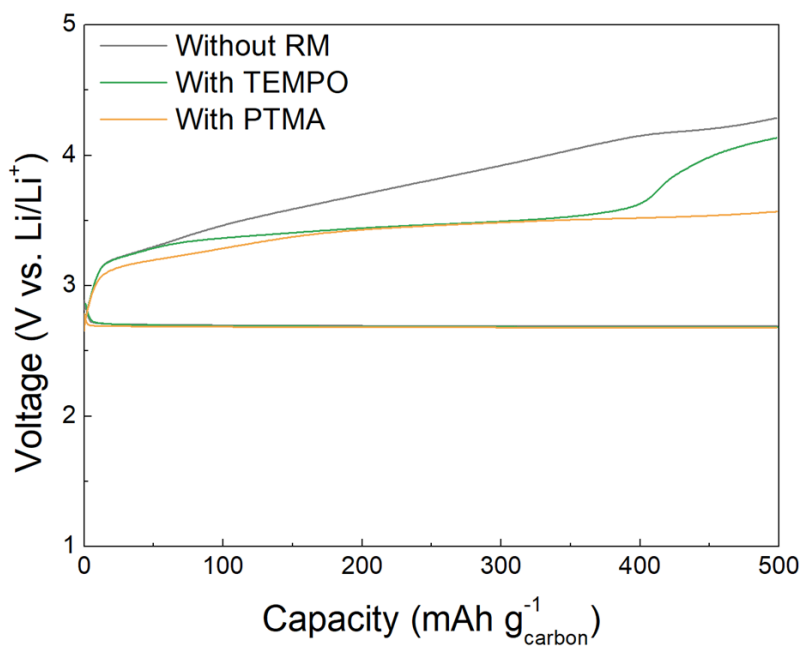


Figure 4.15. Profile of first galvanostatic cycle of PTMA-containing lithium–oxygen cell compared with those without PTMA or TEMPO. The cell was cycled using 2 M LiTFSI TEGDME at a current density of 300 mA g_{carbon}⁻¹.

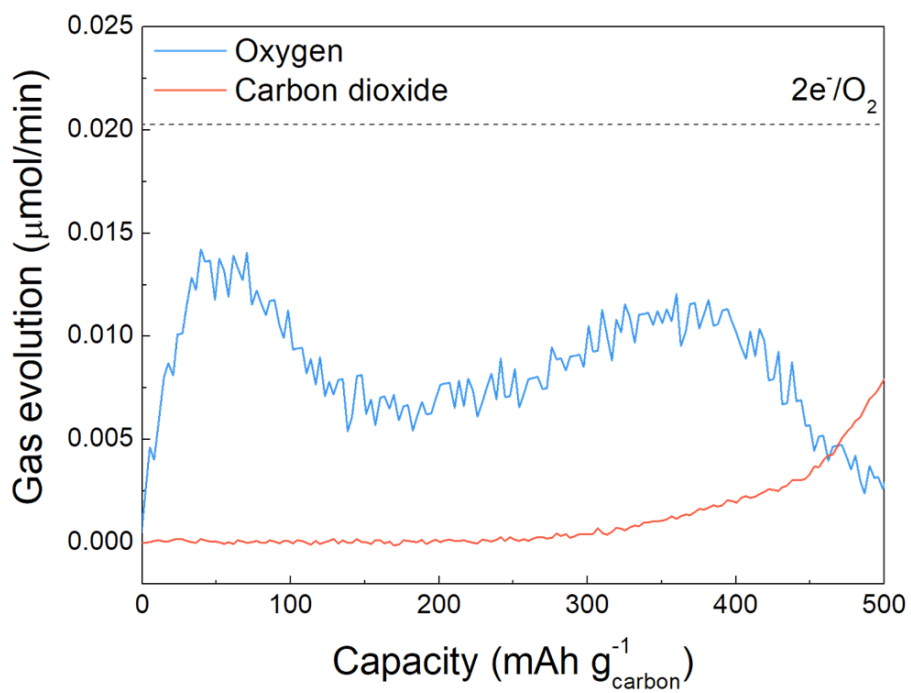


Figure 4.16. Gas evolution profile during the first charging.

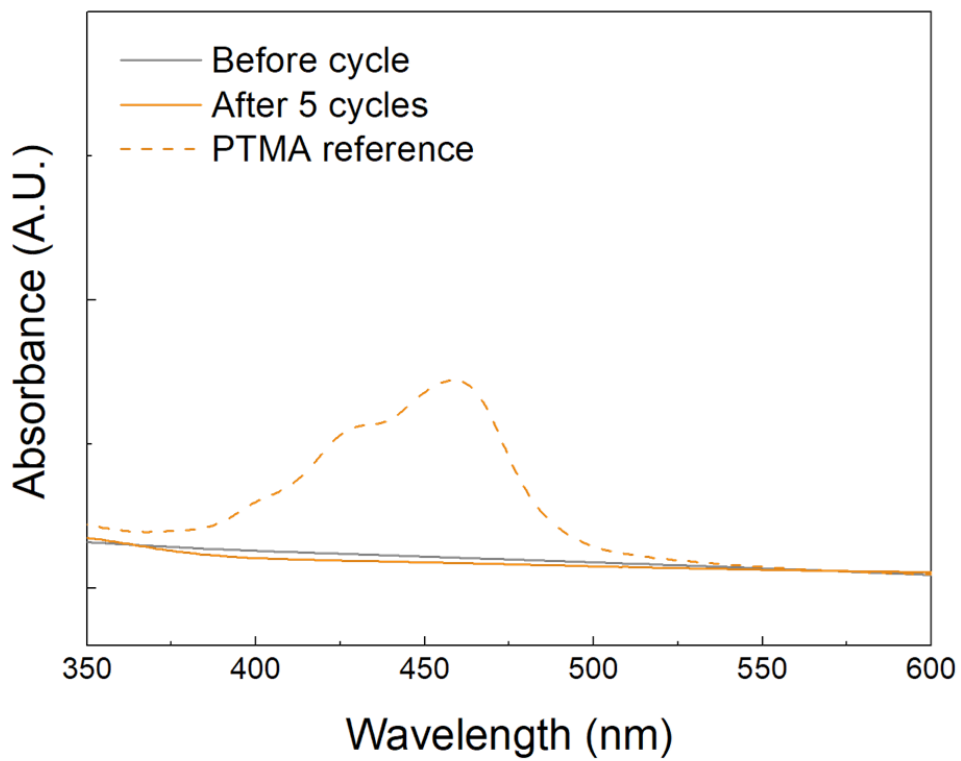


Figure 4.17. UV-vis absorption spectra of electrolyte of PTMA-containing lithium-oxygen cell before and after 5 cycles.

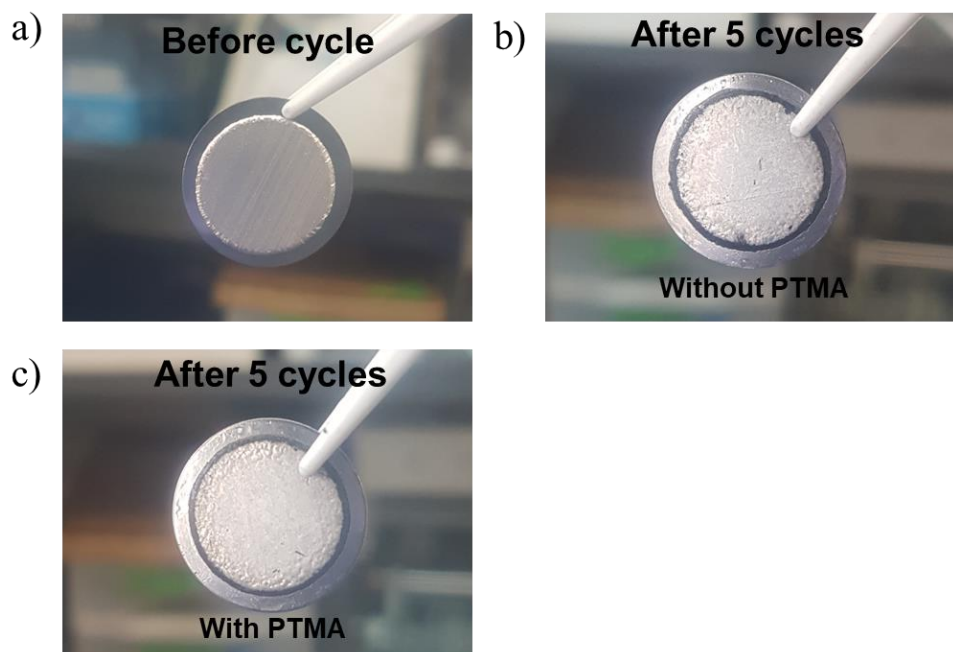


Figure 4.18. Images of (a) pristine lithium metal anode and anode after 5 cycles (b) without and (c) with PTMA.

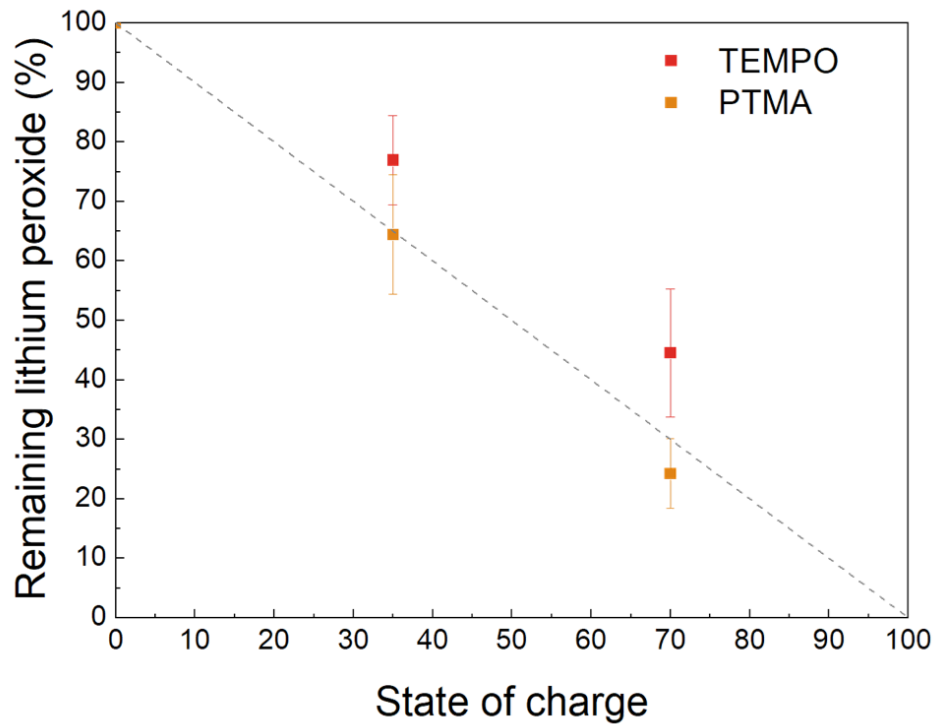


Figure 4.19. Titration result for Li_2O_2 pre-loaded electrode after charging with TEMPO and PTMA. The standard deviation is also displayed.

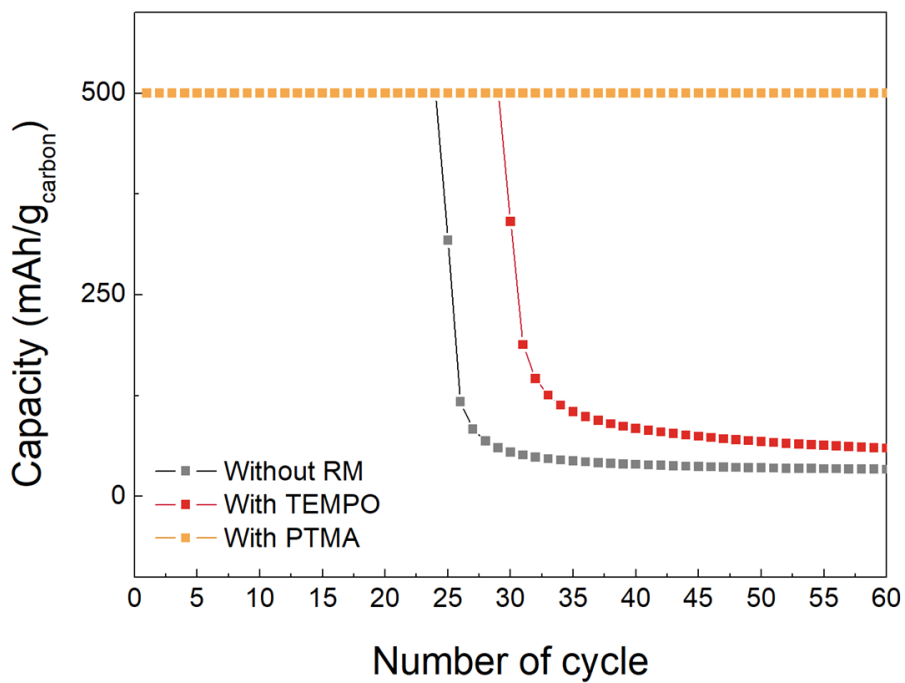


Figure 4.20. Cyclability of RM-free and TEMPO-/PTMA-containing lithium–oxygen cells. All the cells were cycled at a current density of 300 mA g_{carbon}⁻¹.

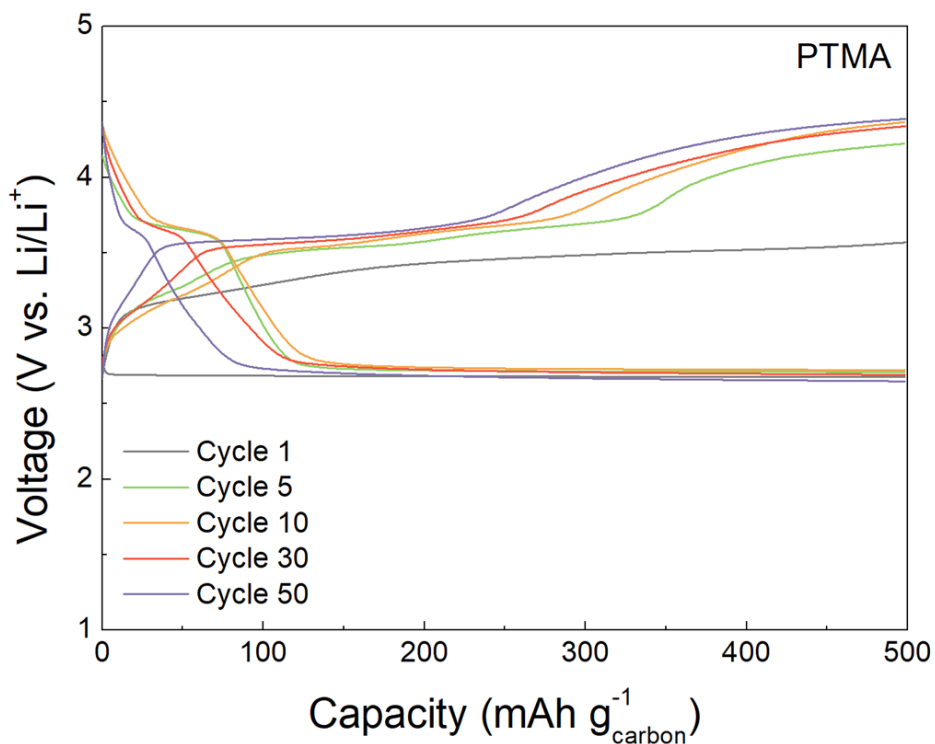


Figure 4.21. Profile of PTMA-containing lithium–oxygen cell showing the sustainable charge voltage plateau from PTMA for more than 50 cycles, which is attributed to the prevention of shuttling.

4.1.4 Supplement note

4.1.4.1 Calculations of Nitroxyl Radical Concentration

To calculate the nitroxyl radical concentration of PTMA, a superconducting quantum interference device (SQUID) was used. The magnetic moment at the specific magnetic field (5000 Oe) was measured by varying the temperature from 2 K to 270 K. Using equation 1, the paramagnetic susceptibility ($\chi_{\text{paramagnetic}}$) of the polymer was determined by eliminating the temperature-independent terms ($\chi_{\text{diamagnetic}}$ and χ_{Pauli}) from the measured total magnetic susceptibility (χ).⁴⁵

$$\chi = \chi_{\text{diamagnetic}} + \chi_{\text{paramagnetic}} + \chi_{\text{Pauli}} \quad \text{Equation 1}$$

The Curie constants of the two polymers were calculated using the Curie–Weiss law by taking the reciprocal of the slope from plots of $\chi_{\text{paramagnetic}}^{-1}$ vs. temperature using the following equation 2:

$$\chi_{\text{paramagnetic}} = \frac{M}{H} = \frac{C}{T} \quad \text{Equation 2}$$

where M is the magnetization (magnetic moment per unit volume), H is the magnetic field, and C is the Curie constant. The calculated Curie constants were 0.353 K emu mol⁻¹ Oe⁻¹ and 0.264 K emu mol⁻¹ Oe⁻¹ for GTP-PTMA and RP-PTMA, respectively.

Then, the Curie constant was defined by the following equation 3:

$$C = \frac{\mu_0 \mu_B^2}{3k_B} N g^2 J(J + 1) \quad \text{Equation 3}$$

where k_B is the Boltzmann constant, N is the number of magnetic molecules per unit volume, g is the Landé g-factor, μ_B is the Bohr magneton, J is the angular momentum

number ($J=1/2$). The g value of the polymers was determined to be 2.00 from the EPR spectra. Finally, the numbers of nitroxyl radicals of the polymers were calculated to be $5.66 \times 10^{23} \text{ mol}^{-1}$ and $4.23 \times 10^{23} \text{ mol}^{-1}$, respectively.⁴⁶

4.1.4.2 Electron diffusion phenomenon in PTMA

Radical polymer refers to the group of polymers that bears robust organic radicals as pendant groups at every repeating unit.⁴⁷ Among them, radical polymers bearing TEMPO group with nitroxyl radical such as PTMA³⁶ and poly(2,2,6,6-tetramethylpiperidineN-oxyl-4-vinyl ether) (PTVE)⁴⁸ are the most representative case. The characteristic feature is the presence of electron (or hole) diffusion in polymer materials by self-exchange following the reaction: $R_{(1)}^+ + R_{(2)}^\cdot \rightarrow R_{(1)}^\cdot +$

$R_{(2)}^+$. (R denotes nitroxyl redox center and \cdot denotes radical species) In case of PTMA, for example, the electron self-exchange rate and the electron diffusion coefficient by self-exchange are in the order of 10^5 - $10^7 \text{ M}^{-1} \text{ s}^{-1}$, and 10^{-8} - $10^{-10} \text{ cm}^2 \text{ s}^{-1}$, respectively.^{29, 47}

4.1.4.3 PTMA as catalysts for lithium–oxygen batteries

To investigate the activity of PTMA in full discharge and charge condition, we conducted the full galvanostatic cycling of PTMA-loaded cell with the voltage cut-off of 2.2 V as shown in figure 4.22.a. While most of lithium-oxygen cells typically fail to cycle sufficiently with the full discharge mode due to many issues, thus the discharge capacity-limit cycling is often employed, we also observed that the performance of the cell becomes inferior with the full discharge mode even using

PTMA. And, the effect of PTMA as catalysts were not pronounced in the full discharge mode as much as the case of the capacity-limit cycling. The low-voltage charge plateau of the characteristic PTMA oxidation was substantially reduced compared with the capacity-limiting cycle case as shown in main figure 4.15. We speculate that the catalytic activity of the PTMA was partly hampered by the full discharge of the cell, which leads to the complete passivation of the carbon electrode surface with the insulating discharge products. On the other hand, when the cycling of the cell was carried out to partly prevent the complete passivation of the electrode, the catalytic activity of the PTMA could be still observed (red line in figure 4.22.a). The figure illustrates that, with a slightly higher voltage cut-off of 2.6 V, the characteristic charge plateau from PTMA redox reappears, indicating the redox mediating role of the PTMA. Despite the reduced activity of the PTMA at the full discharge mode, we could confirm that the stability of the PTMA was not deteriorated even after the full discharge and charge in the following experiment. In figure 4.22.b, when the capacity-limiting cycle test was carried out again at the subsequent cycle after the full discharge/charge mode, the redox mediating activity of the PTMA could be fully recovered. The reappearance of the characteristic PTMA oxidation is clearly observed in the charge process, exhibiting much lowered charge polarization. The profile of PTMA-free cell following the same experiment sequence with 2.2 V cut-off is plotted together as a reference (black line), which supports the catalytic activity of the PTMA. It confirms that the absence of characteristic PTMA oxidation in case of 2.2V-cut cycling is not attributed to the activity loss of the PTMA

catalyst, but to the complete passivation of the carbon electrode, inducing a large increase in the electrode impedance. These series of observations indicate that the reversibility of the lithium-oxygen cells employing PTMA is also strongly dependent on the amount of the discharge products at the end of the discharge, which can be the limitations of PTMA redox mediator. Thus, the rational cycle conditions should be considered in employing PTMA redox mediators for the optimal performance.

4.1.4.4 Degradation mechanism of the lithium–oxygen cell containing PTMA

The charge voltage of the PTMA cell exhibited a positive shift after the fifth cycle, similar to the TEMPO case. We suppose such increase in the charge potential for both PTMA and TEMPO cases, despite the prolonged cycle life of PTMA, could be attributed to the commonly known factors, which have been found to deteriorate the cycle performance of conventional lithium-oxygen batteries. For example, the combination of carbon-based air electrode and ether-based electrolyte for lithium-oxygen cell has been reported to be susceptible to the formation of side product such as Li_2CO_3 , which leads to the yield of Li_2O_2 less than 100 %.^{34, 42, 43, 49} With the repeated cycling, the side product keeps accumulated, which becomes more problematic after cycles. Given that the oxidation potential of Li_2CO_3 is ~ 3.8 V (vs. Li/Li^+),⁵⁰ it is not probable to decompose Li_2CO_3 with redox mediator such as PTMA whose redox potential is lower than 3.8 V (vs. Li/Li^+). Accordingly, electrochemical decomposition of accumulated Li_2CO_3 leads to the enhanced charge voltage higher than 3.8 V (vs. Li/Li^+) even with the presence of PTMA.

4.1.4.5 Abnormal initial discharge plateau

The initial discharge plateau around 3.5 V is attributed to the redox reaction of PTMA in the electrode, which remained oxidized at the end of the previous charging step. When the PTMA is oxidized but could not chemically reduce Li_2O_2 for some reason, the reduction reaction of PTMA itself can take place during the subsequent discharge process. It is supposed that some amount of PTMA remained oxidized after the charge process due to the limited yield of Li_2O_2 during discharge. The discharge product of lithium–oxygen cell often contains byproducts such as Li_2CO_3 resulting from side reactions, reducing the yield of the Li_2O_2 during discharge.^{42, 49} Since the electrochemical oxidation potential of Li_2CO_3 is higher than the intrinsic redox potential of PTMA,⁵⁰ the oxidized PTMA fails to chemically decompose Li_2CO_3 . The substantial amount of byproducts such as Li_2CO_3 in the discharged electrode, thus, would make PTMA remain oxidized. And, the reduction of such PTMA will appear during the subsequent discharge process. It should be noted that, unlike the RM–free cell, which typically involves the charging over ~ 4.0 V (vs. Li/Li^+) and electrochemically decomposes the byproducts, the charging voltage remains under ~ 4.0 V (vs. Li/Li^+) with the cell employing PTMA, leaving the byproducts such as Li_2CO_3 behind. Since RM itself is in the electrochemically oxidized state at this case, it is reduced at the following discharge, resulting in abnormal discharge plateau.⁴⁴ We would like to note that, on the other hand, this abnormal discharge plateau is not frequently observed in the cell employing liquid-type RMs. It is because the oxidized RMs are usually consumed at the lithium anode due to the shuttle effect of RM in the cell. The oxidized RMs in the air-electrode migrate to the anode, making

themselves reduced. Therefore, the electrochemical reduction of RM in the air-electrode, which results in the abnormal discharge plateau, gets typically mitigated in the following discharge.^{44, 51} Nevertheless, this kind of RM reduction in the subsequent discharge reaction was often detected at high current rate tests even in the cell employing liquid-type RMs.^{44, 52} It is because, in the fast charge/discharge conditions, the remaining oxidized RM would not have sufficient time to migrate to the counter electrode, thus practically stationed in the air-electrode, whose reduction reaction appears in the following discharge process. In this regard, we suppose that the presence of abnormal discharge plateau in case of PTMA, as contrast to the TEMPO case, supports the absence of the shuttle effect, as a posteriori. Enhancing the Li_2O_2 yield during the discharge along with the prevention of shuttle effect should be accomplished simultaneously to eliminate this abnormal discharge plateau.

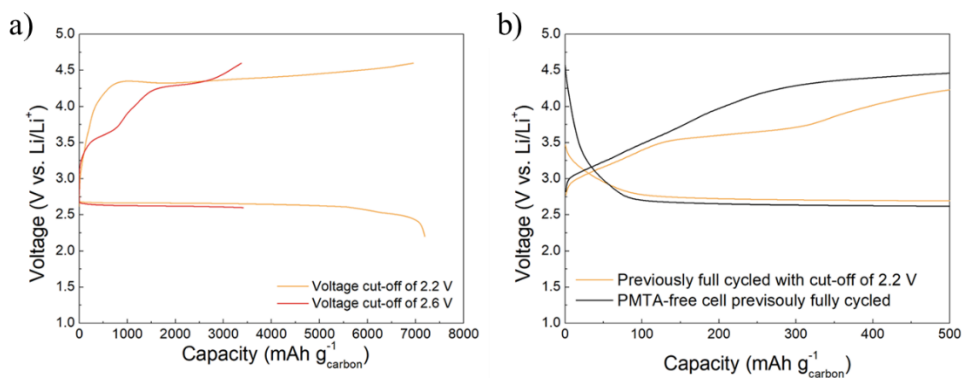


Figure 4.22. (a) Galvanostatic full discharge and charge profile of PTMA-loaded lithium-oxygen cells with voltage cut-off of 2.2 V (orange line) and 2.6 V (red line). (b) Galvanostatic cycling profile with the capacity cut-off of 500 mAh g⁻¹ after experiencing a full cycling with the voltage cut-off of 2.2 V (orange line). For comparisons, the profile of the PTMA-free cell following the same experimental sequence with 2.2 V cut-off is displayed together. (black line)

4.1.5 Concluding remarks

In summary, we successfully decoupled the charge-carrying redox property of RMs and the shuttling phenomenon by introducing a polymer-based RM, PTMA, where the typical charge carrying by mass diffusion in the electrolyte was replaced by charge carrying by electron transfer between polymer chains while retaining the redox-mediating capability. The suppression of shuttling was enabled by anchoring of TEMPO in the form of PTMA at an air electrode with reduced solubility. The stability of lithium metal and the efficiency of RM-assisted Li_2O_2 decomposition were substantially improved by inhibiting the migration of the RMs within the PTMA polymer. Consequently, the sustainable use of RMs was achieved, leading to significantly improved electrochemical performance of the RM-containing lithium-oxygen cell. This study suggests a new pathway for the more effective use of RMs in lithium-oxygen batteries, regulating the transport of the RMs without compensating for their redox-mediating capability.

4.1.6 References

1. Bruce PG, Freunberger SA, Hardwick LJ, Tarascon J-M. Li–O₂ and Li–S batteries with high energy storage. *Nat. Mater.* 2011, **11**: 19.
2. Lim H-D, Lee B, Bae Y, Park H, Ko Y, Kim H, *et al.* Reaction chemistry in rechargeable Li–O₂ batteries. *Chem. Soc. Rev.* 2017, **46**(10): 2873-2888.
3. Ko Y, Park H, Lee B, Bae Y, Park SK, Kang K. A comparative kinetic study of redox mediators for high-power lithium–oxygen batteries. *J. Mater. Chem. A* 2019, **7**(11): 6491-6498.
4. Woo H, Kang J, Kim J, Kim C, Nam S, Park B. Development of carbon-based cathodes for Li-air batteries: Present and future. *Electron. Mater. Lett.* 2016, **12**(5): 551-567.
5. Girishkumar G, McCloskey B, Luntz A, Swanson S, Wilcke W. Lithium–air battery: promise and challenges. *J. Phys. Chem. Lett.* 2010, **1**(14): 2193-2203.
6. Christensen J, Albertus P, Sanchez-Carrera RS, Lohmann T, Kozinsky B, Liedtke R, *et al.* A critical review of Li/air batteries. *J. Electrochem. Soc.* 2011, **159**(2): 1-30.
7. Lu Y-C, Xu Z, Gasteiger HA, Chen S, Hamad-Schifferli K, Shao-Horn Y. Platinum– gold nanoparticles: a highly active bifunctional electrocatalyst for rechargeable lithium– air batteries. *J. Am. Chem. Soc.* 2010, **132**(35): 12170-12171.

8. Lu Y-C, Gasteiger HA, Shao-Horn Y. Catalytic activity trends of oxygen reduction reaction for nonaqueous Li-air batteries. *J. Am. Chem. Soc.* 2011, **133**(47): 19048-19051.
9. Ma S, Wu Y, Wang J, Zhang Y, Zhang Y, Yan X, *et al.* Reversibility of noble metal-catalyzed aprotic Li-O₂ batteries. *Nano Lett.* 2015, **15**(12): 8084-8090.
10. Lim H-D, Song H, Gwon H, Park K-Y, Kim J, Bae Y, *et al.* A new catalyst-embedded hierarchical air electrode for high-performance Li-O₂ batteries. *Energy Environ. Sci.* 2013, **6**(12): 3570-3575.
11. Débart A, Paterson AJ, Bao J, Bruce PG. α -MnO₂ Nanowires: A Catalyst for the O₂ Electrode in Rechargeable Lithium Batteries. *Angew. Chem., Int. Ed.* 2008, **47**(24): 4521-4524.
12. Lee YJ, Kim DH, Kang T-G, Ko Y, Kang K, Lee YJ. Bifunctional MnO₂-Coated Co₃O₄ Hetero-structured Catalysts for Reversible Li-O₂ Batteries. *Chem. Mater.* 2017, **29**(24): 10542-10550.
13. McCloskey BD, Scheffler R, Speidel A, Bethune DS, Shelby RM, Luntz AC. On the efficacy of electrocatalysis in nonaqueous Li-O₂ batteries. *J. Am. Chem. Soc.* 2011, **133**(45): 18038-18041.
14. Chen Y, Freunberger SA, Peng Z, Fontaine O, Bruce PG. Charging a Li-O₂ battery using a redox mediator. *Nat. Chem.* 2013, **5**: 489.
15. Lim H-D, Lee B, Zheng Y, Hong J, Kim J, Gwon H, *et al.* Rational design of redox mediators for advanced Li-O₂ batteries. *Nat. Energy* 2016, **1**:

16066.

16. Ko Y, Park H, Kim B, Kim JS, Kang K. Redox Mediators: A Solution for Advanced Lithium–Oxygen Batteries. *Trends Chem.* 2019, **1**: 349-360.
17. Bergner BJ, Schürmann A, Pepler K, Garsuch A, Janek J. TEMPO: A Mobile Catalyst for Rechargeable Li-O₂ Batteries. *J. Am. Chem. Soc.* 2014, **136**(42): 15054-15064.
18. Ko Y, Park H, Kim J, Lim HD, Lee B, Kwon G, *et al.* Biological Redox Mediation in Electron Transport Chain of Bacteria for Oxygen Reduction Reaction Catalysts in Lithium–Oxygen Batteries. *Adv. Funct. Mater.* 2019, **29**(5): 1805623.
19. Park H, Lim H-D, Lim H-K, Seong WM, Moon S, Ko Y, *et al.* High-efficiency and high-power rechargeable lithium–sulfur dioxide batteries exploiting conventional carbonate-based electrolytes. *Nat. Commun.* 2017, **8**: 14989.
20. Lim HD, Song H, Kim J, Gwon H, Bae Y, Park KY, *et al.* Superior rechargeability and efficiency of lithium–oxygen batteries: hierarchical air electrode architecture combined with a soluble catalyst. *Angew. Chem., Int. Ed.* 2014, **53**(15): 3926-3931.
21. Kwak W-J, Hirshberg D, Sharon D, Afri M, Frimer AA, Jung H-G, *et al.* Li–O₂ cells with LiBr as an electrolyte and a redox mediator. *Energy Environ. Sci.* 2016, **9**(7): 2334-2345.

22. Zhang J, Sun B, Zhao Y, Kretschmer K, Wang G. Modified Tetrathiafulvalene as an Organic Conductor for Improving Performances of Li–O₂ Batteries. *Angew. Chem., Int. Ed.* 2017, **56**(29): 8505-8509.
23. Fang R, Zhao S, Sun Z, Wang DW, Cheng HM, Li F. More reliable lithium-sulfur batteries: status, solutions and prospects. *Adv. Mater.* 2017, **29**(48): 1606823.
24. Lee DJ, Lee H, Kim Y-J, Park J-K, Kim H-T. Sustainable Redox Mediation for Lithium–Oxygen Batteries by a Composite Protective Layer on the Lithium-Metal Anode. *Adv. Mater.* 2015, **28**(5): 857-863.
25. Bergner BJ, Busche MR, Pinedo R, Berkes BB, Schröder D, Janek J. How To Improve Capacity and Cycling Stability for Next Generation Li–O₂ Batteries: Approach with a Solid Electrolyte and Elevated Redox Mediator Concentrations. *ACS Appl. Mater. Interfaces* 2016, **8**(12): 7756-7765.
26. Qiao Y, He Y, Wu S, Jiang K, Li X, Guo S, *et al.* MOF-Based Separator in an Li–O₂ Battery: An Effective Strategy to Restrain the Shuttling of Dual Redox Mediators. *ACS Energy Lett.* 2018, **3**(2): 463-468.
27. Gao X, Chen Y, Johnson LR, Jovanov ZP, Bruce PG. A rechargeable lithium–oxygen battery with dual mediators stabilizing the carbon cathode. *Nat. Energy* 2017, **2**(9): 17118.
28. Kentaro N, Kenichi O, Hiroyuki N. Organic Radical Battery Approaching Practical Use. *Chem. Lett.* 2011, **40**(3): 222-227.
29. Wang S, Li F, Easley AD, Lutkenhaus JL. Real-time insight into the

- doping mechanism of redox-active organic radical polymers. *Nat. Mater.* 2019, **18**(1): 69.
30. Bugnon L, Morton CJ, Novak P, Vetter J, Nesvadba P. Synthesis of poly (4-methacryloyloxy-TEMPO) via group-transfer polymerization and its evaluation in organic radical battery. *Chem. Mater.* 2007, **19**(11): 2910-2914.
 31. Kurosaki T, Lee KW, Okawara M. Polymers having stable radicals. I. Synthesis of nitroxyl polymers from 4-methacryloyl derivatives of 2, 2, 6, 6-tetramethylpiperidine. *J. Polym. Sci., Part A: Polym. Chem.* 1972, **10**(11): 3295-3310.
 32. Guo W, Yin Y-X, Xin S, Guo Y-G, Wan L-J. Superior radical polymer cathode material with a two-electron process redox reaction promoted by graphene. *Energy Environ. Sci.* 2012, **5**(1): 5221-5225.
 33. Zhang J, Sun B, Xie X, Zhao Y, Wang G. A Bifunctional Organic Redox Catalyst for Rechargeable Lithium–Oxygen Batteries with Enhanced Performances. *Adv. Sci.* 2016, **3**(4): 1500285.
 34. McCloskey BD, Valery A, Luntz AC, Gowda SR, Wallraff GM, Garcia JM, *et al.* Combining accurate O₂ and Li₂O₂ assays to separate discharge and charge stability limitations in nonaqueous Li–O₂ batteries. *J. Phys. Chem. Lett.* 2013, **4**(17): 2989-2993.
 35. Yin W, Grimaud A, Azcarate I, Yang C, Tarascon J-M. Electrochemical Reduction of CO₂ Mediated by Quinone Derivatives: Implication for Li–

- CO₂ Battery. *J. Phys. Chem. C* 2018, **122**(12): 6546-6554.
36. Bugnon L, Morton CJH, Novak P, Vetter J, Nesvadba P. Synthesis of Poly(4-methacryloyloxy-TEMPO) via Group-Transfer Polymerization and Its Evaluation in Organic Radical Battery. *Chem. Mater.* 2007, **19**(11): 2910-2914.
37. Nakahara K, Iwasa S, Satoh M, Morioka Y, Iriyama J, Suguro M, *et al.* Rechargeable batteries with organic radical cathodes. *Chem. Phys. Lett.* 2002, **359**(5): 351-354.
38. Wong RA, Yang C, Dutta A, O M, Hong M, Thomas ML, *et al.* Critically examining the role of nanocatalysts in Li–O₂ batteries: viability toward suppression of recharge overpotential, rechargeability, and cyclability. *ACS Energy Lett.* 2018, **3**(3): 592-597.
39. Bae Y, Ko DH, Lee S, Lim HD, Kim YJ, Shim HS, *et al.* Enhanced stability of coated carbon electrode for Li-O₂ batteries and its limitations. *Adv. Energy Mater.* 2018, **8**(16): 1702661.
40. Bae Y, Yun YS, Lim H-D, Lee H, Kim Y-J, Kim J, *et al.* Tuning the carbon crystallinity for highly stable Li–O₂ batteries. *Chem. Mater.* 2016, **28**(22): 8160-8169.
41. Freunberger SA, Chen Y, Drewett NE, Hardwick LJ, Bardé F, Bruce PG. The Lithium–Oxygen Battery with Ether-Based Electrolytes. *Angew. Chem., Int. Ed.* 2011, **50**(37): 8609-8613.
42. McCloskey B, Speidel A, Scheffler R, Miller D, Viswanathan V,

- Hummelshøj J, *et al.* Twin problems of interfacial carbonate formation in nonaqueous Li–O₂ batteries. *J. Phys. Chem. Lett.* 2012, **3**(8): 997-1001.
43. Ottakam Thotiyl MM, Freunberger SA, Peng Z, Bruce PG. The carbon electrode in nonaqueous Li–O₂ cells. *J. Am. Chem. Soc.* 2012, **135**(1): 494-500.
44. Wu S, Qiao Y, Deng H, He Y, Zhou H. Minimizing the Abnormal High-Potential Discharge Process Related to Redox Mediators in Lithium–Oxygen Batteries. *J. Phys. Chem. Lett.* 2018, **9**(23): 6761-6766.
45. Kahn O. Molecular magnetism. *VCH Publishers, Inc.(USA), 1993* 1993: 393.
46. Nishide H, Iwasa S, Pu Y-J, Suga T, Nakahara K, Satoh M. Organic radical battery: nitroxide polymers as a cathode-active material. *Electrochim. Acta* 2004, **50**(2-3): 827-831.
47. Oyaizu K, Nishide H. Radical polymers for organic electronic devices: a radical departure from conjugated polymers? *Adv. Mater.* 2009, **21**(22): 2339-2344.
48. Suguro M, Iwasa S, Kusachi Y, Morioka Y, Nakahara K. Cationic Polymerization of Poly (vinyl ether) Bearing a TEMPO Radical: A New Cathode-Active Material for Organic Radical Batteries. *Macromol. Rapid Commun.* 2007, **28**(18-19): 1929-1933.
49. Freunberger SA, Chen Y, Drewett NE, Hardwick LJ, Bardé F, Bruce PG. The lithium–oxygen battery with ether-based electrolytes. *Angew. Chem.,*

- Int. Ed.* 2011, **50**(37): 8609-8613.
50. Mahne N, Renfrew SE, McCloskey BD, Freunberger SA. Electrochemical oxidation of lithium carbonate generates singlet oxygen. *Angew. Chem., Int. Ed.* 2018, **57**(19): 5529-5533.
51. Bergner BJ, Busche MR, Pinedo R, Berkes BzB, Schröder D, Janek Jr. How to improve capacity and cycling stability for next generation Li–O₂ batteries: approach with a solid electrolyte and elevated redox mediator concentrations. *ACS Appl. Mater. Interfaces* 2016, **8**(12): 7756-7765.
52. Kwak W-J, Hirshberg D, Sharon D, Shin H-J, Afri M, Park J-B, *et al.* Understanding the behavior of Li–oxygen cells containing LiI. *J. Mater. Chem. A* 2015, **3**(16): 8855-8864

4.2 Janus liquid electrolyte for shuttle-free redox mediation in lithium-oxygen batteries

4.2.1 Research Background

Electrolytes are one of the essential components of electrochemical energy storage systems, providing ion-conduction paths to support the electrochemical reduction and oxidation in electrodes.^{1,2} For the stable operation of an electrochemical cell, in addition to high ionic conductivity, electrolytes must also satisfy requirements such as electrochemical stability over a wide voltage window and chemical stability with electrode materials. The conventional electrolyte system most widely adopted to date was optimized for performance and safety for lithium-ion batteries (LIBs) with respect to its compatibility with a graphite anode and lithium transition-metal oxide cathode.²⁻⁷ Slight modification of the electrolyte system is often made when implementing new electrode materials in LIBs; however, the overall change has not been notable. However, the emergence of post-LIB chemistries including lithium–oxygen, lithium–sulfur, and organic-based batteries has resulted in a variety of anode and cathode electrochemical reactions, which are often incompatible with the conventional electrolyte, necessitating the development of a new electrolyte system.⁸⁻¹⁰ Although substantial efforts have been devoted to the search for a reliable electrolyte for these batteries, it has been challenging to identify an electrolyte that can simultaneously optimize the performance of both the anode (*e.g.*, compatibility with lithium metal) and the cathode (*e.g.*, stability with oxygen radicals for lithium–oxygen batteries or polysulfides for lithium–sulfur batteries), each of which requires

distinct electrolyte properties.^{11, 12}

Some of the promising post-LIB chemistries rely on an electrochemical reaction involving soluble redox species during the cell operation. In advanced lithium–oxygen battery systems, these species include oxygen radicals, lithium superoxides produced at the cathode, and/or redox mediators (RMs) that catalyze the charge process of the cathode.^{11, 13-17} Although these soluble redox species are indispensable in the electrochemical reaction, they may cause severe side reactions when migrating to the counter electrode, leading to rapid cycle degradation.^{13, 18-20} This phenomenon, known as the shuttle effect, is also commonly observed in other post-LIB systems such as lithium–sulfur and organic batteries.^{10, 21-23} Various attempts have been made to employ physical barriers in the cell to inhibit this migration^{18, 19, 24-26}; however, the complete blockage of this migration is not feasible while maintaining high lithium ionic transport. As an alternative solution, hybrid electrolytes with a bi-layer^{27, 28} (solid/solid²⁹ or solid/liquid) or tri-layer^{11, 12, 19, 28, 30} (liquid/solid/liquid) structure have been exploited, whose solid compartments physically block the migration of the soluble species. Nevertheless, the use of a rigid solid electrolyte generally results in undesired increases in the cell resistance, weight, and processing cost.²⁷

Herein, we report a novel all-liquid-based hybrid electrolyte, a so-called Janus liquid electrolyte, and employ it as a versatile electrolyte system in redox-mediated lithium–oxygen batteries. The Janus liquid electrolyte consists of two different liquid phases separated by an immiscibility-driven liquid/liquid interface, where one liquid phase serves as the electrolyte for the anode and the other serves as the electrolyte

for the cathode. Thus, in principle, the specific requirements of the electrolyte for the lithium-metal anode and air cathode can be decoupled by selecting two different liquid phases in the Janus electrolyte. Moreover, by taking advantage of the different solubility properties of specific target species in two different media, crossover issues and shuttle effects can be potentially resolved in a Janus liquid electrolyte. In this work, as a model electrolyte system for a lithium–oxygen cell, dimethylsulfoxide (DMSO) and tetraethylene glycol dimethyl ether (TEGDME) were selected as the base electrolytes for the cathode and anode, respectively, and we demonstrate that lithium–oxygen batteries employing our Janus liquid electrolyte can effectively confine RM^+ within the cathode side of the liquid electrolyte without the use of a solid compartment, as verified by *in-situ* analysis of the lithium–oxygen cell. Consequently, the shuttle effect of the RM was successfully suppressed, thereby improving the stability and reversibility of the redox-mediated lithium–oxygen cell. It is our belief that this new approach exploiting a Janus liquid would make identification of optimal electrolyte systems more viable and rejuvenate the development of lithium–oxygen batteries.

4.2.2 Experimental Method

4.2.2.1 Materials preparation

Lithium bis(trifluoromethane)sulfonimide (99.95% trace metals basis) was purchased from Sigma-Aldrich and dried under vacuum at 150 °C for at least 3 days. Dimethylsulfoxide (DMSO; anhydrous, $\geq 99.9\%$) was purchased from Sigma-Aldrich and used as received. Dimethoxyethane (DME; anhydrous, 99.5%) and tetraethylene glycol dimethyl ether (TEGDME) were purchased from Sigma-Aldrich and dried using a molecular sieve (type 3 Å, Sigma Aldrich) for more than 24 h. Lithium iodide (anhydrous, beads, -10 mesh, 99.999% trace metals basis) was purchased from Sigma-Aldrich and used as received. Ethoxylated trimethylolpropane triacrylate (ETPTA) and diphenyl (2,4,6-trimethylbenzoyl)-phosphine oxide (TPO) were purchased from Sigma-Aldrich and used as received. The electrolyte was prepared by dissolving the targeted amounts of lithium bis(trifluoromethane)sulfonamide and lithium iodide in prepared organic solvents. The final water content of the electrolytes was measured to be less than 50 ppm by Karl Fischer titration. The slurry for the air electrode was prepared by mixing 0.08 g of Ketjen black and 0.02 g of poly(tetrafluoroethylene) binder in 2400 μl of N-methylpyrrolidone and 1600 μl of isopropanol. The air electrode was fabricated by coating the slurry on carbon paper (TGPH030, Toray) and drying under vacuum. To fabricate the gel-state electrolytes, the liquid electrolyte (2.3 M LiTFSI in TEGDME or 1 M LiTFSI in DMSO with 50 mM LiI) was mixed with UV-curable ETPTA monomer (incorporating 1 wt% TPO as a photoinitiator). The composition ratio of

the liquid electrolyte/ETPTA was set as 85/15 (w/w). The electrolyte/monomer mixture was cast onto a lithium metal anode and then exposed to UV irradiation (Hg UV-lamp, Lichtzen) with an irradiation peak intensity of approximately 2000 mW cm⁻², yielding the gel-state electrolyte on the lithium-metal anode.

4.2.2.2 Cell assembly and conditions for electrochemical test

Lithium metal with a thickness of 300 μm was used as the anode. A sheet of glass fiber (GF/F, Whatman) was used as the separator. Ketjen-black-coated carbon paper was used as the cathode. All the cell components (the lithium metal anode, separator, and air electrode) were assembled in a 2032 coin cell to construct a lithium–oxygen cell with 85 μl of electrolyte. The assembly was performed in an Ar-filled glove box (H₂O level < 0.5 ppm and O₂ level < 0.5 ppm), followed by storage of the cell in a cell container with a gas chamber. The air inside the gas chamber was changed from Ar to pure O₂ gas, and the cell was operated in a closed environment. A three-electrode transparent-beaker cell was constructed using Au, nickel foam, and a Ag/Ag⁺ electrode as the working, counter, and reference electrode, respectively. The surface of the Au electrode was polished using alumina powder before use. Operation of the lithium–oxygen cell and three-electrode beaker cell was performed using a potentiogalvanostat (WonA Tech, WBCS 3000, Korea). The cycling of the lithium–oxygen cell was conducted under galvanostatic condition with voltage and capacity cut-offs. The operation of the beaker cell was conducted under potentiostatic condition. For the Li/Cu cell employing the 20-μm thin lithium metal electrode, 1 M LiTFSI in DME/1,3-dioxolane with 2 wt% lithium nitrate was used as the electrolyte

to promote stable lithium stripping and deposition. All the electrochemical tests were performed at room temperature.

4.2.2.3 Characterization

For analysis of the cell components after cycling, the cell was disassembled in an Ar-filled glove box. The cell components were washed with pure organic solvent of the used electrolyte before analysis except for the quantitative analysis of Li_2O_2 using the iodometry titration method. Field-emission scanning electron microscopy (FE-SEM; SUPRA 55VP, Carl Zeiss, Germany) was used to examine the morphology of the electrodes. X-ray diffraction (D2 Phaser, Bruker, Germany) was used to identify the discharge product. To analyze the mutual immiscibility of the Janus liquid electrolyte, ^1H NMR spectra were recorded on a 400-MHz AVANCE III HD instrument (Bruker) in CD_3OD (selected as a reference), and Raman spectra were collected using an Alpha 300R (WITec) with a 532-nm laser. The UV-curing reaction of the gel-state electrolyte was examined using a Fourier-transform infrared spectrometer (FT-IR, Alpha Platinum ATR (Bruker)). Quantification of the amount of Li_2O_2 in the air electrode was performed using the iodometry titration method. *In-situ* gas evolution analysis during charge was conducted using a mass spectrometer (HPR-20, Hiden Analytical, UK) connected to a potentiostat-galvanostat (WonA Tech, WBCS 3000, Korea).

4.2.3 Results and Discussions

4.2.3.1 Design and preparation of Janus liquid electrolyte

In the design of a Janus liquid electrolyte for lithium–oxygen batteries, we selected DMSO and TEGDME as the base-electrolyte solvents because they are known to be the most stable for lithium–oxygen chemistry among reported electrolytes and have thus been widely used.^{14, 31-33} TEGDME was selected for the anode side, as it was previously demonstrated to be stable with lithium-metal anodes in lithium–oxygen cells.³³⁻³⁵ DMSO was selected for the cathode side because of its relative stability for the oxygen electrochemistry^{14, 31, 32} Making these two solvents immiscible and dissolving lithium salts in each solvent were prerequisites for the Janus liquid electrolyte. However, the conventional TEGDME-based electrolyte containing 1 M LiTFSI is completely miscible with DMSO of the same salt concentration, as shown in figure 4.23 (left). Thus, we attempted to make them immiscible by maximizing the difference in the solubility parameters between the two base electrolytes, which governs the miscibility; this was achieved by systematically altering the ion–dipole interaction between the lithium ions and solvent molecules in the TEGDME electrolyte by adjusting the salt concentrations.^{34, 36} From this systematic search, we determined that the conventional 1 M LiTFSI DMSO (hereinafter, DMSO-EL) was mutually immiscible with 2.3 M LiTFSI TEGDME (hereinafter, TEGDME-EL). figure 4.23 (right) clearly illustrates the immiscibility of DMSO-EL and TEGDME-EL, with the two electrolytes (1:1 volume ratio) coexisting in a vial with a sharp interface. The immiscibility of the Janus liquid electrolyte was more clearly verified

by analyzing the chemical structures of the top and bottom phases in the vial. The ^1H nuclear magnetic resonance (NMR) spectra in figure 4.24.a display the characteristic peaks of DMSO³⁷ exclusively for the top phase, whereas those of TEGDME³⁸ appear only for the bottom phase. Raman spectra in figure 4.24.b also confirmed the phase separation of DMSO and TEGDME in the Janus liquid electrolyte. The C–S stretching modes (671 and 701 cm^{-1}), which are characteristics of DMSO,^{39,40} were exclusively observed for the top phase, whereas CH_2 rocking/C–O–C stretching modes at 870 cm^{-1} corresponding to TEGDME were only observed for the bottom phase.^{41,42}

Because one of the goals in using the Janus liquid electrolyte was to inhibit the shuttle effect of RM^+ in the redox-mediated lithium–oxygen cell, the exclusive dissolution/confinement of RM^+ on one side of the electrolyte, *i.e.*, the cathode-side electrolyte, was also required. We speculated that this arrangement could be potentially achieved by maximizing the solvation preference of RM^+ in the cathode-side electrolyte in the Janus system. The dissolution property of RM^+ in a media can be determined by its solvation free energy, which is related to the dielectric constant (ϵ) of a solvent by the Born equation:⁴³

$$\Delta G = -\frac{N_A z^2 e^2}{8\pi\epsilon_0 r_0} \left(1 - \frac{1}{\epsilon_r}\right) \quad \text{Born equation}$$

where ΔG is the Gibbs free energy of solvation of the ion, N_A is Avogadro's constant, z is the charge of the ion, e is the elementary charge, ϵ_0 is the permittivity of free space, r_0 is the effective radius of the ion, and ϵ_r is the dielectric constant of the solvent. This equation indicates that the preference for RM^+

dissolution in a Janus electrolyte can be primarily regulated by modifying the difference in the dielectric constants of the two media, with a solvent with higher ϵ_r resulting in stronger solvation of RM^+ owing to its more negative solvation free energy. The equation also implies that de-solvation of RM^+ in a more solvating medium and re-solvation in a less solvating medium are likely to be energetically unfavorable. Because DMSO is expected to be a more solvating medium with a higher ϵ (46.7) than TEGDME ($\epsilon=7.8$), the potential cross-over of RM^+ from DMSO to TEGDME in the Janus electrolyte would be subsequently suppressed, restricting the shuttle effect. As a proof of concept, we employed LiI as an RM^{44-47} , dissolved it selectively in the cathode-side electrolyte, *i.e.*, DMSO-EL, and monitored its diffusion over time. Figure 4.25 (left image) shows that the DMSO-EL/TEGDME-EL Janus electrolyte successfully confined the oxidized RM (16.7 mM I_3^-) within the DMSO-EL phase without any apparent cross-diffusion toward the TEGDME-EL phase. In contrast, a control electrolyte system of 1 M LiTFSI in TEGDME and DMSO resulted in homogeneous dissolution of I_3^- (figure 4.25 (right image)), thus failing to confine the RM.

The capability of the Janus liquid electrolyte to confine the RM/RM^+ was further confirmed by *in-situ* observation of the electrochemical cell. A three-electrode transparent-beaker cell was constructed to enable visualization of the cross-over behavior of I_3^- , as shown in figure 4.26.a. Gold and nickel foam were used as the working and counter electrodes, respectively. The working electrode was positioned at the cathode side of the Janus liquid electrolyte to mimic the I^- oxidation (50 mM)

occurring at the air electrode in a lithium–oxygen cell. For comparison, a similar beaker cell was also constructed with a single-phase electrolyte (1 M LiTFSI in DMSO) with 50 mM LiI dissolved. The generation of the oxidized species and its diffusion behavior were monitored while continuously oxidizing I^- at the working electrode under constant-voltage condition. Figure 4.26.b shows the time-dependent diffusion behavior of the oxidized I^- (brown color). For the single-phase electrolyte, the oxidized I^- began to diffuse from the start of oxidation because of the concentration gradient. After 120 min, it diffused to all the areas of the electrolyte in the beaker cell, which turned yellow. In contrast, the migration of the oxidized I^- was successfully regulated in the Janus liquid electrolyte. Figure 4.26.b shows that the brown I^{3-} ions were continuously produced upon electrochemical oxidation, diffusing out of the working electrode. However, they were remarkably confined to the cathode-side electrolyte, not diffusing toward the anode-side electrolyte. The magnified image in figure 4.26 clearly demonstrates that the brown RM^+ ions did not cross the sharp interface between the two media in the Janus electrolyte system, with the anode-side electrolyte remaining completely transparent. This *in-situ* experiment confirms that the Janus liquid electrolyte effectively suppressed the cross-over of the oxidized I^- to the reactive anode side and was thereby capable of preventing the detrimental shuttle effect.

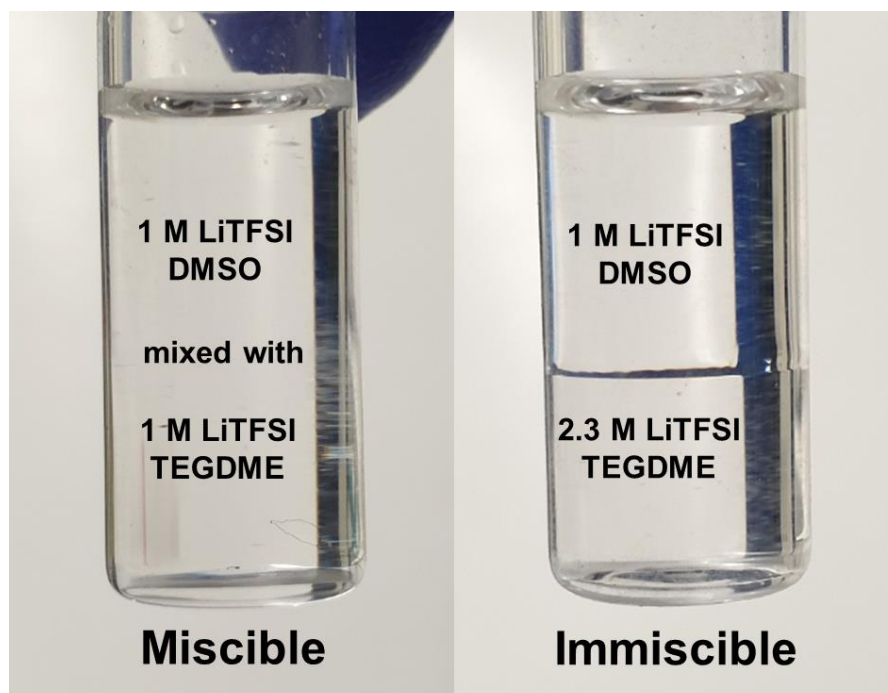


Figure 4.23. Photographs showing the immiscibility behavior of the control electrolyte (1 M LiTFSI DMSO/1 M LiTFSI TEGDME) (left) and Janus liquid electrolyte (1 M LiTFSI DMSO/2.3 M TEGDME) (right).

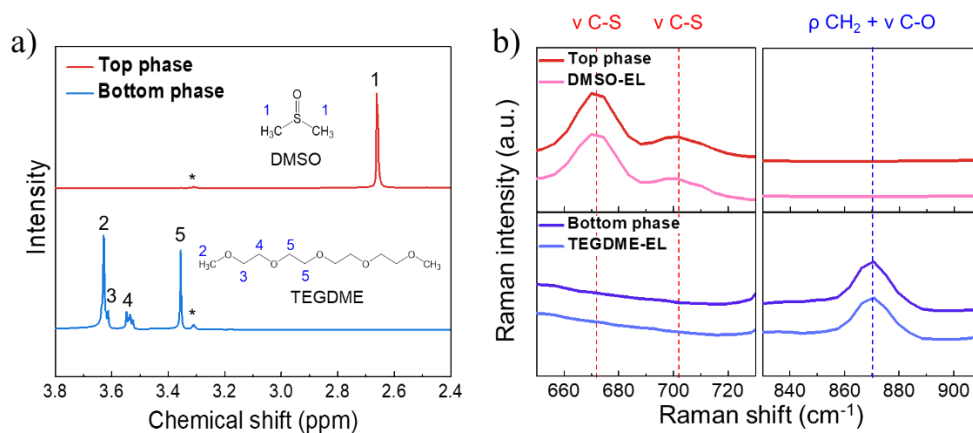


Figure 4.24. (a) NMR and (b) Raman spectra of the top and bottom phases of the Janus liquid electrolyte (shown in figure 4.23, left)

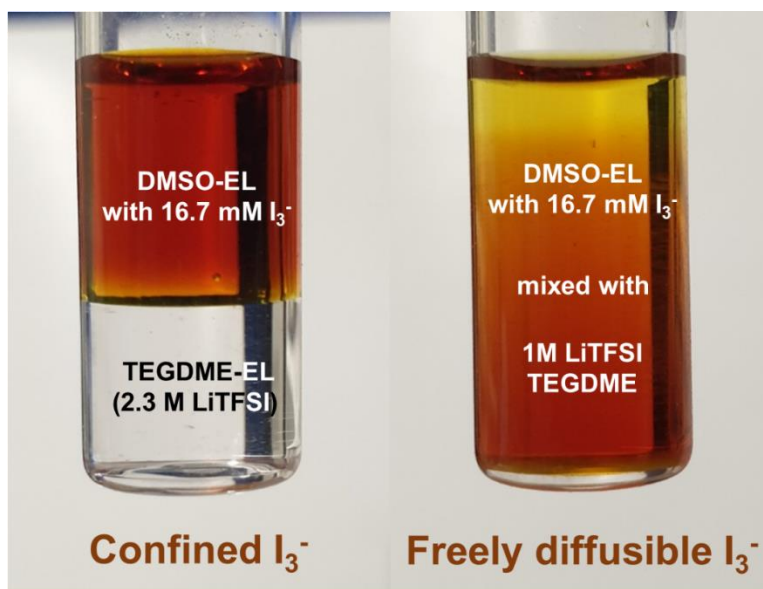


Figure 4.25. Photographs showing the dissolution of 16.7 mM I_3^- (oxidized RM) in the control electrolyte (left) and Janus liquid electrolyte (right).

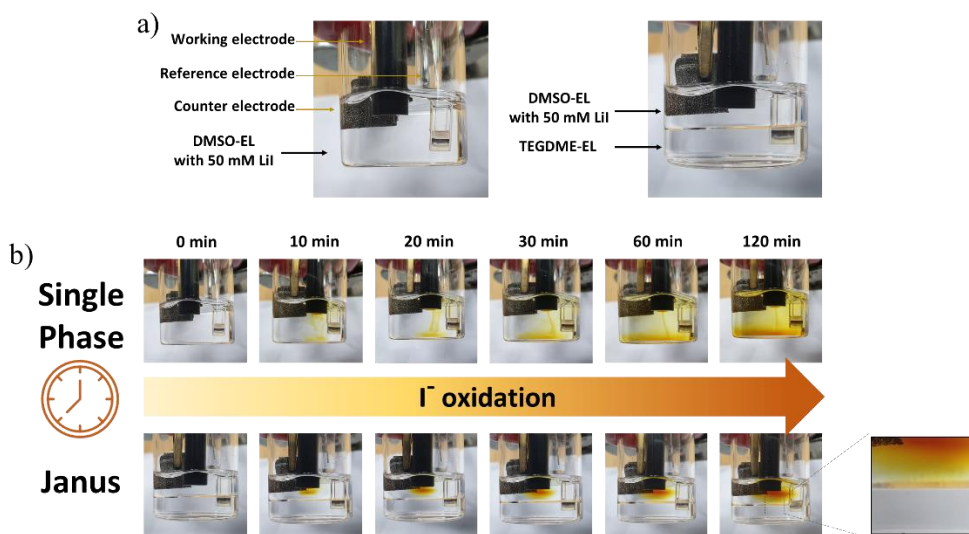


Figure 4.26. *In-situ* observation of I_3^- diffusion behavior using transparent beaker cell. (a) The beaker-cell construction with the single-phase electrolyte (left) and Janus liquid electrolyte (right). Gold and nickel foam were used as the working and counter electrode, respectively. A Ag/Ag^+ electrode was used as the reference electrode. (b) Time-dependent I_3^- diffusion behavior in single-phase and Janus liquid electrolyte. In the single-phase electrolyte, the yellow I_3^- diffused to all areas of the electrolyte after 120 min of oxidation. In contrast, for the Janus liquid electrolyte, I_3^- did not diffuse to the anode side and instead remained at the cathode side.

4.2.3.2 Electrochemical properties of lithium–oxygen cell employing Janus liquid electrolyte

To assess whether controlled diffusion of the RM^+ by the Janus liquid electrolyte leads to the actual suppression of the shuttle effect in a cell environment, a coin-type lithium–oxygen cell was prepared and its electrochemical properties were investigated. Note that the anode-side electrolyte was assembled in a coin-type cell structure in a gel state for mechanical stability, as depicted in figure 4.27 (details of the cell fabrication are provided in the experimental method). For comparison, lithium–oxygen cells with the DMSO-EL single-phase electrolyte were similarly fabricated and examined. As the shuttle effect has been reported to promote substantial degradation of lithium-metal anodes,^{18, 44, 48, 49} the anode of each cell was inspected to immediately verify the effect of the Janus liquid electrolyte (DMSO-EL with 50 mM LiI/TEGDME-EL). Figure 4.28 presents photographs of the lithium-metal anode retrieved from the lithium–oxygen cells, which were cycled at a current density of 1000 mA g^{-1} with a capacity cut-off of 500 mAh g^{-1} . The lithium metal cycled with the single-phase electrolyte (DMSO-EL with 50 mM LiI) was significantly degraded by the repeated cycling, as shown in figure 4.28.b, compared with the pristine state of lithium metal (figure 4.28.a). Even after 20 cycles, the surface of the lithium-metal anode turned black, indicating that extensive side reactions occurred at the surface. This degradation is attributed to the diffusion of the oxidized RM toward the anode and the corresponding side reactions with the lithium metal. It is notable that degradation of the lithium-metal anode was not

observed in a lithium-metal symmetric cell employing DMSO electrolyte, as shown in figure 4.29, confirming that the degradation was not caused by any intrinsic issue between lithium metal and the DMSO solvent^{50, 51}. In sharp contrast, the lithium-metal anode cycled with the Janus liquid electrolyte remained stable without any significant deterioration after 20 cycles, as depicted in figure 4.28.c. This finding suggests that the Janus liquid electrolyte successfully confined the redox reaction related to the RM to the cathode-side electrolyte and prevented potential side reactions with lithium metal, thus improving the stability of the anode. The surfaces of the lithium-metal anodes were further examined using scanning electron microscopy, as shown in figure 4.30. The clean pristine lithium-metal surface (figure 4.30.a) was well retained in the Janus electrolyte after the electrochemical cycling (figure 4.30.c), whereas that in the single-phase electrolyte degraded substantially, with the formation of non-regular-shaped byproducts (figure 4.30.b).

It was also verified that the electrochemical reversibility of the lithium-metal anode could be subsequently improved in the Janus electrolyte system. In a separate experiment, we investigated the amount of active lithium remaining in the anode as a function of cycle number using a thin lithium foil with a thickness of 20 μm . The thin lithium-metal anode was retrieved after cycling and reassembled to construct a Li/Cu cell to quantify the remaining active lithium (see experimental details in Experimental section). Figure 4.31 compares the capacities obtainable from the Li/Cu cells employing the lithium-metal anodes retrieved from the cells of the single-phase and Janus liquid electrolytes. Whereas the pristine 20- μm lithium anode

delivered a capacity of 3.96 mAh in a fresh cell, the lithium anode retrieved from the single-phase-electrolyte cell only delivered a capacity of 0.80 mAh, implying that a major portion of the active lithium, corresponding to as much as 3.16 mAh of the capacity, was lost during the prior cycling, which was attributed to the significant side reactions and passivation. However, the lithium-metal anode retrieved from the cell using the Janus liquid electrolyte maintained a high discharge capacity corresponding to 3.27 mAh, with lithium loss of 0.69 mAh. This loss is more than four times less than that for the single-phase-electrolyte cell, indicating the improved reversibility of the lithium anode in the Janus electrolyte. This series of qualitative and quantitative analyses clearly demonstrate that the use of the Janus liquid electrolyte enhances the lithium-metal stability by preventing side reactions between lithium and RM^+ through the suppression of cross-over and shuttle effects. It is noteworthy that the improved lithium-metal stability is not associated with the presence of the gel-state electrolyte on lithium metal. We constructed a single-phase bi-layer electrolyte using DMSO-EL gel-state, as illustrated in figure 4.32, and significant degradation of the lithium metal was consistently observed due to the cross-over and shuttle effect of RM (figure 4.33); thus, the enhanced lithium anode stability can be solely attributed to the liquid phase separation in the Janus liquid electrolyte.

The cross-over and shuttling of RM^+ is also known to affect the Li_2O_2 decomposition efficiency in extended cycles, as RM^+ are progressively consumed at the lithium anode side.¹⁸ To study the consequence of this effect on the performance of the air

electrodes, we examined the air electrodes in the two systems after cycling and quantitatively measured the amount of remaining Li_2O_2 that could not be decomposed. In figure 4.34, the amounts of residual Li_2O_2 in the air electrodes are plotted as a function of cycle number comparatively for the two cases. The results indicate that after 10 and 20 cycles, the air electrode retrieved from the single-phase electrolyte contained undecomposed Li_2O_2 corresponding to as much as $\sim 30\%$ and $\sim 48\%$ of that of the targeted state of charge (SoC), respectively. This finding implies that all the RM^+ that were charged could not be used to decompose Li_2O_2 but were instead substantially consumed, resulting in the continuous accumulation of Li_2O_2 in the air electrodes. However, when the cells were cycled with the Janus liquid electrolyte, the amount of residual undecomposed Li_2O_2 in the air electrode was significantly lower than that in the conventional one-electrolyte system, with less than 10% – 20% of the discharge products remaining undecomposed after 20 and 40 cycles. This result confirms that the use of the Janus liquid electrolyte successfully suppressed the consumption of RM^+ by preventing the shuttle effect, leading to the sustained high Li_2O_2 decomposition efficiency.

Inspired by the enhanced anode stability and cathode reversibility, the performance of the RM-containing lithium–oxygen cell was further scrutinized by conducting a galvanostatic cycling experiment employing the Janus liquid electrolyte. Figure 4.35 present galvanostatic profiles of the lithium–oxygen cell cycled with the single-phase and Janus liquid electrolytes, respectively, using the capacity cutoff mode. The cell with the Janus liquid electrolyte clearly exhibited a more stable electrochemical

profile at a current density of 1000 mA g^{-1} compared with that of the cell with the single-phase electrolyte. It is notable that a voltage plateau at $\sim 3.3 \text{ V}$ (*vs.* Li/Li^+) emerged during discharging for the cell cycled with the Janus liquid electrolyte. We assign this plateau to the reduction of the remaining RM^+ (oxidized I^-) during the previous charging.^{49, 52} Considering the limited Li_2O_2 yield during discharge of the lithium–oxygen cell,^{35, 53-55} it is expected that unused RM^+ remains after the end of charge unless it is consumed at the lithium-metal anode. Accordingly, we attribute the evolution of the plateau at $\sim 3.3 \text{ V}$ (*vs.* Li/Li^+) to the absence of the shuttle effect/loss of RM^+ enabled by the Janus liquid electrolyte, as reported elsewhere.^{49, 52} Figure 4.36 show the capacity retention over the cycles for the cells with the single-phase and Janus electrolyte at high (1000 mA g^{-1}) and low (200 mA g^{-1}) current densities, respectively. These results indicate that substantially improved cycle stability was achieved using the Janus electrolyte. Schematics in figure 4.37 illustrates the synergetic effect of the enhanced anode stability and cathode reversibility from the suppressed RM cross-over and confinement in the cathode side can aid in improving the electrochemical stability of lithium–oxygen batteries.

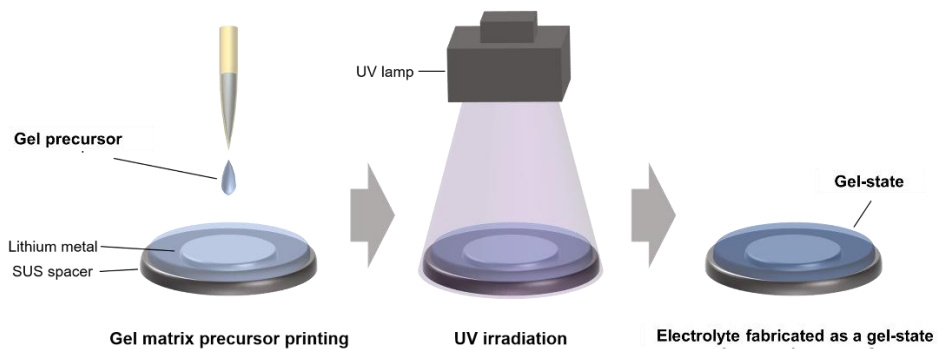


Figure 4.27. Schematic illustration of the fabrication of the gel-state electrolyte using UV-curing-assisted printing process. Details of the procedure are elaborated in the experimental section.

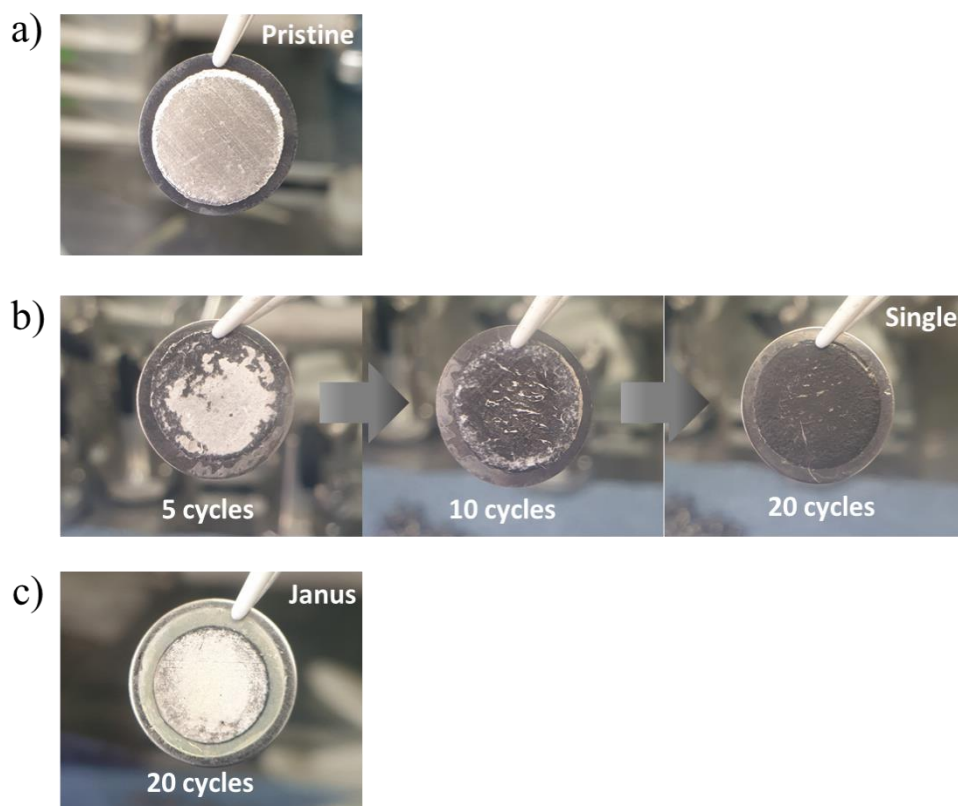


Figure 4.28. Photographs of lithium metal anode: (a) pristine, (b) cycled with single-phase electrolyte, and (c) cycled with Janus liquid electrolyte.

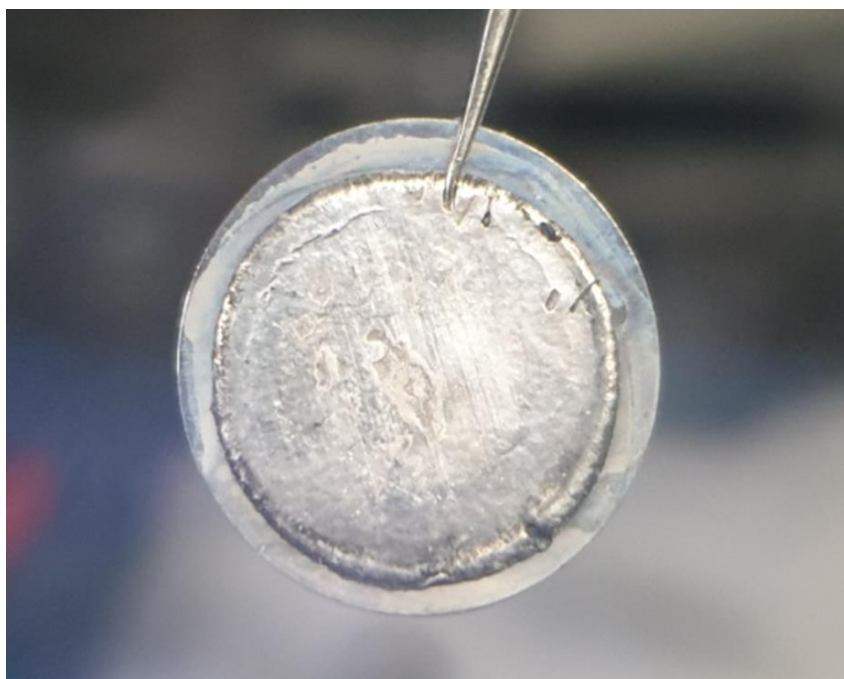


Figure 4.29. Photographs of lithium metal after cycling 20 times in a lithium/1 M LiTFSI DMSO/lithium symmetric cell under oxygen atmosphere.

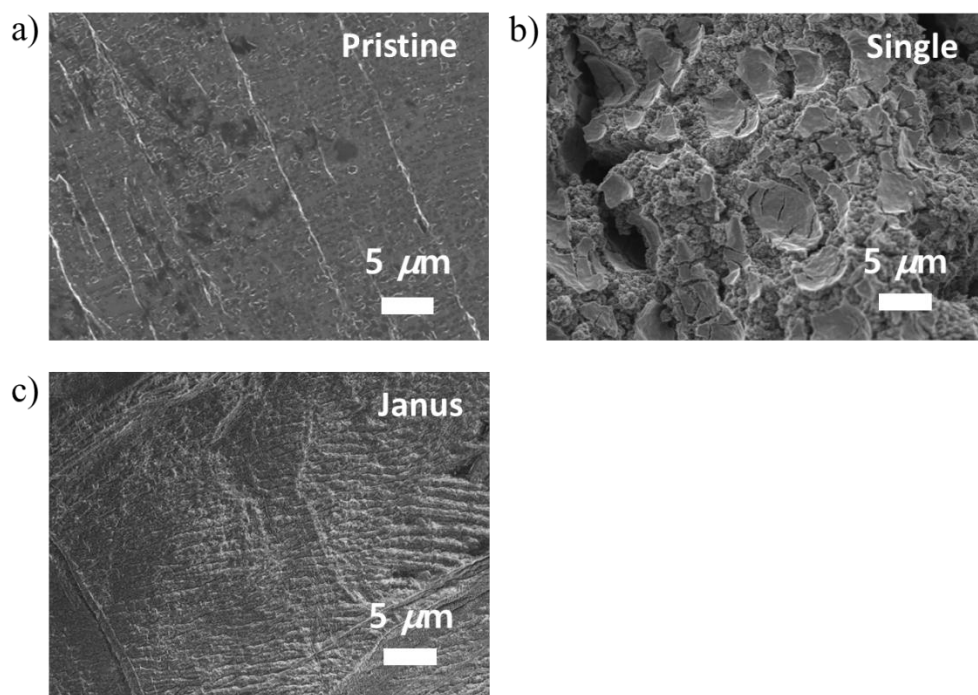


Figure 4.30. SEM images of lithium metal surface: (a) pristine, (b) cycled 20 times with single-phase electrolyte, and (c) cycled 20 times with Janus liquid electrolyte.

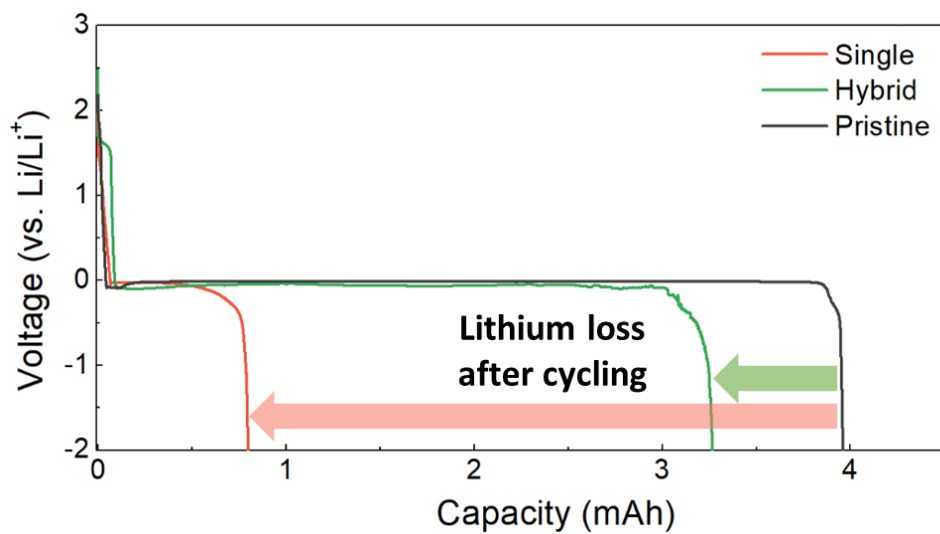


Figure 4.31. Galvanostatic profiles showing remaining active lithium metal after cycling with single-phase and Janus liquid electrolyte. Thin lithium metal foil with a thickness of 20 μm was used.

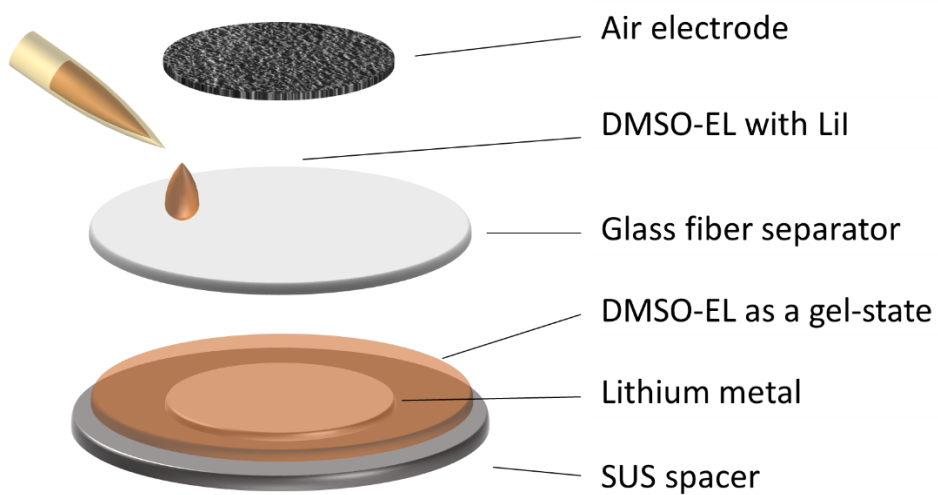


Figure 4.32. Structure of lithium–oxygen cell with single-phase bi-layer electrolyte. For the bottom layer, DMSO-EL was fabricated as a gel-state electrolyte. For the upper layer, a glass fiber separator was soaked in the same DMSO-EL as that used in the bottom layer.

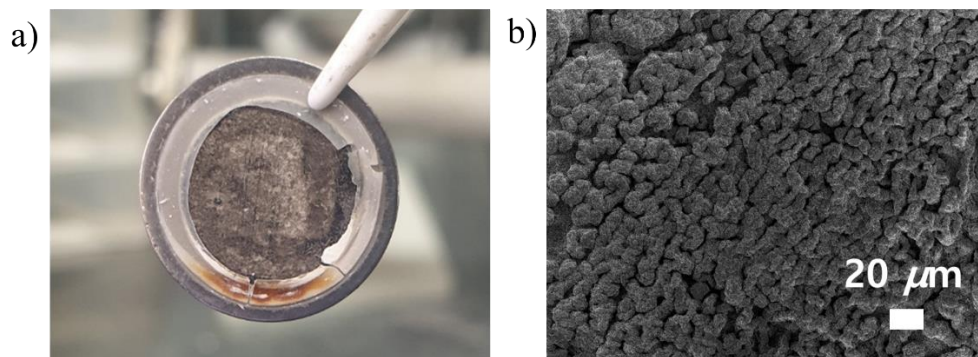


Figure 4.33. (a) Digital and (b) SEM images of lithium metal cycled 20 times in the cell with single-phase bi-layer electrolyte, showing that the presence of the gel-state electrolyte does not improve the stability of lithium metal.

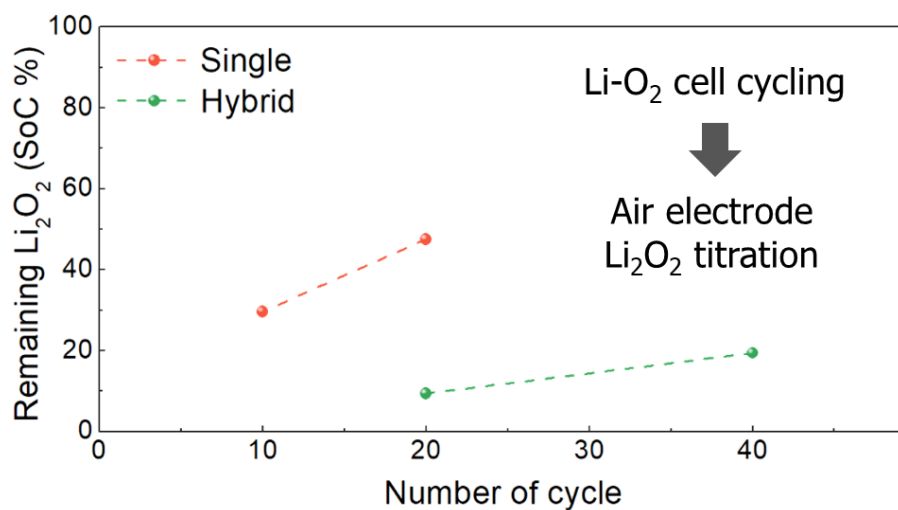


Figure 4.34. Quantitative analysis of the remaining Li_2O_2 in the air electrode after cycling with the single-phase and Janus liquid electrolytes.

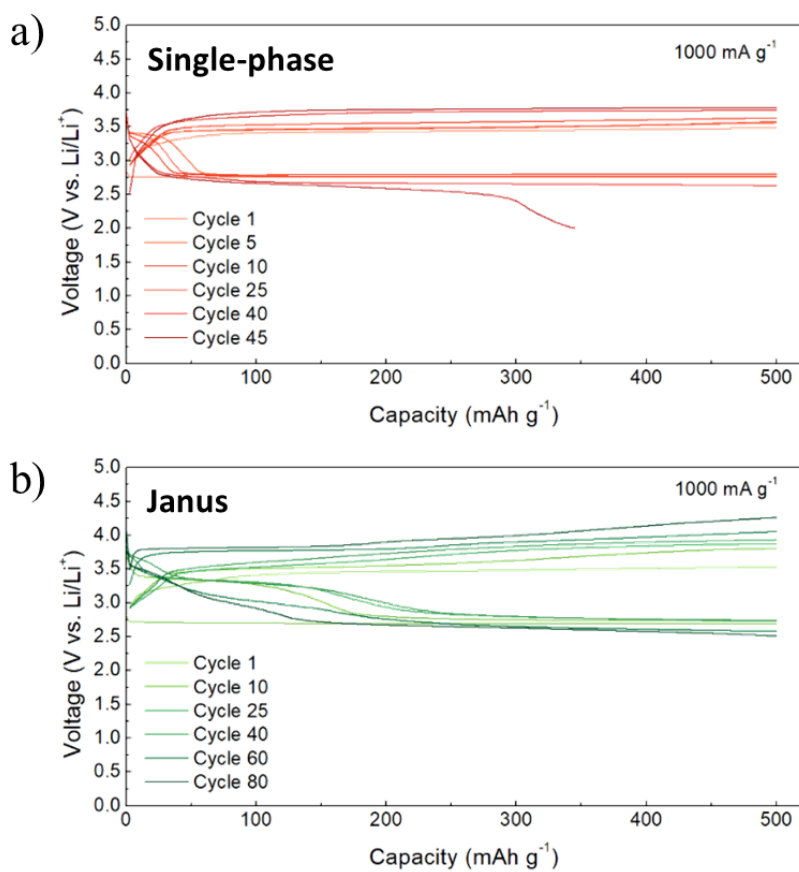


Figure 4.35. Galvanostatic cycling profile of cell with (a) single-phase electrolyte and (b) Janus liquid electrolyte under current rate of 1000 mA g⁻¹.

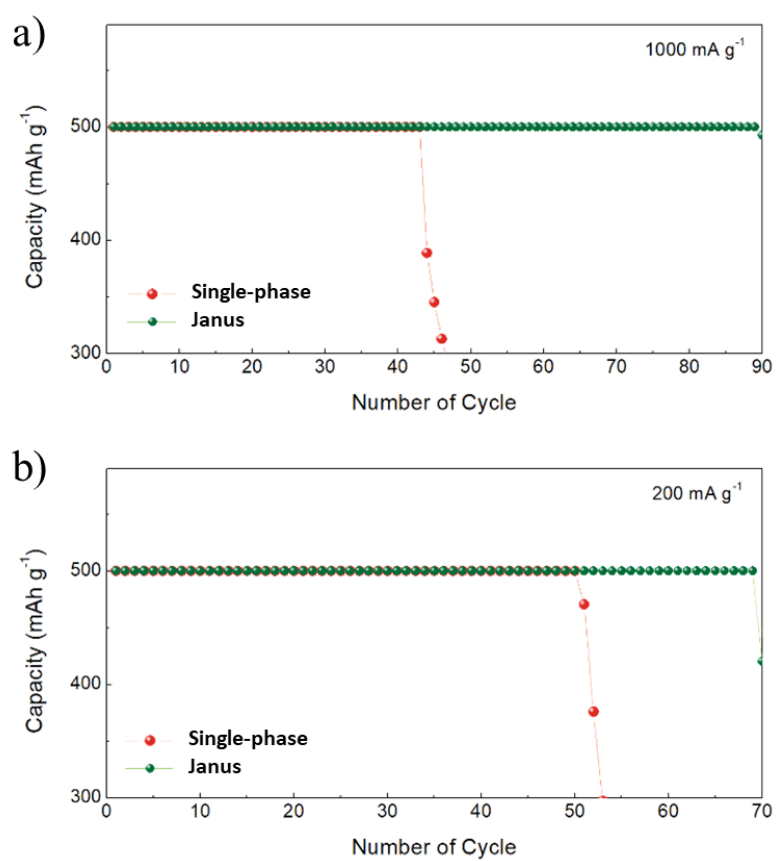


Figure 4.36. Cycling performance of cells under current rate of (c) 1000 mA g⁻¹ and (d) 200 mA g⁻¹.

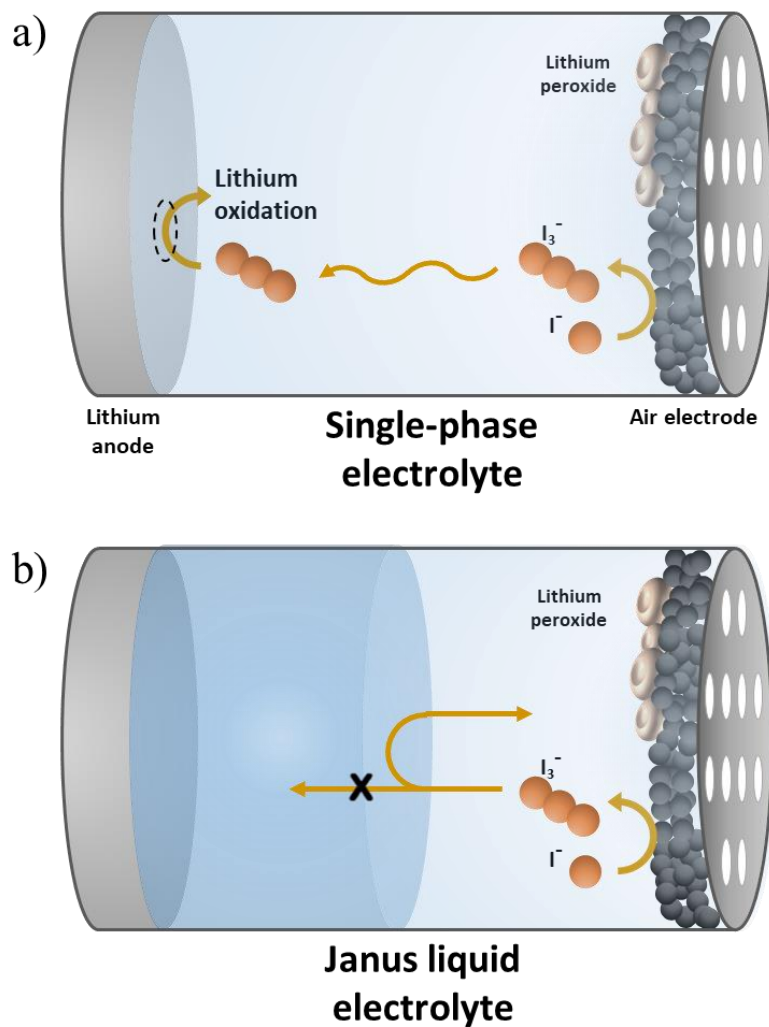


Figure 4.37. Schematic illustrations of RM diffusion behavior in cell with (left) single-phase and (right) Janus liquid electrolyte. (left) The oxidized RM freely diffuses toward the reactive lithium-metal anode, which causes lithium-metal degradation and the consumption of oxidized RM. (right) The oxidized RM does not diffuse through the phase interface and thus remains at the cathode side without the shuttle effect.

4.2.4 Concluding remarks

In summary, we demonstrated the efficacy of exploiting a novel Janus liquid electrolyte in lithium–oxygen batteries. The Janus liquid electrolyte was designed by considering its compatibility with the lithium–oxygen cell system, the RM-solvating property, and the mutual immiscibility of the two liquid phases. The selected Janus liquid electrolyte system, DMSO-EL/TEGDME-EL, enabled the confinement of the oxidized RM^+ species to the cathode-side electrolyte, as demonstrated by a phase-separation experiment and *in-situ* observation of the diffusion behavior. The controlled diffusion resulted in improved lithium metal stability and reversibility of the air electrode, suggesting the successful prevention of the detrimental shuttle effect. Consequently, a lithium–oxygen cell exploiting the Janus liquid electrolyte exhibited much more sustainable cycling performance. We believe that the concept of Janus liquid electrolytes will spur renewed efforts to address the challenging issues to identify stable electrolytes for both lithium-metal and air cathodes in lithium–oxygen batteries.

4.2.5 References

1. Xu K. Nonaqueous liquid electrolytes for lithium-based rechargeable batteries. *Chem. Rev.* 2004, **104**(10): 4303-4418.
2. Yoshio M, Brodd RJ, Kozawa A. *Lithium-ion batteries*, vol. 1. Springer, 2009.
3. Dunn B, Kamath H, Tarascon J-M. Electrical energy storage for the grid: a battery of choices. *Science* 2011, **334**(6058): 928-935.
4. Armand M, Tarascon J-M. Building better batteries. *nature* 2008, **451**(7179): 652.
5. Kang K, Meng YS, Bréger J, Grey CP, Ceder G. Electrodes with high power and high capacity for rechargeable lithium batteries. *Science* 2006, **311**(5763): 977-980.
6. Goodenough JB, Park K-S. The Li-ion rechargeable battery: a perspective. *J. Am. Chem. Soc.* 2013, **135**(4): 1167-1176.
7. Xu K. Electrolytes and interphases in Li-ion batteries and beyond. *Chem. Rev.* 2014, **114**(23): 11503-11618.
8. Freunberger SA, Chen Y, Peng Z, Griffin JM, Hardwick LJ, Bardé F, *et al.* Reactions in the rechargeable lithium–O₂ battery with alkyl carbonate electrolytes. *J. Am. Chem. Soc.* 2011, **133**(20): 8040-8047.
9. Li F, Zhang T, Zhou H. Challenges of non-aqueous Li–O₂ batteries: electrolytes, catalysts, and anodes. *Energy Environ. Sci.* 2013, **6**(4): 1125-1141.

10. Mikhaylik YV, Akridge JR. Polysulfide shuttle study in the Li/S battery system. *J. Electrochem. Soc.* 2004, **151**(11): A1969-A1976.
11. Lim H-D, Lee B, Zheng Y, Hong J, Kim J, Gwon H, *et al.* Rational design of redox mediators for advanced Li–O₂ batteries. *Nat. Energy* 2016, **1**(6): 16066.
12. Wang L, Wang Y, Xia Y. A high performance lithium-ion sulfur battery based on a Li₂S cathode using a dual-phase electrolyte. *Energy Environ. Sci.* 2015, **8**(5): 1551-1558.
13. Ko Y, Park H, Kim B, Kim JS, Kang K. Redox Mediators: A Solution for Advanced Lithium–Oxygen Batteries. *Trends Chem.* 2019.
14. Chen Y, Freunberger SA, Peng Z, Fontaine O, Bruce PG. Charging a Li–O₂ battery using a redox mediator. *Nat. Chem.* 2013, **5**(6): 489.
15. Ko Y, Park H, Lee B, Bae Y, Park SK, Kang K. A comparative kinetic study of redox mediators for high-power lithium–oxygen batteries. *J. Mater. Chem. A* 2019, **7**(11): 6491-6498.
16. Ko Y, Park H, Kim J, Lim HD, Lee B, Kwon G, *et al.* Biological redox mediation in electron transport chain of bacteria for oxygen reduction reaction catalysts in lithium–oxygen batteries. *Adv. Funct. Mater.* 2019, **29**(5): 1805623.
17. Bae Y, Park H, Ko Y, Kim H, Park SK, Kang K. Bifunctional Oxygen Electrocatalysts for Lithium–Oxygen Batteries. *Batteries & Supercaps* 2019, **2**(4): 311-325.

18. Qiao Y, He Y, Wu S, Jiang K, Li X, Guo S, *et al.* MOF-Based Separator in an Li–O₂ Battery: An Effective Strategy to Restrain the Shuttling of Dual Redox Mediators. *ACS Energy Lett.* 2018, **3**(2): 463-468.
19. Bergner BJ, Busche MR, Pinedo R, Berkes BzB, Schröder D, Janek Jr. How to improve capacity and cycling stability for next generation Li–O₂ batteries: approach with a solid electrolyte and elevated redox mediator concentrations. *ACS Appl. Mater. Interfaces* 2016, **8**(12): 7756-7765.
20. Yin W, Grimaud A, Azcarate I, Yang C, Tarascon J-M. Electrochemical Reduction of CO₂ Mediated by Quinone Derivatives: Implication for Li–CO₂ Battery. *J. Phys. Chem. C* 2018, **122**(12): 6546-6554.
21. Liang Y, Tao Z, Chen J. Organic electrode materials for rechargeable lithium batteries. *Adv. Energy Mater.* 2012, **2**(7): 742-769.
22. Lee S, Kwon G, Ku K, Yoon K, Jung SK, Lim HD, *et al.* Recent progress in organic electrodes for Li and Na rechargeable batteries. *Adv. Mater.* 2018, **30**(42): 1704682.
23. Moy D, Manivannan A, Narayanan S. Direct measurement of polysulfide shuttle current: A window into understanding the performance of lithium-sulfur cells. *J. Electrochem. Soc.* 2015, **162**(1): A1-A7.
24. Bai S, Liu X, Zhu K, Wu S, Zhou H. Metal–organic framework-based separator for lithium–sulfur batteries. *Nat. Energy* 2016, **1**(7): 1-6.
25. Lee SH, Park JB, Lim HS, Sun YK. An advanced separator for Li–O₂ batteries: maximizing the effect of redox mediators. *Adv. Energy Mater.*

- 2017, **7**(18): 1602417.
26. Song Z, Qian Y, Otani M, Zhou H. Stable li–organic batteries with nafion-based sandwich-type separators. *Adv. Energy Mater.* 2016, **6**(7): 1501780.
 27. Gao X, Chen Y, Johnson LR, Jovanov ZP, Bruce PG. A rechargeable lithium–oxygen battery with dual mediators stabilizing the carbon cathode. *Nat. Energy* 2017, **2**(9): 17118.
 28. Zhou H, Wang Y, Li H, He P. The development of a new type of rechargeable batteries based on hybrid electrolytes. *ChemSusChem* 2010, **3**(9): 1009-1019.
 29. Li T, Wang C, Cheng J, Guo J, Xiao A, Hou H, *et al.* Janus Polymer Composite Electrolytes Improve the Cycling Performance of Lithium Oxygen Battery. *ACS Appl. Mater. Interfaces* 2020.
 30. Black R, Adams B, Nazar L. Non-aqueous and hybrid Li-O₂ batteries. *Adv. Energy Mater.* 2012, **2**(7): 801-815.
 31. Peng Z, Freunberger SA, Chen Y, Bruce PG. A reversible and higher-rate Li-O₂ battery. *Science* 2012, **337**(6094): 563-566.
 32. Thotiyl MMO, Freunberger SA, Peng Z, Chen Y, Liu Z, Bruce PG. A stable cathode for the aprotic Li–O₂ battery. *Nat. Mater.* 2013, **12**(11): 1050-1056.
 33. Jung H-G, Hassoun J, Park J-B, Sun Y-K, Scrosati B. An improved high-performance lithium–air battery. *Nat. Chem.* 2012, **4**(7): 579-585.
 34. Cho S-J, Jung GY, Kim SH, Jang M, Yang D-K, Kwak SK, *et al.*

- Monolithic heterojunction quasi-solid-state battery electrolytes based on thermodynamically immiscible dual phases. *Energy Environ. Sci.* 2019, **12**(2): 559-565.
35. Freunberger SA, Chen Y, Drewett NE, Hardwick LJ, Bardé F, Bruce PG. The Lithium–Oxygen Battery with Ether-Based Electrolytes. *Angew. Chem., Int. Ed.* 2011, **50**(37): 8609-8613.
36. Hansen CM. The three dimensional solubility parameter. *Danish Technical: Copenhagen* 1967, **14**.
37. Gottlieb HE, Kotlyar V, Nudelman A. NMR chemical shifts of common laboratory solvents as trace impurities. *J. Org. Chem.* 1997, **62**(21): 7512-7515.
38. Huff LA, Rapp JL, Zhu L, Gewirth AA. Identifying lithium–air battery discharge products through ^6Li solid-state MAS and ^1H – ^{13}C solution NMR spectroscopy. *J. Power Sources* 2013, **235**: 87-94.
39. Yamada Y, Usui K, Chiang CH, Kikuchi K, Furukawa K, Yamada A. General observation of lithium intercalation into graphite in ethylene-carbonate-free superconcentrated electrolytes. *ACS Appl. Mater. Interfaces* 2014, **6**(14): 10892-10899.
40. Bocklitz T, Dörfer T, Heinke R, Schmitt M, Popp J. Spectrometer calibration protocol for Raman spectra recorded with different excitation wavelengths. *Spectrochim. Acta, Part A* 2015, **149**: 544-549.
41. Ruther RE, Yang G, Delnick FM, Tang Z, Lehmann ML, Saito T, *et al.*

- Mechanically Robust, Sodium-Ion Conducting Membranes for Nonaqueous Redox Flow Batteries. *ACS Energy Lett.* 2018, **3**(7): 1640-1647.
42. Yang H, Yin L, Shi H, He K, Cheng H-M, Li F. Suppressing lithium dendrite formation by slowing its desolvation kinetics. *Chem. Commun.* 2019, **55**(88): 13211-13214.
43. Atkins PW, De Paula J, Keeler J. *Atkins' physical chemistry*. Oxford university press, 2018.
44. Zhang T, Liao K, He P, Zhou H. A self-defense redox mediator for efficient lithium–O₂ batteries. *Energy Environ. Sci.* 2016, **9**(3): 1024-1030.
45. Yu M, Ren X, Ma L, Wu Y. Integrating a redox-coupled dye-sensitized photoelectrode into a lithium–oxygen battery for photoassisted charging. *Nat. Commun.* 2014, **5**: 5111.
46. Nakanishi A, Thomas ML, Kwon H-M, Kobayashi Y, Tatara R, Ueno K, *et al.* Electrolyte Composition in Li/O₂ Batteries with LiI Redox Mediators: Solvation Effects on Redox Potentials and Implications for Redox Shuttling. *J. Phys. Chem. C* 2018, **122**(3): 1522-1534.
47. Zhang X-P, Li Y-N, Sun Y-Y, Zhang T. Inverting the Triiodide Formation Reaction by the Synergy between Strong Electrolyte Solvation and Cathode Adsorption for Lithium–Oxygen Batteries. *Angew. Chem., Int. Ed.* 2019, **58**(51): 18394-18398.

48. Zhang J, Sun B, Zhao Y, Kretschmer K, Wang G. Modified tetrathiafulvalene as an organic conductor for improving performances of Li–O₂ batteries. *Angew. Chem., Int. Ed.* 2017, **56**(29): 8505-8509.
49. Ko Y, Park H, Lee K, Kim SJ, Park H, Bae y, *et al.* Anchored mediator enabling shuttle–free redox mediation in lithium–oxygen batteries. *Angew. Chem.* 2020.
50. Moon S, Park H, Yoon G, Lee MH, Park K-Y, Kang K. Simple and Effective Gas-Phase Doping for Lithium Metal Protection in Lithium Metal Batteries. *Chem. Mater.* 2017, **29**(21): 9182-9191.
51. Liu B, Xu W, Yan P, Kim ST, Engelhard MH, Sun X, *et al.* Stabilization of Li Metal Anode in DMSO-Based Electrolytes via Optimization of Salt–Solvent Coordination for Li–O₂ Batteries. *Adv. Energy Mater.* 2017, **7**(14): 1602605.
52. Wu S, Qiao Y, Deng H, He Y, Zhou H. Minimizing the Abnormal High-Potential Discharge Process Related to Redox Mediators in Lithium–Oxygen Batteries. *J. Phys. Chem. Lett.* 2018, **9**(23): 6761-6766.
53. Barde F, Chen Y, Johnson L, Schaltin S, Fransaer J, Bruce PG. Sulfone-Based Electrolytes for Nonaqueous Li–O₂ Batteries. *J. Phys. Chem. C* 2014, **118**(33): 18892-18898.
54. McCloskey BD, Valery A, Luntz AC, Gowda SR, Wallraff GM, Garcia JM, *et al.* Combining Accurate O₂ and Li₂O₂ Assays to Separate Discharge and Charge Stability Limitations in Nonaqueous Li–O₂

Batteries. *J. Phys. Chem. Lett.* 2013, **4**(17): 2989-2993.

55. McCloskey B, Speidel A, Scheffler R, Miller D, Viswanathan V, Hummelshøj J, *et al.* Twin problems of interfacial carbonate formation in nonaqueous Li–O₂ batteries. *J. Phys. Chem. Lett.* 2012, **3**(8): 997-1001.

Chapter 5. Conclusion

Nowadays, the development of next-generation energy storage system is indispensable to fulfill the increasing demand on high energy battery system. Li-O₂ battery is most promising candidate to replace a commercial Li-ion battery due to its extremely high theoretical energy density. However, the current state of Li-O₂ battery technology does not guarantee satisfactory performance for practical use of the system. Exploiting catalysts, especially redox mediators, is considered powerful approach to remarkably improve the performance of Li-O₂ battery, which promotes worldwide research effort to discover suitable catalysts to enhance cell performance. To develop highly performing redox mediator, multidisciplinary research is required. From exploring new catalysts, to fundamental study and dealing with practical issue, multifaceted approach can facilitate optimized utilization of redox mediators.

Exploring new materials is a first and essential step in development process. When searching materials, requirements that candidates must satisfy needs to be defined and based on such design rule appropriate screening can be conducted. Once appropriate requirements was set, turning eyes to another system sometimes inspire new finding. For example, redox mediator for oxygen reduction reaction in Li-O₂ battery should ensure its appropriate redox potential and redox reversibility. Interestingly, there exists catalyst working similarly in biological respiration system and it was found that it satisfies the requirements to be adopted in Li-O₂ cell. Inspired by the similarity between two system, biological catalyst, vitamin K₂ was successfully introduced into Li-O₂ battery as a redox mediator improving the performance of the cell.

Not only search for new materials, but also understanding fundamental aspects is crucial in designing catalyst. For example, reaction mechanism and intrinsic property of catalyst play an important role in determining the performance of heterogeneous electrocatalyst. To better understand fundamentals of redox mediator, comparative study employing various materials was conducted. On discharge, it was found that kinetics of redox mediator is controlled by steric hindrance around redox center, which further implies inner-sphere electron transfer occurs with the formation of intermediate state. The implication of kinetics on catalytic performance was investigated and it was demonstrated that mediators with intermediate kinetics induces best cell performance. Similar comparative study regarding charge process revealed that kinetics of redox mediator is governed by Marcus theory and it directly determines the power capability of the cell.

Although the property of redox mediator is optimally designed, its actual performance in cell environment can be deteriorated by practical issues. For example, shuttle effect is one of the most harmful phenomena when utilizing soluble species such as redox mediator. Dissolved in liquid electrolyte, redox mediator freely diffuses even toward reactive anode side, causing degradation of anode and mediator itself. Accordingly, preventing shuttle effect is necessary step for sustainable use of mediator. To this end, the strategy to anchor redox mediator in polymer chain was employed. Limited solubility of polymer suppresses the diffusion of redox mediator and at the same time, in-chain electron transfer mechanism in polymer maintains the hole-carrying property. As the next approach, Janus electrolyte consisting of two different immiscible liquid electrolytes was employed to ensure free diffusion of redox mediator in liquid phase and suppress shuttle effect, simultaneously. Those

approaches successfully prevented detrimental shuttle effect and led to sustainable redox mediation.

In conclusion, multifaceted research strategy, 1) exploring new materials, 2) studying fundamental aspect, and 3) addressing practical issues with the aim of developing and designing high performance redox mediator was introduced in this dissertation. This study will found a solid basis for developing catalysts for Li-O₂ battery and contributes to realizing practically feasible Li-O₂ battery. Furthermore, it will provide stong research insight in developing various next-generation energy storage systems that necessitates the development of optimal catalysts.

국 문 초 록

환경과 에너지 문제는 인류에게 있어서 깨끗하고 지속 가능한 미래 실현을 위해 마주해야만 하는 쟁점이다. 이러한 흐름에서, 신재생 에너지의 사용을 용이하게 해주는 에너지 저장 장치의 개발은 아주 중요한 문제이다. 수 십년의 개발을 거쳐 현재 리튬 이온 전지가 최첨단의 상용 전지로서 널리 사용되고 있다. 하지만, 무거운 전이 금속을 필수 요소로 사용한다는 점으로 인해 리튬 이온 전지는 에너지 밀도 증가 관점에서 확실한 한계점을 지니고 있다. 이를 대체하기 위하여 과학자들은 금속-공기 전지, 금속-황 전지, 유기물 전지 등과 같은 차세대 전지 시스템에 대하여 꾸준히 연구를 진행해오고 있다. 그 중에서 리튬-공기 전지는 3500 Wh kg^{-1} 에 달하는 높은 이론 에너지 밀도로 인해 많은 관심을 받고 있다. 하지만 높은 잠재성에도 불구하고 시스템의 내재적 문제에서 기인하는 많은 한계점들로 인해 리튬-공기 전지의 상용화는 실현되지 못하고 있다.

이 학위 논문에서는, 산화 환원 매개체를 이용하여 고성능 리튬-공기 전지를 개발하는 것을 주요 주제로 다루고 있다. 반응 경로를 제어할 수 있는 산화 환원 매개체를 이용하여 문제점이 많은 리튬-공기 전지의 기존 충/방전 반응 경로를 우회할 수 있으며 이를 통해 많은 문제들을 해결 할 수 있다. 우수한 성능의 산화 환원 매개체를 개발하기 위하여, 새로운 촉매의 개발에서부터 촉매 성능에 대한 기초적인 연구에 이르는 다방면의 연구가 진행되었다. 또한, 촉매 사용 과정에서 발생하는 셔틀 현상과 같은 실제적인 문제들에 대한 해결법 또한 연구되었다.

제 2장에서는, 생체 시스템으로부터 새로운 촉매를 개발하는 과정을 소개한다. 세포 호흡과정에서의 전자 전달 과정과 리튬-공기 전지 내에서 산화 환원 매개체를 이용한 산소 환원과정간의 유사성에서

영감을 받아 생체 촉매인 비타민 K₂가 리튬-공기 전지용 방전 촉매로도 도입되었으며, 이것이 촉매로서 성공적으로 작용하고 전지 성능을 월등히 향상시킨다는 것이 밝혀졌다. 이를 통해 두 시스템간의 유사성이 어떻게 새로운 발견을 이끌어 낼 수 있는지 보여주고 있다.

제 3장에서는, 산화 환원 매개체의 반응 속도, 반응 메커니즘 등과 같은 기초적인 사항들에 대해 이해하기 위한 연구 방법들을 소개한다. 다양한 매개체를 활용한 비교 연구를 통해 매개체의 반응 속도에 영향을 주는 인자들과 반응 속도와 전지 성능 간의 상관 관계를 규명하였다. 방전 과정 중의 매개체의 반응 속도는 산화 환원 중심부 주변의 입체 구조적 간섭 크기에 영향을 받는다는 것이 밝혀졌으며, 이를 통해 중간체 형성이 동반되는 내부권 전자 전달이 산화 환원 매개체를 이용한 방전 중에 일어난다는 것을 규명하였다. 추가적인 연구를 통해 산화 환원 매개체의 반응 속도와 실제 전지 성능 간에 불케이노 상관 관계가 있는 것이 관찰되었다. 유사한 속도론 관점에서의 연구가 충전 과정에 대해서도 진행되었으며, 산화 환원 매개체의 충전 중 반응 속도는 마커스 이론을 따라 매개체의 이론 전압에 의해 결정된다는 것을 확인하였다. 추가적으로, 매개체의 반응 속도가 전지의 충전 출력 특성과 직접적으로 영향이 있는 것을 확인하였다. 이 장에서는, 우수한 성능의 촉매를 개발하기 위하여 촉매의 기초적인 특성을 파악하는 것의 중요성에 대해 다루고 있다.

마지막으로 제 4장에서는, 산화 환원 매개체의 문제점인 셔틀 현상을 해결하는 연구 전략들을 다루고 있다. 자유롭게 움직이는 특징으로 인해 산화 환원 매개체는 반응성이 높은 음극 쪽으로 쉽게 확산하게 되고 이는 음극 열화, 매개체 분해 등과 같은 많은 문제들을 야기한다. 이를 해결하기 위해 산화 환원 매개체를 고분자에 고정하고 고정형 촉매를 도입하여 셔틀 현상을 억제할 수 있었으며, 고분자 내에

존재하는 전자 확산 기구로 인해 매개체의 전하 전달 특성도 유지할 수 있었다. 두 번째 접근법으로서, 산화 환원 매개체의 이동성을 완전히 유지하면서 셔틀 현상을 억제하기 위하여 새로운 형태의 야누스 액체 전해질이 도입되었다. 상이한 용해 특성을 가진 두 액체 전해질을 각각 음극 및 양극 측에 동시에 사용함으로써, 산화 환원 매개체의 확산 및 셔틀 현상을 완벽히 억제할 수 있었다. 이 장에서는, 전지 구성요소들의 적절한 변형을 통해 셔틀 현상이 억제될 수 있으며 이는 산화 환원 매개체의 장시간 사용을 가능케한다는 것을 확인하였다.

이 학위 논문에서 진행 된 산화 환원 매개체에 대한 1) 새로운 촉매의 개발, 2) 촉매에 대한 기초 연구, 3) 실제적인 문제의 해결과 같은 다방면의 연구는 리튬-공기 전지용 고성능 산화 환원 매개체를 개발하는 것에 대해 기초적인 토대가 될 것이다. 더 나아가, 금속-공기 전지 및 그 외 차세대 전지를 위한 우수한 촉매를 개발함에 있어서 연구적인 통찰력을 제공해 줄 것이다.

주요어: 전기화학, 이차 전지, 리튬-공기 전지, 산화 환원 매개체, 반응 속도론, 셔틀 현상

학 번: 2016-20847